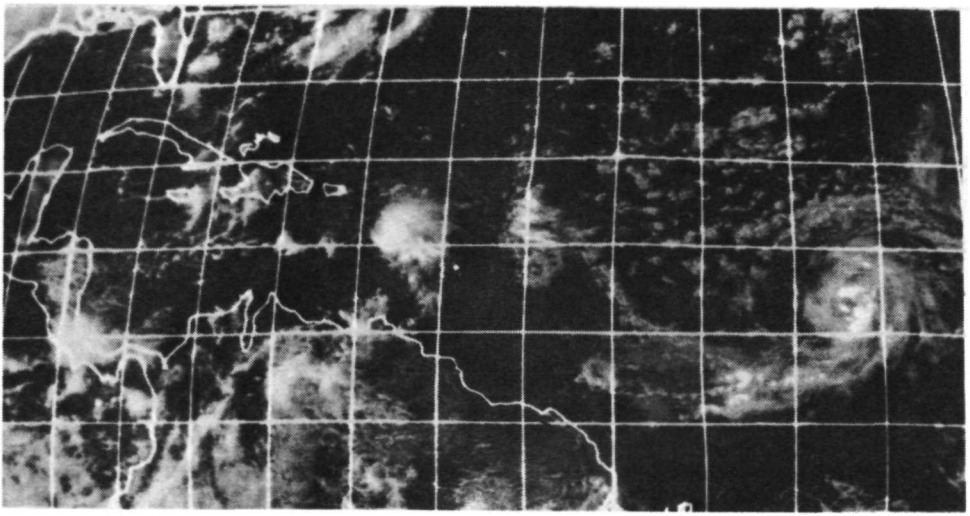

MEASUREMENTS FROM SATELLITE PLATFORMS

Annual Scientific Report on NAS5-11542

1971-1972

Space Science and Engineering Center
University of Wisconsin
Madison, Wisconsin

Cover Picture

Two tropical weather phenomena of great interest to meteorologists are prominent in this picture. Hurricane Anna (17 July 1969) revolves in growing intensity at the right, but the two cloud clusters in the center of the picture are the subjects of particular interest in Dr. Sikdar's paper included in this report. Perhaps cloud clusters are less spectacular than hurricanes, but in the long run it is probably more important to understand their dynamics if we are to understand the meteorology of the tropics better than we do now. Most of the Sun's energy received by the Earth is absorbed in the tropics and cloud clusters appear to be a key factor in the major atmospheric process of energy redistribution. Since our temperate zone weather is a by-product of the energy redistribution process, the study of cloud clusters is a matter of importance.

Space Science and Engineering Center
The University of Wisconsin
Madison, Wisconsin

METEOROLOGICAL MEASUREMENTS FROM SATELLITE PLATFORMS

Annual Scientific Report

on

NAS5-11542

1971-1972

The research in this document has been supported in whole or in part by the National Aeronautics and Space Administration.

December 1972

Verner E. Suomi, Principal Investigator

Contributors

B. Auvine
A. Das
D. Sikdar
F. Stremler

Preface

Quantitative exploitation of meteorological data from geosynchronous satellites is starting to move from the laboratory to operational practice. The papers in this report investigate several aspects of the data applications portion of the total meteorological satellite system.

The first two papers are concerned with measurements taken from geosynchronous satellite data as indicators of atmospheric physical processes. Professor Stremler reports in the third paper on the results of a preliminary study of a method to detect and measure rainfall from geosynchronous orbit. While the concept does not appear feasible at this time, the study did indicate that relatively modest technological advances could provide the necessary capability in the future. The fourth paper documents the first half of a two-year effort to construct a broadly applicable model of geosynchronous orbit satellite attitude and pointing control systems. When completed, it is hoped that this model will assist systems designers and data users in minimizing and correcting geometric inaccuracies in satellite data.

I join with the authors in expressing sincere appreciation to the members of the Space Science and Engineering Center who have assisted in the work reported here, and in thanking the members of the National Aeronautics and Space Administration who have provided the necessary sponsorship of our efforts.

Verner E. Suomi
Principal Investigator

Page Intentionally Left Blank

Contents

Tropospheric Wind Shear and the Related Severe Storm Circulations—
A View from a Geostationary Altitude,
by B. Auvine and D. N. Sikdar 1

On Some Kinematic Properties of the Tropical Atmosphere
as Derived from Cloud Motion Vectors, by D. N. Sikdar 28

The Feasibility of the Application of a Geostationary Satellite
Rake System to Measurements of Rainfall, by F. G. Stremler . . 62

Pointing Error Analysis of Geosynchronous Satellites,
by A. Das and T. C. Huang 99

Page Intentionally Left Blank

TROPOSPHERIC WIND SHEAR AND THE RELATED SEVERE STORM CIRCULATIONS— A VIEW FROM A GEOSTATIONARY ALTITUDE

B. Auvine and D. N. Sikdar

ABSTRACT:

Three severe storm complexes are investigated by means of satellite data to reveal salient differences in circulation features, namely volume flux and anvil divergence. Two of these complexes grew in strongly sheared environments, the third in a nearly shearless one.

The analyses indicate hardly any significant differences in the storm severity, growth features or circulation characteristics, except that in the strong sheared environment multiple cells in a squall-line configuration were embedded within a cloud complex while in the weak-shear environment only single "supercell" storms seemed to be favored. A possible reason for this difference may be due to the downward flux of momentum associated with the presence of a high level jet.

1. Introduction

Meteorological literature has concentrated most of its attention on shear-related storms. Numerous case studies (e.g. Miller, 1959; Browning and Donaldson, 1963) have pointed to shear as an important factor in severe storm formation. Indeed, many severe storm analysts regard vertical wind shear as a virtual prerequisite to severe storm formation (Fawbush et al., 1951; Endlich and Mancuso, 1968).

Numerical models of convection have had varying results when shear is included in the system. Asai (1968) has indicated that shear will suppress shallow convection. Others have suggested that shear under the proper conditions can lead to the formation of significant and even self-perpetrating convection (Jih Ping and Li-Shoo, 1964; Takeda, 1971). Takeda in particular suggests that whereas steady-state storms may be achieved with shear as a mechanism involved in creating or releasing instability in a synoptic situation, there is also a class of storms which can grow, provided the ambient shear is very weak and the atmosphere is sufficiently statically unstable. It is in such situations, we believe, that the moisture front may play a role. Carlson and Ludlum (1968) describe the moisture front as a mechanism capable of releasing

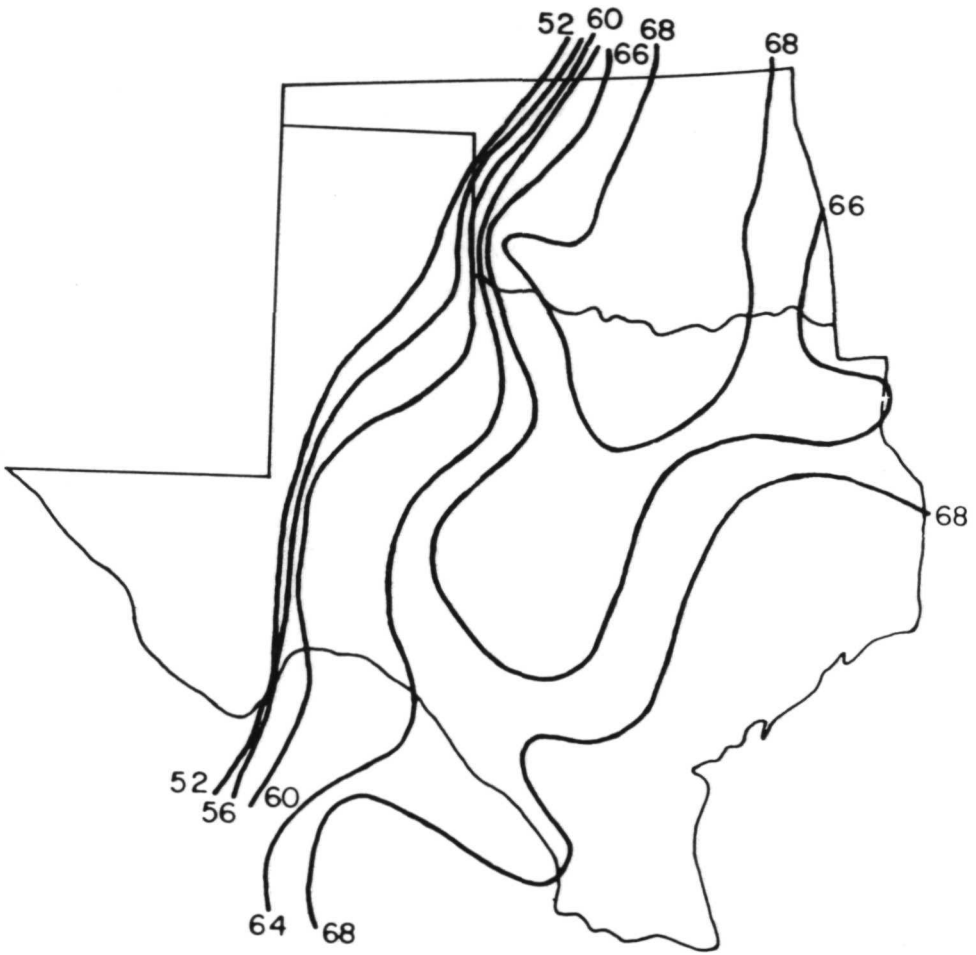

Figure 1. Isopleths of dewpoint (°F) in the Texas-Oklahoma area at 0000Z, May 12, 1970. The moisture front can be seen cutting across Western Texas and Oklahoma from NE to SW.

instability in a violent way and have documented several cases in which synoptic conditions were similar to the case presented in this paper.

The purpose of this paper is to compare some of the ATS-III observed severe storm circulation features such as volume flux, anvil divergence and precipitation efficiency in a weak-shear environment (Lubbock storm of May 11, 1970) to the same features found in environments with strong upper tropospheric wind shear (in particular the cases of April 19 and 23, 1968, and already discussed by Sikdar et al., 1970). Also briefly discussed is the structure of the Lubbock storm using time lapse radar data (WSR 57) taken from Amarillo, Texas.

2. Synoptic Features Related to Three Severe Storms Situations

On May 11, 1970, Lubbock, Texas was struck by two tornadoes, the second of which was violently destructive. The synoptic conditions that day indicated a westward moving moisture front (Figure 1) along which a number of convective cloud masses had their origin. This moisture front consisted essentially of moist Gulf air flowing in to meet dry desert air, with little contrast in temperature between the two air masses. While it has already been documented that such moisture discontinuities in the Gulf region can be associated with severe convective activity (Bradbury, 1969), the May 11 storms are notable for being spawned in a subtropical environment essentially lacking in large vertical wind shear (although Reuss, 1961, reports the existence of a giant cumulonimbus cell growing in a nearly calm atmosphere).

The situation in regard to low and high level winds on May 12 (00 Z) can be seen in Figures 2a,2b while Figure 3a presents an east-west cross-section of isentropes, mixing ratios and isotachs through the convection area. Similar conditions prevailed 12 hours prior to the storms. At 850 mb one can easily see the flow of air northward from the Gulf. It is notable, however, that in the moist airflow from Amarillo (AMA) to Topeka (TOP), a region of relatively no shear exists as can be seen by comparing the low and high level wind speeds. At both AMA and TOP the wind vectors remain relatively constant from 30 kts at the surface to similar wind speeds at higher levels. Further to the south at Midland, Texas (MAF), a significant shear is, however, present, due evidently to the influence of the subtropical jet over north Mexico. What is significant in this May 11 case is the fact that severe weather is not associated with this strongly sheared regime where vertical differential advection could be expected to encourage convection, but with the moderate- to low-shear area further north. At the time of these synoptic charts, vigorous convection was to be found at Lubbock (about midway between MAF and AMA) northeastwards to the east of AMA and again in northeast Kansas. Thus, while the shear at Midland of about 1.7×10^{-3} sec^{-1} is somewhat below that prescribed by Marwitz (1972) for supercell storms (2.5 to 4.0×10^{-3} sec^{-1}), values at Lubbock likely averaged 0.9×10^{-3} sec^{-1} with even smaller values to the north of Lubbock and in Kansas.

One may also note in the 200 mb map that the region of severe weather may be said to be in a "diffluence" region between the polar jet over Nevada and the subtropical jet over northern Mexico. A similar situation is to be found in other severe storm situations, as, for instance,

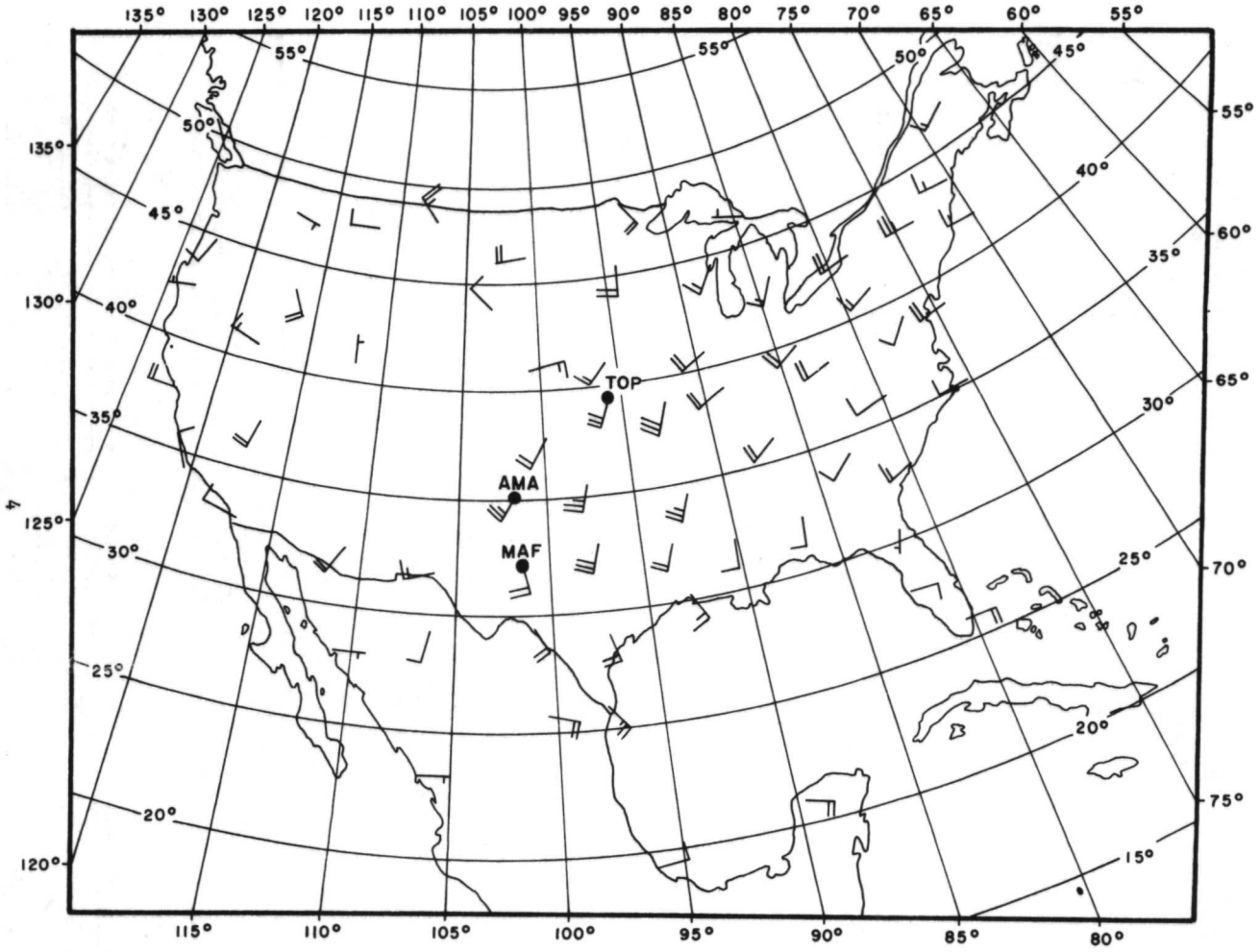

Figure 2. a) 850 mb winds, 0000Z May 12, 1970.

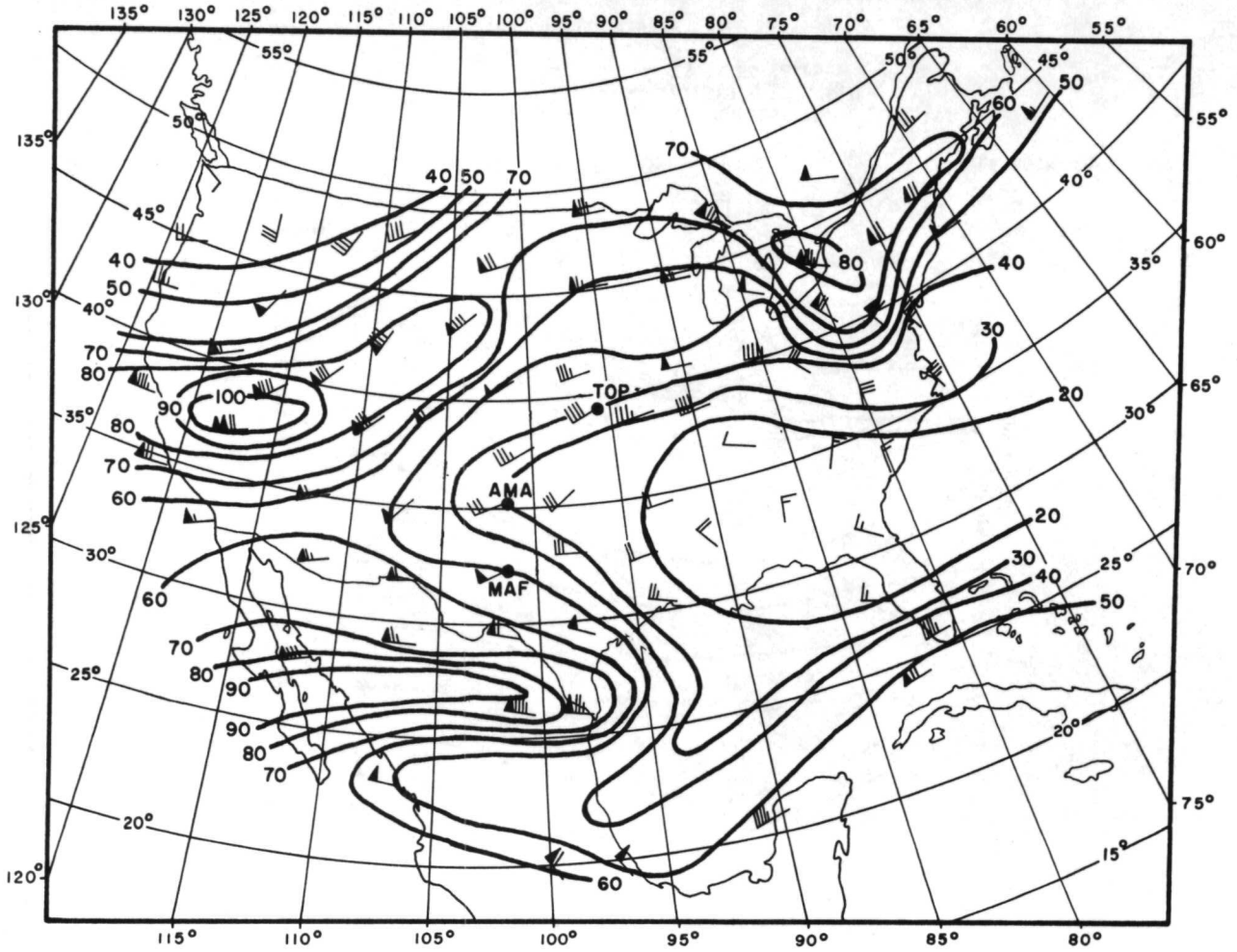

Figure 2. b) 200 mb winds, 0000Z May 12, 1970 with isotachs.

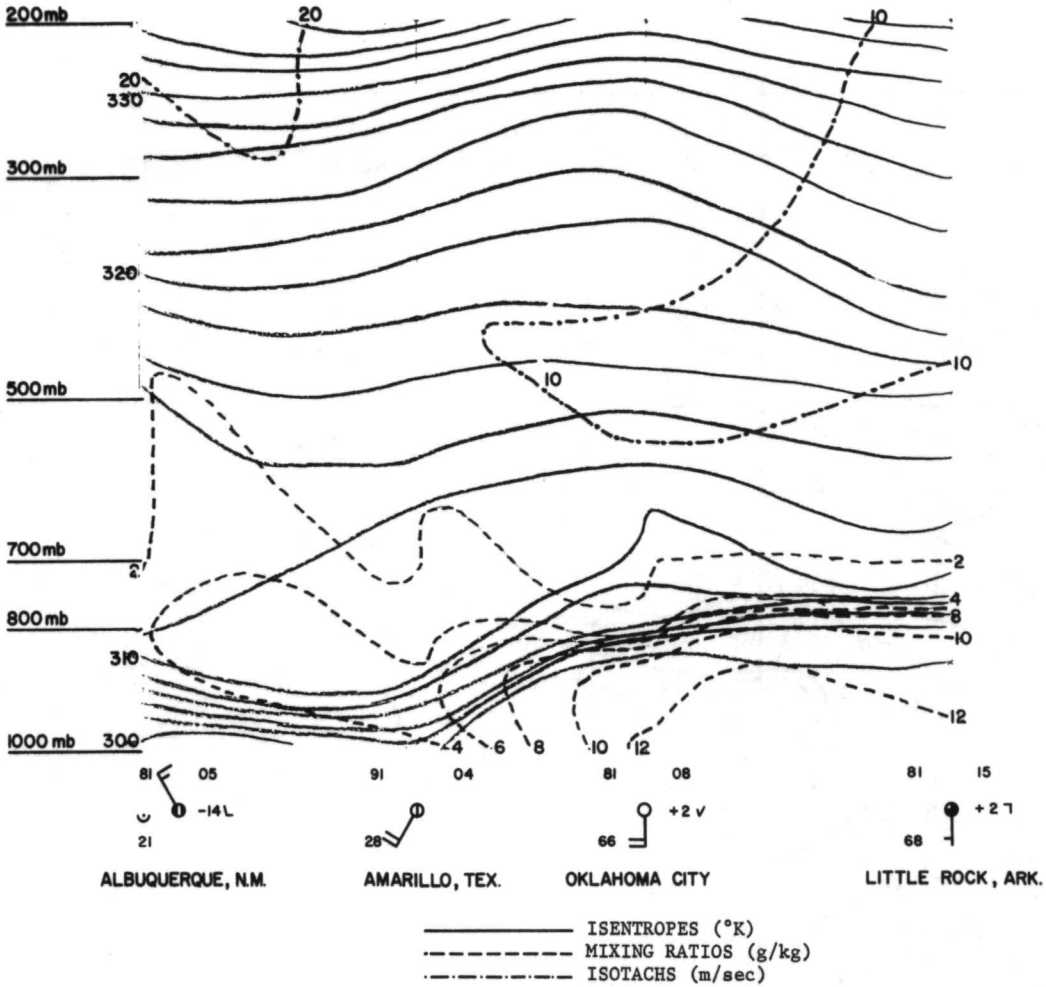

Figure 3. a) East-west cross-section through severe storm area, 0000Z, May 12, 1970.

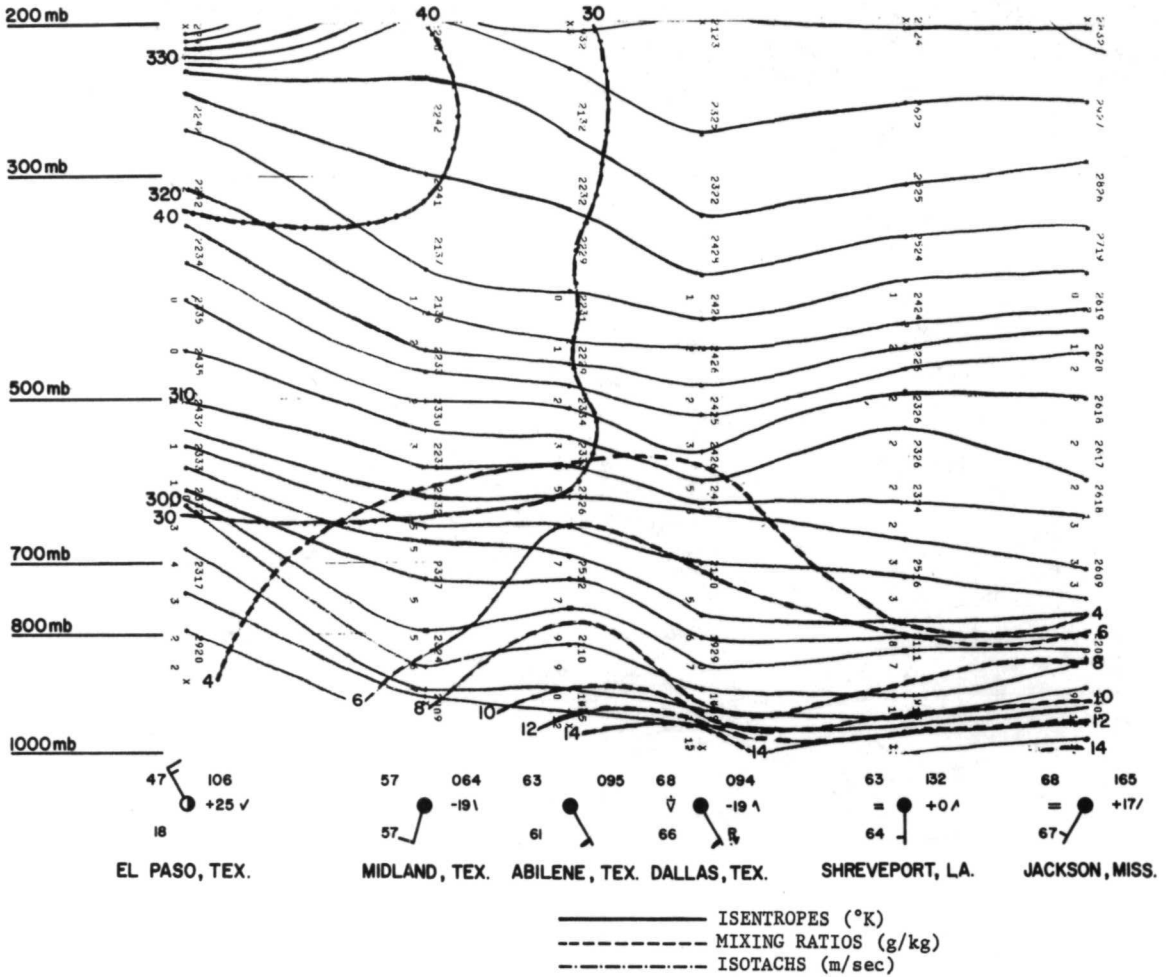

Figure 3. b) East-west cross-section through severe storm area, 1200Z, April 19, 1968.

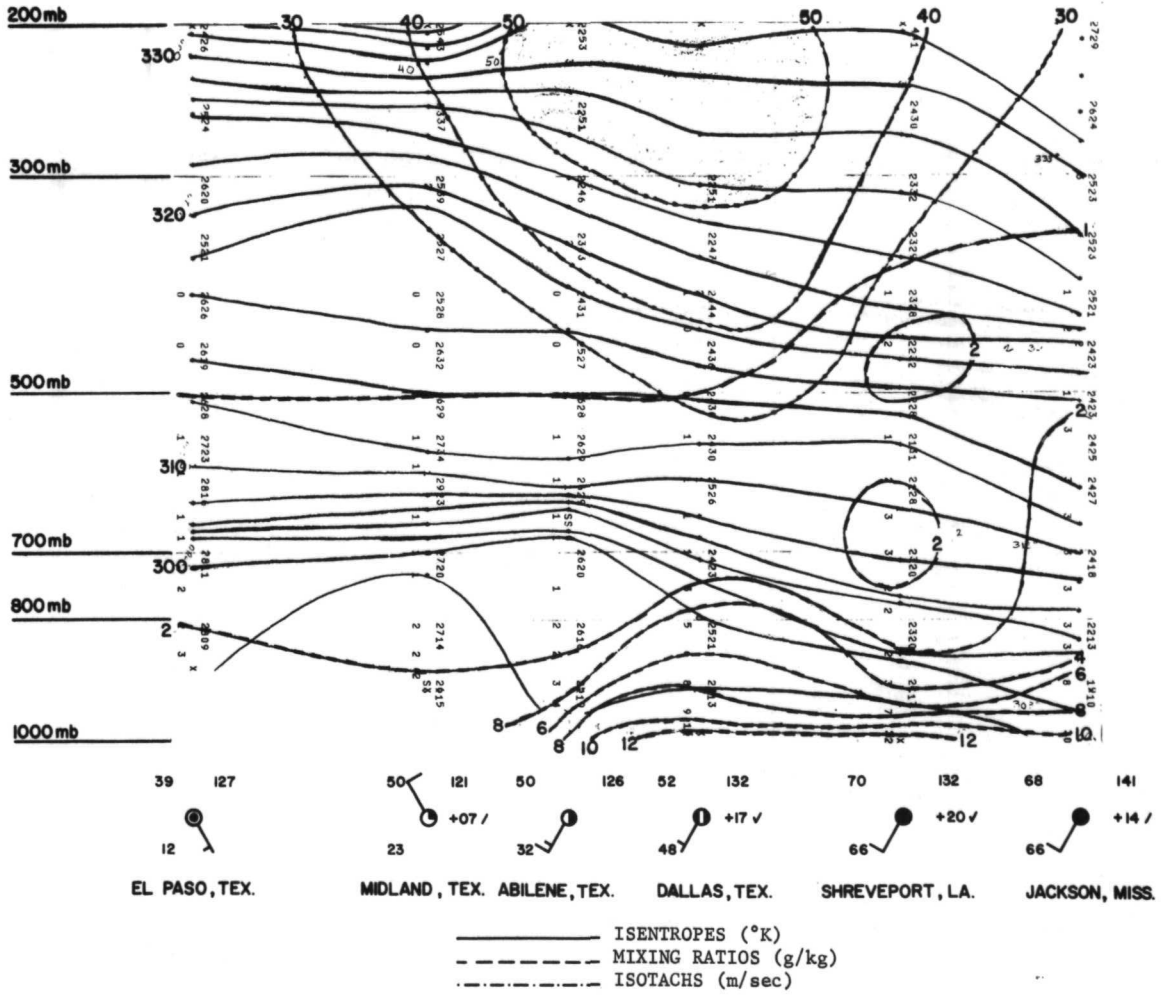

Figure 3. c) Same, except for 0000Z, April 20, 1968.

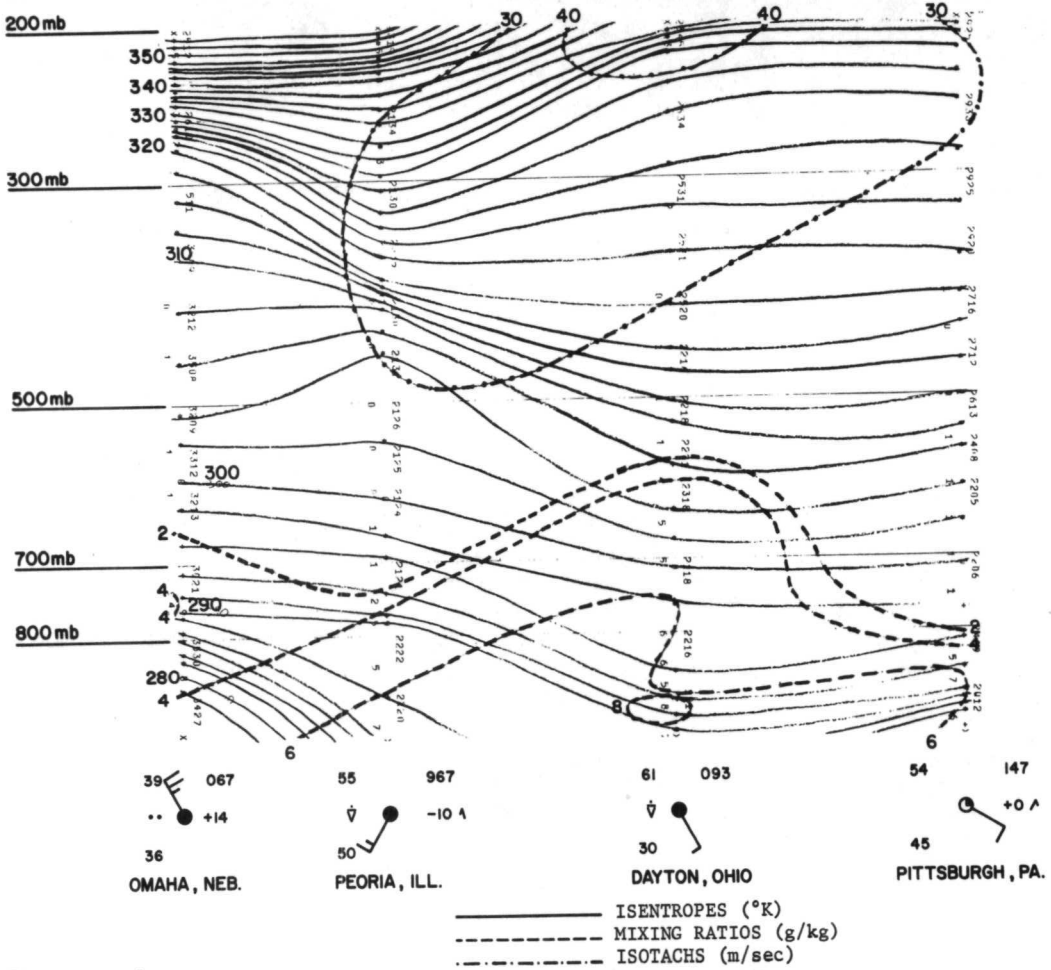

Figure 3. d) East-west cross-section through severe storm area, 1200Z, April 23, 1968.

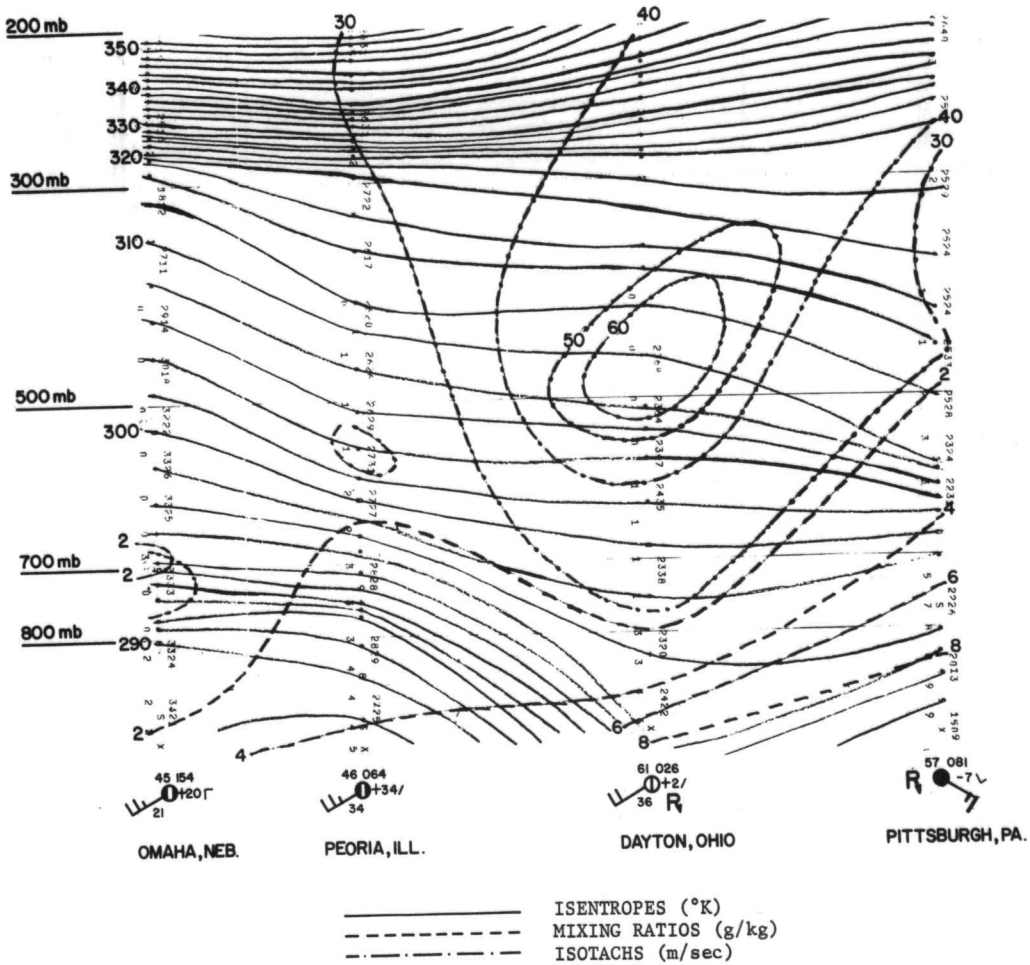

Figure 3. e) Same, except for 0000Z, April 24, 1968.

April 23, 1968. The sudden decrease in wind speeds west of northern Texas would seem to require a subsidence region in this same area and, indeed, the area to the west of the moisture front is perfectly clear on the ATS cloud photographs. How this subsidence is in fact related, if at all, to the formation of convection is not known.

Included for comparison are the cross sections of April 19 and 23, 1968 (Figure 3b to 3e), two days when strong shear was prominent in its association with severe weather. Note that for these two days momentum appears to be transported downwards in the area of convection (the area identified by the vertical transport of moist air above the inversion, and the surface weather reports). As opposed to the May 12 storm where only two isolated tornadic storms were reported, April 19 and 23 produced severe weather over an area of several states. The increase of low level wind speeds has been related among other factors to severe weather development in midlatitude frontal zones by Johnson and Sechrist (1970) and Ninomiya (1971). The May 11 case serves as a reminder by its weak shear that, despite recent emphasis on the role of the jet stream, strong shear in the region of convection is not a necessary condition for severe weather.

The cross-sections also reveal three different surface mechanisms associated with the storm outbreaks. While April 19 has a dry front, and April 23 a cold front, May 11 features the previously mentioned moisture front. The contrast of the two air masses associated with this front leads to conditions of high instability with dry air having a steep lapse rate overlying moist Gulf air. However, an inversion between the air masses discourages convection. The moist air, moving westward, has covered areas to Amarillo, Texas (AMA) with mixing ratios up to 12 g/kg. At Amarillo and roughly in a north-south line, the storms broke out late in the day of May 11. The Lubbock storms themselves had developed and were near maturity by 00Z, May 12, and are responsible for the upward transport of moisture at Amarillo seen on the 00Z cross-section. We may conclude, then, that while upper tropospheric wind shear may enhance growth of severe storms, some such storms nevertheless can develop without such winds, given the right conditions of instability.

3. Data Analysis Techniques

The first Lubbock tornado struck an hour and a half after darkness had fallen. The cloud photographs of storm growth from ATS-III satellite are available, until 0100 GMT on May 12, both for the Lubbock tornadic storm and the several smaller storms around it. The elements in each of these photographs—five in number spaced 20 minutes apart—have been recorded in terms of brightness levels on digital tapes. Mesoscale convection systems which are difficult to analyze on photographic images because of their limited dynamic range can easily be treated on digital contour displays. Such a display gives a detailed and enlarged portrait of each cloud, particularly of cumulonimbi and of their associated anvils, provided it is properly brightness normalized for sun-satellite-cloud geometry. The brightness of a cloud mass on a satellite photograph depends on many variables including solar zenith angle, satellite zenith or viewing angle, the relative azimuth between the sun and satellite measured from the view spot, satellite characteristics, and the picture processing

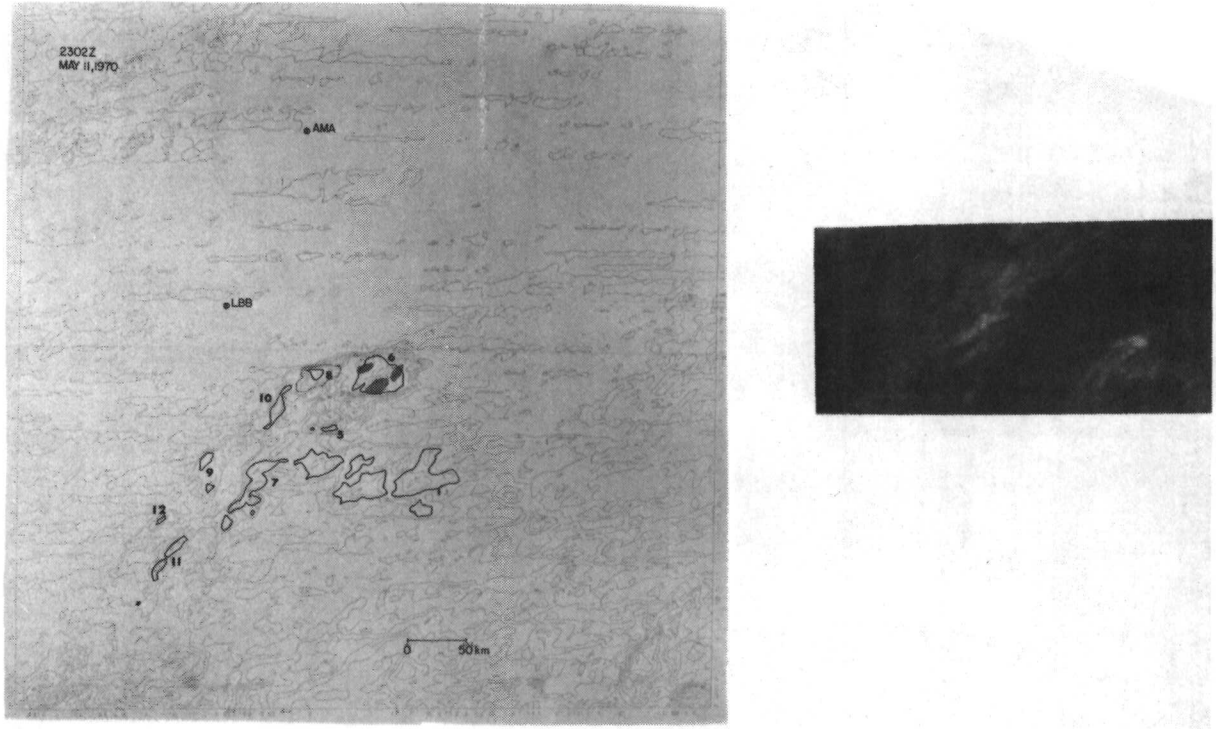

Figure 4. a) ATS-III brightness contour display and photograph of storm clouds on 2302 Z May 11, 1970. Clouds outlined in black are the same as those viewed in the lower left hand corner of the photograph. Clouds are numbered for reference in flux calculations.

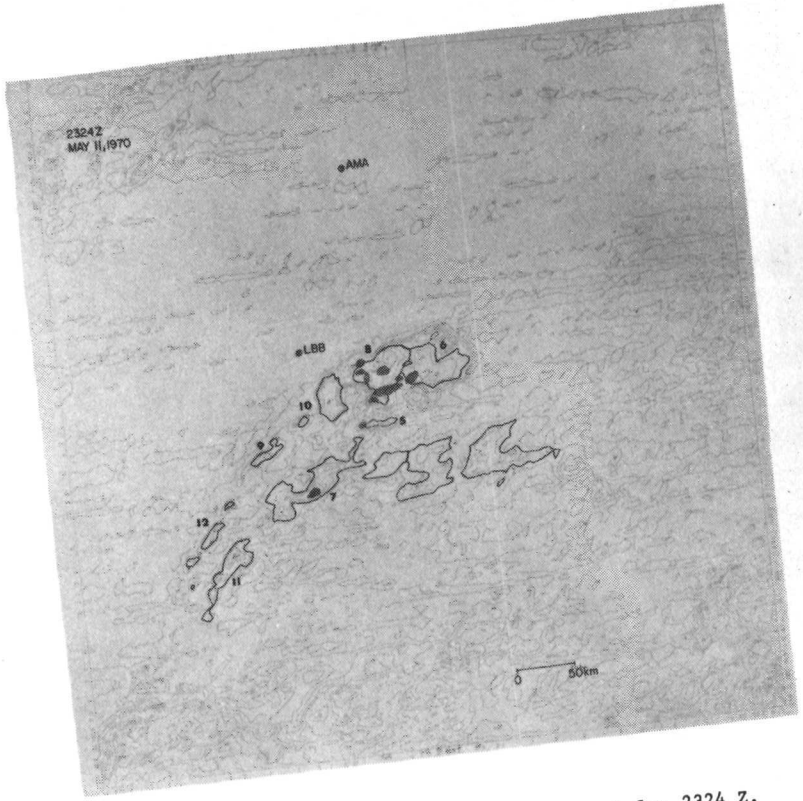

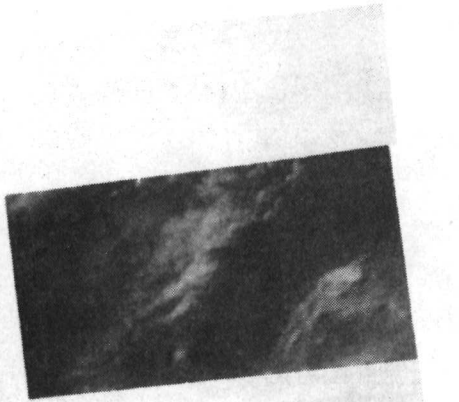

Figure 4. b) Same, except for 2324 Z.

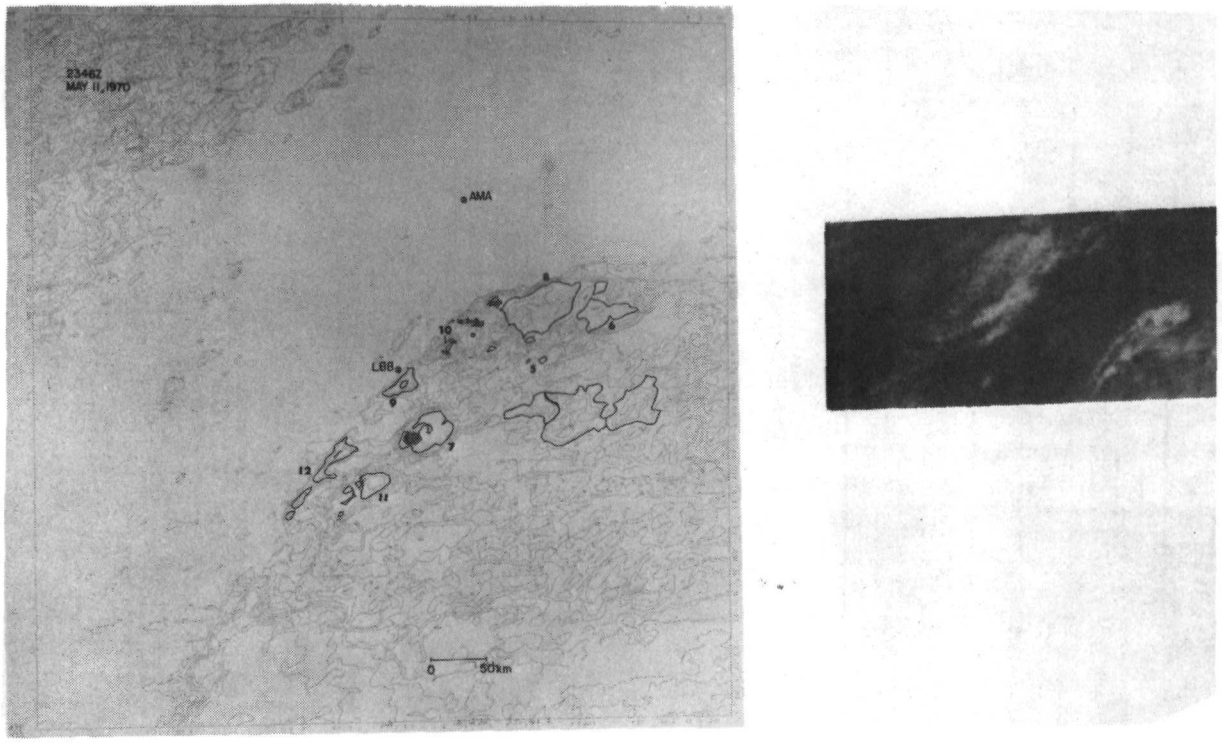

Figure 4. c) Same, except for 2346 Z.

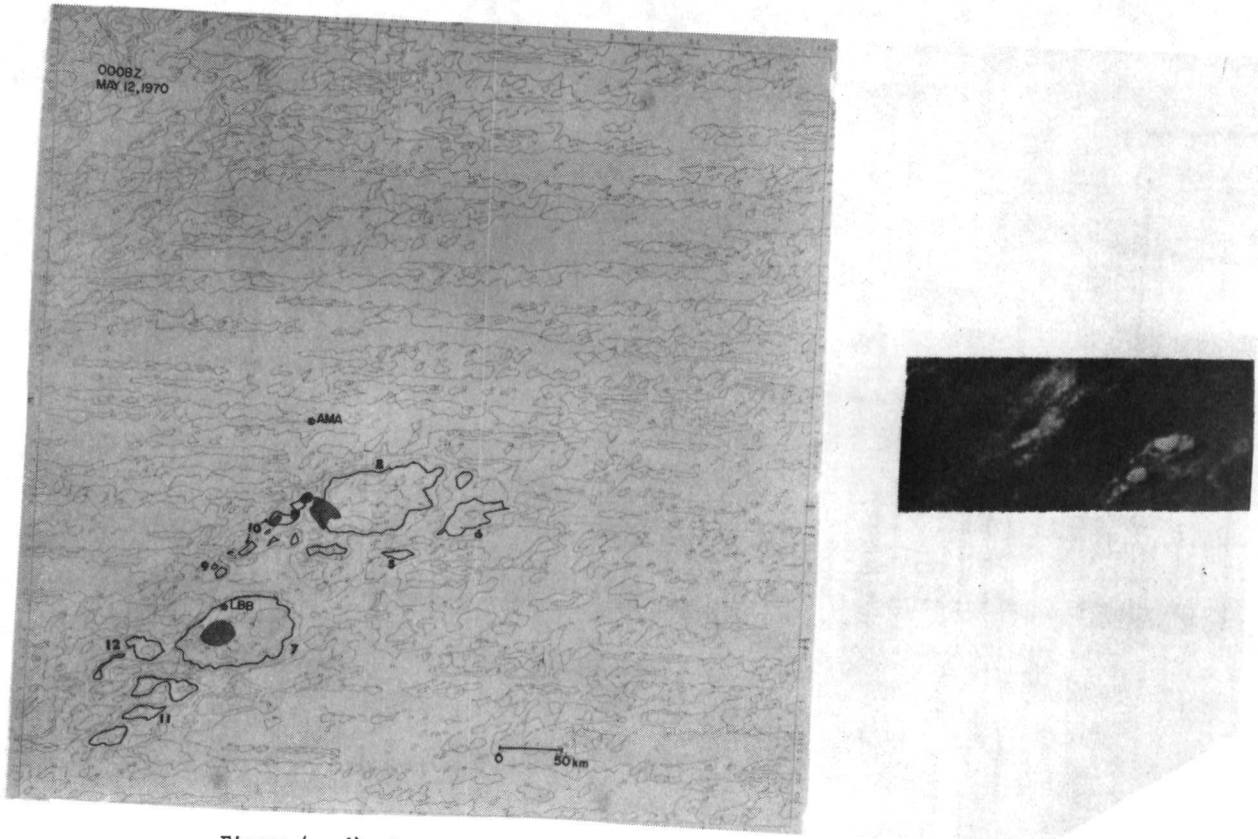

Figure 4. d) Same, except for 0008 Z, April 12, 1970.

technique. Unfortunately, to date we have no unique brightness normalization technique available. As pointed out by Martin and Suomi (1971), the cloud brightness largely depends on solar zenith angle, and a uniform thick cirrus canopy atop a deep convection system can be treated as a quasi-Lambertian reflector. Although the solar zenith angle in the case of the Lubbock storm of May 11, 1971, is large, we have assumed the visually evident uniform cirrus canopy is such a reflector. The brightness data analyzed in this paper have therefore been corrected for sun angle change only, and it is hypothesized that the time-change in the cumulonimbus brightness field can be attributed for the most part to cloud evolution process, and that the brightest portion of the growing cloud would correspond to active portions of the complex that had penetrated to a significant depth of the troposphere and to the areas of precipitation (Sikdar, 1972). Four such brightness contour displays along with corresponding satellite photographs are presented in Figure 4. The clouds are arbitrarily numbered from 5 to 12. The dotted areas in the contour displays are the transposed radar echoes observed from Amarillo, Texas. In most cases a given cloud seems to be associated with only one precipitation echo. Cloud #7 is the tornado-producing cloud. A particular feature of this cloud not evident in similar studies of the April 19 and 23 storms is a clearly defined tower penetrating the tropopause on the southwest side of the cloud as evidenced by the protruded bright spot with its shadow stretching to the north. A simple geometrical computation using the length of this shadow and the zenith angle of the sun yields a height of about 6 km above the cirrus layer, an observation in close agreement with that of Roach (1967).

As for the determination of volume flux atop a severe storm, we have assumed following Newton (1966) that "essentially all the air originating in the updraft remains in the upper troposphere, spreading out mainly in the anvil plume downshear but appreciably also in the upshear side." In a great plain thunderstorm the cirrus shield appears several kilometers thick; however, only the top portion, say one kilometer, probably contains the air originating in the subcloud layer and in the remaining part the anvil air probably originates essentially from the strongly entrained air around the updraft. Fujita and Byers (1962) show an anvil thickness of 1.5 kilometers from photogrammetric measurements of a severe storm, and Ludlum (1966) quotes 1.0 kilometer anvil thickness for moderate cumulonimbus clouds. In view of these observations and the fact that not all of the anvil is part of the outflow layer, an assumption of 1.0 kilometer thickness for the layer of outflow seems more appropriate. In any case, our desire here is to provide an approximate estimate of the actual volume outflow in individual storm complexes.

Assuming that evaporation at the anvil edge is small (Darkow, 1963) and relatively constant for a 15-minute interval period, one may use time changes in anvil expansion as a legitimate tool for measuring the volume flux in a storm or group of storms (Sikdar et al., 1970). The anvil area expansion can be easily determined following normalized isopleths of brightness field appropriate for cirrus shield on time-lapse digital displays, and then volume fluxes obtained with 1.0 kilometer thickness outflow layer.

The anvil divergence can be determined from the expression

$$\nabla_H \cdot \vec{u} = \frac{1}{A} \cdot \frac{dA}{dt} \qquad (1)$$

where A is the cirrus shield area and t is time. The magnitude of divergence gives a measure of the storm's severity. The volume flux can be related to anvil divergence by the expression

$$\frac{dV}{dt} = A \cdot [\nabla_H \cdot \vec{u}] \cdot \Delta Z \qquad (2)$$

where ΔZ = 1.0 kilometer (assumed thickness of cirrus shield).

4. Results: The Circulation Features as Observed from ATS-III

Shown in Figure 5 is a plot of volume flux versus time for the May 11 storm. Numbers on the curves correspond to the numbered clouds in Figure 4. Note that the volume flux is not constant for all the clouds but shows a tendency to fluctuate. One cannot, therefore, characterize these storms as steady-state, at least for variations on the scale of 20 minutes. Similar fluctuations can be observed in the volume fluxes for April 19 (Sikdar et al., 1970). As one might expect, the tornado storm #7 has the largest value of volume flux. Although the latter observations could not be presented for lack of good quality digital tapes, the measurements obtained from enlarged photographs indicate that the volume flux of cloud #7 increased to a maximum of 1.5 km^3/sec at around 0018 GMT, and thereafter remained more or less steady until the last picture taken at 0051 GMT. The next largest storm in terms of volume flux, cloud #8, was also associated with considerable radar echo activity—more so than any of the other neighboring clouds besides #7.

Figure 6 gives a plot of anvil divergence as a function of time. While the anvil divergence magnitude atop a severe storm is a direct measure of the storm intensity (Sikdar et al., 1970), it is not correct to assume that all parts of a storm cloud are equally divergent. As will be seen from Eq. (1), the computed divergence will depend on the size of the area included in the measurement, i.e. on the scale chosen, even if the rate of area change may remain constant. The decline of anvil divergence magnitudes with time shown in Figure 6 is consistent with the findings of Auvine and Anderson (1972), namely that we are dealing with a highly divergent core region surrounded by a region of nondivergent flow resembling the behavior of a point source. The anvil divergence of cloud #7 in Figure 6 is an order of magnitude higher than that of an ordinary thunderstorm, in agreement with Sikdar et al. (1970). One may conclude from these measurements that a severe storm growth need not always be coupled directly to the presence of upper tropospheric wind shear.

Table 1 provides a comparison of the computed volume flux and anvil divergence of storm #7 with those observed on April 19 and 23 in sheared environment. The average volume flux on May 11, 1970, was somewhat smaller in magnitude although the anvil divergence was significantly higher. Referring back to Eq. (2), one can visualize that the volume fluxes determined from area measurements depend on scale size of the clouds. The average cloud size of cloud #7 as shown in Table 1 was at least an order of magnitude smaller than those of April's two cases. Furthermore, as evidenced from the radar echo distributions, the May 11

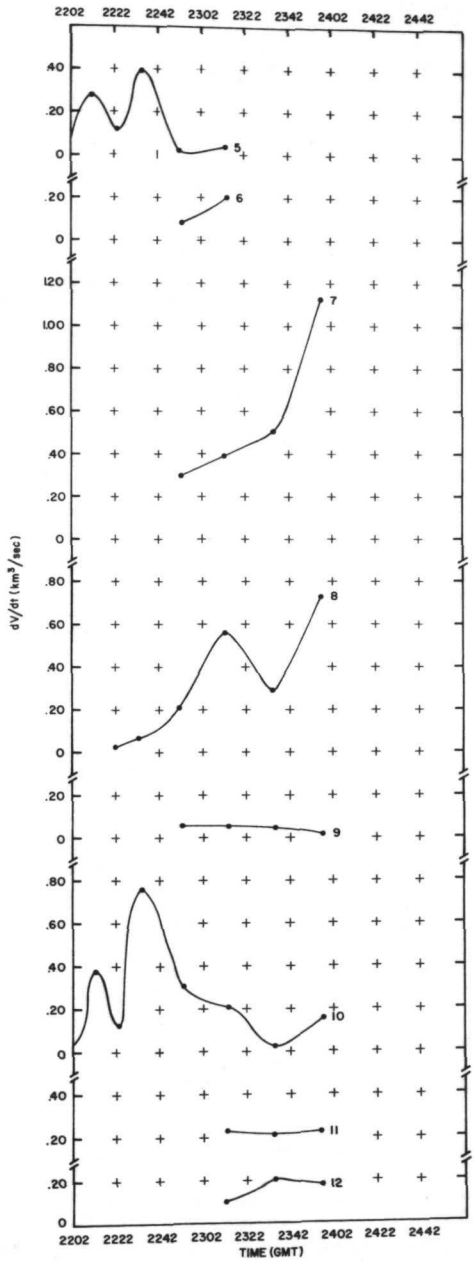

Figure 5. Anvil volume flux (km^3/sec) versus time. Figures next to curves refer to clouds numbered in Figure 4.

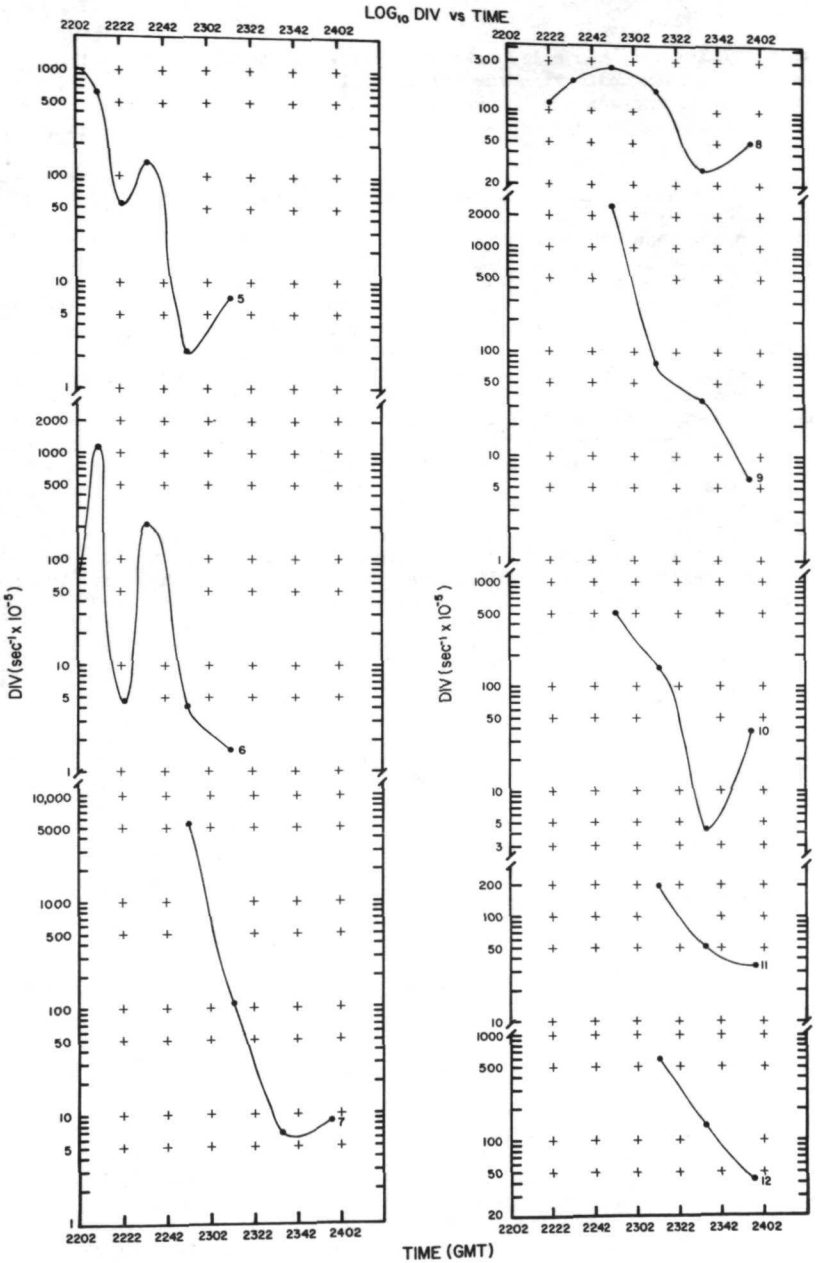

Figure 6. Log_{10} Anvil divergence ($sec^{-1} \times 10^{-5}$) versus time.

storm #7 had only one solid echo while those on April 19 and 23 had several in them indicating the presence of multiple point sources contributing to the average volume fluxes. Nevertheless, the volume fluxes and divergences of these three storm systems appear to have the same order of magnitude.

On the basis of these growth parameters, one cannot distinguish between shear-associated and shearless storms: a shearless environment is capable of producing storms as intense as any found in the midlatitude frontal zones.

Severe storms have generally been found to have higher precipitation efficiencies than smaller and more ordinary storms. To see if the Lubbock storm conformed to this expectation, we computed the precipitation efficiency using the mass flux at 0048Z on May 12 obtained from the last two photographs. The volume flux at this time had become fairly constant. It was assumed that the precipitation output in this storm also remained approximately constant during the time Lubbock, Texas, recorded precipitation (0053Z to 0415Z). Using this precipitation record, an inflow layer into the storm based on an LCL of 11,000 ft, an average mixing ratio for this layer of 9.25 g/kg, and a standard atmospheric density of $.5 \times 10^{-3}$ gcm^{-3} at the top of the storm, one obtains a precipitation efficiency of 51%. This compares to values of 10% for light thunderstorm (Braham, 1952), to values of 50% (Newton, 1966; Auer and Mauritz, 1968) and 60% (Fankhauser, 1971) for severe storms.

Table 1

	Average cloud size ($10^2 km^2$)	dV/dt (km^3/sec)	Anvil divergence (sec^{-1})
May 11, 1970	0.15	1.2	1.0×10^{-3}
April 19, 1968	1.5	3.2	3.0×10^{-4}
April 23, 1968	2.5	4.6	5.0×10^{-4}
Average for mod. thunderstorms	-	0.2 or less	-

5. Some Comments on the Growth and Structure of the Lubbock Storm

We have shown that from the viewpoint of the ATS satellite, the Lubbock thunderstorm is, in regard to mass flux, quantitatively similar to shear-induced thunderstorms. We may still ask, however, whether this storm is qualitatively different from its midlatitude counterparts. In other words, is the structure and growth of this storm similar to that of the typical Colorado and South Dakota hailstorm (documented by Dennis et al., 1970), or to the severe storms found in the plains states to the east (Browning, 1963; Newton, 1966, etc.), or is it unlike either of these?

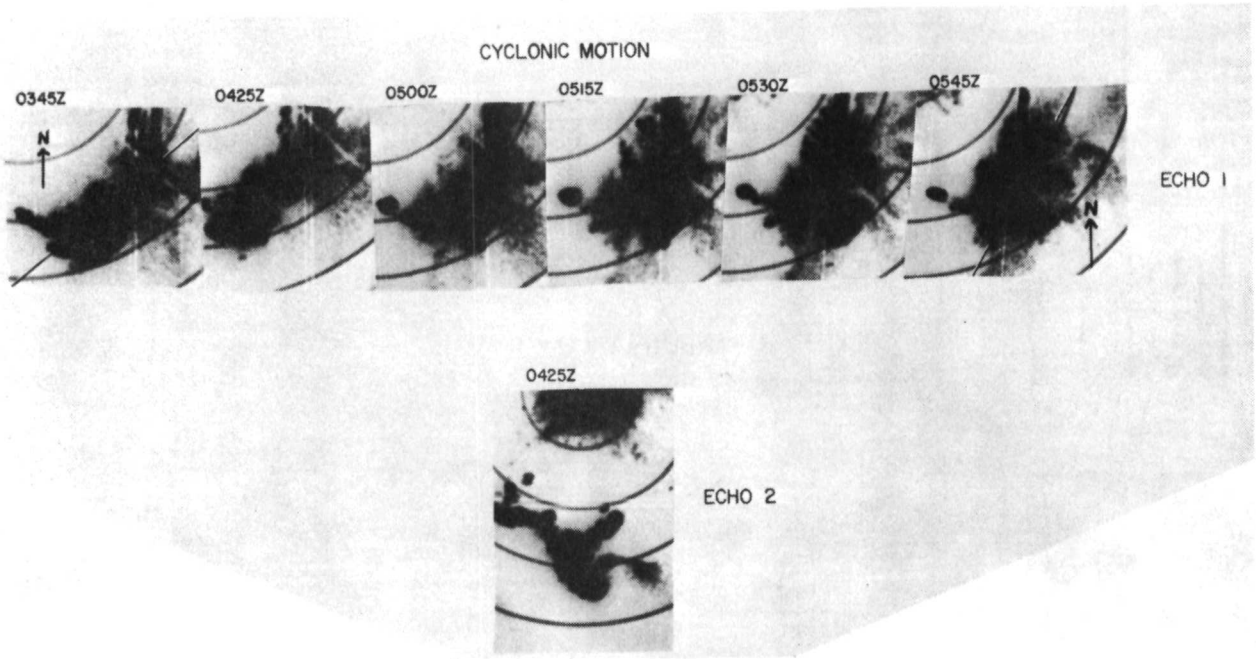

Figure 7. a) Radar (WSR-57) photographs of the Lubbock tornado echo (Echo I) and a nearby echo (Echo II) depicting cyclonic motions. Note the turning of the Echo I axis from a NE-SW to a N-S orientation, and the meso-low appearance of Echo II.

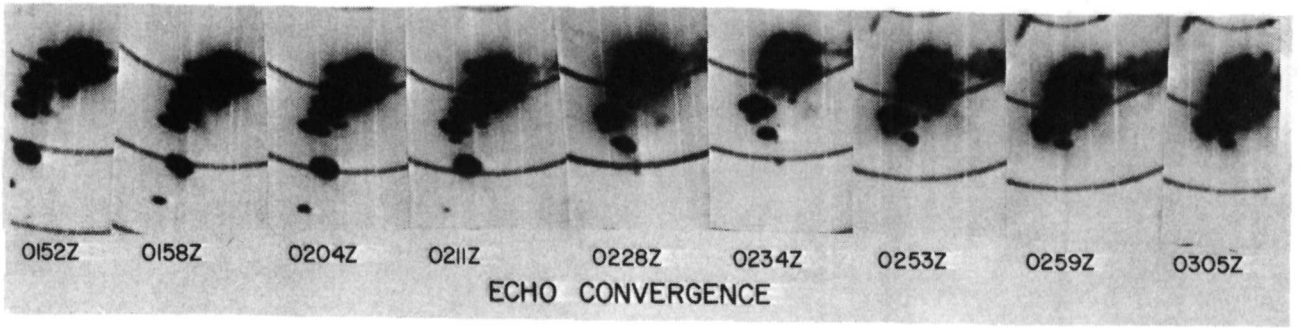

Figure 7. b) Radar photographs depicting the convergence of several smaller echoes into the main Lubbock storm echo.

Some light can be shed on this question by looking at the Amarillo radar photograhs. Figure 7 reveals two interesting features of the storms associated with or close to the Lubbock tornado. After 0300, Echo I, the Lubbock tornado cloud shows definite signs of rotary motion as the axis of the storm moves from a NE-SW to a N-S orientation. During the same period a nearby echo, Echo II, demonstrates what appears to be a meso-low structure such as that found by Fujita (1958) in his examination of tornadic mesoscale systems in Illinois.

Earlier—between the occurrence of the two tornadoes—Echo I also is subject to a convergence of echoes which had grown up to the rear of the storm. As the storm is moving approximately northward, and the echoes converge in the south, growth seems to be taking place to the rear of the storm, the same growth mechanism described by Dennis et al. (1970) for South Dakota hailstorms.

On the basis of this admittedly meager evidence, there is reason to believe that the Lubbock storm resembles in growth and structure the two types of storms cited above, both of which are known to exist in sheared environments. A difference in starting mechanism and environmental wind conditions may not necessarily affect the structure of a severe storm formed.

6. Concluding Remarks

In this paper we have demonstrated that in regard to the nature of severe storm growth, namely the rapid expansion of cirrus shield in advance of the tornado occurrences, the Lubbock storm closely resembles the two severe storms of April 19 and 23, 1968 (Sikdar et al., 1970) and that the magnitudes of anvil divergences and mass fluxes are comparable. In addition, several structural characteristics cited by investigators relating to shear affected storms seem to apply to the Lubbock storm as well. These characteristics include the rotating cells and the growth of the cells by means of feeder clouds to the rear of the storm. Such observations, however, are not conclusive and further study will be needed to determine the exact nature of circulations in nearly shearless storms in contrast with what has been learned of severe storms experienced in midlatitude frontal zones.

The difference in starting mechanism in the subcloud layer and environmental wind conditions as discussed in Section 2 may not necessarily affect the growth rate of a single isolated severe storm cell. However, such factors may be importantly related to the occurrences of widespread multiple convection cells as seen in the storm complexes of April 19 and 23, and their nonoccurrence on May 11. Whereas in the former cases the presence of a jet stream in the region of convection allows for the formation of a large region of synoptic scale instability and the subsequent formation of a large, severe, multi-storm complex, the lack of such a condition in the Lubbock region allowed only the formation of one large "super-cell."

That the presence of wind shear in some way favors the formation of larger or more intense storm complexes is illustrated in Figure 8 where cirrus shield area expansion rate is plotted against the maximum wind

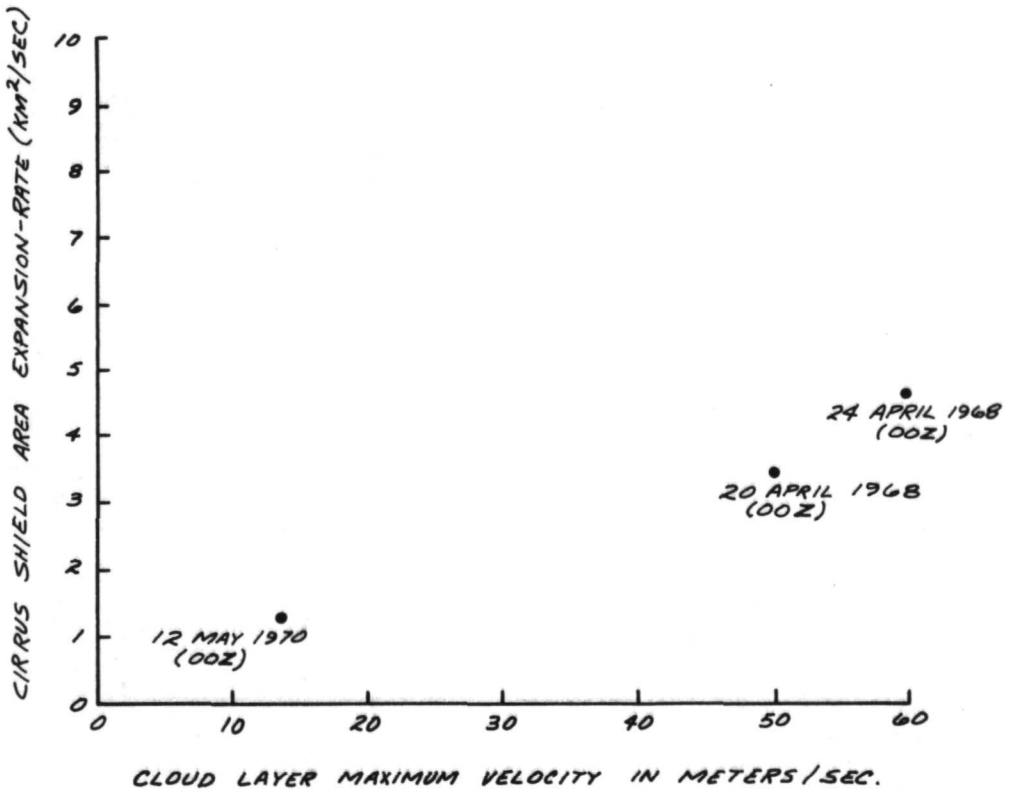

Figure 8. Anvil expansion rate (km^2/sec) versus maximum wind speed in the severe storm environment. Cloud layer (≃ 850-200 mb)

in cloud layers (850-200 mb) in the vicinity of these three storms. Of course, the most intense outbreak of severe storms is associated with high wind shear while the isolated May 11 storm has hardly any. The mechanism of interaction between the severe storm growth and the environmental wind shear is not yet clearly understood; it may be a result of a "chimney effect" where the flow past the top of the rising updraft air tends to increase the rate of mass transport through the storm. The transport of environmental momentum downward as evidenced in Figure 3 may also encourage the formation of a large area of severe convection. Time lapse information from ATS on the evolution of such severe storm complexes on a shorter time-scale should hopefully reflect on the multi-cell growth mechanism in the near future.

Acknowledgment

The authors wish to thank Professors Donald R. Johnson and Frank Sechrist of the Department of Meteorology for reviewing the manuscript. Thanks are also due to many individuals at the Space Science and Engineering Center for contributing in many ways in this research program. The research reported in this paper was in part supported by NOAA under grant E-230-68(g) and partly by NASA under contract NAS5-21650.

References

Asai, T., 1964: "Cumulus Convection in the Atmosphere with Vertical Wind Shear: Numerical Experiment," *J. Met. Soc. Jap.* 42, 245-259.

Auer, A. and J. Marwitz, 1968: "Estimate of Air and Moisture Flux into Hailstorms on the High Plains," *J. Appl. Meteor.*7, 196-198.

Auvine, B. and C. Anderson, 1972: "The Use of Cumulonimbus Anvil Growth Data for Inferences About the Circulation in Thunderstorms and Severe Local Storms," *Tellus*, 24, 4.

Bradbury, D., 1969: "Development of a Dry Line as Shown by ATS Cloud Photography and Verified by Radar and Conventional Aerological Data," Satellite and Mesomet. Res. Proj. Res. Pap. #80, U. Chicago, 16 pp.

Braham, R., 1952: "The Water and Energy Budgets of the Thunderstorm and Their Relation to Thunderstorm Development," *J. Meteor.* 9, 227-242.

Browning, K., 1963: "The Basis of a General Model of the Airflow and Precipitation Trajectories within Persistent Convective Storms," Proc. 3rd Conf. Sev. Local Storms, AMS, Champaign-Urbana, Ill.

Browning, K. and R. Donaldson, 1963: "Air Flow and Structure of a Tornadic Storm," *J. Atmos. Sci.*, 20, 533-545.

Browning,K. and F. Ludlum, 1968: "Airflow in Convective Storms," *Quart. J. Roy. Meteor. Soc.*, 88, 117-135.

Carlson, T. and F. Ludlum, 1968: "Conditions for the Occurrence of Severe Local Storms," *Tellus*, 20, 203-226.

Darkow, G., 1963: "A Study of Infrared Radiation Measurement in the Vicinity of the Subtropical Tropopause," Ph.D. Thesis, U. Wis., 67 pp.

Dennis, A., C. Schock and A. Koscielski, 1970: "Characteristics of Hailstorms of Western South Dakota," *J. Appl. Meteor.*, 127-135.

Endlich, R. and R. Mancuso, 1968: "Objective Analysis of Environmental Conditions Associated with Severe Thunderstorms and Tornadoes," *Mon. Wea. Rev.*, 96, 342-350.

Fankhauser, J., 1971: "Thunderstorm-environment Interactions Determined from Aircraft and Radar Observations," *Mon. Wea. Rev.*,99, 171-192.

Fawbush, E., R. Miller and L. Starrett, 1951: "An Empirical Method of Forecasting Tornado Development," *Bull. Amer. Meteor. Soc.*, 40, 465-472.

Fujita, T., 1958: "Mesoanalysis of the Illinois Tornadoes of 9 April 1953," *J. Meteor.*, 15, 288-296.

Fujita, T. and H. Byers, 1962: "Model of a Hail Cloud as Revealed by Photogrammetric Analysis," Tech. Rep. #3, U. Chicago, 9 pp.

Johnson, D. and F. Sechrist, 1970: "On the Isentropic Representation of Storms, Dynamic Destabilization and Squall Line Formation," EOS Trans. AGU, 51, 294.

Ludlum, F., 1966: "Cumulus and Cumulonimbus Convection," *Tellus*, 4, 699-713.

Miller, R., 1959: "Tornado-producing Synoptic Patterns," *Bull. Amer. Meteor. Soc.*, 40, 465-472.

Newton, C., 1966: "Circulations in Large Sheared Cumulonimbus," *Tellus*, 18, 699-713.

Martin, D. W., and V. E. Suomi, 1971: "A Satellite Study of Cloud Clusters over the Tropical North Atlantic Ocean," Final report on STAG contract E-127-69-(N), The National Oceanographic and Atmospheric Administration.

Marwitz, J., 1972: "The Structure and Motion of Severe Hailstorms; Part I: Supercell Storms," *J. Appl. Meteor.*, 11, 166-179.

Reuss, J., 1961: "Ein Gewitter bei Windstille," *Beit. Phys. Atmos.* 34, 259-273.

Roach, W., 1967: "On the Nature of the Summit Areas of Severe Storms in Oklahoma," *Quart. J. Roy. Meteor. Soc.*, 93, 318-336.

Sikdar, D. N., V. Suomi and C. Anderson, 1970: "Convective Transport of Mass and Energy in Severe Storms over the United States—An Estimate from a Geostationary Altitude," *Tellus*, 22, 521-532.

Sikdar, D. N., 1972: "ATS-III Observed Cloud Brightness Field Related to a Meso-to-Subsynoptic Scale Rainfall Pattern. *Tellus*, 24, 5.

Takeda, T., 1971: "Numerical Simulation of a Precipitating Convective Cloud: The Formation of a "Long-lasting" Cloud," *J. Atmos. Sci.*, 28, 350-376.

ON SOME KINEMATIC PROPERTIES OF THE TROPICAL ATMOSPHERE AS DERIVED FROM CLOUD MOTION VECTORS

D. N. Sikdar

ABSTRACT:

Using the WINDCO system (Smith and Phillips 1972), vectors of small cloud movement were obtained from ATS-III picture sequences for the period 26-28 July 1969 in the tropical Atlantic. These were analyzed for various kinematic properties such as cloud trajectories, divergence, relative vorticity and specific kinetic energy. Among the significant findings are the following:

1. A significant latitudinal wind shear exists north and south of the ITCZ, especially in the zonal component.

2. Cloud clusters are found in the general areas of convergence (-D) and positive relative vorticity (ζ).

3. The vorticity magnitudes appear to be scale-dependent while the divergences are not, at least in the scale 100-600 nautical miles on a side.

4. The grid point values of ζ and D in large nephsystems are approximately related by the empirical equation $\zeta = -1.5\ D$ implying that the low level divergence decreases with the increase of relative vorticity in an active cloud cluster; however, for some cloud clusters this relationship is missing.

5. Specific kinetic energy fields for the three days investigated show regions of maxima at the locations of strong zonal wind shear.

It may be concluded from this preliminary investigation that the WINDCO data are very useful for examining various scales of tropical circulations, especially in the data-void regions, and has good potential for input to a global numerical prediction model.

1. Introduction

A recent technological development (WINDCO: an electronic animation system for obtaining accurate cloud motion) at the Space Science and Engineering Center (SSEC), University of Wisconsin—Madison, has made possible the measurement of cloud displacements to an accuracy of less than 3 knots, a primary requirement of the Global Atmospheric Research Program (GARP). Attempts are in progress to employ these data to improve understanding of atmospheric circulations, especially in the data-void tropical oceanic regions.

The visible sensors of the geostationary satellites ATS-I and III have limited resolution in the vertical. However, from a comparison of conventional wind data with small cloud motion vectors, Hasler (1971) found the best fit level for low cloud trajectories to be around 950 mb, which approximately corresponds to the base of tropical cumuli. For the 950 mb level, 68% of the direction differences were less than 30°. Fujita et al. (1969) also stated 950 mb as the best fit level while Hubert and Whitney (1972) and Serebreny et al. (1969) arrive at 950-850 mb from their comparisons.

Future geostationary meteorological satellites equipped with infrared sensors will greatly reduce the present uncertainties of cloud height determination of large and thick clouds, but for moving thin cirrus shields the uncertainties due mainly to emissivity and transmissivity will remain. In this connection it should be mentioned that a preliminary investigation in progress at this Center suggests a reasonable correlation between the cloud brightness and thickness (Park 1972). If this is so, one should be able to assign a cloud displacement to a level depending on the integrated cloud brightness. Pending establishment of such a relationship, we will proceed with the hypothesis that small clouds in ATS-III images are at the trade cumulus level.

The need to identify small clouds on a series of successive pictures at intervals of 23 minutes imposes some restrictions on the data selection scheme. Nevertheless, our experiences are that the numbers of even such restricted cloud displacement vectors are enough to give adequate two-dimensional coverage of kinematic parameters such as stream function, vorticity and divergences. Of course, one should keep in mind that such data on occasions may be very few in areas dominated by subsidence as, for example, in the subtropical oceanic highs and ridges.

The purpose of this paper is to demonstrate the potential of WINDCO-derived cloud motion vectors for synoptic and dynamical analyses of tropical weather systems in the absence of upper air data.

2. Data Selection and the Analysis Technique

During the development and testing phase of WINDCO, cloud displacement vectors were generated for three days—26, 27 and 28 July 1969—from Phase IV of BOMEX. These data were quality controlled and accessible, and therefore were selected for analysis of various kinematic properties.

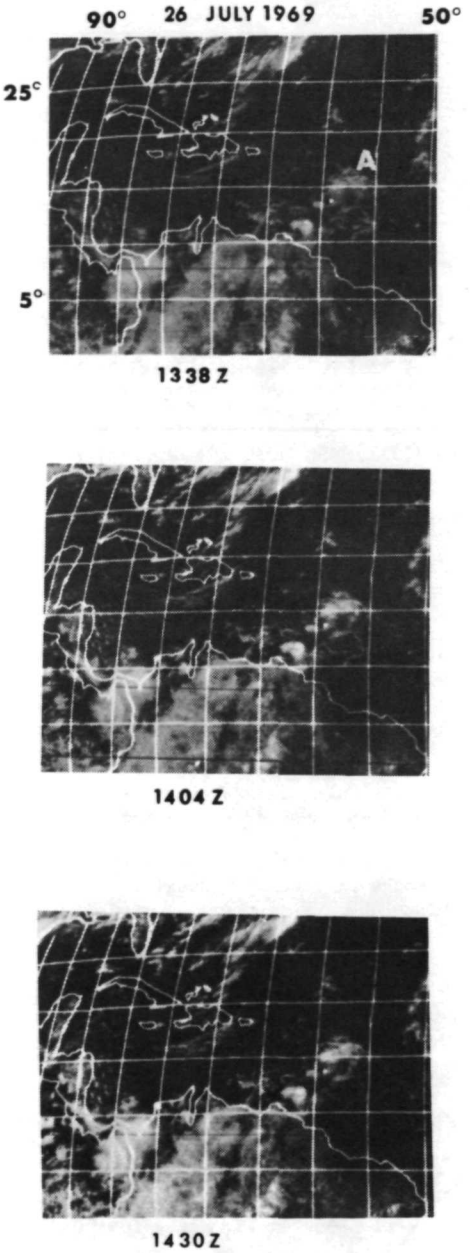

Figure 1a. Satellite photos showing cloud cluster activity in the western Atlantic on 26 July 1969.

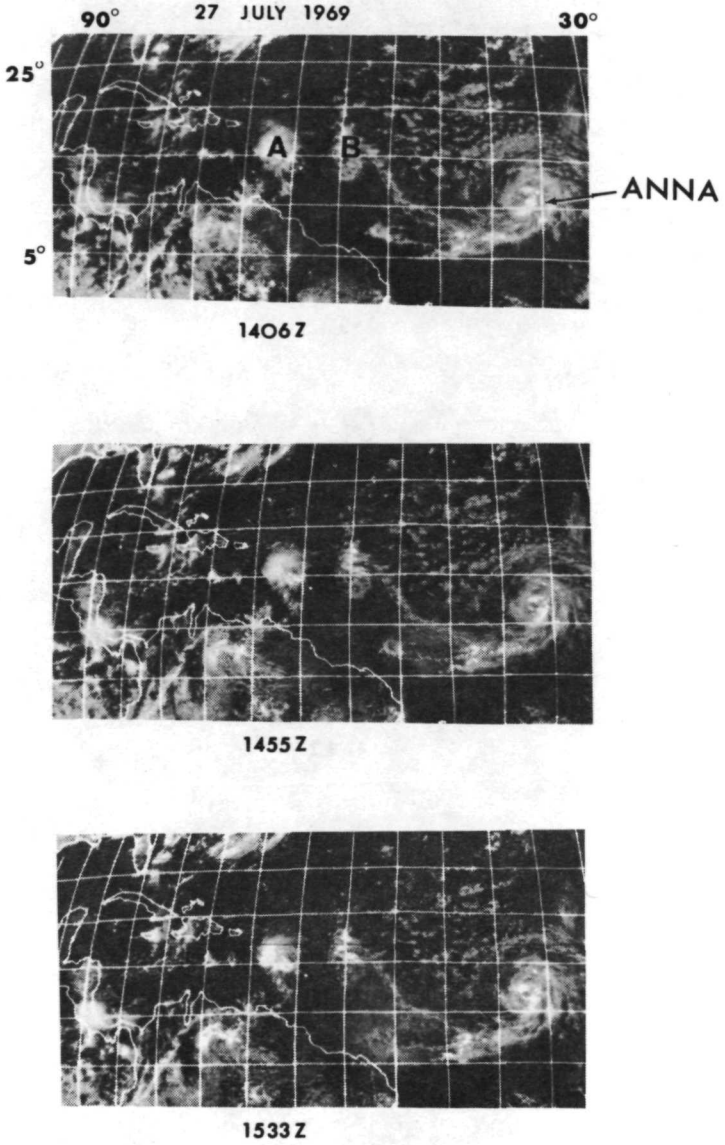

Figure 1b. Same as 1a except for 27 July 1969.

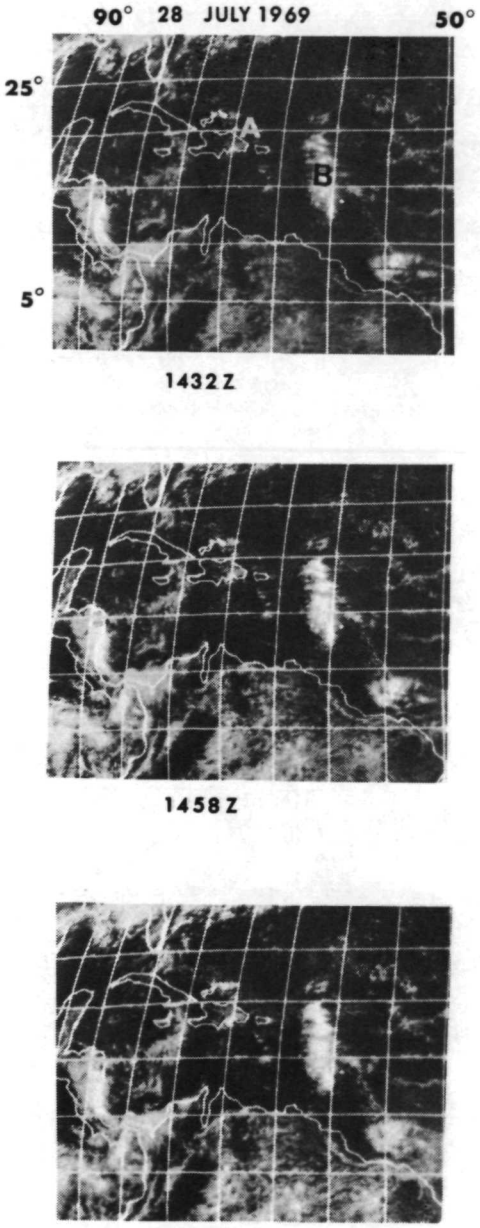

Figure 1c. Same as 1a except for 28 July 1969.

The WINDCO system measures cloud motions by tracking clouds over two digital pictures and applying a two-dimensional cross-correlation analysis. A precise alignment of ATS picture sequences is crucial to the accurate measurement of these cloud displacements. The second important step involves finding the coordinates of each selected cloud tracer on the digital pictures, the primary criteria being that the cloud tracer should be found in all the pictures in the selected sequence and its location should not be near the limb. For details the reader is referred to Smith and Phillips (1972).

The cloud displacement vectors produced by WINDCO were first resolved into u and v components and averaged in an area of 2.5° x 2.5°. This procedure gave a matrix of uniform field of u and v in the latitude band 10° - 30°N and longitude band 50° - 90°W. Approximately 150 vectors were obtained on the 26th and 28th with over 400 vectors on the 27th in the area bounded by 5°S - 40°N and 10° - 100°W. The time intervals between picture pairs on the 26th and 28th were 26 minutes in all four cases but on the 27th the first interval was 49 minutes and the second 38 minutes. Doubtful data, namely, wind vectors with speed greater than 30 m/s or direction opposed to smoothed stream line flow ($\pm$ 20°), were considered to be mistracks of clouds or at different heights than the majority of the winds and therefore were excluded from the analyses. The number of such rejected vectors was hardly 5-6%.

A contour analysis of u and v components derived from cloud displacement vectors revealed the horizontal gradient field from which basic meteorological parameters such as divergence and relative vorticity fields were constructed as a function of time. In addition, the cloud displacement vectors were averaged to study their latitudinal and longitudinal variations. Also produced from the u and v fields were specific kinetic energy fields as a function of time.

3. Satellite Time-Lapse Pictures and Cloud Motion Vectors

A Satellite View of the Cloud Clusters on 26, 27 and 28 July 1969

A cloud cluster identified as A in Figure 1a at 57°W, 15°N in the western Atlantic was the only active cluster in the selected grid zone on 26 July 1969. Associated cloudiness appears to extend southwestward over South America. The cluster moved westward to the 63°W meridian on 27 July, implying a speed of $\simeq$ 5°/day and became disorganized as it passed to the east of Cuba on 28 July. Initial westward movement became northwestward on 28 July. The cloud cluster B located at 54°W, 15°N in Figure 1b was just entering the grid zone in Figure 1a and was apparently linked to the dominant cyclonic circulation to its east-southeast at 35°W, 10°N (tropical storm Anna). A wide field of stratocumulus clouds is seen to the north of this latter system extending to latitudes as high as 25°N. The cloud cluster B can be followed to the location 62°W, 15°N on 28 July (Figure 1c) thereby indicating an apparent speed of 8° of longitude per day, which is faster than cluster A on 26-27 July. The implication that the trade-circulation was stronger on the 27th in the easter part of the zone than on the 26th is confirmed by the fields of cloud motion vectors discussed below.

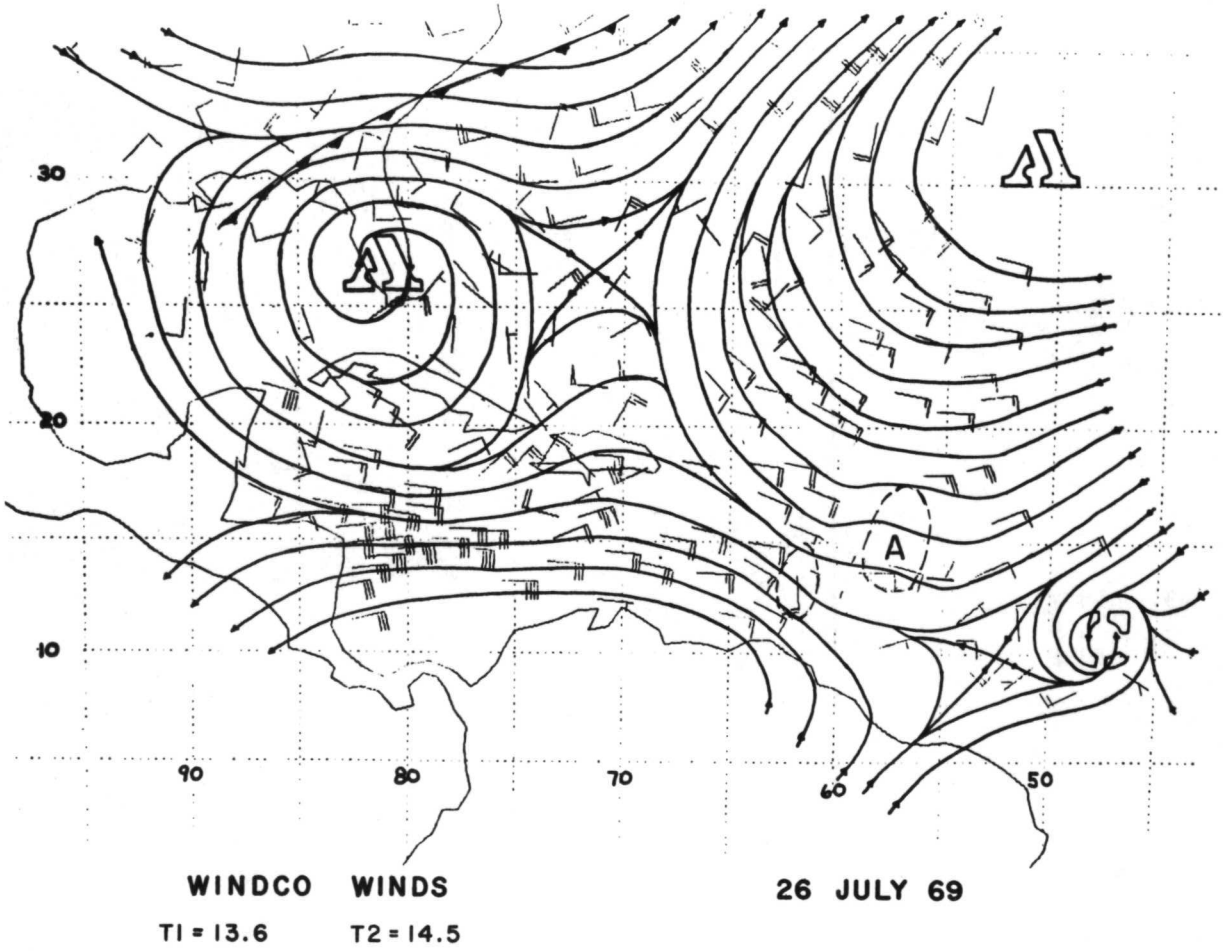

Figure 2a. Cloud trajectories obtained from WINDCO on 26 July 1969 in the western Atlantic area.

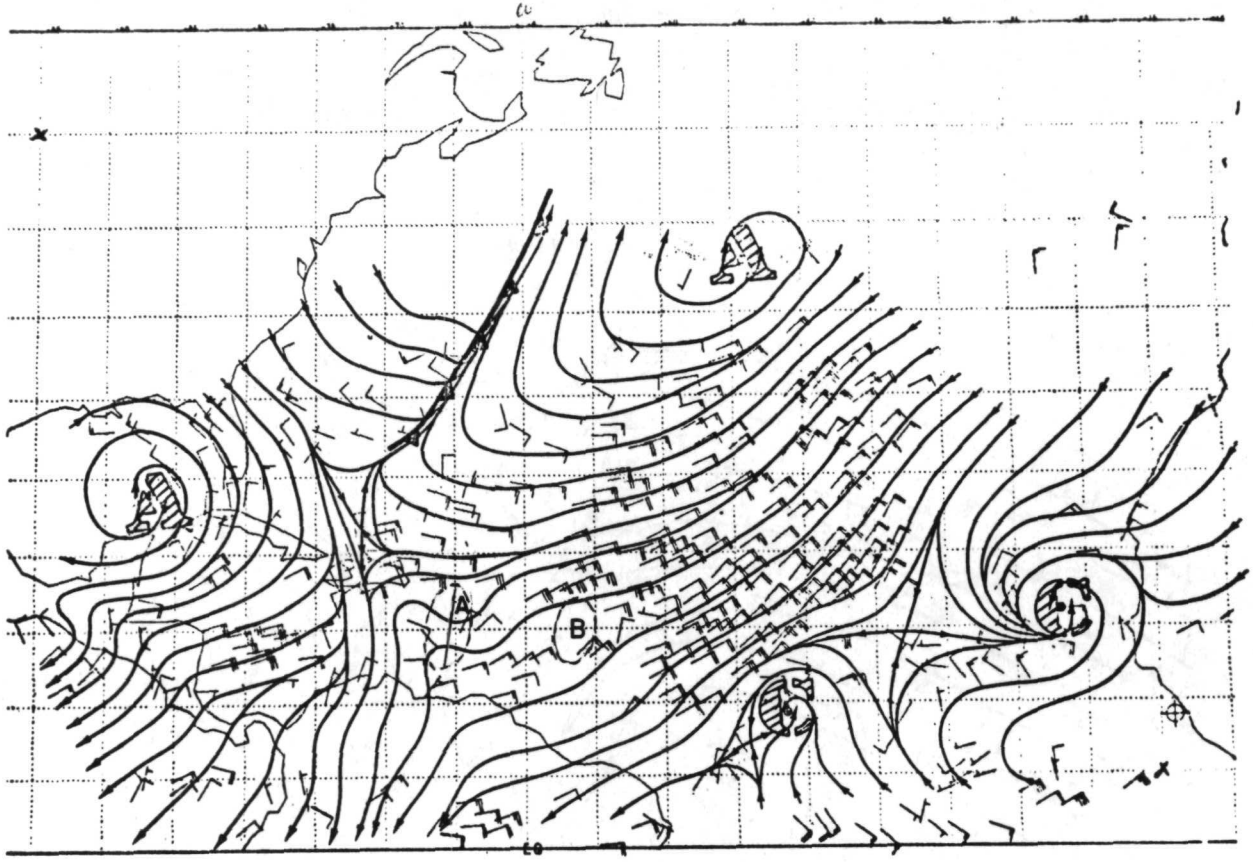

Figure 2b. Same as 2a except for 27 July 1969 and in the whole Atlantic.

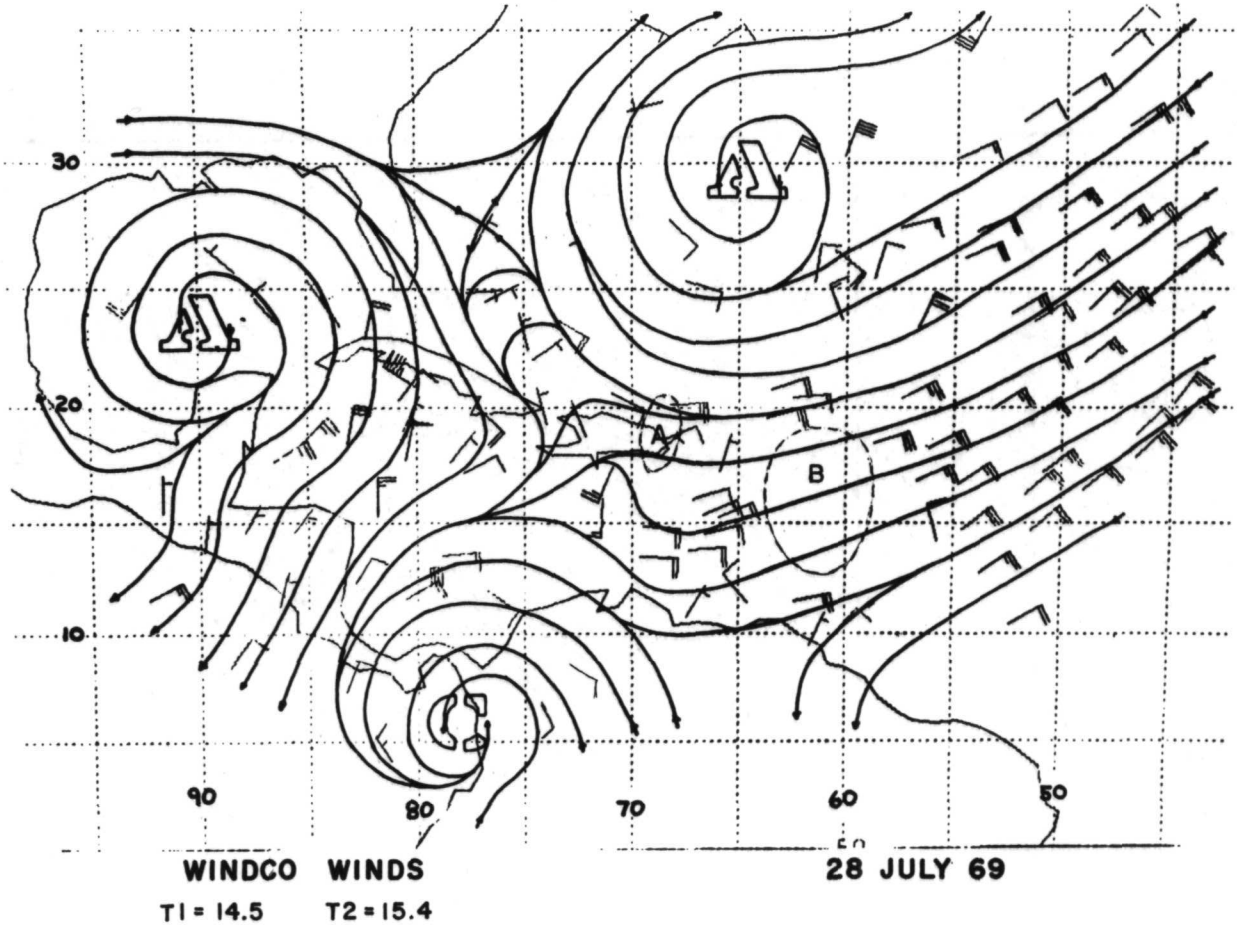

Figure 2c. Same as 2a except for 28 July 1969.

Circulation Features as Revealed From the Cloud Trajectories

Figures 2a, b and c present the corrected cloud motion vectors obtained from WINDCO. One can see from these diagrams that the data density is high, much higher than once can expect from land based rawin network. For comparison the streamline flow charts at 3000 ft obtained from the WMO Regional Center at Miami are presented in Figures 3a, b and c. The subjectivity introduced in the analysis of widely spaced rawin, aircraft and ship data in these charts is evident. A comparison of Figures 2 and 3 reveals in general an agreement between 3000 ft level streamlines and the low cloud trajectories presented.

Cloud trajectories on the 26th indicate a cyclonic circulation centered near 47°W, 11°N. Two dominant subtropical anticyclonic vortices are located at around 50°W and 80°W. Cloud motions were generally from east to southeast in the eastern half of the box; in the western sector they were light to variable. A pronounced latitudinal wind shear can be seen in the Caribbean Sea area to the north of the ITCZ at 12°N but to the west of the active cloud band.

On 27 July (Figure 2b), there appears a change in the circulation regime; northerly to northeasterly flow seems to dominate south of 12°N. A quasi-steady northeasterly flow is found in the eastern half of the extended grid box while winds appear light and variable in the western Atlantic. Two cyclonic vortices, one at 15°N, 25°W and the other at 10°N, 40°W, are evident on this chart. The anticyclonic vortex observed north of Cuba on the 26th moved a few degrees westward. A weak trough aligned

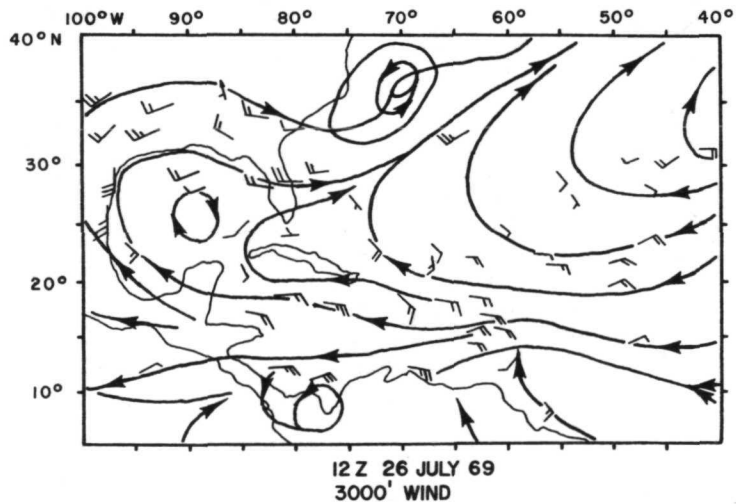

Figure 3a. Conventional wind analysis at 3000 ft level in the area shown in Figure 2a for 26 July 1969.

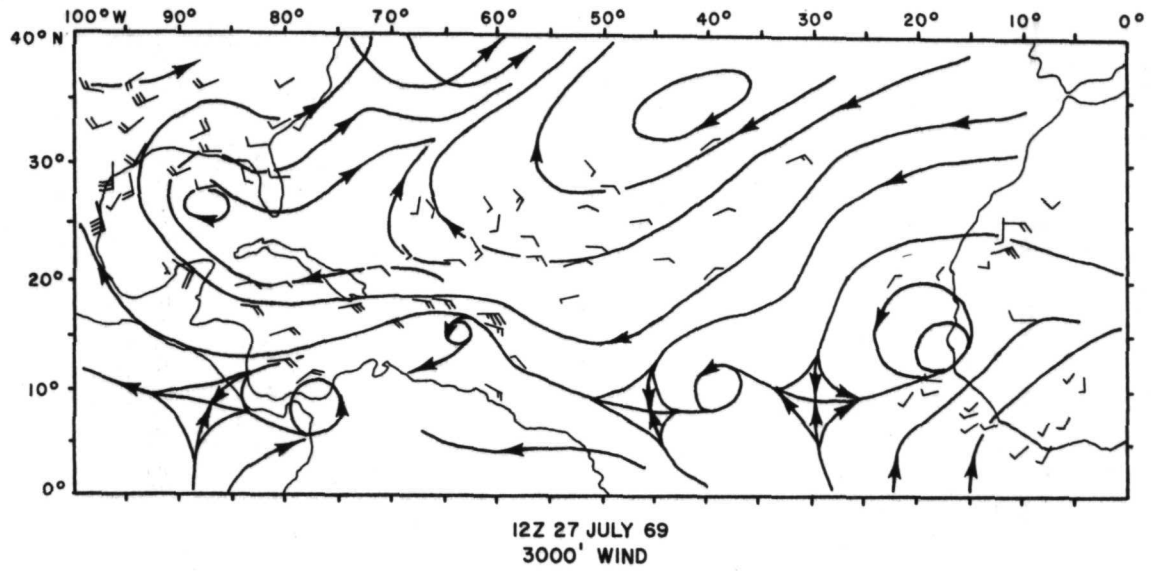

Figure 3b. Same as 3a except for 27 July 1969 and over the whole Atlantic.

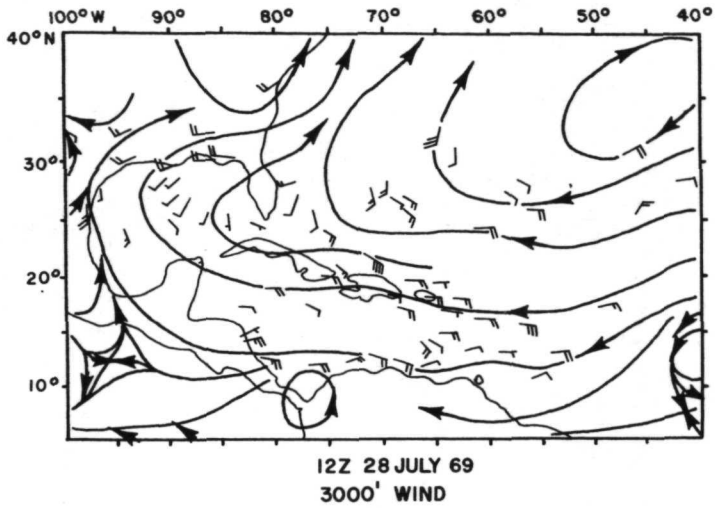

Figure 3c. Same as 3a except for 28 July 1969.

northwest-southeast is located in the general area extending 15°N through 5°N along the 67°W meridian. An eastward moving midlatitude cold front extending as low as 27°N in the western Atlantic was captured by expanding the data coverage northward. With only data from conventional systems over the ocean, it is not uncommon to miss such a midlatitude trough. Strong latitudinal wind shear persists in the Caribbean Sea east of Panama.

By 28 July the wave to the north of the ITCZ moved to the 72°W meridian. The anticyclonic vortices to the northeast and northwest also moved westward a few degrees. A new cyclonic circulation is seen centered approximately around 7°N, 78°W.

The details in these wind fields offer a possibility of testing the "easterly wave" concept (Palmer, 1952; Riehl, 1954), which holds that wave perturbations of the easterly trade flow are associated with disturbed, showery weather of the kind to be expected under a cloud cluster and that this disturbed weather typically occurs on the upwind side of the wave trough. To examine whether the cloud clusters are related to any such wind perturbations, the low cloud trajectories were carefully scanned and approximate locations of the clusters circled. Offhand, one can hardly identify any clear-cut wind discontinuity in the cloud cluster area except on a few occasions; for example, at the location of cluster "A" in Figure 2b where a very weak amplitude wave is indicated. In contrast to this, one would find an area of weak convergence near cloud cluster "B" marked by relatively stronger wind in the upwind than in the downwind from the cluster. In general, however, one finds a stronger

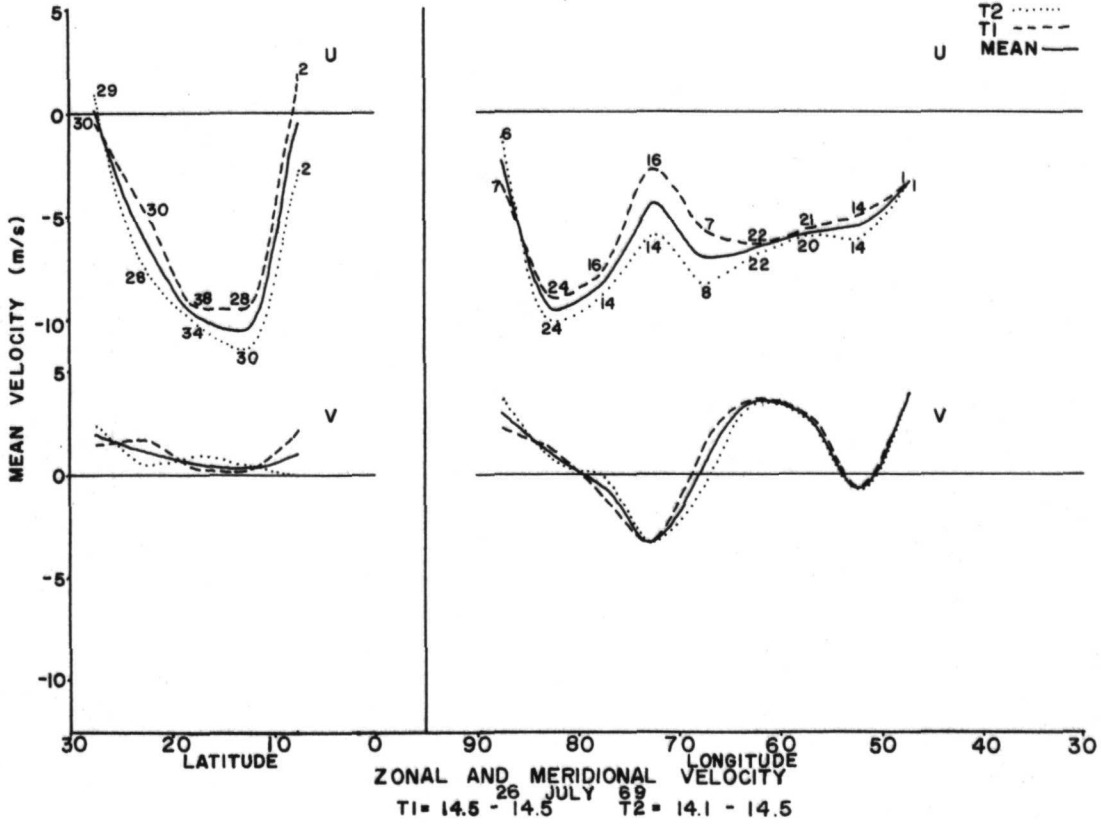

Figure 4a. Mean zonal and meridional winds on 26 July 1969.

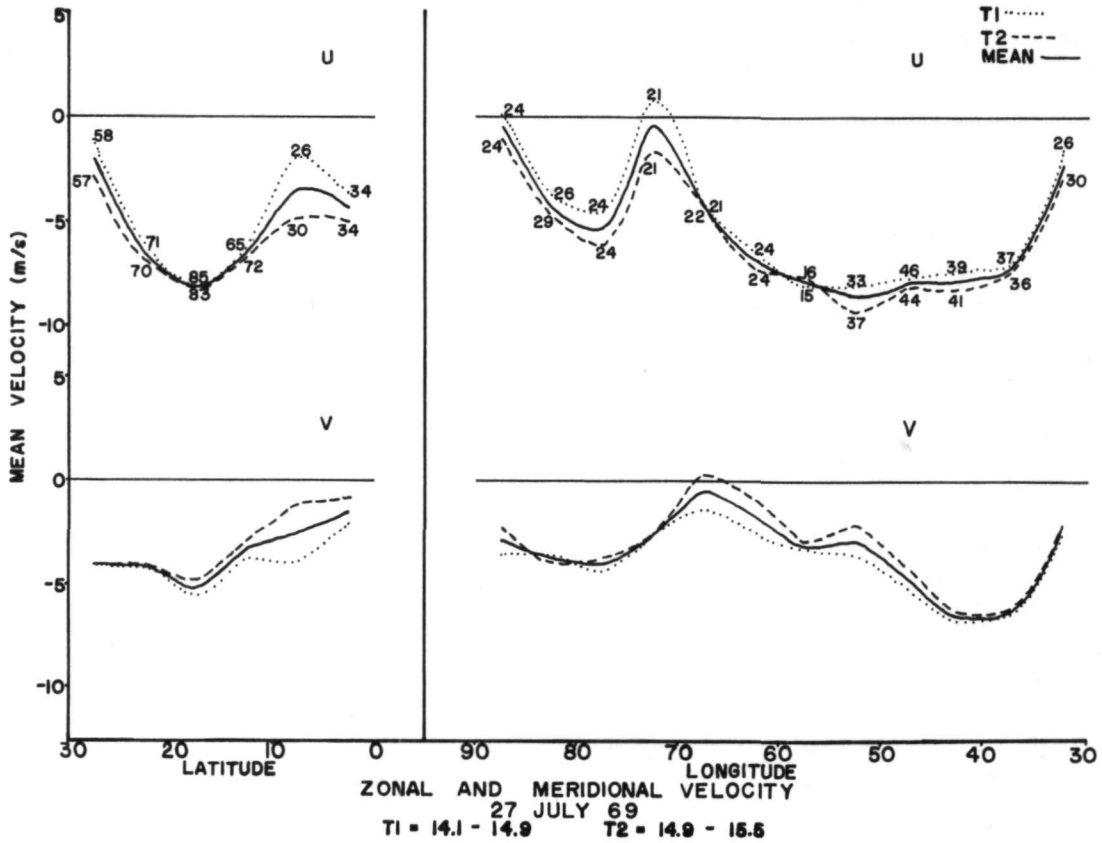

Figure 4b. Same as 4a except for 27 July 1969.

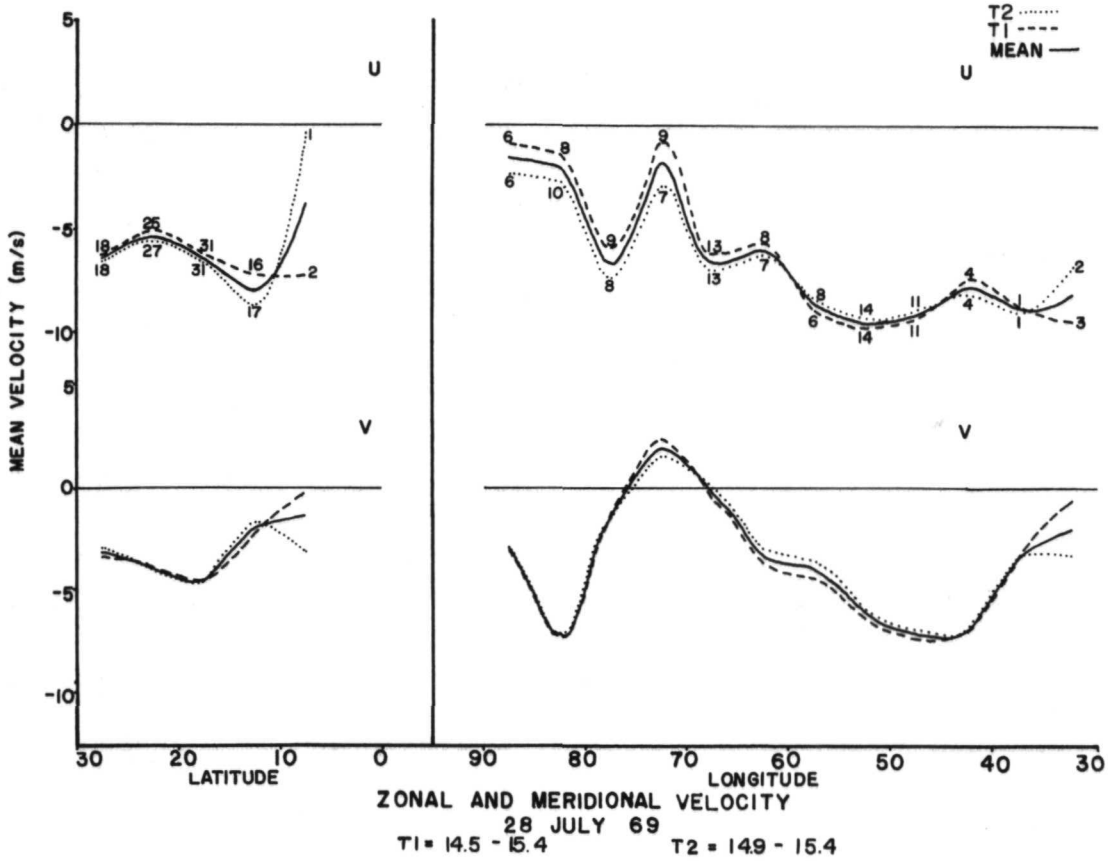

Figure 4c. Same as 4a except for 28 July 1969.

trade flow north of a cloud cluster location than to the south and that all clusters may not be associated with wave troughs.

These cloud trajectory charts clearly demonstrate superiority in data density over the oceanic regime where, in spite of the uncertainties involved in the estimation of cloud heights, an analyst is able to follow the cloud-cluster-scale circulation more closely than otherwise would be possible. In most areas the data density satisfies the two-degree horizontal grid mesh spacing considered necessary for a global numerical model.

4. Mean Zonal and Meridional Winds

From the isotach analyses of zonal and meridional components of cloud motion vectors, means as a function of time, latitude and longitude are constructed (see Figures 4a,b,c). The number of observations used in finding the means are indicated against each data point. A significant zonal wind shear north and south of the ITCZ at 12°N is apparent in these diagrams especially on the 26th and the 27th. Although not very pronounced, the meridional components exhibit confluence to the south of the ITCZ, and particularly so on the 27th and 28th of July.

The longitudinal distributions of mean u and v fields show patterns seemingly influenced by the location of vortices. In the zonal profiles the low magnitude between 70° - 75°W and also around 85 - 90°W meridians may be related to a col region between the two anticyclonic vortices. Interestingly the locations of these regions of low zonal wind speed are constant on the three days investigated in spite of slow westward movement of the anticyclonic cells. While the zonal winds exhibited more or less the same pattern, the meridional wind distribution significantly changed; namely, the bump indicating southerly flow of 3-4 mps at around 63°W on 26 July (Figure 3a) became weaker on subsequent days and shifted westward to approximately 72°W on 28 July. In the vicinity of cloud clusters the average zonal shear was found $\simeq 7 \times 10^{-6}$ sec^{-1} (cyclonic) and the average meridional shear was around 3×10^{-6} sec^{-1} (cyclonic).

5. Divergence and Relative Vorticity Fields Related to Cloud Population

Divergence Fields

Figures 5a,b,c are low level divergence fields produced from cloud motion fields upon which are superimposed clouds from ATS photos. The major areas of convergence are found located near the cloud cluster in agreement with what Hasler (1971) has found. The magnitudes of convergence ranged from 3×10^{-5} sec^{-1} to 9.0×10^{-5} sec^{-1} depending on the intensity of cluster activity. In intense growing storms the magnitudes may be as high as 10^{-4} sec^{-1} (in 2° x 2° zone) which is about two orders of magnitude higher than the value 10^{-6} sec^{-1} frequently quoted of large scale motions. The divergence magnitudes in the clear environment ranged between $0.2 - 5.0 \times 10^{-5}$ sec^{-1} on the average. There are occasions

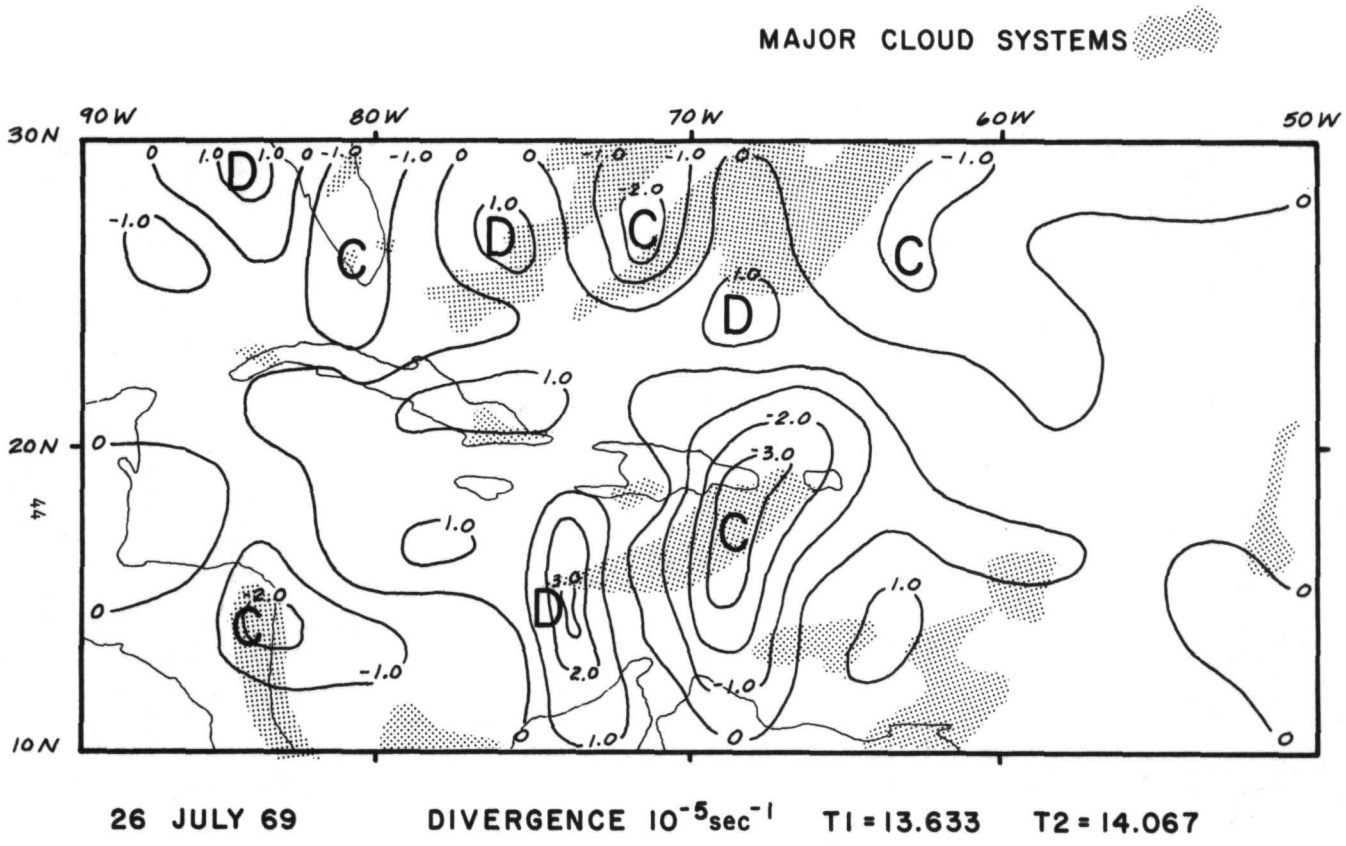

Figure 5a. Divergence map upon which is superimposed the cloud field on 26 July 1969.

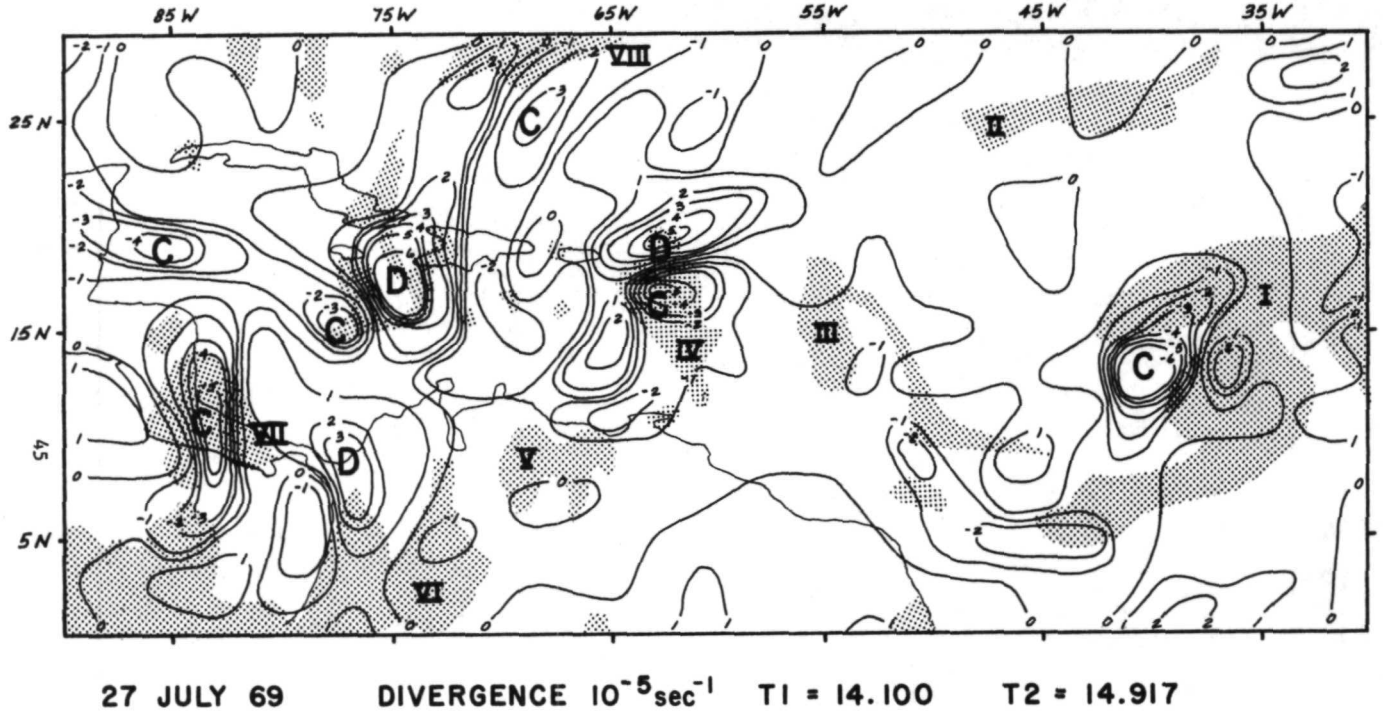

Figure 5b. Same as 5a except for 27 July 1969.

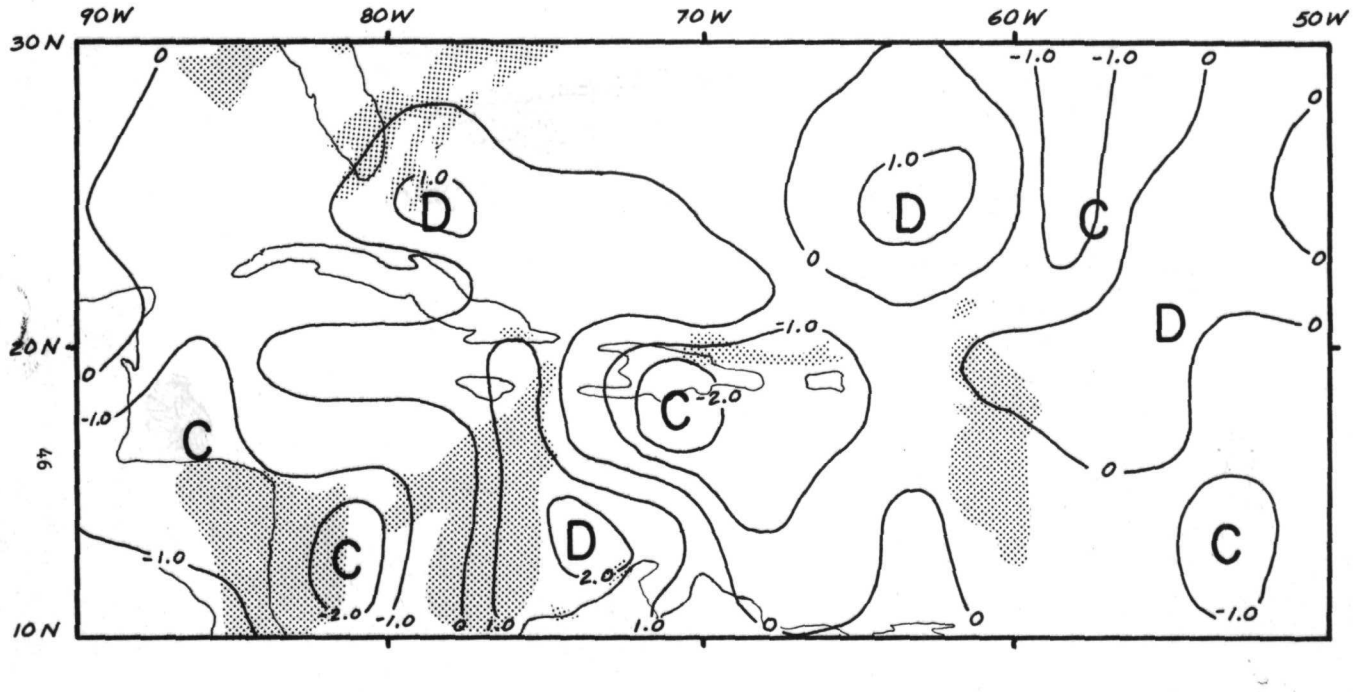

Figure 5c. Same as 5a except for 28 July 1969.

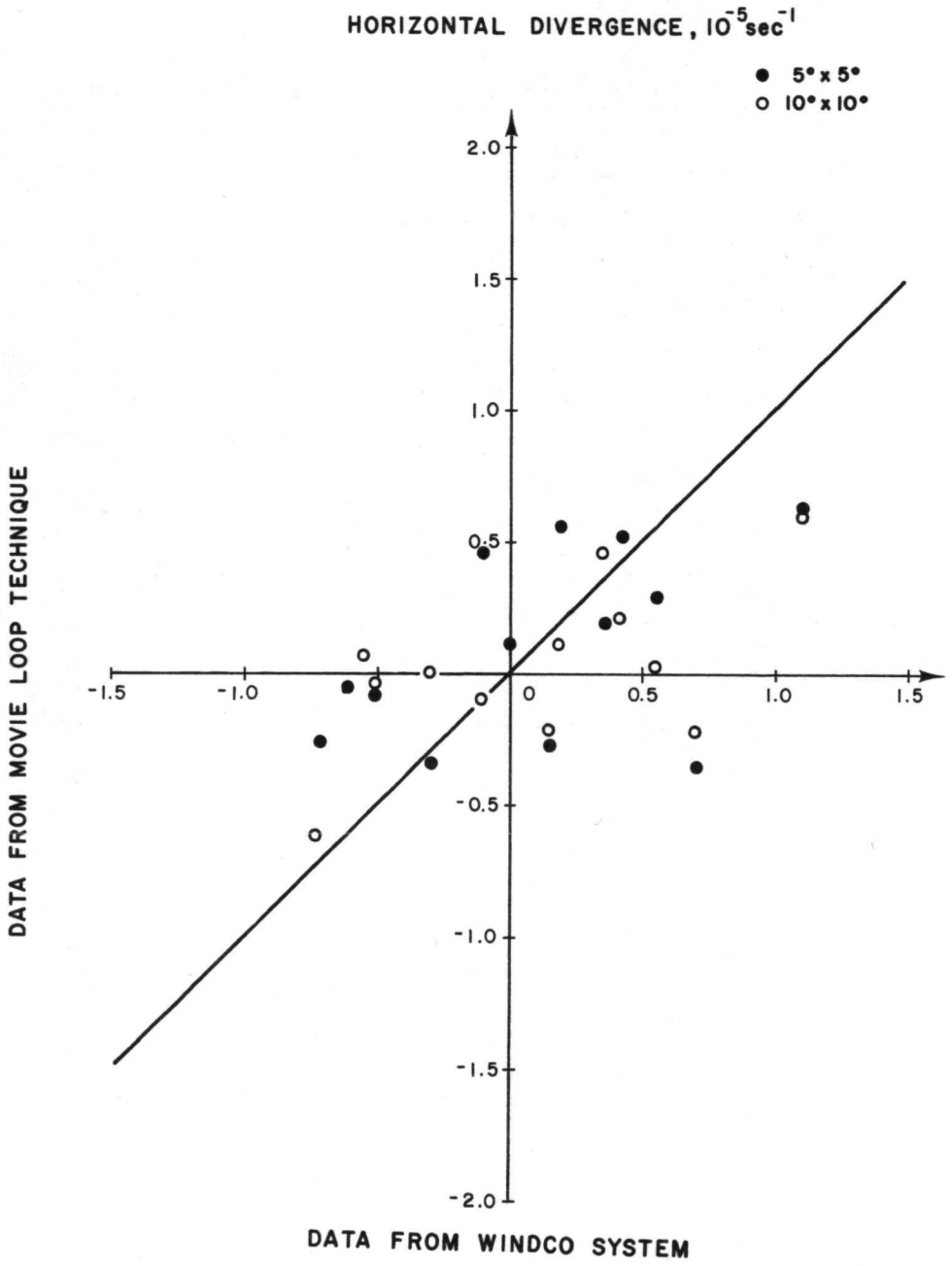

Figure 6. Scatter diagram showing the dependence of divergence magnitude on scale size.

when clouds are present in the areas of no significant convergence field. This may be attributed to inactivity within the cloud clusters at the time of observation; some might simply have been composed of debris left over from previous convection. To test this suggestion one could check the cirrus expansion rate atop a cluster using Sikdar's (1969) technique.

While editing and smoothing is necessary because some signal noise is unavoidable, the extent to which this can be done without concealing desired meteorological information is yet an unanswered question. Space-smoothing is effectively done by the choice of grid size. It is generally accepted that meteorological parameters like divergence and vorticity fields are scale dependent. To test the validity of this concept we have plotted in Figure 6 divergences obtained from movieloop technique after Hasler (1971) averaged in 5° × 5° and 10° × 10° (latitude x longitude) grid spacing for the same area and date against those obtained from the WINDCO system (spacing 2.5° × 2.5° on the 26th and 28th while 2° × 2° on the 27th). The absence of any large scatter probably suggests that the low level divergence or convergence around a tropical cluster hardly depends on the scale size in the range 100 to 600 nautical miles on a side; in other words, B and C scales are effectively coupled to large scale motions. In interpreting these data one should realize, however, that some discrepancies will be obvious because of the differences in the technique and also because the same cloud may not have been followed as a tracer by the two techniques. Even so, the independently derived wind fields exhibited excellent agreement (Hasler, 1971).

Relative Vorticity Fields

Figures 7a,b,c show clouds superimposed on relative vorticity fields for the three days investigated. Patterns are complex and occasionally difficult to interpret. In general the large clouds are located westward or downstream in the regions of large positive relative vorticity with a vorticity maximum often located to the west of the cloud cluster. The large positive values to the east and northeast of the cloud cluster are probably related to wind shear.

Figure 8 is a scatter diagram illustrating the effect of scale size on the averaged relative vorticity fields. A wide scatter probably means that the relative vorticity field is more difficult to predict from large-scale motions than the divergence field and is scale dependent. A spatial analysis of components $\partial u/\partial y$ and $\partial u/\partial x$ (not presented here) reveals that a major contribution to relative vorticity field in the cluster area comes from the shear in the zonal flow, i.e., $-\partial u/\partial y$. The ratio of the zonal to the meridional shear ranges from 2:1 to 5:1 depending on the intensity of cloud activity. While in the vicinity of a cloud cluster the shear is cyclonic; the clear environment exhibits predominantly anticyclonic wind shear.

Relationship Between Divergence and Vorticity Fields

In this section we look for relationships between the divergence and vorticity fields related to the location of a cloud cluster. Of the three days presented, the 27th has the best data coverage and two active

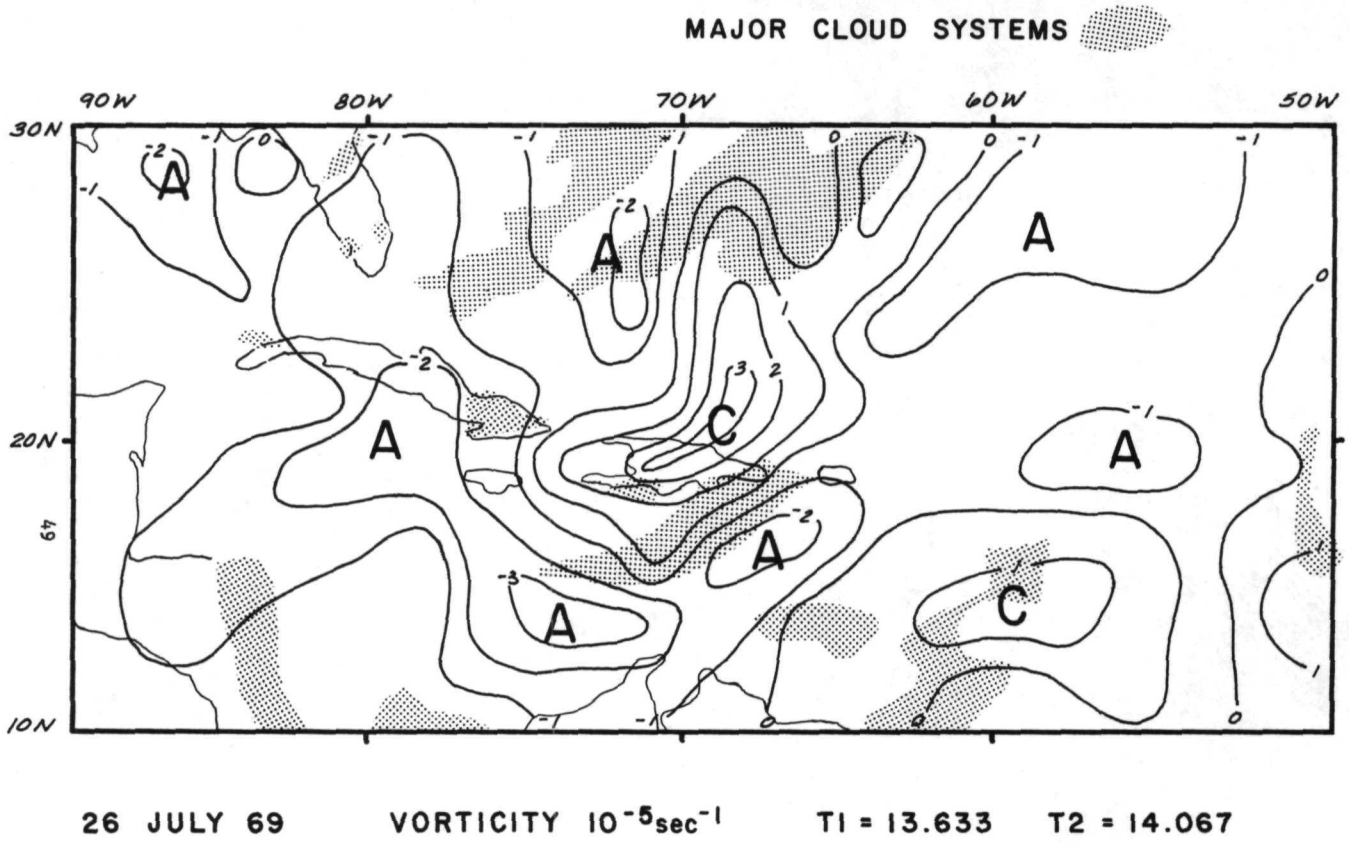

Figure 7a. Relative vorticity map upon which is superimposed the cloud field on 26 July 1969.

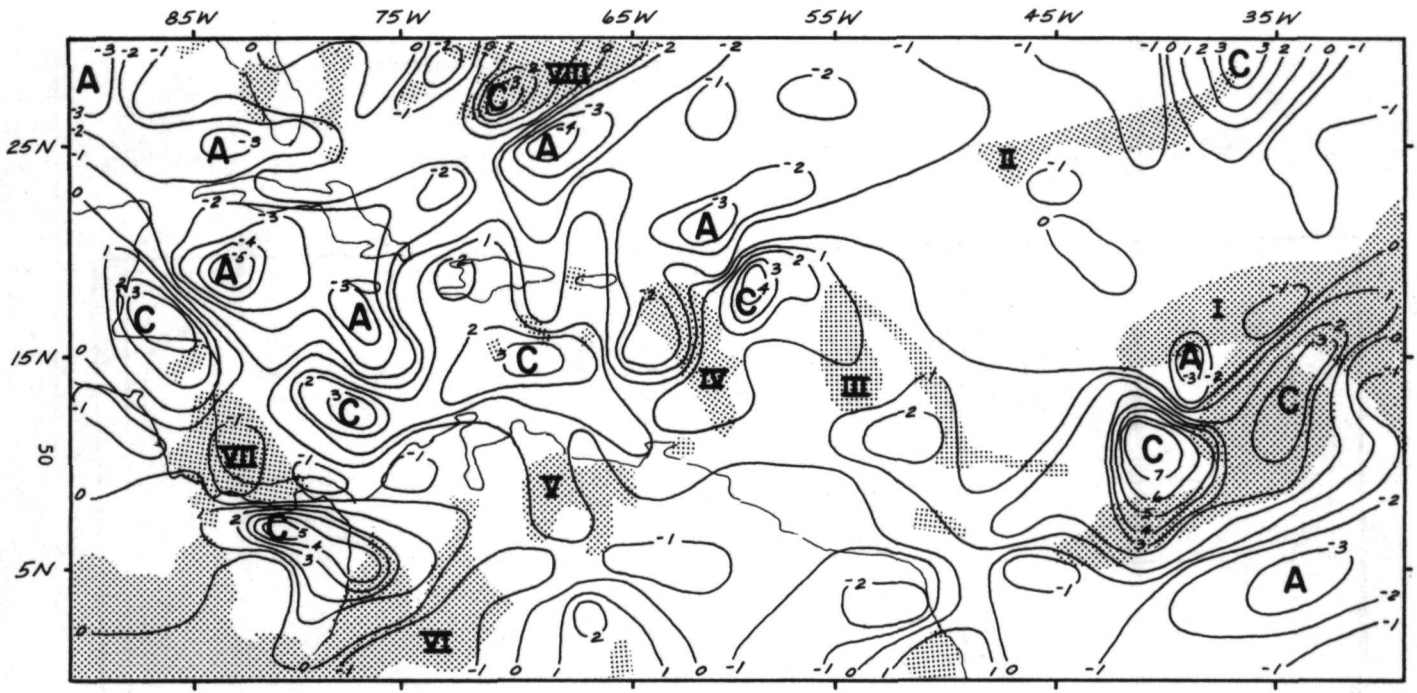

Figure 7b. Same as 7a except for 27 July 1969.

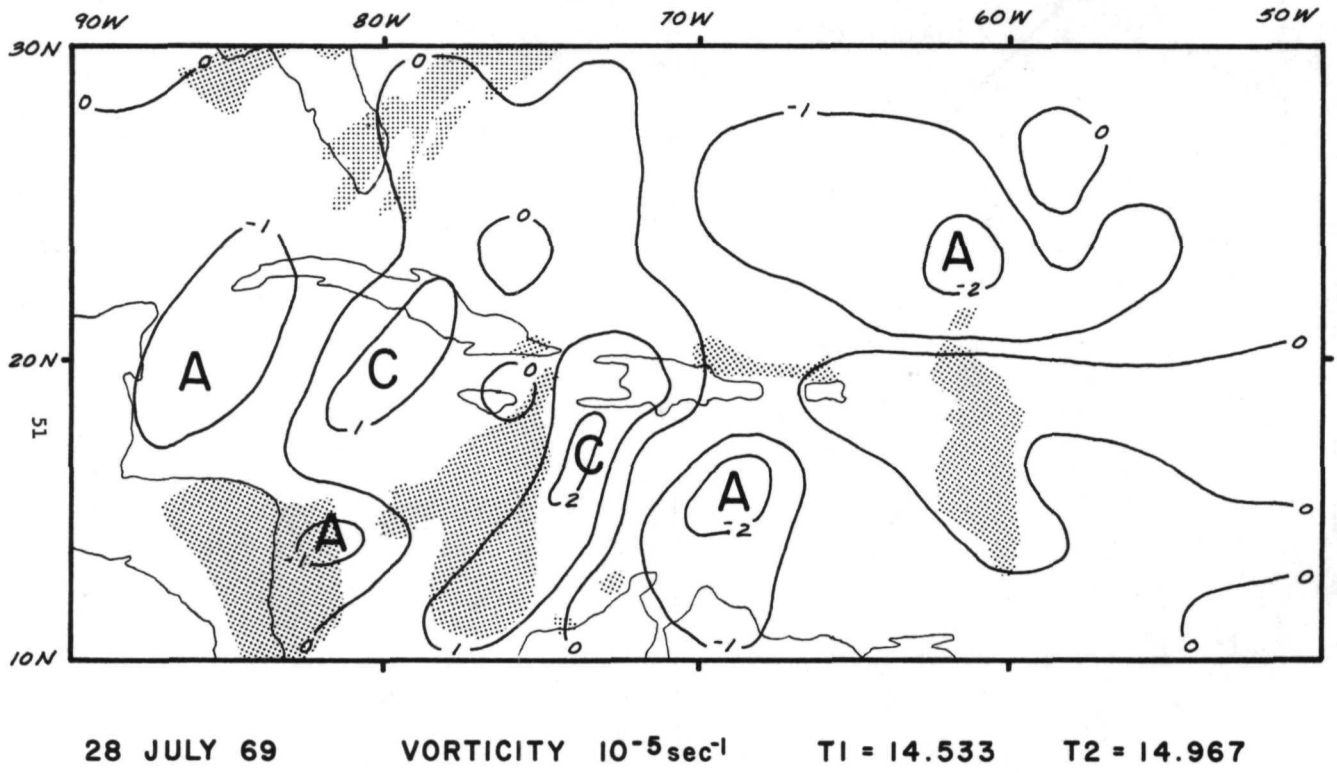

Figure 7c. Same as 7b except for 28 July 1969.

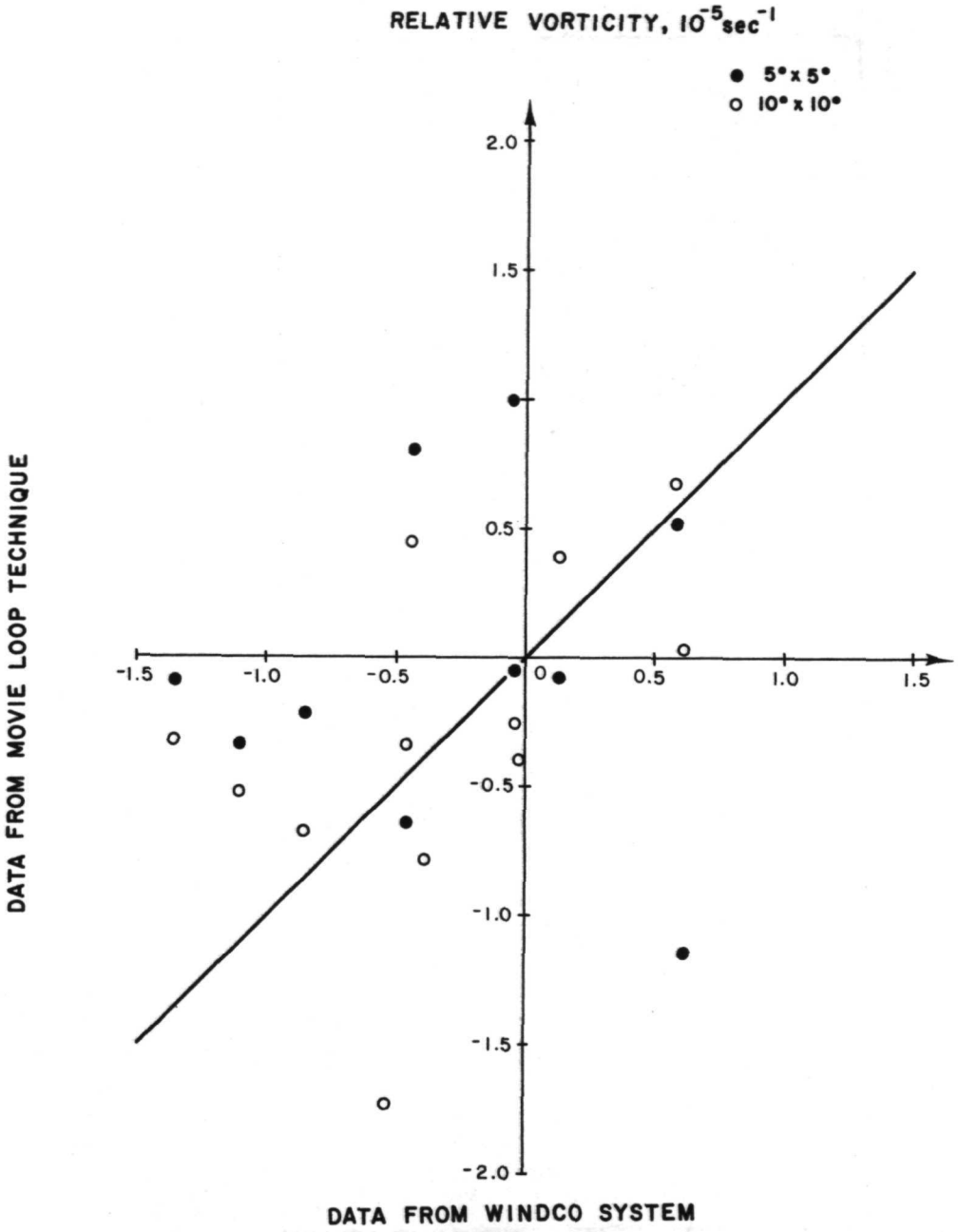

Figure 8. Scatter diagram showing the dependence of relative vorticity magnitudes on scale size.

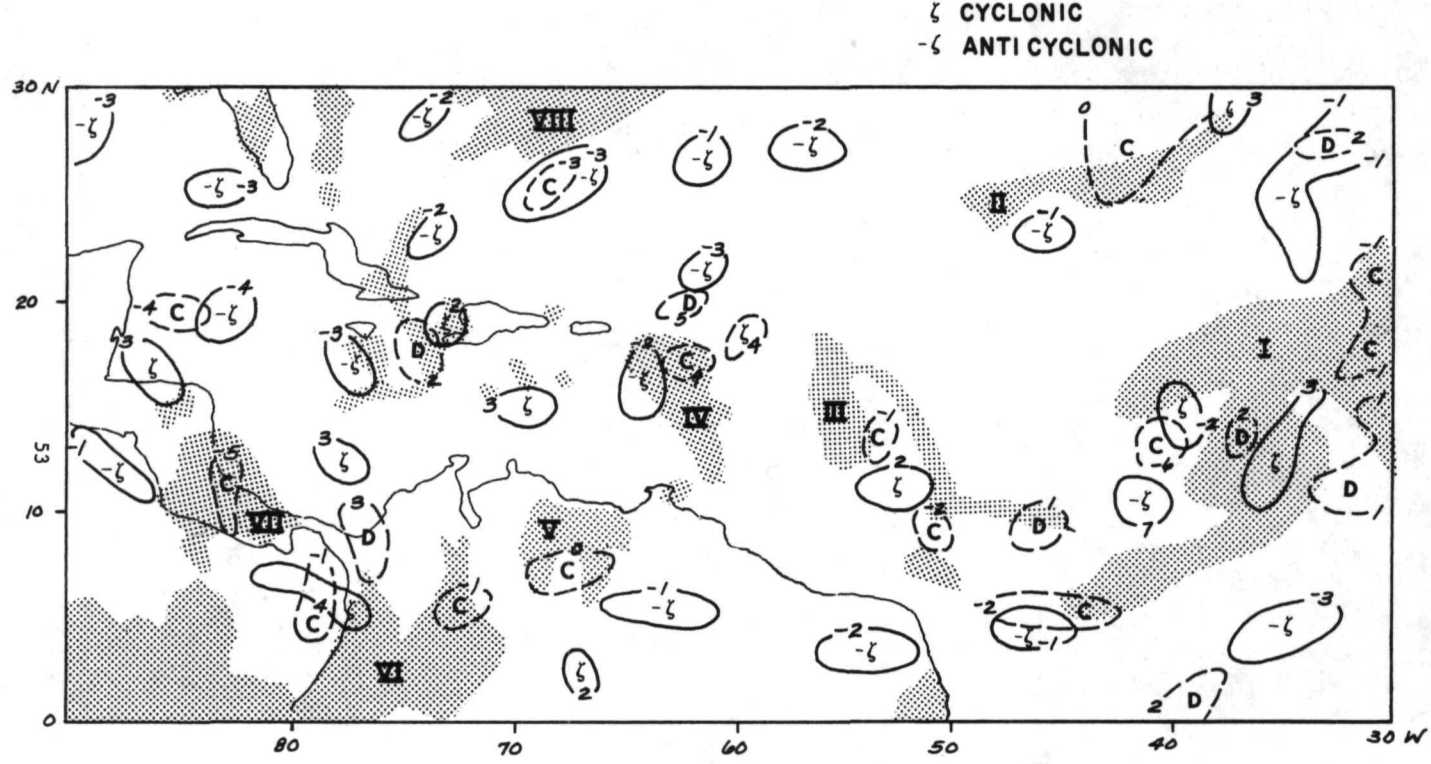

Figure 9. Locations of D_{max} and ζ_{max} for 27 July 1969.

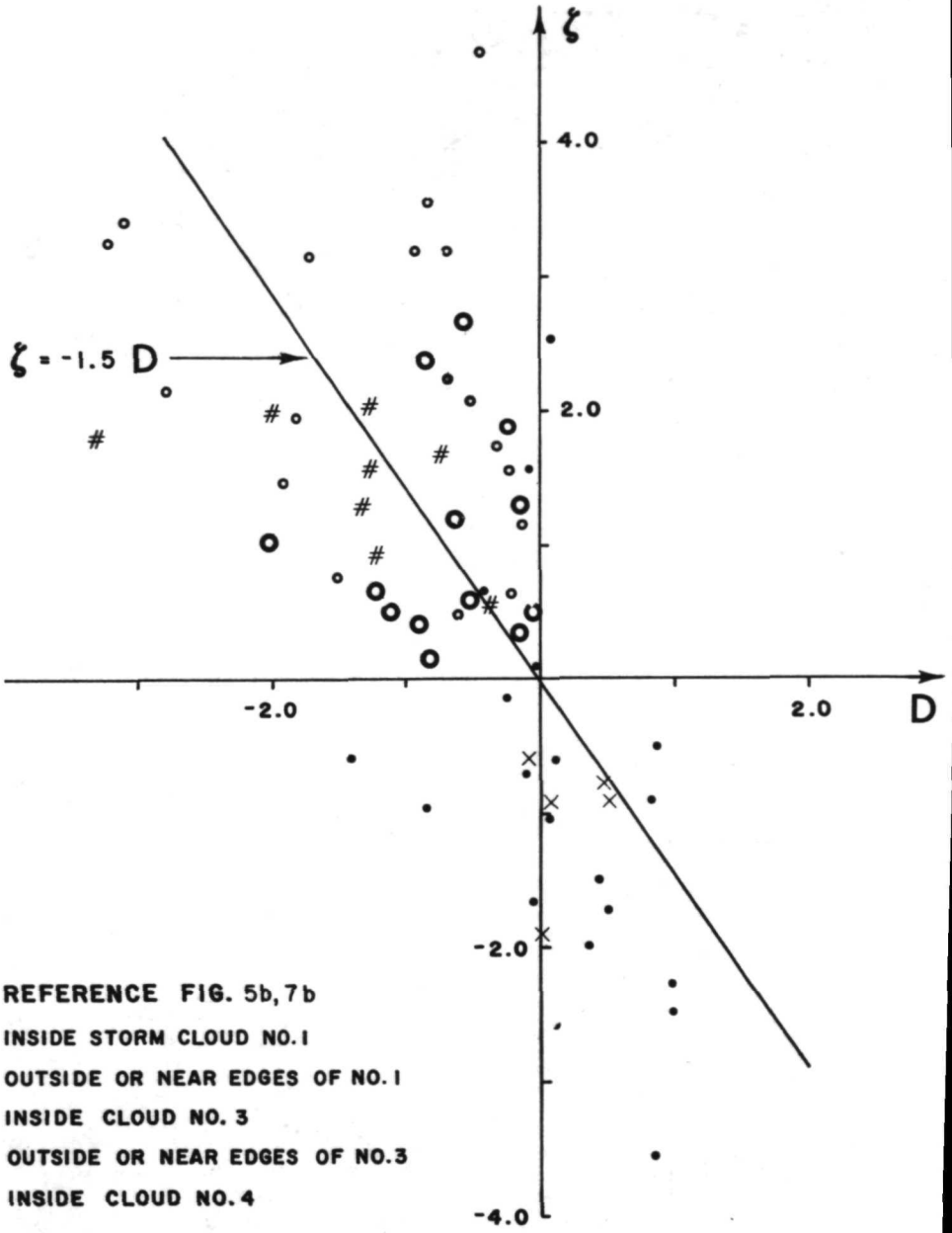

Figure 10a. Scatter diagram for relative vorticity versus divergence for clouds #1, 3, 4 in Figure 9.

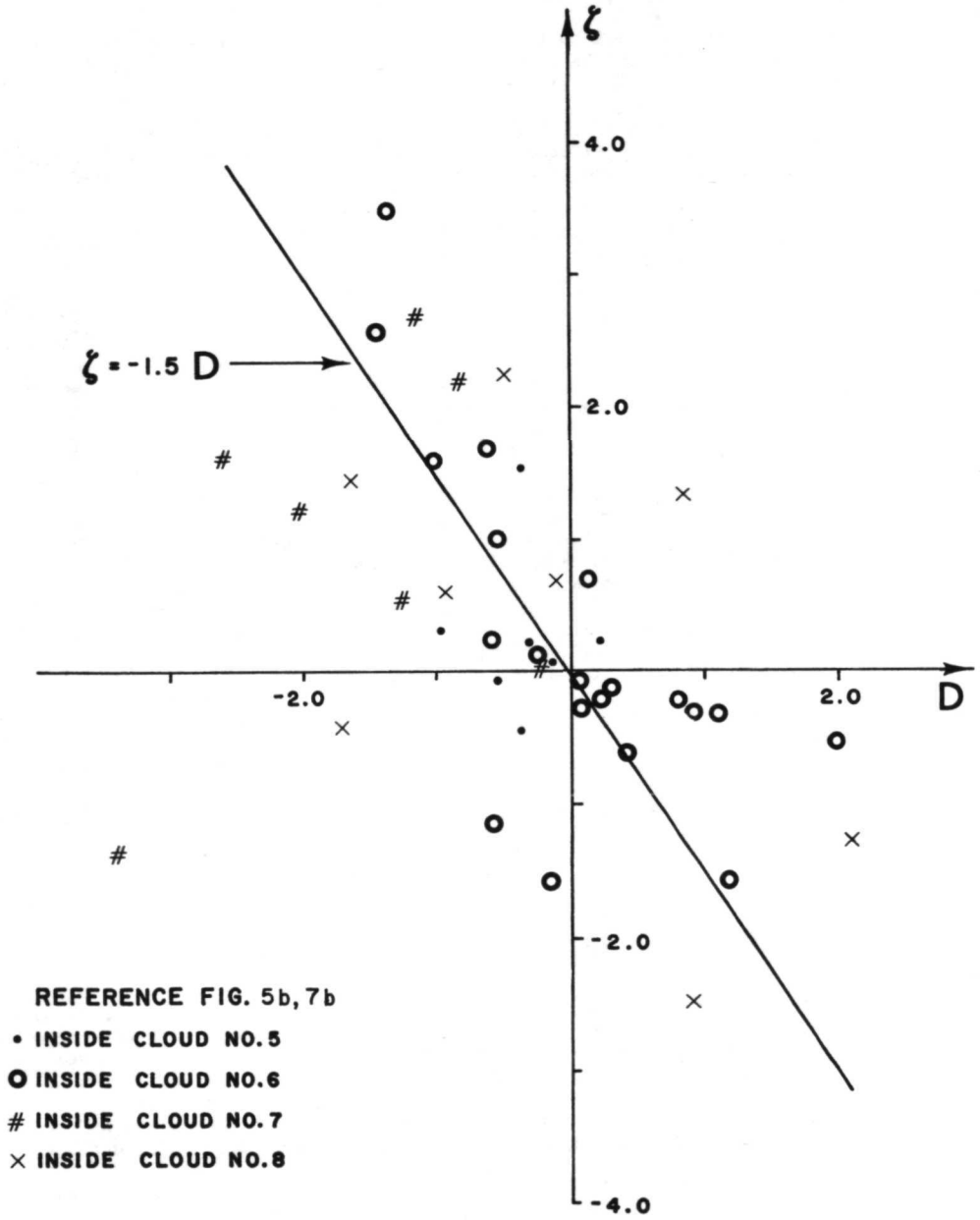

Figure 10b. Same as 10a but for clouds #5, 6, 7 and 8.

clusters in the central North Atlantic, with an intense cyclonic circulation near the ITCZ in the eastern North Atlantic. Therefore, only the analysis for the 27th is presented.

Figure 9 indicates the locations of maxima of relative vorticy (ζ) and of divergence (D) related to the cloud cluster. One clearly finds in this diagram that the locations of ζ_{max} and $-D_{max}$ are separated by a considerable distance. In the case of intense cyclonic circulation (Anna), however, both ζ_{max} (cyclonic) and $-D_{max}$ (convergence) are located near the storm's circulation center; this may imply a different flow pattern than is typically associated with a cloud cluster.

Although the locations of ζ_{max} and $-D_{max}$ and the cloud cluster do not exactly coincide, the cloud cluster growth is closely dependent on the convergence, for the latter becomes a dynamic necessity for the air to rise to the cirrus outflow layers through convective towers embedded in active cloud clusters. Charney and Eliassen (1964), Ooyama (1964) had proposed CISK (Conditional Instability of the Second Kind) as an important mechanism for the intensification of cloud clusters and tropical storms. If CISK is the mechanism of convergence, one would expect a clear-cut relationship between the grid point values of ζ and D obtained from this analysis, and the intensity of cluster activity. We assumed here that the small clouds used as tracers of air motion are tied to the boundary layer dynamics.

Figures 10a and b are scatter diagrams, presenting grid point values of ζ and D inside and near the cloud edges. The diagram reveals in general that in the cloud cluster vicinity, the divergence or convergence usually do not exceed 2.5×10^{-5} sec^{-1} and the relative vorticity is predominantly anticyclonic; the cloud cluster area is characterized by positive relative vorticity and negative divergence and the grid-point values of ζ and D inside an intense cyclonic circulation (for example, cloud #1 in Figure 9) are located in the same domain. The magnitudes are, however, significantly higher than in an ordinary cluster, and the relative vorticity is dominant. An approximate relationship $\zeta = -1.5D$ emerges from the scatter diagram implying a decrease of low level divergence with increasing relative vorticity in the ratio 1:-0.67.

7. Specific Kinetic Energy

Figures 11a, b, c present specific kinetic energy fields defined by $\frac{1}{2}(u^2 + v^2)$ for 26, 27 and 28 July, respectively. No specific conclusions can be drawn from such an analysis except that one finds consistency in the location of specific kinetic energy generation sources on the three successive days investigated. The maxima are approximately where horizonal wind shears have the highest values, i.e., at the southern periphery of the anticyclonic vortex in the western as well as in the eastern North Atlantic (Figures 2a,b,c). Two dominant source regions are noted during this study period: one centered around 17°N, 60°W and the other around 15°N, 80°W. On extended charts of the 27th, another source region is around 12°N, 40°W on the ITCZ west of Africa.

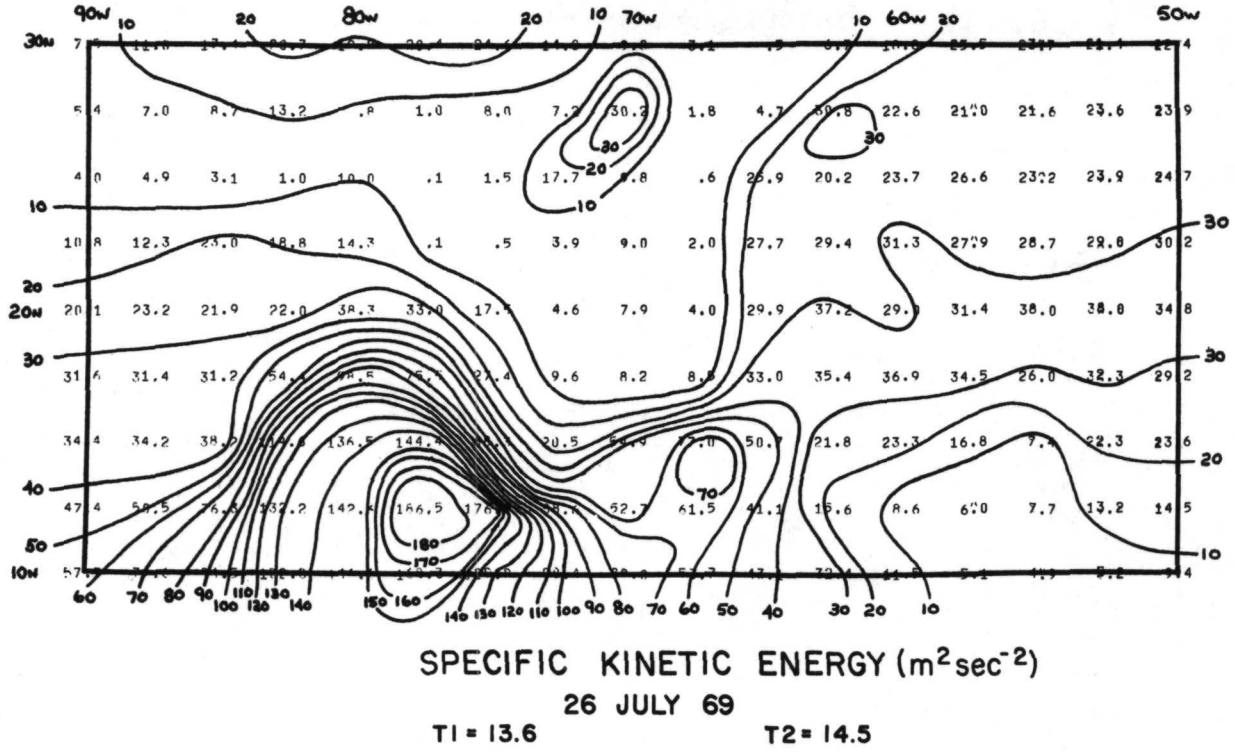

Figure 11a. Specific kinetic energy field constructed from 26 July 1969. data.

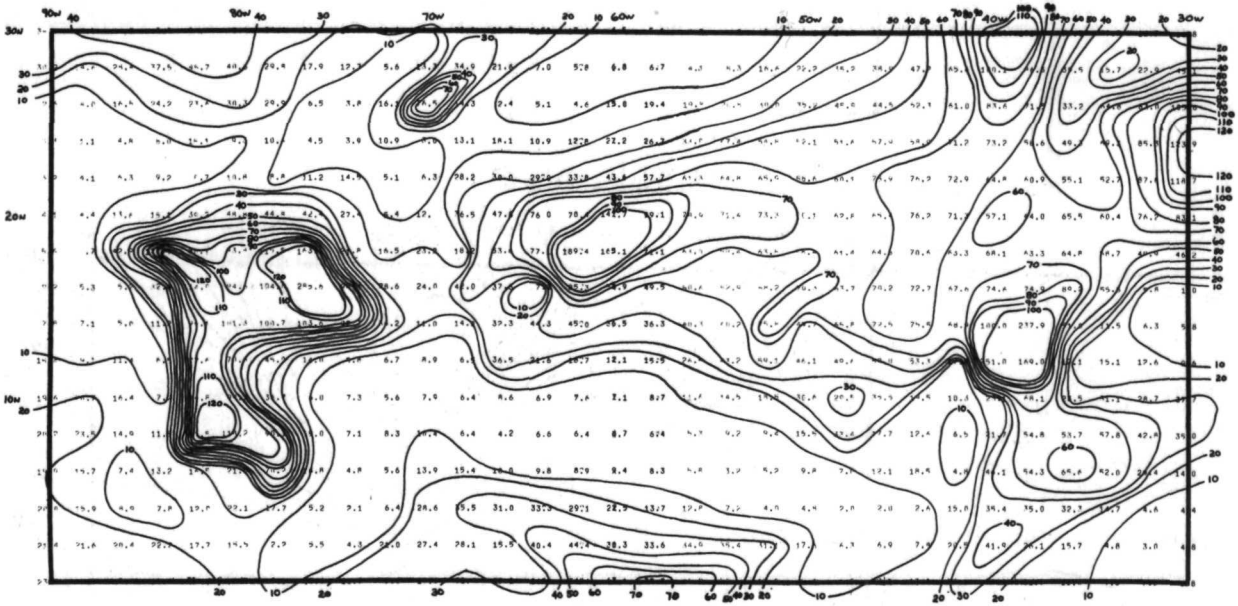

Figure 11b. Same as 11a except for 27 July 1969.

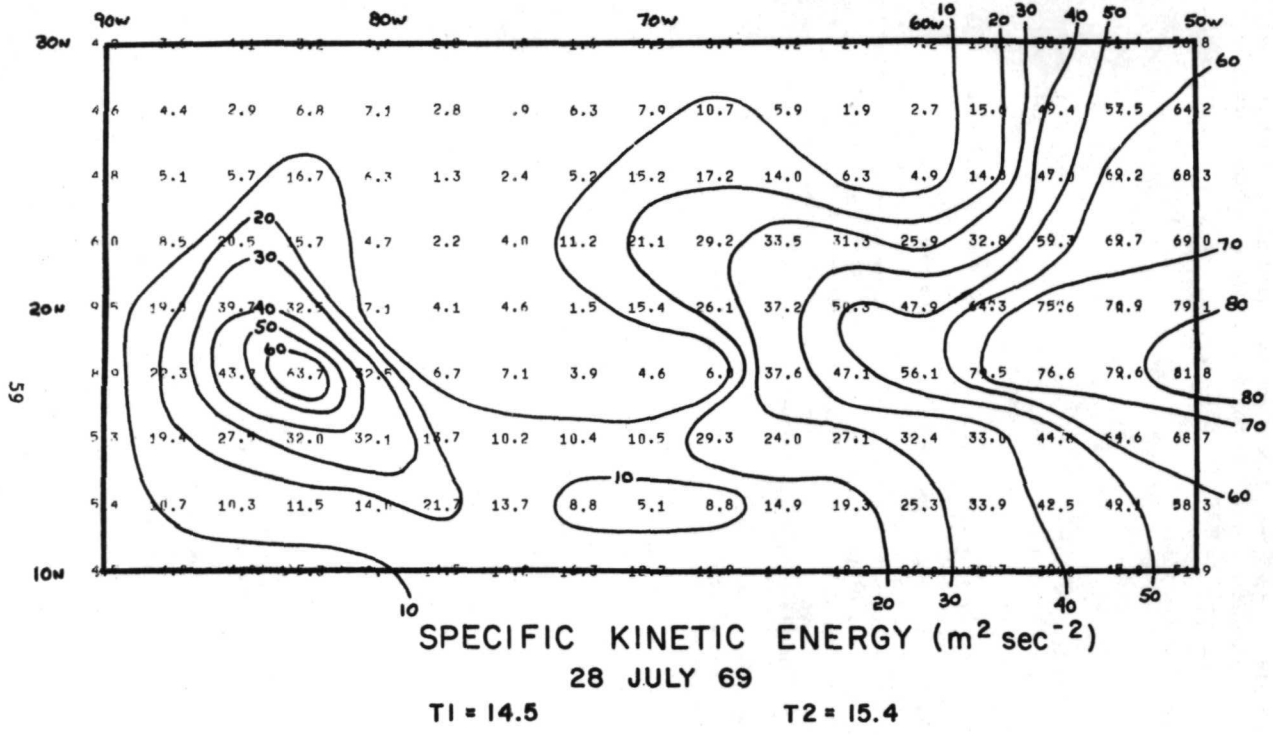

Figure 11c. Same as 11a except for 28 July 1969.

One can hardly infer on the kinetic energy production and destruction from this simple approach, but future possibilities exist in exploiting the data from three-dimensional viewpoint (SMS) when one should be able to compute $-u \frac{\partial \phi}{\partial x}$ and $-v \frac{\partial \phi}{\partial y}$ (ϕ = geopotential), both as a function of latitude-longitude and time.

8. Concluding Remarks

In this sample study of the one-layer model, we have seen that the low level cloud trajectories obtained from the WINDO system exhibit patterns comparable to streamlines at lower tropospheric levels (3000 ft).

In the u and v fields analyzed from these data we do see significant changes in large-scale motion field on a time scale of a few hours. Assuming the wind finding technique to be working proficiently, this short time change may be attributed to cloud evolution processes or real changes in the horizontal wind field, for the cloud targets selected as tracers may not be individual cumuli but small clusters and patches. Also seen in the u and v fields is a significant latitudinal wind shear north and south of the ITCZ, especially in the zonal wind. Meridional components also exhibit shear south of 15°N.

Superimposing divergence and vorticity fields on the cloud field, one gets the general impression that the cloud clusters are in the areas of convergence and positive relative vorticity. The vorticity magnitudes appear to be scale-dependent while the divergences are not, at least in the scale 100-600 nautical miles on a side. The grid point values of ζ and D are found approximately related by the equation $\zeta = -1.5D$, implying that the low level divergence generally decreases with increasing relative vorticity in an active cloud cluster; however, for some clouds such a relationship is missing. One may conclude from this sample study that the CISK mechanism may be valid for large tropical nephsystems with intense convective activity in them—but may not be true for all tropical cloud clusters.

Finally, the specific kinetic energy patterns consistently show two dominant source regions to the north of the ITCZ during the study period which are possibly related to zonal wind shear.

ACKNOWLEDGMENTS

The author is grateful to Mr. Richard Cram for his assistance in processing, analyzing and interpreting the data presented in this paper. Thanks are due to Professor V. E. Suomi and Dr. David Martin for reviewing the manuscript, and to many individuals at SSEC who helped in various ways in this research program. The research reported in this paper was partly supported by NOAA under grant E-230-68(g) and partly by NASA under contract NAS5-21650.

References

Charney, J. G., 1964: Growth of the hurricane depression. *J. Atmos. Sci.*, 21, 68-75.

Hasler, A. F., 1971: Properties of tropical cloud clusters determined from geostationary satellite pictures. Ph.D. thesis, Dept. of Meteorology, University of Wisconsin.

Hubert, L. F. and L. F. Whitney, Jr., 1972: Wind estimation from geostationary satellite pictures. *Mon. Wea. Rev.*, 99, 665-672.

Fujita, T. T., K. Watanabe and T. Izawa, 1969: Formation and structure of equatorial anticyclones caused by large-scale cross-equatorial flows determined by ATS-I photographs. *J. Appl. Meteor.*, 8, 649-667.

Ooyama, K., 1964: A dynamical model for the study of tropical cyclone development. *Geofisica. International*, 4, 187-198.

Park, S., 1972: M.S. Thesis in progress.

Serebreny, S. M., R. G. Hadfield, R. M. Truden and E. J. Wiegman, 1969: Comparison of cloud motion vectors and rawinsonde data. Final Report SRI Project 7257, 62 pp.

Sikdar, D. N., 1969: Convective heat transport over the tropical mid-Pacific as estimated from a geosynchronous satellite altitude. Ph.D. thesis, Dept. of Meteorology, University of Wisconsin, 130 pp.

Smith, E. and D. Phillips, 1972: Automated cloud tracking using precisely aligned digital ATS pictures. *IEEE Transactions on Computers*, 4, 187-198.

THE FEASIBILITY OF THE APPLICATION OF A GEOSTATIONARY SATELLITE RAKE SYSTEM TO MEASUREMENTS OF RAINFALL

F. G. Stremler

This is a report on a feasibility study of the use of a RAKE radar system in a geostationary earth satellite to measure rainfall budgets for large, normally inaccessible regions of the earth's surface. A subcontract report of the Collins Radio Company is appended as a major portion of this study [1]. Professor Birkemeier of the Department of Electrical Engineering has been very successful in applying RAKE techniques to tropo-scatter measurements [2], and his comments and advice have also been valuable in this study.

Major problems confronting the use of a RAKE radar system to synchronous meteorological coverage are:

(1) a doppler spectrum, arising from rainfall, that is not sharply defined (i.e., large variance);

(2) an unfavorable signal-to-clutter ratio resulting from the relatively small returned radar power from rainfall in the presence of a strong return from the earth; and

(3) lack of a suitable satellite for a RAKE experiment as a result of the high power and frequencies.

These are discussed here with particular reference to the Collins report.

Because of the distribution of drop sizes in precipitation, a radar pointing vertically will observe a doppler spread resulting from a distribution of fall velocities. Measurements and data in the literature on doppler spectra from rainfall are very meager. Calculations made by Collins (see their Figure A-6) show that the standard deviation of fall velocities is about 2 m/sec and is fairly independent of rain intensity. Calculations using a Marshall-Palmer distribution for drop size [3] and measurements of fall velocities versus drop size found in Medhurst [4] yield very similar results, with slightly smaller variance. Lhermite as quoted by Nathanson [5], states that the standard deviation of fall velocities is approximately 1.0 m/sec; Nathanson also adds a turbulence factor of about 0.7 m/sec. These references and a limited set of measurements reported by Nathanson and Davidson [5] reveal that the assumption of a standard deviation of 2 m/sec, as used by Collins, is certainly not unreasonable though perhaps a little pessimistic. The

outcome of this is that even if the earth return were not present, the minimum doppler bandwidth arising from rainfall is on the order of 400 cm/sec or $B_d = 2v/\lambda = 800/\lambda$ Hz where λ is in cm. An earlier estimate of performance by Collins [6] was based on the possibility of using a doppler bandwidth $B_d = 1$ Hz resulting in significantly better receiver sensitivities.

It is assumed that the tropics is the region of interest for RAKE rainfall measurements. In this region the source of heavy rainfall is primarily from cumulonimbus clouds, and the water content and characteristics of such clouds are fairly well known [7],[8]. Representative numbers chosen in the Collins report to compute signal attenuations are not extreme and appear to be reasonable for a 95% probability-of-detection performance [9]. Expected radar signal return levels calculated on the basis of a transmitted power of 100 watts and the attenuations used by Collins are shown in Figure 1 together with receiver noise levels corresponding to a 1 Hz and a $800/\lambda$ Hz doppler bandwidth. As the transmitted power levels are changed, the returned power levels move on the graph but the receiver noise thresholds remain fixed. Conclusions are that about 150 watts are needed to detect a rainfall rate of 10 mm/hr over a region 50 km in diameter at $\lambda = 2$ cm using a 10 m antenna (ideal) (also see Figure A-10 in the Collins report). As a more practical case, 1 kw is required at a wavelength of 4 cm if the antenna gain is limited to 50 dB. These numbers are determined by adding the required dB to raise the rainfall return power curves in Figure 1 to match the receiver noise levels.

To complicate matters, a very large earth return arrives at the receiver a few microseconds after the rainfall return. This received power level (P_{rE}) is large compared to the earth return, as illustrated in Figure 1. There are several options open to suppress this strong ground clutter return. The first method assumes that the doppler of the satellite with respect to the earth can be removed and that the earth return can then be separated from the rainfall return on the basis of doppler shift. This is the assumption used in the Collins report.

Doppler clutter return for land masses will be very low while doppler returns from waves will vary with sea state, but will rarely exceed 2 m/sec [10]. Therefore, the doppler spectra from the earth return and the rainfall return are nonoverlapping and can be separated by filtering. Assuming a 40 dB attenuation on this basis, the remainder of the attenuation required (on the order of 50 dB) must be picked up using the proper signal design. Collins used the clutter rejection capabilities of a RAKE signal long enough to fill the time delay to the earth and return.

Several alternatives can be considered in the earth return problem. One method is to use short coherent code words spaced just far enough apart so that the earth return is received between words. Another possibility is to employ frequency agility instead of time agility in separating the rainfall returns from the earth returns. Answers to how these signal changes affect RAKE system performance are not presently known [11] and furnish an impetus to new research in signal design in this area. These methods, while perhaps promising better clutter rejection, increase the complexity of the satellite RAKE system and should be studied in depth before dependence on them is assumed.

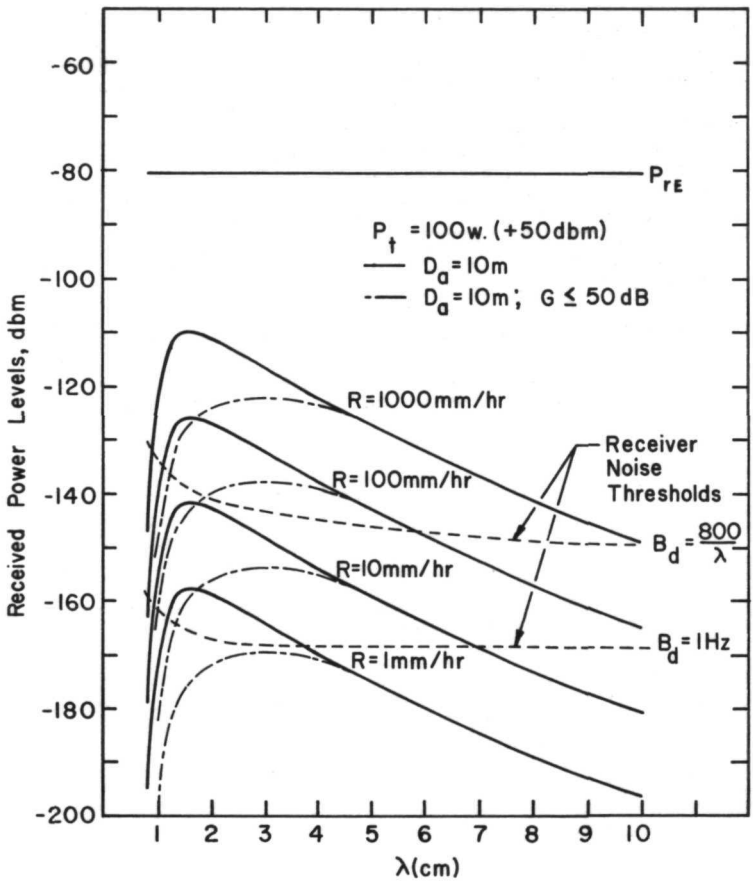
-60
-80
-100
-120
-140
-160
-180
-200
Received Power Levels, dbm
1
2
3
4
5
6
7
8
9
10
λ(cm)
P_{rE}
P_t = 100w. (+50dbm)
D_a = 10m
D_a = 10m; G ≤ 50 dB
R=1000mm/hr
R=100mm/hr
R=10mm/hr
R=1mm/hr
Receiver
Noise
Thresholds
$B_d = \frac{800}{\lambda}$
B_d = 1Hz

Figure 1

A third area of investigation is the availability of existing or planned satellites on which a RAKE rainfall detection experiment could be attempted. The Collins report cites the status of the ATS-G. Availability of a suitable satellite or pair of satellites is generally precluded for one or more of the following reasons [12]: 1) Radio frequencies above 6 GHz are not currently used in satellites (except ATS); 2) few satellites, if any, could meet the power and/or bandwidth requirements needed; 3) satellite communication systems frequencies are chosen so that no frequency used on the downlink of one satellite is used on the uplink of another. Some military satellites might have the capability to try such an experiment but data have not been available on this.

In conclusion, the Collins report has correctly defined the problem and estimated the feasibility of the RAKE radar rainfall measurement based on available theory and data from the literature. This study points out several main problems in the implementation of such a system and areas for further work and investigation:

(1) Can the doppler dependence on rainfall rate be checked with experimental data?

(2) Given these data, can rainfall rates be reliably made using doppler estimators?

(3) Can suppression of earth return clutter be improved using different signal design techniques?

(4) Can a satellite be found to try the experiment without excessive changes in the satellite?

References

1. Pool, R. H., Hise, T. L., and Hamilton, A. R., 1972: "The Feasibility of the Application of a Geostationary Satellite RAKE System of Measurements of Rainfall," Collins Radio Company Report, August 1972 (see Appendix).

2. Birkemeier, W. P., et al., 1969: "Indirect Atmospheric Measurements Utilizing RAKE Tropospheric Scatter Techniques—Part II: Radiometeorological Interpretation of RAKE Channel-Sounding Observations," *Proc. IEEE*, 57, No. 4, April 1969, 537.

3. Marshall, J. S., and Palmer, W. M., 1948: "The Distribution of Raindrops with Size," *Journal of Meteor.*, Aug. 1948, 165.

4. Medhurst, R. G., 1965: "Rainfall Attenuation of Centimeter Waves: Comparison of Theory and Measurement," *IEEE Trans. Ant. & Prop.*, July 1965, 550.

5. Nathanson, F. E., 1969: *Radar Design Principles*, McGraw-Hill, N.Y., Ch. 6.

6. Pool, R. H., 1972: "Geostationary Satellite RAKE Feasibility Study Proposal," Collins Radio Company.

7. Byers, H. R., 1949: *The Thunderstorm*, U.S. Department of Commerce—Weather Bureau.

8. Byers, H. R., 1953: *Thunderstorm Electricity*, University of Chicago Press.

9. Private communication with Dr. William L. Woodley, Experimental Meteorology Laboratory, University of Miami Branch, Coral Gables, Florida, July 1972.

10. Pidgeon, V. W., 1968: "The Doppler Dependence of Radar Sea Return," *J. Geophys. Res.*, February 15, 1968.

11. Private communication with Prof. W. P. Birkemeier, Dept. of Electrical Engineering, University of Wisconsin, Madison, Wis., September 1972.

12. Private communication with Dr. W. R. Bandeen, NASA, Goddard Space Flight Center, Greenbelt, Maryland, September 1972.

APPENDIX

The Feasibility of the Application of a Geostationary Satellite RAKE System to Measurements of Rainfall*

1. Introduction

Preliminary analysis has suggested the use of the unique radar mapping capabilities of a RAKE system incorporated into a geostationary satellite implementation, as graphically illustrated in Figure A-1, to obtain measures of rainfall budget for the relatively large, but normally inaccessible, tropic regions of the earth.

The geostationary satellite RAKE approach to measurement of rainfall budget involves the transmission of a probing signal consisting of a microwave frequency carrier, biphase modulated by a bilevel pseudorandom noise sequence, from the satellite toward the earth with vertical or near-vertical incidence to the earth's surface. Portions of the transmitted signal are reflected from rain at various altitudes and from the earth's surface to return to the satellite as a signal similar to the transmitted signal but dispersed in both time and frequency dimensions. The satellite directs this dispersed signal to the RAKE receiver wherein the signal is cross-correlated with appropriately delayed replicas of the transmitted signal to effectively separate the received signal into a series of time delay increments. Since the desired rain return signal, which corresponds to rain observed in a given altitude region, differs in delay from rain

*Prepared by R. H. Pool, T. L. Hise and A. R. Hamilton; Collins Radio Company, Cedar Rapids, Iowa, August 1972.

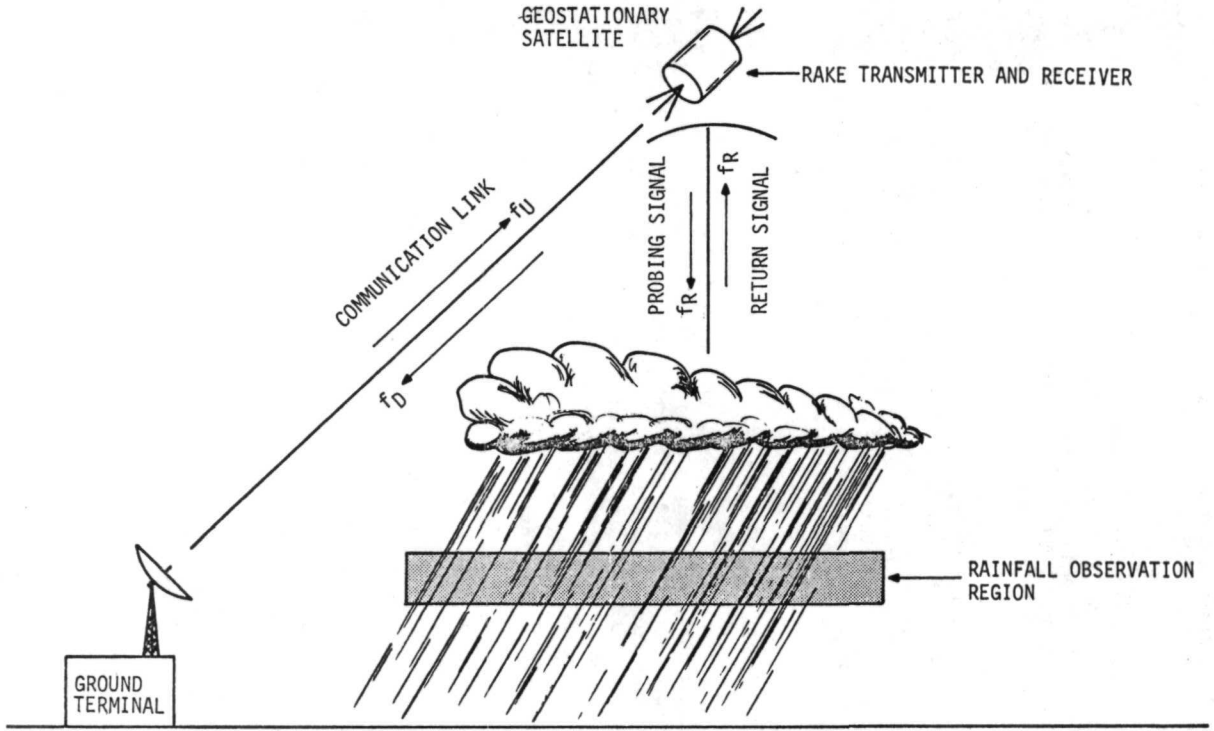

Figure A-1. Geostationary satellite RAKE rainfall measurement concept.

returns of other altitude regions and from the earth return, the desired rain return signal can ideally be isolated from the others through the RAKE receiver cross-correlation process. The recovered rain return signal can then be spectrally processed to obtain a doppler frequency spectrum that relates to the distribution of rainfall velocity within the observed altitude region. From the relationship of rainfall velocity and raindrop radii distributions and a knowledge of the antenna beam-filling factor of the observed rainfall region, perhaps determined optically, the rain return signal power and its frequency distribution can be employed to obtain a measure of rainfall rate. Subsequent time integration of rainfall rate will allow a value for total rainfall to be determined.

This report relates the procedures followed and the results obtained during the performance of an in-depth analysis of the above described geostationary satellite RAKE system concept to determine the feasibility of its application to measurement of rainfall budget. Consideration is given to optimization of the system concept, determination of a "best" technique for implementation and the possibilities of implementing the system on the basis of planned geostationary satellite configurations.

2. System Analysis and Optimization

In this section the basic equations, parameters and parameter relationships defining the geostationary satellite RAKE system are presented. These are then applied to the problems of optimization of the system concept on a theoretical basis without regard to a specific form of system implementation, although practical limitations and constraints are included in the optimization procedures.

2.1 Basic Equations and Parameters

Two equations relating the signal power returned to the satellite from rain and the earth's surface form the basis for determination of system feasibility. These two equations involve relationships of the many meteorological and radio parameters that define the characteristics of the radio propagation path and terminal equipment.

The first of these equations, basically from Battan [1], defines the total average signal power returned to the satellite from spherical water particles contained in an observation region above the earth's surface having a volume determined by the area illuminated by the antenna and a height h.

$$\bar{P}_{raR} = \left[\frac{\pi^5}{72}\frac{P_t A_p^2 \theta\phi h\psi F|K|^2}{\lambda^6}\right]\frac{Z}{r^2}\,10^{-0.2\int_0^r kdr}\,10^{-0.2L} \qquad (2\text{-}1)$$

where

$\bar{P}_{arR}$ = Average rain return signal power (watts)

P_t = Transmitted power (watts)

A_p = Apertural area of satellite antenna (cm^2)

θ = Antenna azimuth beamwidth (radians)

ϕ = Antenna elevation beamwidth (radians)

h = Height of rain observation zone (cm)

ψ = Beam-filling factor (%/100)

F = Correction factor (see L. J. Battan, 1959)

$|K|^2$ = Complex index of refraction (see L. J. Battan, 1959)

λ = Wavelength of transmitted center frequency (cm)

Z = Reflectivity factor (cm^6/cm^3)

r = Range (one-way, satellite-to-reflector distance)(cm)

k = Propagation attenuation rate, one-way (dB/km) = $k_g + k_c + k_p$ (gases, k_g; clouds, k_c; precipitation, k_p)

L = Equipment losses, one-way (dB)

The second equation, based upon work by Beckmann and Spizzichino [2], defines the received power reflected from a diffuse scattering sea surface.

$$P_{rE} = \frac{P_t A_p^2 \theta\phi 10^{-0.2L}}{36\lambda^2 r^2} \cot^2\beta_0 \exp[-\tan^2\alpha/\tan^2\beta_0] \qquad (2\text{-}2)$$

where P_{rE} is the received earth return power, α is the angle of signal incidence to the earth's surface measured from vertical, and β_0 is the mean slope of the sea surface irregularities. The remaining parameters are as previously defined.

These two equations will be used in various forms throughout the remainder of the report. The need for the rain return power equation is perhaps obvious. The earth return power equation enters into the problem due to the finite clutter rejection capability of the RAKE system. If the earth return power exceeds the rain return power by an excessive amount, the correlation processes of the RAKE receiver and the spectral processing that follows may not be capable of adequately isolating the two signals. The sea surface return, much stronger than the ground return, provides for a worstcase, but certainly reasonable, situation.

2.2 Parameter Relationships

The progression toward system optimization and finally the determination of system feasibility on a theoretical basis requires a knowledge of the parameter relationships presented in the following paragraphs. Since the basic power return equations expressed in the previous paragraph 2.1 are functions of such a large number of variables, it is necessary to develop these parameter relationships in order to reduce the number of variables involved in the basic equations. Also, reasonable constant values will be chosen for certain parameters. Further, the range of certain variables will be restricted, from practical considerations, to provide additional simplification relative to the totally general case. After optimization is completed, it will be possible to evaluate the effects of variations in the restricted variables as perturbations rather than true variables.

2.2.1—Pseudorandom Sequence Clock Frequency. Starting with a given value for the height of the rain observation region h, the effective transmission bandwidth W can be determined as

$$W = \frac{c}{2h} \tag{2-3}$$

where c is the magnitude of the free-space propagation velocity. Using the definition of W provided by Berkowitz [3], W is found to also be approximately equal to the pseudorandom sequence generator clock frequency f_c if the actual RAKE transmitted signal bandwidth is $2f_c$. With f_c set equal to W, then f_c is defined as a function of h by Eq. (2-3).

2.2.2—Correlation Time. The RAKE receiver correlation process requires a correlation bandwidth W_c that is sufficiently wide to pass all expected doppler frequency shifts of the rain return signal. If equivalent low-pass, in-phase and quadrature-phase correlator outputs are employed to reduce the data sampling rate to a minimum, then

$$W_c = 2|f_{dm}| \tag{2-4}$$

where f_{dm} is the maximum doppler frequency, positive or negative, observed at the correlator outputs. A correlation time T_c is defined as

$$T_c = \frac{1}{W_c} = \frac{1}{2|f_{dm}|} \quad . \tag{2-5}$$

The repetition period of the pseudorandom sequence is T_0; therefore, the product $WT = f_cT_0$ defines the length of the sequence in terms of the number of clock periods or so-called "chips" involved in generating one complete sequence. Similarly, WT_c is the number of chips involved in the RAKE correlation process.

2.2.3—Clutter Rejection. The rain return signal from a selected altitude region above the earth's surface is recovered through the correlation process. However, the returns from other rain regions and the very strong return from the earth's surface, although at differing time delays, are not totally rejected in the correlation process and therefore appear at reduced levels as a part of the desired output. The degree to which

the undesired, or clutter, signal powers can be reduced is dependent upon a clutter rejection factor W_T that is related to both WT_0 and WT_c. Lindholm [4] develops an equation describing the second moment of the clutter level of the pseudorandom sequence correlation process for the case where $WT_c \leq WT_0$. These results were employed to develop an equation for W_T of the form

$$W_T = \frac{WT_0 - WT_c + 1}{(WT_0)(WT_c)} \tag{2-6}$$

again for the region where $WT_c \leq WT_0$. This latter equation indicates a best clutter rejection factor value of $(1/WT_0)^2$ is obtained when $WT_c = WT_0$. As WT_c becomes increasingly greater than WT_0, it appears that W_T tends to follow an envelope somewhat similar in form to $\sin^2 x/x^2$ with minimum values of $(1/WT_0)^2$ rather than zero, asymptotically approaching a constant value of $(1/WT_0)^2$. Best clutter rejection is obtained with $T_0 = T_c$; therefore T_0, the repetition period of the pseudorandom sequence, is defined by Eq. (2-5).

The pseudorandom sequence parameters f_c and T_0 as defined by Eqs. (2-3) and (2-5), respectively, can be combined to determine the sequence length as

$$f_c T_0 = WT_0 = \frac{c}{4h|f_{dm}|} \tag{2-7}$$

and the best clutter rejection factor W_{Tm} as

$$W_{Tm} = \frac{1}{(f_c T_0)^2} = \frac{4|f_{dm}|^2}{f_c^2} . \tag{2-8}$$

In order for the bilevel pseudorandom sequence to be developed as a maximal length shift-register sequence [4], it is necessary that $f_c T_0 = 2^n - 1$, where n is a positive integer. It may be necessary to slightly adjust either f_c or T_0, preferably f_c, to satisfy this latter equality. It should also be noted that T_0 must be maintained at a greater value than the maximum delay range of the signal returns (on the order of 200 microseconds) to prevent time ambiguity problems.

2.2.4—Transmission Duty Cycle. For a satellite RAKE system involving a single satellite and a common transmit-receive antenna, it will be necessary to alternately gate the transmit and receive functions. The maximum usable transmit period is equal to the satellite-to-earth round trip delay T_r where

$$T_r = \frac{2r}{c} \tag{2-9}$$

which is approximately 250 milliseconds. A 50% duty cycle will provide a receive period or measured interval of length T_r. Spectral processing resolution will be limited to $1/T_r$ corresponding, in this case, to about 4 Hz. For the satellite RAKE system, T_r can always be greater than the correlation time T_c; therefore, the transmitter and receiver pseudorandom sequence generators can operate continuously with no dependence upon the transmission duty cycle.

2.2.5—Doppler Frequency Shift. In the previous equations of this section, the only parameter relating to rainfall is f_{dm}, the maximum doppler frequency shift. Raindrops moving toward or away from the satellite with velocity V will cause a carrier frequency shift according to the equation

$$f_d = \frac{-2V}{\lambda} \qquad (2\text{-}10)$$

where λ is the wavelength of the transmitted carrier frequency. Godard [5] indicates that the maximum fall velocity V_m of raindrops is on the order of nine meters per second. Using this value for V_m, Figure A-2 shows the relationship of $|f_{dm}|$ to λ.

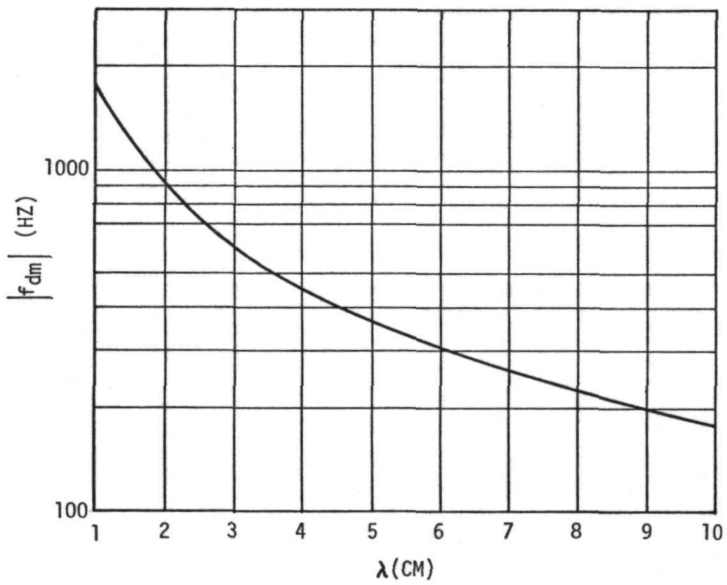

Figure A-2. Maximum doppler frequency shift as a function of wavelength.

Eccentricities of the geostationary satellite orbit can also cause a doppler frequency shift to all returning signals. ATS-5, for example, has a maximum earth radial velocity on the order of 41 meters per second corresponding to an 820 Hz frequency shift for a 10 cm wavelength signal. Considering that any geostationary satellite orbit will have some eccentricity, satellite-caused doppler shifts must be expected and the satellite RAKE system implemented accordingly. Since the satellite doppler shifts the earth return and rain return signals by essentially the same amount, it is reasonable to assume that the effects of satellite doppler can be removed from the desired rain return by tracking the earth return signal.

2.2.6—Antenna Beam Width and Beam Filling Factor. The 3 dB beam width of a parabolic reflector antenna is a function of both the reflector diameter D_a and signal wavelength λ as shown by the following equation [6]:

$$\theta = \phi = 1.24 \times 10^{-2} \frac{\lambda}{D_a} \qquad (2\text{-}11)$$

where θ is the antenna 3 dB beam width expressed in radians, with λ and D_a expressed in centimeters and meters, respectively.

The diameter S in kilometers of the area of the earth's surface illuminated by the antenna beam width is

$$S = 2r \tan \theta/2 \qquad (2\text{-}12)$$

where r is the satellite-to-earth range in kilometers. With r equal to 3.59×10^4 km, Eqs. (2-11) and (2-12) result in

$$S = 4.45 \times 10^2 \frac{\lambda}{D_a} \quad . \qquad (2\text{-}13)$$

The beam-filling factor ψ is dependent upon the relative areas of the rainfall region and the antenna beam projection at or near the earth's surface. The area of the rainfall region of concern [7] will typically have diameters in the range of 20 to 50 km. If the rainfall region has an effective diameter in kilometers of D_r, then, with Eq. (2-13), the beam-filling factor is defined as

$$\psi = 5.05 \times 10^{-6} \frac{D_r^2 D_a^2}{\lambda^2} \; ; \quad D_r \leq S$$

$$\psi = 1; \quad D_r > S \; . \qquad (2\text{-}14)$$

In defining ψ through Eq. (2-14), it has been assumed that some independent means is available to align the antenna such that the rainfall region is fully included within the antenna beam. Figures A-3a, 3b, 3c, respectively, illustrate the antenna angular beam width θ, antenna earth coverage diameter S, and beam-filling factor ψ, as functions of wavelength and antenna reflector diameter. It should be emphasized that ψ cannot exceed unity.

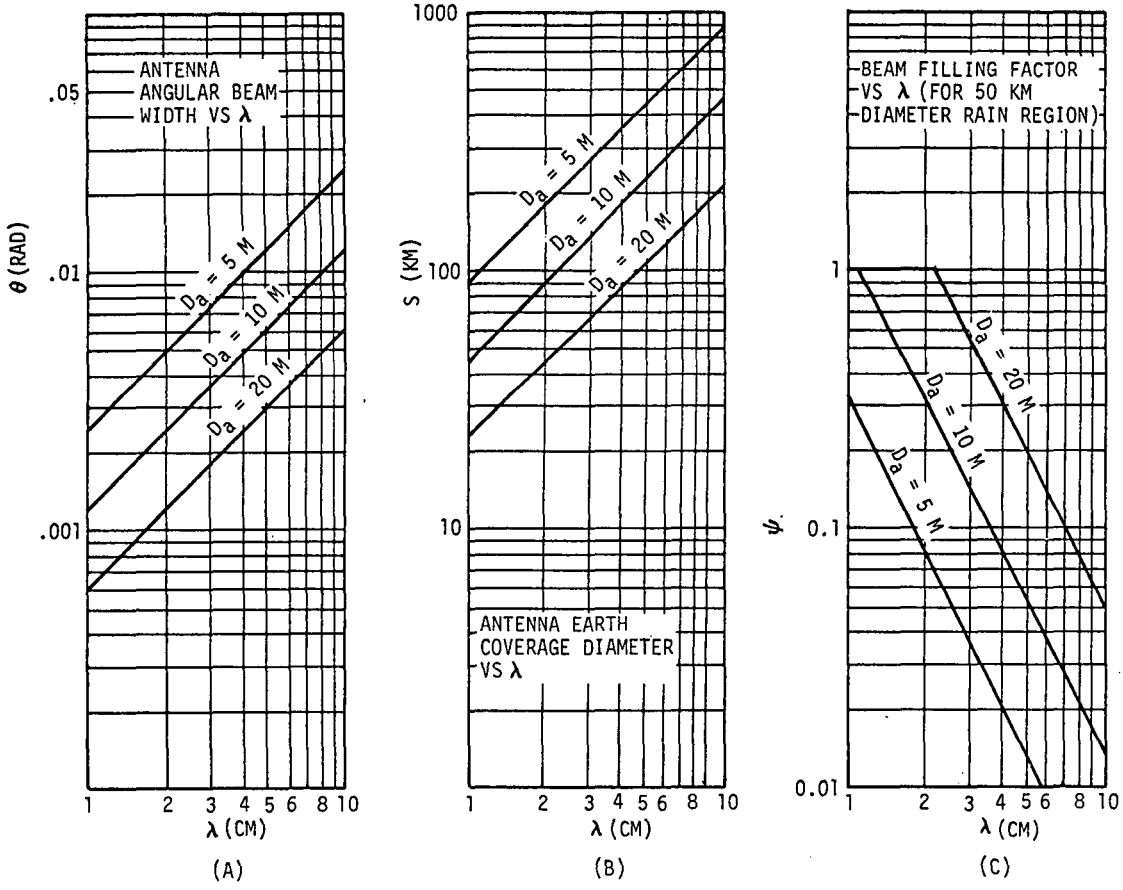

Figure A-3. Antenna beam width and beam-filling factor relationships.

2.2.7—Atmospheric Attenuation. The equations for $\bar{P}_{ra_R}$ and P_{rE} (Eqs. (2-1) and (2-2)), each contain an expression for atmospheric attenuation of the form

$$A_a = 10^{-0.2 \int_0^r kdr} \tag{2-15}$$

where k, expressed in dimensions of dB/km, is some function of the path characteristics and wavelength with r being the path length. Three sources of attenuation are significant in the wavelength range being considered (1 cm $\leq \lambda \leq$ 10 cm). These sources are as follows:

a. Attenuation by atmospheric oxygen and water vapor absorption.
b. Attenuation in clouds by water droplets less than 100 microns in diameter.
c. Attenuation due to scattering by raindrops.

The integral expression of Eq. (2-15) can be represented as a sum of integrals for each source of attenuation. In equation form,

$$\int_0^r kdr = \int_0^r k_g dr + \int_0^r k_c dr + \int_0^r k_p dr$$

$$= \alpha_g + \alpha_c + \alpha_p \tag{2-16}$$

where k_g, k_c, and k_p are the attenuation rate factors for gases, clouds and precipitation, respectively, and α_g, α_c, and α_p represent their respective attenuation values in dB.

The absorption by gases is essentially independent of meteorological conditions depending only upon wavelength and path length. The curve of Figure A-4, labeled α_g, shows the attenuation of atmospheric gases as a function of wavelength for a vertical path through the atmosphere. These values were computed for a uniform atmosphere 8 km thick with uniform characteristics throughout. These values closely correspond to values given by Hogg [8] although calculated on different bases.

Attenuation within clouds is caused by water droplets with radii of 100 microns or less. The amount of attenuation is dependent upon the liquid water content of the cloud. The curve of Figure A-4, labeled α_c, was obtained using data from Bean and Dutton [9], p. 291. The assumed meteorological conditions for this calculation are graphically illustrated by Figure A-5. This figure also shows the typical conditions assumed throughout this report except where otherwise stated.

The attenuation due to rain is a function of rainfall rate. The values for rain attenuation shown in Figure A-4 as α_p are from data for an average rainfall rate of 25 mm/h [9], and assumes a 1 km thickness of rain above the observation region.

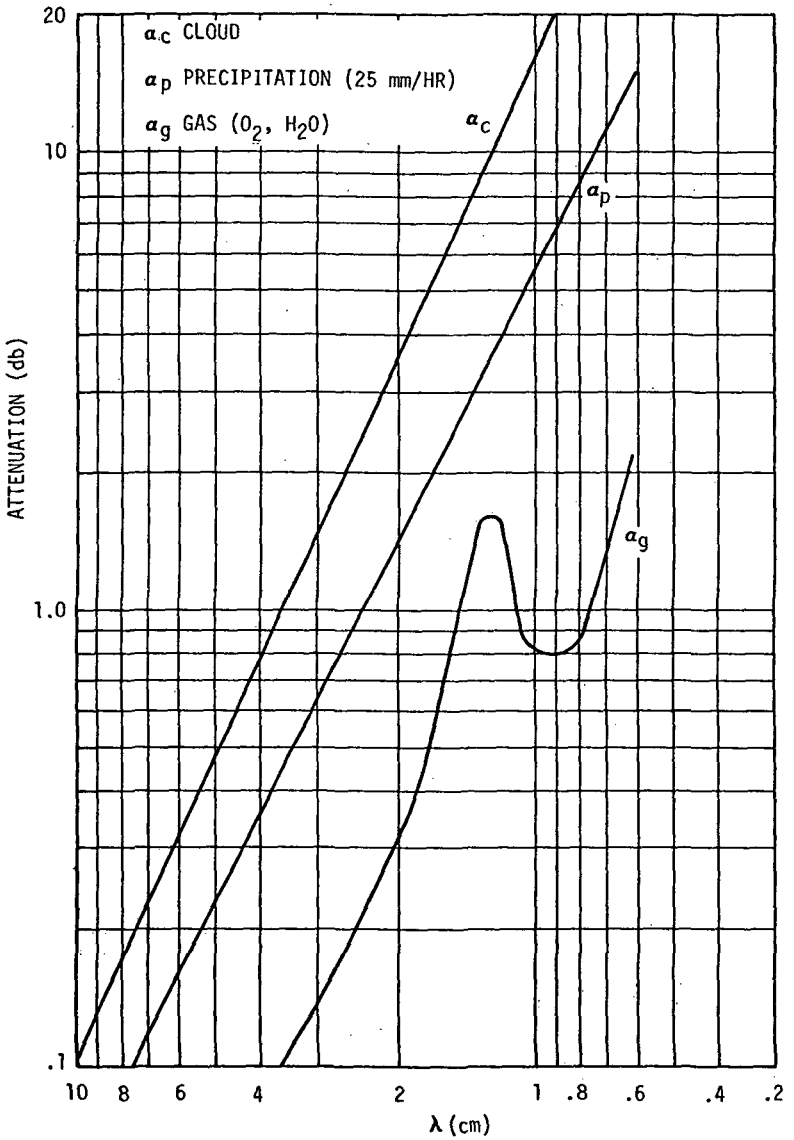

Figure A-4. One-way signal attenuation.

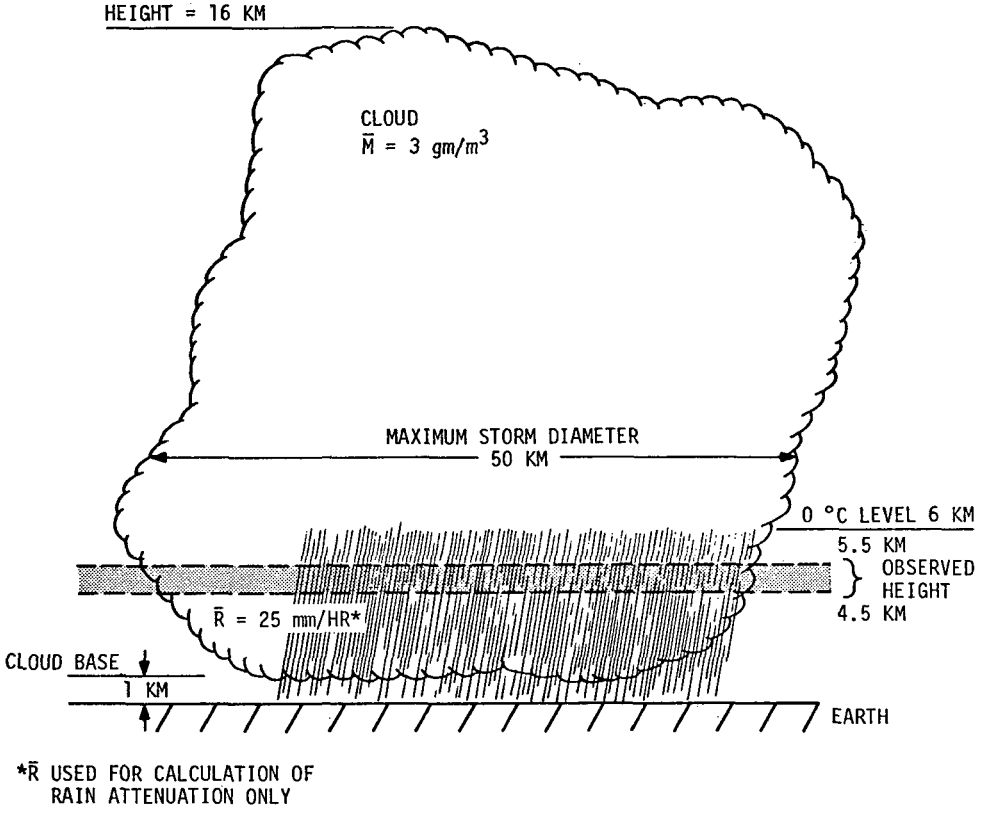

Figure A-5. Storm cloud model for signal attenuation calculations.

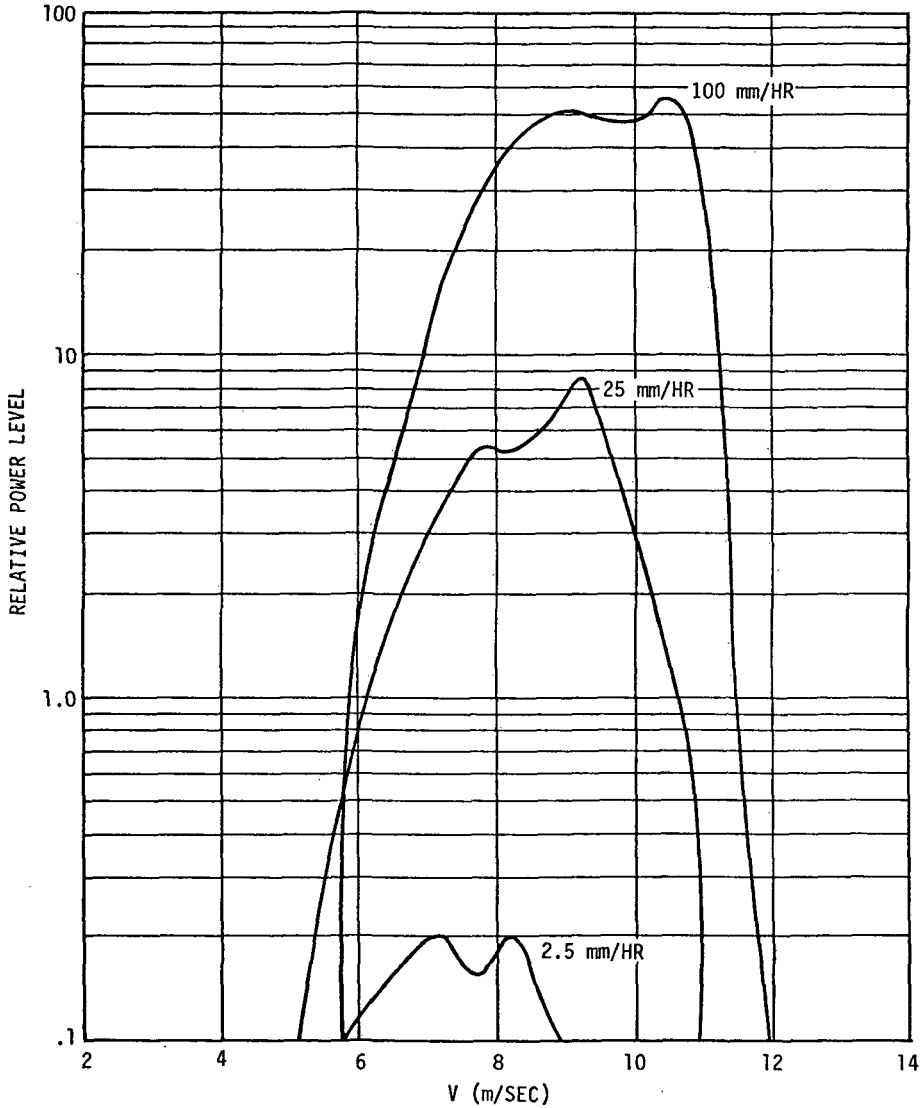

Figure A-6. Relative power return versus raindrop terminal velocity.

2.2.8—Rain Doppler Spectrum Estimate. In order to determine a value for $\bar{P}_{raRm}$, the minimum detectable received signal power, it is necessary to have some estimate of the doppler spectrum of the rain return signal. Each raindrop will have a radar cross-section σ proportional to D_d^6, where D_d is the drop diameter. The total reflected power on a relative basis can then be expressed as

$$P_r = C_1 \sum_{i=1}^{N} D_{di}^6 \tag{2-17}$$

where N is the total number of drops in the observation region. By grouping the drops into intervals according to their diameter, Eq. (2-17) can be written as

$$P_r = C_2 \sum_{j=1}^{m} D_{dj}^6 \frac{P_j N}{100} \tag{2-18}$$

where P_j is the percentage of the total number of drops that fall into the jth interval of diameter and m is the number of intervals.

Figure A-6 illustrates the relative rain-power distribution as a function of raindrops terminal fall velocity. This figure is a plot of Eq. (2-18) with P_j data obtained from Table 1. C_2 was chosen to give powers proportional to $R^{1.6}$ (R = rainfall rate in mm/h) as in the equation for $\bar{P}_{raR}$. In addition, drop velocities were derived from drop diameter using the relationship [10]

$$V_d = 13\sqrt{D_d} \quad . \tag{2-19}$$

It is apparent from Figure A-6 that the half-power response points correspond to a three- to four-meters per second spread, regardless of the rainfall rate. Designating this velocity spread value as ΔV, the equivalent doppler frequency spread (or doppler bandwidth) can be obtained from

$$B_d = \frac{2\Delta V}{\lambda} \quad . \tag{2-20}$$

Assuming the four meters per second velocity spread value,

$$B_d = \frac{800}{\lambda} \tag{2-21}$$

with λ expressed in centimeters.

2.2.9—RAKE Receiver Sensitivity. The minimum detectable received power is a function of both the effective noise temperature of the system receiver, T_{sys}, and the rain doppler spread or bandwidth B_d, where B_d is defined by Eqs. (2-20) and (2-21), and

Table 1

Raindrop Size Distributions*
(Percent of volume contained drops of size D_d)

Drop Size (D_d mm)	Rainfall Rate R (mm/hr)		
	2.5	25	100
.5	7.3	1.7	1.0
1.0	27.8	17.6	4.6
1.5	32.8	18.4	7.6
2.0	19.0	23.9	11.7
2.5	7.9	19.9	13.9
3.0	3.3	12.8	17.7
3.5	1.1	8.2	16.4
4.0	0.6	3.5	11.9
4.5	0.2	2.1	7.7
5.0		1.1	3.6
5.5		0.5	2.2
6.0		0.2	1.2
6.5			1.0
7.0			0.3

*From Radio Meteorology, Bean and Dutton NBS Monograph 92, 1966, p. 296.

$$T_{sys} = \alpha T_A + T_L(1-\alpha) + T_1 + \sum_{m=2}^{M} \frac{T_m}{G_{m-1}} \qquad (2\text{-}22)$$

with

α = Transmission line loss between antenna and receiver

T_A = Effective antenna temperature

T_L = Transmission line temperature

T_1 = Effective noise temperature of the first stage amplifier

T_m = Effective noise temperature of the mth stage amplifier

G_{m-1} = Gain of the (m-1)st stage amplifier.

For the satellite RAKE application, T_A and T_L are both reasonably assumed equal to 290°K and only the first two amplifier stages are considered such that

$$T_{sys} = 290 + T_1 + \frac{T_2}{G_1} . \qquad (2\text{-}23)$$

The minimum detectable received power P_{rm} is assumed to be equal to the noise power of the receiver system within the detection bandwidth. The receiver noise power is determined by the equation

$$P_n = k T_{sys} \Delta f \qquad (2\text{-}24)$$

where

k = Boltzmann's constant = 1.38×10^{-23} joules/°K

T_{sys} = Effective receiver noise temperature (°K)

Δf = Noise bandwidth (Hz)

Curves of $P_{rm} = P_n$ are shown in Figure A-7 for various bandwidths, $B = \Delta f$ as a function of wavelength or frequency, considering the noise temperatures of receiver front-end devices tht are practical for satellite use.* The curve of Figure A-7 for $B = B_d$ represents the minimum detectable rain return power, $\overline{P_{raRm}}$. For the frequency range from 3 to 18 GHz, field-effect transistor (FET) or tunnel diode preamplifiers are employed. Above 18 GHz, mixer type front-ends are used. More sophisticated preamplifiers, such as parametric amplifiers and masers, can provide lower receiver noise temperatures; however, these devices are not considered suitable for satellite applications at this time.

2.2.10—Empirical Correction Factor. The correction factor F used in the basic rain return equation is based on data from Battan [1], p. 60. A linear relationship with λ was assumed in the plot shown in Figure A-8. This correction factor is purely an empirical relationship and is based on the discrepancies between observed and calculated rain return powers.

2.2.11—Reflectivity Factor and Rainfall Rate. The reflectivity factor Z is equal to the sum of the reflectivity of each drop throughout the rainfall volume, as discussed in paragraph 2.2.8. Data have been collected on the relationship between Z and the rainfall rate R. Battan [1], p. 56, gives 23 different relationships for various types of rainfall and locations. The representative equation that best fits these data and that will be used throughout this study is:

$$Z = 2 \times 10^{-10} R^{1.60} \qquad (2\text{-}25)$$

where Z has dimensions of cm^6/cm^3 with R in mm/hr.

2.3 Optimization Procedures

Two criteria for optimization were considered. It was first assumed that the system performance would be limited by the presence of an earth return signal of sufficient strength to obscure the rain return signal. Earth return-to-rain return power ratios of up to the order of 90 dB can be expected. Assuming the RAKE correlation process can reduce the power level of the earth return by at least 40 dB, the first criterion was based

---

*Receiver noise figures ranging in value from 4.5 dB at $\lambda = 10$ cm to 12 dB at $\lambda = 1$ cm were assumed. These variations with λ are reflected in the graphs in Figure A-7.

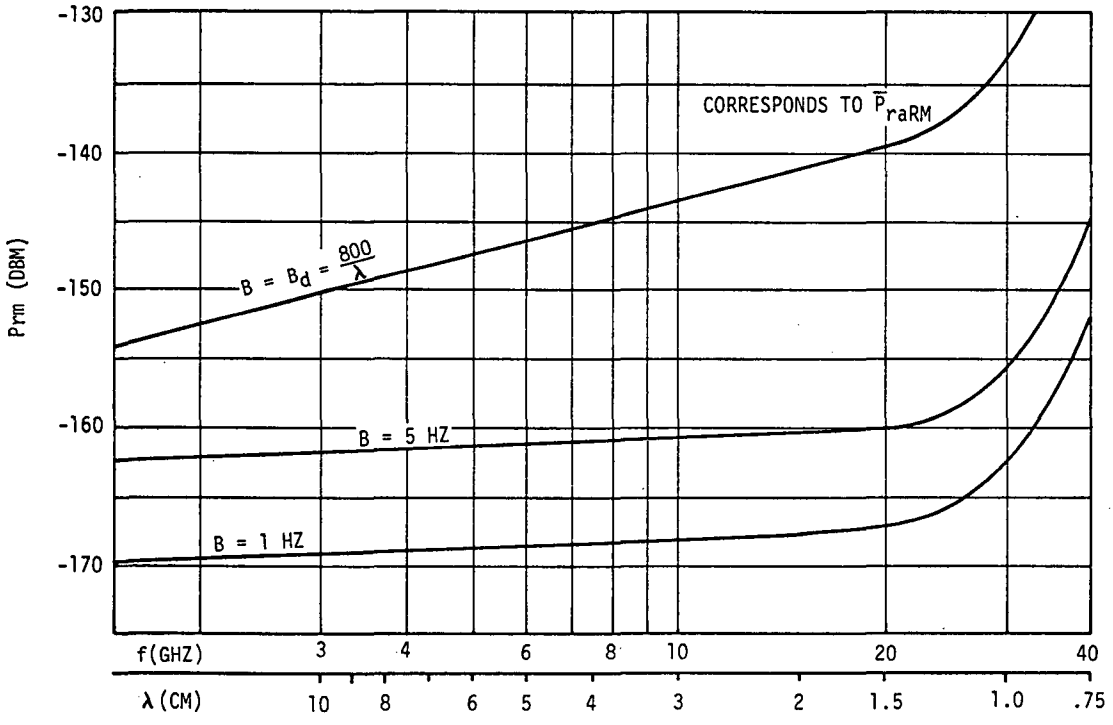

Figure A-7. Minimum detectable received power in bandwidth B.

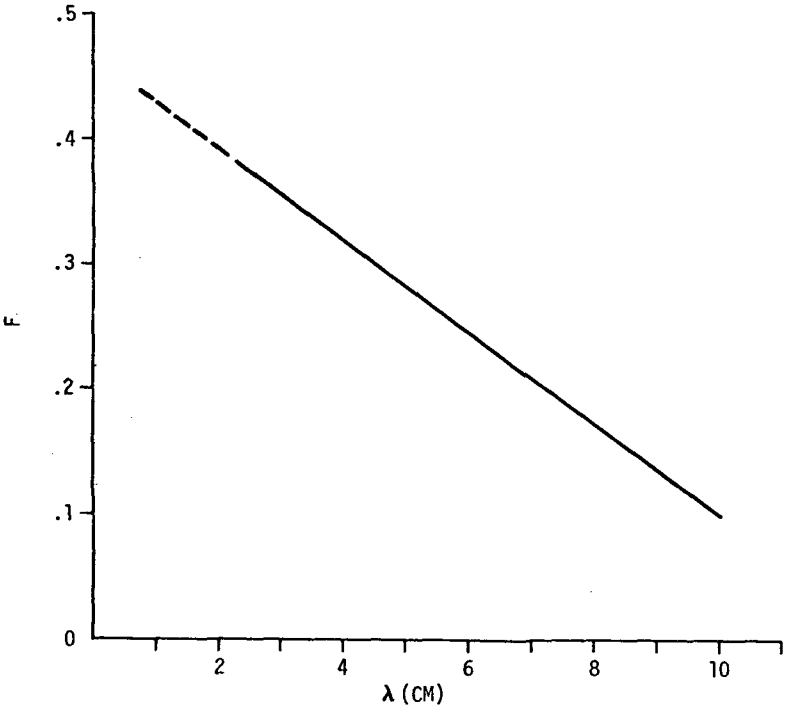

Figure A-8. Correction Factor F versus λ.

upon the capabilities of the receiver (after correlation) and spectral processing to separate the desired rain return from the reduced earth return for a rain return-to-reduced earth return power ratio R_d of -50 dB or 10^{-5}.

The earth return power P_{rE} will be reduced by the clutter rejection factor W_T; therefore the desired rain return-to-reduced earth power ratio will be

$$\frac{\bar{P}_{raR}}{W_{Tm} P_{rE}} = R_d \, . \tag{2-26}$$

Starting with basic Eqs. (2-1) and (2-2) for $\bar{P}_{raR}$ and P_{rE}, respectively, and using Eq. (2-8) for W_{Tm} and appropriate substitutions of Eqs. (2-7), (2-10), (2-14) and (2-25), an equation defining the minimum detectable rainfall rate for the constraints imposed by Eq. (2-26) can be derived as

$$R_{min} = \left\{ \frac{R_d[\cot^2\beta_0 \exp(-\tan^2\alpha/\tan^2\beta_0)]}{(8.76 \times 10^{-3})\pi^5 F |K|^2 10^{-0.2\int_0^r kdr} D_r^2 D_a^2} \frac{h\lambda^4}{} \right\}^{0.625} . \quad (2\text{-}27)$$

This latter equation is plotted in Figure A-9(a) as a function of λ for $R_d = 10^{-5}$, $\beta_0 = 5°$, $\alpha = 0°$, $|K|^2 = 0.92$, $h = 10^5$ cm, $D_r = 50$ km and $D_a = 10$ m with the atmospheric attenuation and F factors as shown in Figures A-4 and A-8, respectively.

Now, by substituting R_{min} of Eq. (2-27) into the rain return Eq. (2-1) and through use of the relationships defined by Eqs. (2-11) and (2-25) plus the previously undefined relationship between antenna apertural area and antenna reflector diameter,

$$A_p = 7.85 \times 10^3 D_a^2 , \quad (2\text{-}28)$$

an equation defining the minimum transmitter power required to observe the previously related minimum detectable rainfall rates is derived as

$$P_{t_{min}} = \frac{6.6 \times 10^{10} \lambda^2 r^2 10^{0.2L} (\bar{P}_{ra_R})_{min}}{D_a^2 R_d h^2 [\cot^2\beta_0 \exp(-\tan^2\alpha/\tan^2\beta_0)]} \quad (2\text{-}29)$$

where $(\bar{P}_{ra_R})_{min}$ is the minimum detectable rain return power in bandwidth B_d shown in Figure A-7. Equation (2-29) is shown plotted in Figure A-9(b) as a function of λ for antenna diameters of 10 m and 20 m, $L = 2.5$ dB and $r = 3.59 \times 10^9$ cm with the remaining parameter values as employed in determining R_{min}.

The second criterion for optimization was simply to determine the transmitter power required so that the rain return power, $\bar{P}_{ra_R}$, would exceed the receiver threshold sensitivity, $(\bar{P}_{ra_R})_{min}$, for a constant value of rainfall rate R. In this case, starting with Eq. (2-1) for $\bar{P}_{ra_R}$, substituting the relationships defined by Eqs. (2-11), (2-14), (2-25), and (2-28), letting $\bar{P}_{ra_R} = (\bar{P}_{ra_R})_{min}$ and solving for P_t,

$$P_t = \frac{0.483 \lambda^6 r^4 10^{0.2L} (\bar{P}_{ra_R})_{min}}{\pi^5 D_a^4 D_r^2 h F |K|^2 R^{1.6} 10^{-0.2\int_0^r kdr}} \quad (2\text{-}30)$$

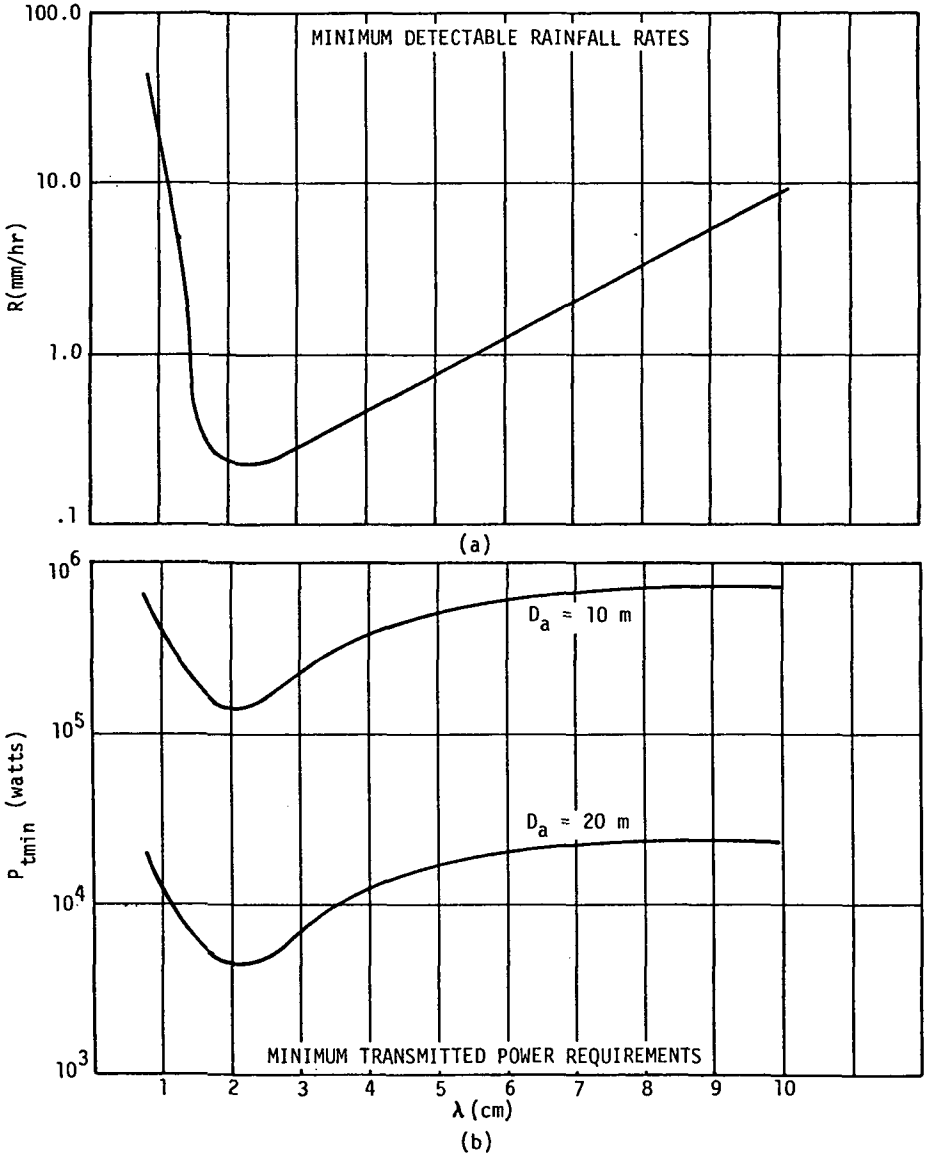

Figure A-9. Minimum detectable rainfall rates and transmitted power requirements for $R_d = 10^{-5}$.

P_t from Eq. (2-30) is plotted in Figure A-10 as a function of λ for rainfall rates of 10, 30 and 100 mm/hr with $r = 3.59 \times 10^9$ cm, $D_a = 10$m, $D_r = 50$ km, $|K|^2 = 0.92$, $h = 10^5$ cm and $L = 2.5$ dB. Attenuation factor $(\bar{P}_{raR})_{min}$ and F are, respectively, as defined in Figures A-4, A-7 and A-8.

2.4 Discussion of Optimization Results

The curve of Figure A-9(a) indicates that for a rain return-to-reduced earth return ratio of 10^{-5} and with the other assumed conditions, an absolute detectable rainfall rate theoretically occurs at a wavelength of approximately 2 cm, or 15 GHz. However, to observe the slightly more than 0.2 mm/hr value of rainfall rate at that wavelength requires a transmitted power of more than three kilowatts when using a 20-meter diameter antenna reflector. Higher values of rainfall rate can be observed using lower transmitted powers. However, lower rainfall rates cannot be observed if higher transmitted powers are employed because of the rain return-to-reduced earth return ratio limitation. One obvious way to reduce the transmitted power requirement would be to increase the antenna diameter beyond 20 meters. Antenna size cannot be increased without limit, however, because the earth coverage area decreases as antenna size increases. Too small a coverage area increases the problems of obtaining integrated rainfall rate data. Also, since antenna diameter really implies antenna gain there is a practical limit to antenna gain due to the precision with which the parabolic reflector can be constructed. A further discussion of practical limitations is presented in paragraph 2.5.

The curves of Figure A-10 indicate that optimization on the basis of receiver sensitivity is the more realistic approach. Again, the minimum transmitted power required is theoretically obtained at a wavelength of about 2 cm regardless of rainfall rate if the rainfall rate is above the minimum indicated in Figure A-9. In order to observe a rainfall rate of 10 mm/hr using a 10-meter antenna, a transmitted power at 2 cm of 100 watts is required. For a 20-meter antenna, the transmitted power is reduced to about 7 watts.

2.5 Practical Limitations

In the previous discussions the values of antenna gain, as related to antenna diameter, and transmitter power have been allowed to vary essentially without limit. The results obtained on this basis tend to indicate the geostationary satellite RAKE concept for measuring rainfall rate is theoretically feasible, assuming a reasonable interpretation of the rainfall doppler spectrum is possible. Before the concept can be considered feasible on a more practical basis, however, it is necessary to consider the effects of antenna gain and transmitted power limitations imposed by present and near future state-of-the-art technology.

The satellite antenna gain that can be obtained is limited by the precision with which the parabolic reflector can be constructed and assembled in space. Earth antennas have been constructed that have 70 dB and more of gain in the 3 to 15 GHz range. However, the antennas for the

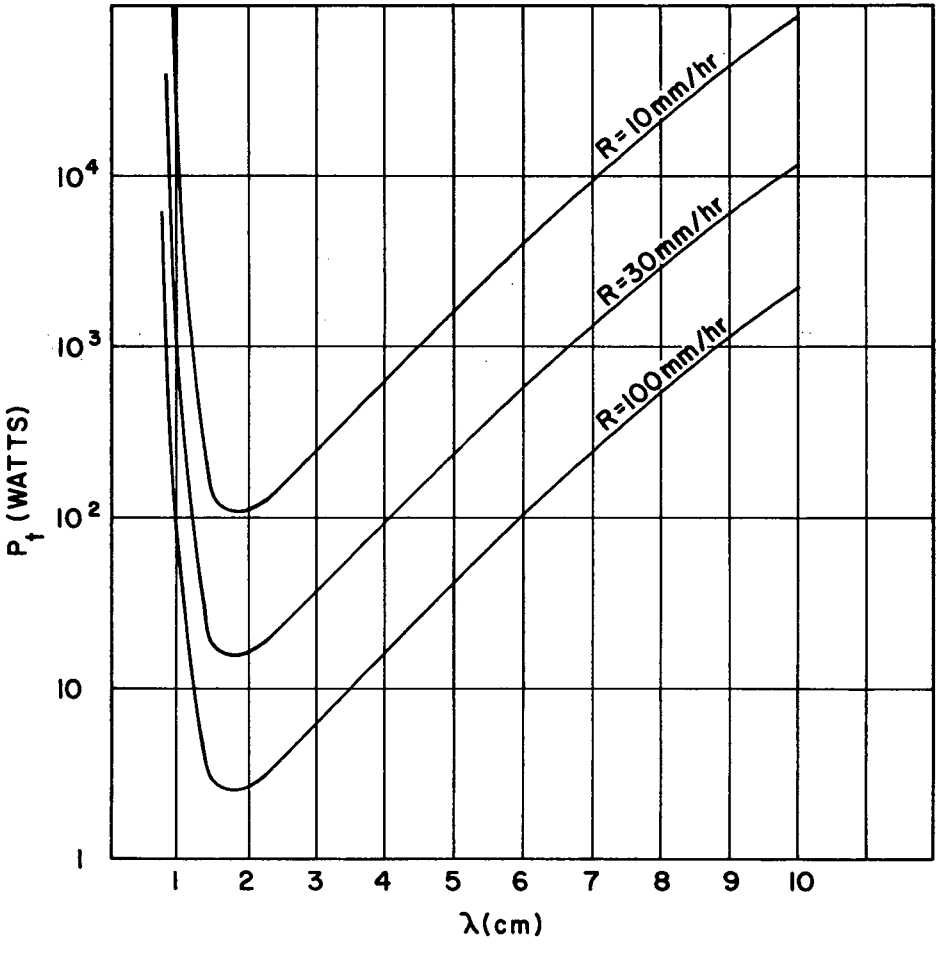

Figure A-10. Transmitter power required versus λ, R.

lower frequencies are several hundred feet in diameter and at the higher frequencies are precision ground solid reflectors. It is known that satellite antennas with gains up to 54 dB are under consideration for some future space stations, but these are on the order of 15 ft in diameter and are not folded for launch. For the present and immediate future a 50 dB antenna gain for the 3 to 15 GHz range seems to be a reasonable limit. In the near future, antenna gains of 60 dB may be possible in satellite applications. It is also considered that for both the present and near future, satellite antenna diameters will be limited to about 20 meters, particularly for wavelengths in the 2 to 5 cm range.

The most desirable method of power amplification is solid state because of its ruggedness, high reliability, low weight and high efficiency. However, the present state of microwave semiconductors limits the power generation to about 200 watts at 1 GHz and 40% efficiency, declining to about 30 watts at 4 GHz and 10% efficiency.

The second choice for power generation would be traveling wave tubes (TWT's) because of their moderate ruggedness and weight. However, their efficiency is only 20-25% and the gain is low requiring more preamplification. TWT's that generate 10 kW at 1 GHz and up to 1 kW at 10 GHz are available. However, any over several hundred watts require water cooling which becomes impractical for anything but a very large satellite.

Very high powers, 100 kW and above, can be generated by klystrons in the 1 to 10 GHz range. However, the klystron is the least rugged of the devices and has about 30% efficiency. As with the TWT, water cooling is required for powers above several hundred watts.

For the present, a TWT limited to about 250 watts of power appears to be the best choice for a transmitter power amplifier. As satellite available primary power and weight capacities increase, transmitter output power can also increase. In the near future, transmitter powers on the order of 2.5 kW should be possible.

To best illustrate the effects of the limitations on antenna gain and transmitter power as discussed above, the following equation defining rainfall rate was developed:

$$R = \left\{ \frac{(2.56 \times 10^2)\lambda^2 r^4 10^{0.2\left(L + \int_0^r kdr\right)} (\tilde{P}_{raR})_{min}}{\pi^3 P_t G^2 D_r^2 h F |K|^2} \right\}^{0.625} \qquad (2\text{-}31)$$

where G is the numerical antenna power gain and all other parameters are as previously defined. Equation (2-31) has been employed to determine the two curves of rainfall rate versus wavelength illustrated by Figure A-11. These two curves show what is considered to be the present and near future capabilities of a practical satellite RAKE system.

Figure A-11 indicates that the current state-of-the-art does not permit detection of rainfall rates below about 150 mm/hr. This is not considered suitable. However, with anticipated improvements in antenna

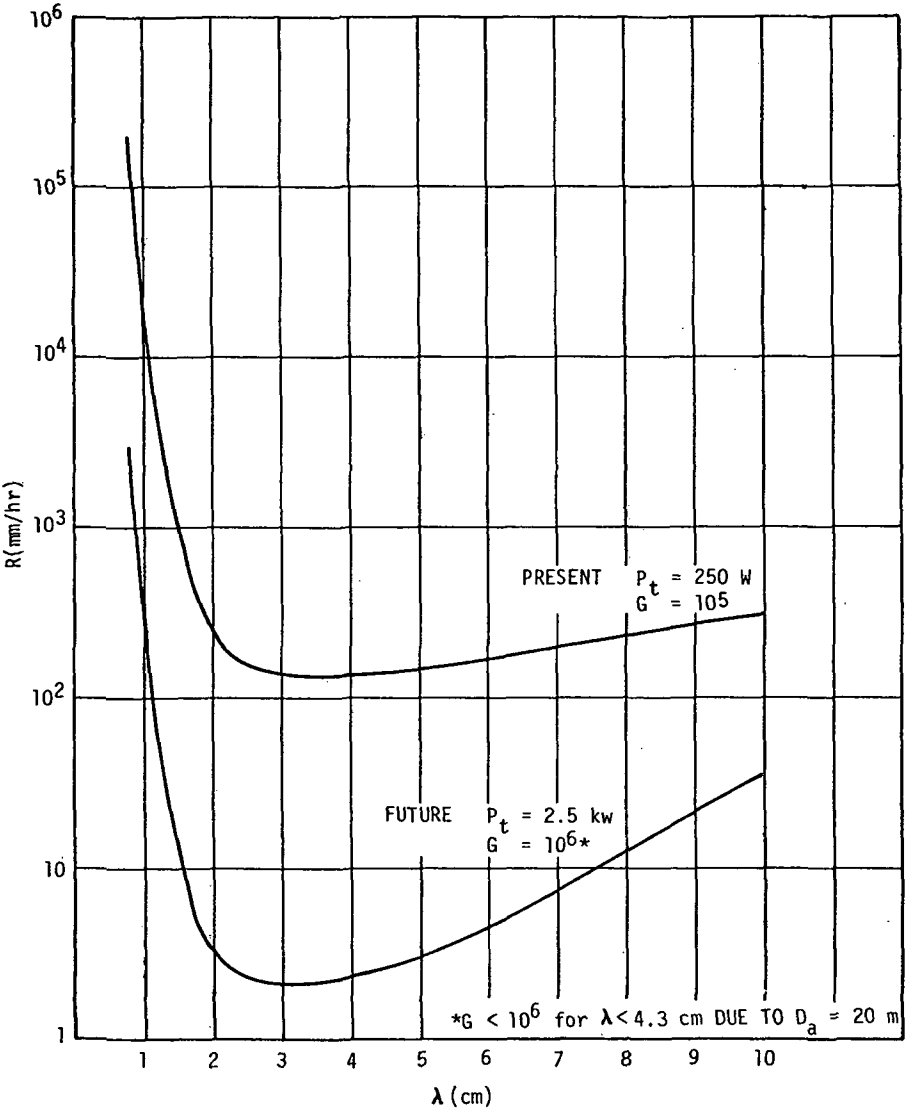

Figure A-11. Practical rainfall rate measurement capabilities, present and future.

gain and transmitted power capabilities, measurement of rainfall rates in the more desirable 10 to 25 mm/hr range will become possible. Both curves of Figure A-11 indicate wavelengths between 2 and 6 cm offer the greatest capability.

3. Techniques for Implementation

The following discussion covers methods of hardware implementation of the RAKE system to obtain the theoretical performance indicated in Section 2. It will consider system problems in the implementation of the hardware necessary to obtain the data, and will not dwell on circuit design. Three approaches to the data collection will be considered. In the first, all of the RAKE equipment is in the satellite with the correlation data telemetered to a ground control station. In the second, the RAKE equipment is in a ground station with only a transponder in the satellite. The third approach uses separate satellites for the RAKE transmitter and receiver to obtain antenna isolation and thereby eliminate the need for transmit-receive signal gating.

3.1 All Measurement Equipment in the Satellite

The first approach to be considered is to place all of the data collection equipment in the satellite. Commands from the ground would be used to initiate the experiment and aim the antenna at the desired ground location. The detected return from the rain would be telemetered back to ground station for further analysis.

Figure A-12 is a block diagram of the RAKE hardware that would be in the satellite. A single parabolic antenna would be used by both the RAKE transmitter and receiver. The use of separate antennas to transmit and receive does not seem practical when considering a satellite perhaps the size of ATS-F. It is of more importance to share as large an antenna as practical rather than have separate but smaller antennas. Since it is not possible to obtain sufficient isolation between a transmitter and receiver sharing the same frequency band, the transmitter must be turned off while receiving. The two-way propagation delay from the satellite to earth is approximately 250 milliseconds. Thus a cycle of transmitting for 250 milliseconds and receiving for 250 milliseconds would be reasonable. Shorter cycles could be used but they do not offer any advantages. Depending upon frequency, some form of circulator would be used to direct the transmitter power to the antenna and the receive power to the receiver.

The transmitter frequency would be a multiple of a stable crystal oscillator with the pseudorandom sequence modulated on the signal. The degree of modulation would be such that after multiplication the modulation would be $\pm$ 90 degrees. If the pseudorandom sequence were perfectly balanced, there would be no carrier remaining for exactly $\pm$ 90 degrees modulation.

Since the satellite can have a vertical component of velocity there will be a doppler on both the return from the earth and from the rain due to the satellite motion. To remove this doppler from the measurement,

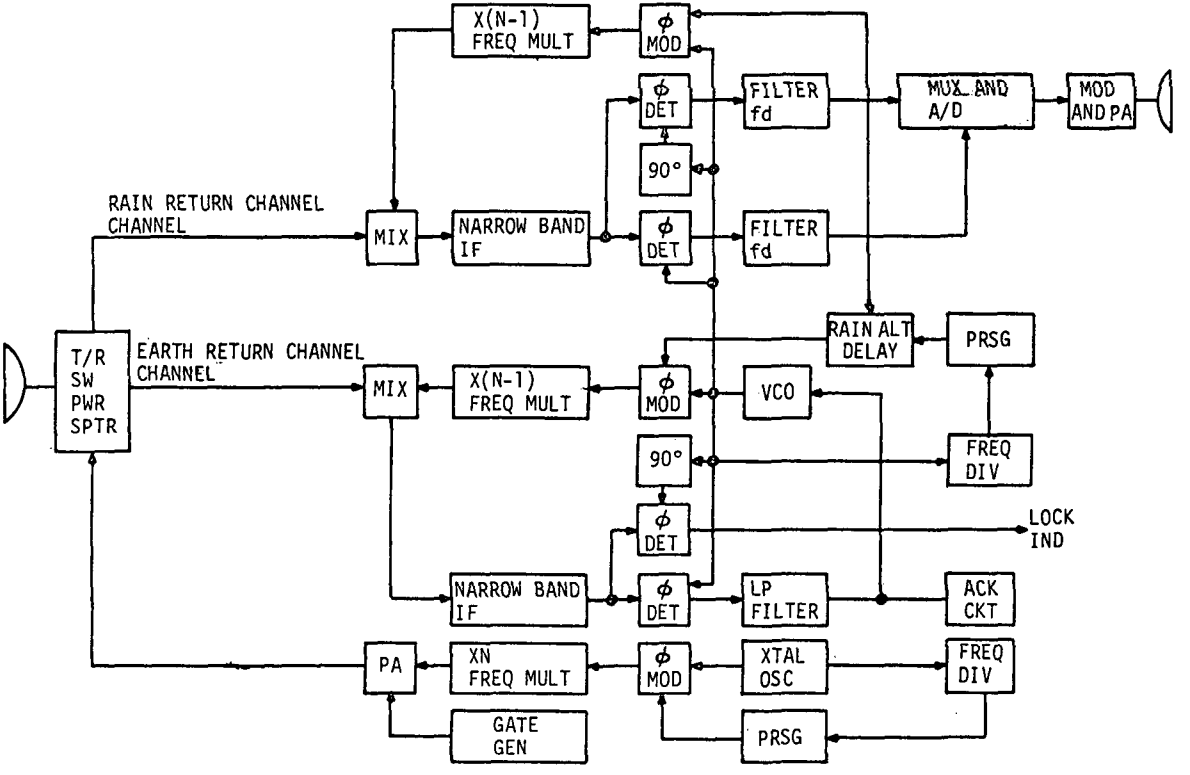

Figure A-12. Satellite RAKE transmitter/receiver, block diagram.

the receiver local oscillator is phase-locked to the earth return. As shown for the earth return channel in Figure A-12, the received signal is mixed with the local oscillator which has been modulated with a replica of the transmitted pseudorandom sequence. When the two sequences are in synchronism, the carrier is regenerated and amplified. The phase detector and VCO complete the loop and maintain the local oscillator in synchronism with the earth return regardless of satellite velocity.

The vertical velocity of the satellite also causes a doppler shift in the clock frequency of the received pseudorandom sequence. Compensation must be made for this received clock frequency shift in order for the sequence generated at the receiver to stay in synchronism with the received sequence. This can be done by making the clock frequency a fraction of the carrier frequency. If at the transmitter the clock is 1/Nth of the carrier, the doppler on the clock in the received signal will be 1/Nth of the doppler on the carrier of the received signal. When the locally generated carrier at the receiver is phase-locked to the received carrier, the carrier can be divided by N to obtain a clock for the receiver sequence which is in phase with the doppler-shifted received clock. This technique for generating sequence clocks is shown in Figure A-12.

The design of the rain return channel presents special problems caused by the large earth return signal. Paragraph 2.3 of this report has indicated that the earth return power can be 90 dB greater than that of the rain return. Any portion of the receiver handling both signals simultaneously must be linear over the 90 dB range to prevent intermodulation and harmonic distortion. Otherwise the ability to select a small rain signal out of the clutter will be greatly reduced impairing the success of the measurement.

For this reason the correlation of the return signal with the local pseudorandom sequence is performed in the first mixer before any amplication to obtain some rejection of the earth return immediately. The mixer can be designated to be linear over this range of signals as long as the total signal power is not greater than about -30 dBm.

The bandwidth of the IF amplifier after the mixer must only be wide enough to pass the doppler spectrum of the rain return which is within $\pm f_{dm}$ from the center frequency of the return. The doppler f_d is caused only by the rain since the satellite doppler has been removed by phase-locking on the earth return. The spectrum of the signal in the IF is anticipated to be essentially as shown in Figure A-13. The earth return has been reduced to a residual carrier and line spectrum, while the rain return is offset by the rain doppler. Section 2 has shown that the residual carrier portion of the earth return can be rejected by

$(\frac{1}{WT_0})^2$, or about 40 dB, by the correlation process. After selecting only the return at $\pm f_d$, the earth return is still about 50 dB above the rain return. A rejection filter in the center of the IF band can further reduce the earth return so that the linearity requirement in the remaining portion of the receiver is minimal.

Two phase detectors in quadrature are used for the final detection of the rain return. The final filters are each f_d wide to pass the rain but ac coupled to reject the remaining earth return at dc.

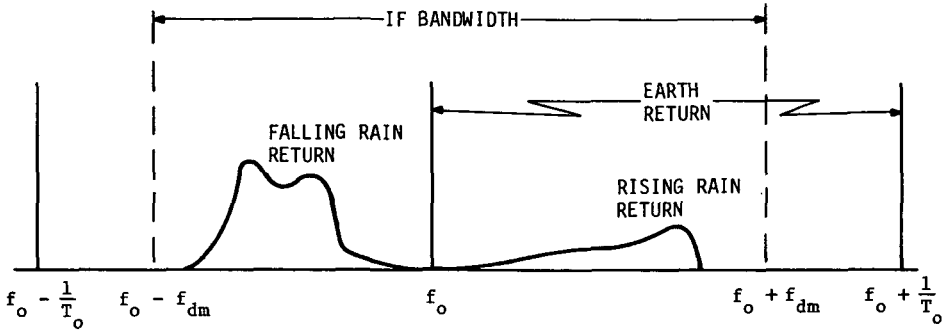

Figure A-13. IF spectrum.

The same pseudorandom sequence generator is used in the earth and rain channels but is delayed for the earth channel by the propagation time corresponding to the altitude above the earth of the rain segment being examined. Once the earth loop is phase-locked, the altitude of the rain segment examined can be selected by changing the relative delay of the sequence applied to the rain channel. This can be controlled by the command link from the ground.

The problem of acquisition of the earth return requires two steps: first, locking on the carrier and then on the pseudorandom sequence. Sufficient carrier power must initially be left in the transmitted signal to obtain phase lock. Then the sequence can be stepped until sync is obtained. After complete acquisition, the residual carrier power in the transmitter can be reduced.

Table 2 shows the expected losses for a telemetry link from the satellite to the ground station. It was assumed that a 30-foot steerable parabolic antenna on the ground can be used for the link. For the lower frequencies considered in the table, little antenna gain can be obtained in the satellite antenna without using a very large array or a parabolic reflector. Thus a dipole antenna was considered appropriate for the lower frequencies. Since it is linearly polarized it will be necessary to use a circularly polarized ground antenna. This results in a 3 dB additional loss.

For the midfrequencies a helical antenna can be used. This antenna provides increased gain over the dipole and eliminates the polarization loss. A helical antenna length of $3\lambda/2$ is typical of the size.

For the higher frequencies, a horn antenna can be used. For this application the gain of the horn antenna is limited so that the 3 dB beamwidth will be on the horizon even when the satellite is tilted to point to the opposite horizon. The horn antenna is also linearly polarized.

Table 2

Transmission Loss — Telemetry Signal

Freq MHz	Isotropic loss (dB)	30-ft ground antenna gain (dB)	Satellite antenna gain (dB)	Polarization loss (dB)	Beam edge loss (dB)	Total transmission loss (dB)
100	165	17	Dipole - 2	3	-	149
200	171	23	Dipole - 2	3	-	149
500	179	31	Helical - 10	-	1	139
1,000	185	37	Helical - 10	-	1	139
2,000	191	43	Helical - 10	-	1	139
5,000	199	51	Parabola - 14	3	3	140
10,000	205	57	Parabola - 14	3	3	140

Table 3

Telemetry Power Requirement

f_d (Hz)	$40 \times f_d$ (dB)	Trans loss (dB)	S/N (dB)	P_N PER Hz (dBW)	P_T (dBW)
100	36	-139	+10	-200	-15
300	41	-139	+10	-200	-10
1000	46	-139	+10	-200	- 5

Table 2 shows that the selection of telemetry frequency is not critical above 500 MHz. Thus the selection can be made based upon other factors such as the availability of equipment.

The bit rate for the data will depend upon the doppler frequency. Assuming a sample rate of twice the doppler (Nyquist rate) and an analog-to-digital converter of 10 bits, the two channels require 40 f_d bits per second.

The data can best be transmitted using coherent phase modulation. For a 10^{-6} bit error rate, a 10 dB signal-to-noise ratio in a bandwidth of 1 bit rate is required. Assuming a 7 dB receiver noise figure, Table 3 shows the required transmitter power. The values are small enough so that no problems should be encountered in supplying the required power.

3.2 Satellite Transponder

The second approach to be considered is to have the RAKE transmitter and receiver on the ground and a transponder in the satellite. The satellite equipment for this approach is shown pictorially in Figure A-14.

While this approach greatly simplifies the satellite hardware, it has one problem that disqualifies it from further consideration. This is the fact that the earth return is on the order of 90 dB above the desired rain return, and linear amplification is required until correlation is performed. Obtaining a high-power amplifier with this characteristic is not feasible. In addition, the satellite power for relaying the signal to the ground station is beyond practical limits. For example, assuming a 300 Hz rain doppler and a 7 dB noise figure, the required satellite power is:

Noise power per Hz	= -200 dBW
Bandwidth (S = N)	= 25 dB
Required signal power	-175 dBW
Loss (Table 2)	= -139 dB
Trans signal power	= - 36 dBW
Earth return to signal ratio	90 dB
Total transceiver power	+ 54 dBW,
	or 600,000 watts

This approach will not be considered further.

3.3 Two-Satellite Configuration

The third approach to be considered is to have the RAKE transmitter in one satellite and the receiver in a second satellite. The division of equipment is obvious from Figure A-12. The advantage of this arrangement over the single satellite is that transmission can be continuous rather than have a 50% duty cycle. Continuous transmission will allow greater resolution in the frequency analysis of the rain return. For example, a sample 250 milliseconds long limits resolution to approximately 4 Hz. However, the cost of obtaining the improved resolution is almost double the single satellite approach and does not appear to be justifiable.

4. Implementation in Planned Geostationary Satellites

In reviewing planned satellites in which the RAKE system might be implemented, the primary characteristics required were as follows:

(a) Geostationary orbit,
(b) Low orbit eccentricity,
(c) Antenna with a gain of 50 dB or better at 3 cm wavelength,

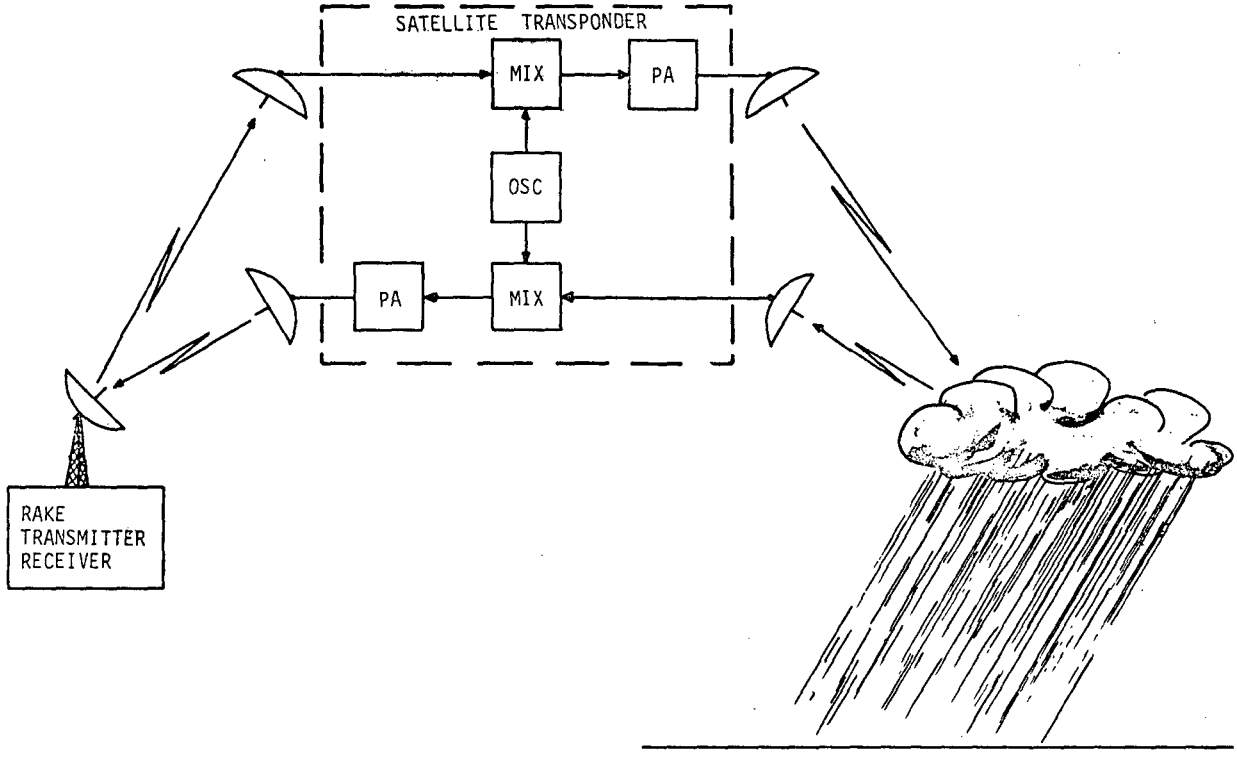

Figure A-14. Satellite Transponder.

(d) Attitude stabilized so antenna pointing of about $\pm$ 0.15 degree (1 dB width) can be maintained,
(e) Space available for the RAKE system.

Inquiries were made to Goddard Space Flight Center, Comsat Corporation, and several private contractors to see what satellites presently being planned would be available and would come close to meeting the primary requirements. The only nonmilitary satellites approaching the requirements appear to be ATS-F and ATS-G. To our knowledge the design of ATS-F which is to be launched in 1974 has been frozen and is no longer open to new experiments. ATS-G design is still open, but some persons have expressed doubt that it would ever be built.

The antenna planned for ATS-G is a 10 meter parabola with a peak gain of about 49 dB at 6 GHz, and a decreasing gain above this frequency. The peak available primary power is about 450 watts so the transmitted power obtainable would be about 125 watts. Thus, if ATS-G were used, the values of present state-of-the-art rainfall detection shown in Figure A-11 would have to be increased slightly to conform with the power and antenna gain available. With a transmitter frequency of 6 GHz and a transmitter power of 125 watts, the minimum detectable rainfall is about 225 mm/hr.

The ATS-G satellite has a ground-to-satellite control system for attitude control and experiment control that appears to be adequate for the RAKE program. It also has a telemetry communication system that would be adequate. The RAKE transmitter, receiver and correlation equipment would have to be developed especially for the satellite as their present transmitters and receivers are not adequate.

5. Conclusions

The results of the system analysis and optimization indicate that the measurement of rain doppler spectrum is feasible using the geostationary satellite RAKE concept. A major problem does appear to exist, not in obtaining the rain doppler spectrum, but rather in interpretation of this spectrum in terms of rainfall rate. Figure A-6 offers a clear illustration of the potential problem. In this figure the doppler spectrum signatures for the three rainfall rates differ little in either frequency value or frequency spread. They do differ more widely in level. However, level variations are related to both rainfall rate and beam-filling factor. It was considered necessary to indicate the presence of this potential problem, although no solution to the problem was pursued during the course of this study.

State-of-the-art limitations to satellite antenna gains and transmitter powers do limit the practicality of employing the geostationary satellite RAKE concept to obtain rain doppler spectra at the present time. The future shows good promise for the concept, however, as satellite antenna gains and transmitter powers are increased.

The portion of the study pertaining to methods of implementing the satellite RAKE system has resulted in a clearly defined "best" method. This method of implementation requires that all RAKE equipment be incorporated into a single satellite with only control signals and RAKE

correlator output data linked to the ground based terminal. ATS-G appears to be the only nonmilitary satellite to be placed in orbit at some near future date that has capabilities approaching those required for satellite RAKE implementation. However, an ATS-G implementation would not be suitable unless greater transmitter powers can be made available.

If the problem of interpreting rain doppler spectra in terms of rainfall rate can be circumvented, the future capabilities of the satellite RAKE system to measure rainfall rate would appear to be assured.

References

1. Battan, L. J., 1959: *Radar Meteorology*, The University of Chicago Press, Chicago and London.

2. Bechman, P., and Spizzichino, A., 1963: *The Scattering of Electromagnetic Waves from Rough Surfaces*, The Macmillan Company, New York.

3. Berkowitz, R. S. (ed.), 1965: *Modern Radar: Analysis, Evaluation, and System Design*, Wiley, New York.

4. Lindholm, J. H., 1968: "An Analysis of the Pseudo-randomness Properties of Subsequences of Long m-sequences," *IEEE Transactions on Information Theory*, Vol. IT-14, No. 4, July 1968, pp. 569-576.

5. Godard, S. S., 1970: "Propagation of Centimeter and Millimeter Wavelengths through Precipitation," *IEEE Transactions on Antennas and Propagation*, Vol. AP-18, No. 4, July 1970, pp. 530-534.

6. *Reference Data for Radio Engineers*, 1968: Howard W. Sams and Co., Inc., Fifth edition.

7. Private communication with Dr. F. Stremler, Space Science and Engineering Center, The University of Wisconsin, Madison, 14 July 1972.

8. Hogg, D. C., 1968: "Millimeter-wave Communication through the Atmosphere," *Science* 159, No. 3810, 5 January 1968, pp. 39-46.

9. Bean, B. R., and Dutton, E. J., 1966: *Radio Meteorology*, US Department of Commerce, National Bureau of Standards Monograph 92, March 1966.

10. Simpson, J., and Wiggert, V., 1971: "1968 Florida Cumulus Seeding Experiment: Numerical Model Results," *Monthly Weather Review*, 99, No. 2, February 1971, pp. 87-118.

POINTING ERROR ANALYSIS OF GEOSYNCHRONOUS SATELLITES

Aniruddha Das and T. C. Huang

FOREWORD

Introduction

The two principal problems in unmanned satellite dynamics are: 1) stability of the satellite; and 2) precise determination of the orientation of the different sensors mounted on the satellite. In the following analysis the latter problem is treated.

To recognize the problem, we have to note the following facts. A satellite usually has two sets of sensors. The first set, the Star Tracking Sensors (STS), looks at some preassigned stars and sends down the signal for the angular positions of the stars relative to the sensors. From these data, the attitude angles of the satellite are calculated. The second set looks at the Earth and is called the Earth Viewing Modules (EVM). For scientific purposes, it is obviously necessary to know the location of the point on the Earth at which the EVM was looking when the data were sensed. So far, the practice has been to calculate the attitude angles of the EVM from the attitude angles of the STS. This would have been satisfactory if both sets of sensors were part of the same rigid body, but in reality the flexible elements on which these sensors are mounted lead to errors in the EVM attitude angle determination.

Another problem is that the data are sensed by both the STS and EVM at discrete time intervals. Also, the sensing time and frequency are not necessarily synchronous for the two sets of sensors, so for correct correlation of data it is necessary to know the motion of the EVM during the interval between two sets of data transmitted by the STS. To do this, an accurate dynamic model of the satellite is required which takes into account the flexibilities, energy dissipative sources and environmental torques influencing the motion.

Now, trying to solve the dynamic equations which involve the angular velocities of the satellite $\underline{\omega}$ leads to further complications. To obtain these angular velocities as a function of time in an interval, say $0 \leq t \leq T$, the magnitudes of $\underline{\omega}$ have to be known at one point in the interval, say at $t = 0$. These initial values of $\underline{\omega}$ have to be obtained from the data sent by the STS. These data are inaccurate, however, as the exact STS angular positions are not known. To calculate the displacement of the STS, $\underline{\omega}$ and the initial values of the coordinates of the STS q_0 have to be known. Since there is no way to measure q_0, one can only obtain the most probable values of $\underline{\omega}$ from a set of assumed values of q_0 to start with and then use improved values of q_0 in successive iteration processes.

The environmental and controlling torques are associated with torque noises. Another source of error is the presence of electrical noise in the data transmitted by the sensors. The presence of these noises makes every variable in the problem a random variable.

The solution of the dynamic problem requires the solution of the associated control problem. In addition, an optimal control system has to be formulated to meet the objectives of accurate prediction of the attitude angles of the satellite.

Literature Review

Most of the early work in satellite dynamics was done to analyze the stability of the motion, and it has thrown a considerable amount of light on this problem.

The "major axis" rule for the stability of freely spinning vehicles was first published by Pilkington [1], Bracewell and Garlott [2], and Perkel [3]. Most of the existing spin-stabilized satellites were designed with this criterion. Quantitative determination of the influence of energy dissipation by dampers on the motion of bodies spinning about their major axes is shown by Thomson and Reiter [4], and Likins [5], [6]. The dual-spin concept was first developed by A. J. Iorillo [7], who also considered simple damper models in both bodies. They were closely followed by Karymov [8], Rossi et al. [9], Likins [10], Likins and Mingori [11], Mingori [12], and Pringle [13].

The usual technique used by these authors was to linearize the rigid body Euler equations and then to apply the Routh-Hurwitz criterion. Mingori [12] compared the linear predictions with Floquet theory. Likins and Mingori [11] obtained a Liapunov function for linear systems. Pringle [13] derived his theorem based on Liapunov's direct method for a lumped mass system, after linearization. An interesting method was shown by Flatley [14], [15]. He used the angular velocities from a rigid body assumption to solve a simple spring-mass-damper model, and obtained results very close to Mingori's Floquet analysis for a similar system.

The most significant contributions to the problem of obtaining the mode shapes for a flexible satellite are from Likins and his associates [16], [17], [18], [19], [20]. They considered distributed mass systems by lumped mass approximation in [16], [18] and [19], and completely linearized the systems with distributed mass mode functions in [17] and [20]. The forcing and controlling torques were not considered. In their formulation, they did not obtain any equations free of the spatial coordinates.

Their approach was fully deterministic, and the problem of nondefinite initial conditions was not considered. Kane and Robe [21] considered two symmetric rigid bodies connected by a flexible beam. A rigid satellite with two torsion pendulums was considered by Bainum and others [22]. Flexible coupling of two rigid spinning bodies was also treated by Cretcher and Mingori [23] and Wenglarz [24]. In a comprehensive report prepared by Avco Systems Division for Goddard Space Flight Center, Maryland [25], the

problem of sensor noise for the angular velocities of a rigid satellite with spring-mass systems was considered. The dependence of the error on the sensor oscillations was not taken into account. Various problems of control were considered in [26] for simple linear systems.

The major area of thermally induced flutter of a general flexible satellite has not been considered thus far. The case of long beams only has been considered in Etkin and Hughes [27]. With the exception of [25] and Zach [29], the system analyses mentioned so far have left out the effect of environmental torques. The torques acting on a rigid satellite are considered in [25]. Zach [29] used a simple torque model for gravity-gradient satellites. In addition, Dobrotin [30] and Tidwell [31] made the only realistic torque models, published so far, without going into the dynamic system. The solution for the vibrations of a fixed base, elastic, distributed-mass structural system, involving shells, plates, beams, rigid bodies and point masses, has been developed by Huang and others [32], [33], [34], and [35]. The present analysis, which also considers translational and rotational motion of such complex structures, will be an extension of that series of work.

We have reviewed the literature dealing only with the general area of satellite dynamics. References related to the methods of analysis will be made when needed.

The Scope of this Study

In the present analysis the basic configuration of a dual-spin satellite has been made. This can be modified to a spinning or a three-axes stabilized satellite. The dynamic model includes elastic shells, plates, beams, rigid bodies and point masses. The effects of thermal stresses, large angular velocities and the effect of the motion to the center of mass due to vehicle deformation are included. In this formulation, the spatial dependences are maintained linear while the time dependences are nonlinear.

The analysis proceeds with the following plan. We start with appropriate partial differential equations for the beams, plates and shells in global coordinates fixed to the satellite. These are then transformed into local coordinates fixed to the nominal positions of each of the elements. Based on the linear theory the solution spaces of the distributed mass elements are chosen; this is done by choosing a finite series of terms of known spatial functions multiplied by unknown time-dependent coefficients q_i. Then, using Galerkin's method, the spatial functions are integrated out of the partial differential equations. This leads to a matrix of ordinary linear second order differential equations in terms of the unknown coefficients of the spatial functions. The coefficient matrices of all but the second derivatives in these equations remain nonlinear functions of the angular velocities ω_i of the satellite. The angular momentum equations for the whole satellite are then obtained, which involve both the sets q_i and ω_i. From all these equations, the unknowns q_i are eliminated leading to nonlinear equations in ω_i only. These equations turn out to be singularly perturbed equations and are scaled out to obtain short-time and long-time equations for the angular velocities ω_i. It is found that

the long-time equations, on being drastically simplified, lead to the usual rigid body equations of motion of satellites. The short-time equations lead to hitherto unknown equations for the transient response of flexible satellites. Solution of this equation requires complete information of the controlling torques for the satellite, so a time-optimal control policy is then assumed and a suitable optimum control system is then formulated. A linearized solution of the system is then subjected to statistical analysis for getting the probability distribution functions of the required variables. The mean values then are to be obtained from the nonlinear equations by a numerical procedure.

The primary advantage of the method outlined is that irrespective of the number of flexible elements in the dynamic model, we will always have to solve only three nonlinear ordinary differential equations in three unknown variables. Also the boundary conditions for the q_i are satisfied before solving the problems by suitably reducing the number of independent elements in the set $\{q_i\}$.

Objectives

The objective of this analysis is to estimate the pointing error of different satellites. For a three-axes stabilized satellite, a very precise determination of instantaneous attitude angles is possible. However, its motion at a subsequent time and the corresponding control is very uncertain. A spinning satellite provides a very stable platform in space, but the attitude measurement is uncertain because of the structural flexibility.

In this study one or more of the rigid bodies will be the model of the attitude determination sensors. The rest of the rigid bodies will be the EVM's. Then, for a particular design, this analysis will provide:

a) the extremes of the attitude error between the different sensors;

b) a probabilistic time history of the magnitude of the error for the transient zone after every control torque pulse;

c) a computer program to plot out the pitch, roll and yaw limit cycles for a 90% probability density bandwidth;

d) an estimate of the stiffness requirement of the flexible elements for a given maximum error limit; and

e) comparison of all these for spinning, nonspinning and dual-spin satellites.

PART I

EQUATIONS OF MOTION OF THE SATELLITE ELEMENTS

Contents

		Page
	Nomenclature	7
	Illustrations	15-23
1.	Expressions for the Displacement of the Center of Mass	24
2.	Beams	27
	a) Inertia forces	27
	b) Thermoelastic forces	29
	c) Elastic forces and the equation of motion	30
	d) Galerkin's method	31
3.	Plates	33
	a) Load system	33
	b) Inertia forces	33
	c) Thermoelastic forces	34
	d) Galerkin's functions for plates 1 and 4	36
	e) Coefficient of $\chi_{i,8}(t)$	40
	f) Final equations for plates 1 and 4	41
	g) Equations for plates 2 and 3	42
4.	Shells	43
	a) Inertia forces	43
	b) Thermoelastic forces	45
	c) Equation of motion	47
	d) Galerkin's functions	50
5.	Beam-end Masses	52
	a) Inertia forces	52
	b) Elastic forces	52
6.	Spring-mass-damper Systems	55
7.	Rigid Bodies	56
	a) Force equations	57
	b) Moment equations	58
8.	Transformation Matrices	60
9.	Contact Forces and Torques	62
10.	Assembled Equations of Motion	66
11.	Error Bounds of the Solutions	67
	References	69

Nomenclature

CM	=	Center of mass of the satellite
A, B, C	=	Satellite subassemblies
m_i; (i = 1 - 4)	=	Masses of rigid bodies having moments of inertia
m_i; (i = 5 - 20)	=	Point masses (scalar)
$\underline{a}_1$, $\underline{a}_2$, $\underline{a}_3$	=	Orthogonal unit vectors, fixed in the body A
$\underline{b}_1$, $\underline{b}_2$, $\underline{b}_3$	=	Orthogonal unit vectors, fixed in the body B
$\underline{n}_1$, $\underline{n}_2$, $\underline{n}_3$	=	Inertially fixed orthogonal unit vectors
$\|\|M\|\|$	=	Total mass of the satellite (scalar)
O	=	Nominal location of the center of mass of the body B
O'	=	Origin of the inertially fixed coordinate axes
Q	=	Reference point, fixed in the body B
$\underline{R}$, R	=	Position vector of Q relative to O, and its B-based matrix
$\underline{X}_B$, X_B	=	Position vector of center of mass of the body B and its matrix, both based in the inertially fixed axes
$\underline{C}_B$, C_B	=	Displacement vector of the center of mass of the body B and its B-based matrix
ω_A, ω_A	=	Angular velocity vector of the body A and its A-based matrix
ω_B, ω_B	=	Angular velocity vector of the body B and its B-based matrix
$\underline{Y}_i$; (i = 1 - 20)	=	Displacement vector of the masses m_i in B-based coordinates
${}_A\underline{Y}_i$; (i = 1 - 20)	=	Displacement vector of the masses m_i in A-based coordinates

$\theta_{i,1}$, $\theta_{i,2}$, $\theta_{i,3}$ ($i = 1 - 4$) = Rotations of the rigid bodies in B-based coordinates

$^A\theta_{i,1}$, $^A\theta_{i,2}$, $^A\theta_{i,3}$ ($i = 1 - 4$) = Rotations of the rigid bodies in A-based coordinates

$\underline{F}$, F = Force vector on satellite and its matrix, both based in the inertially fixed axes

$\|M\|_A$ and $\|M\|_B$ = Total masses of the bodies A and B, respectively

$\underline{F}_i$, F_i ($i = 1-20$) = Force vector on m_i and its B-based matrix

$\underline{T}$, T = Torque vector on the satellite and its B-based matrix

$\underline{T}_i$, T ($i = 1-4$) = Torque vector on the rigid bodies and its B-based matrix

$\underline{H}$ = Angular momentum vector of the satellite about CM

$\underline{H}_i$ ($i = 1-4$) = Angular momentum vector of the rigid bodies about their centers of mass

Q_i ($i = 1-20$) = Nominal position of m_i

P_i ($i = 1-4$) = Center of mass of m_i

$\underline{r}_i$, r_i = Position vector of Q_i relative to Q and its B-based matrix

$^N a_i$ = Acceleration of masses m_i in the inertially fixed axes

Θ = Matrix for transformation from inertially fixed axes to B-based coordinates

$^N(\dot{})$ = Inertial time derivative

$(\dot{})$ = Time derivative in body fixed coordinates

$(\ )$ = Skew symmetric matrix operator

$\underline{\eta}_i$ ($i = 1-8$) = Displacement vector of beams in B-based coordinates

χ_i (i = 1-4) = Displacement vector of plates in B-based coordinates

ξ_B = Displacement vector of shell B in B-based coordinates

${}_b\rho_i$ (i = 1-8) = Mass per unit length of beams

${}_p\rho_i$ (i = 1-4) = Mass per unit area of plates

${}_s\rho_A$, ${}_s\rho_B$ = Mass per unit area of shells A and B

$\mu_{i,1}$; $\mu_{i,2}$; $\mu_{i,3}$ (i = 1-4) = Local orthogonal coordinate axes for beams, and fixed w.r.t. the B-based coordinates

μ_i^B = Matrix for transformation of μ_i-axes to the B-based coordinates

${}_b\underline{F}_{B_i}$ (i = 1-4) = Inertia force on the i^{th} beam element in B-based coordinates

${}_b\underline{F}_{\mu_i}$ (i = 1-4) = Inertia force on the i^{th} beam element in local coordinates

${}_bq_i$ = Elastic deformation vector of the i^{th} beam in local coordinates

$\underline{s}_i$, ${}_A\underline{s}_i$, ${}_B\underline{s}_i$ = Position vectors of the i^{th} beam element from the reference end in local, A-based and B-based coordinates, respectively

${}_B\underline{R}_i$, $\underline{R}_i$ = Position vector to the reference end of the i^{th} beam in B-based and local coordinates, respectively

k_{B_i} = $-\frac{{}_b\rho_i}{\|M\|_B}$

${}_bM_{T_{i,2}}$ and ${}_bM_{T_{i,3}}$ = Thermal bending moments of the i^{th} beam

${}_bE_i$ = Modulus of elasticity for the i^{th} beam

${}_bI_{i,2}$ and ${}_bI_{i,3}$ = Moments of inertia of the i^{th} beam about local coordinate axes

$K_{T_{i,2}}$ and $K_{T_{i,3}}$	=	Thermal curvatures of the i^{th} beam about local coordinate axes
b^{k_i}	=	Thermal bending constant for the i^{th} beam
b^{τ_i}	=	Characteristic time for heat transfer across the i^{th} beam
$\alpha_{i,2}$ and $\alpha_{i,3}$	=	Attitude angles of the i^{th} beam w.r.t. the Sun
$K^{*}_{T_{i,2}}$ and $K^{*}_{T_{i,3}}$	=	Maximum values of the thermal curvatures of the i^{th} beam
$r^{I_{i,jk}}$	=	Mass moment of inertia matrix of the i^{th} rigid body in B-based coordinates
p^{D_i}	=	Stiffness of the i^{th} plate
p^{E_i} , p^{h_i} , p^{μ_i}	=	Modulus of elasticity, thickness and Poisson's ratio of the i^{th} plate
p^{T_i} , p^{α_i}	=	Temperature distribution and thermal coefficient of expansion of the i^{th} plate
p^{k_i} , p^{τ_i} , $p^{\tau_{i,0}}$	=	Thermal constants for the i^{th} plate
p^{β_i}	=	Attitude of the Sun from the plate nominal normal vector
$p^{\beta^{*}_i}$	=	Flexural change of attitude of plate element from the nominal normal vector
$\xi_{B,r}$, $\xi_{B,\theta}$, $\xi_{B,z}$	=	Radial, tangential and axial deformation of an element of shell B in B-based coordinates
$s^{F_{B,1}}$, $s^{F_{B,2}}$, $s^{F_{B,3}}$	=	Inertial force components per unit area of shell B in B-based coordinates
s^{h_B}	=	Thickness of shell B
a_B	=	Nominal radius of shell B and plates 1 and 2

$s^{\mu}B$, $s^{E}B$	=	Poisson's ratio and the modulus of elasticity of shell B
$s^{T}B$	=	Temperature distribution of shell B
$s^{\beta}B$	=	Attitude of the Sun from the nominal normal of an element of shell B
$s^{\beta^*}B$	=	Flexural change of attitude of the normal of an element of shell B
$s^{k}B$, $s^{\tau}B$, $s^{\tau}B,0$	=	Thermal constants for the shell B
$\mathscr{I}$	=	Identity matrix
G_B, $\underline{q}^*_B$	=	Defined by Eq. (1.10)
p_1, $q_{i,1}$, $j q_{i,k}$	=	Defined by Eq. (1.3)
λ_0	=	a scalar, first zero of $J_0(x)$
λ_1, λ_2	=	scalars, second zeros of $J_1(x)$ and $J_2(x)$, respectively
$\{{}_b\underline{q}^*_i\}, [\lambda_j], [{}_bA_{i,k}]$, $j = 1\text{-}3$	=	Defined by Eq. (1.23)
$p\kappa_{i,j}$, $j = 1,2$	=	Thermal curvatures of the i^{th} plate
$p\kappa_{i,0}$	=	$p^{k}i \cdot p^{\tau}i$
$p^{M}T_{i,j}$, $j = 1,2$	=	Thermal bending moments of the i^{th} plate
$p^{R}i$	=	Position vector of the i^{th} plate element in B-based coordinates
$[\mathscr{I}_3]$	=	(3×3) square matrix of zeros except for $[\mathscr{I}_3]_{3,3} = 1$
∇^2_1	=	Laplacian operator, defined by Eq. (1.27)
$[\tau]_i$, $i = 1\text{-}12$	=	(3×3) square matrices, defined by Eqs. (1.107) through (1.115)

r_1, θ = Plane polar coordinates fixed in the body B

r = $\frac{r_1}{a_B}$

$\chi_{1,j}$ $j = 1\text{-}11$ = Defined by Eq. (1.34)

$a_{1,j}$ $j = 1\text{-}15$ = Defined by Eq. (1.35)

$w(z)$ = Mapping, defined by Eq. (1.36)

$[\lambda_j]$, $j = 4\text{-}6$, $[{}_pA_{1,k}]$, $\{{}_pq_1^*\}$ = Matrices, defined by Eq. (1.39)

$[\mu_r^B]$ = Matrix for transformation from rectangular to cylindrical coordinates

$\{{}_sF_B^r\}$ = $[\mu_r^B]\{{}_sF_B\}$

$\underline{R}_B$ = Position vector of an element of shell B in B-based coordinates

$[\mathcal{L}_1]$ = (3 × 3) square matrix of zeros except for $[\mathcal{L}_1]_{1,1} = 1$

${}^sK_{B,\theta}$, ${}^sK_{B,z}$ = Thermal curvature of the shell B in tangential and axial directions

${}^sK_{B,0}$ = ${}^sK_B \cdot {}^sT_B$

${}^sT_{B1}$ = Shell thermal parameter, defined by Eq. (1.49)

${}^s\alpha_B$ = Thermal coefficient of expansion of shell B

α, β = Angles, defined in Fig. 6

b_i, $i = 1\text{-}11$ = Coordinates, defined by Eq. (1.58)

$[\lambda_{1j}]$, $i = 7\text{-}9$, $[{}_sA_j]$, $\{{}_sq_B^*\}$ = Shell parameters, defined in Eq. (1.60)

$\{{}_r\underline{q}_i^*\}$ = Rigid body coordinates, defined by Eq. (1.77)

$P_{2,1}^{(j)}$, j = 7-10 = Plate reaction forces on m_1

$P_{2,2}^{(j)}$, j = 11-14 = Plate reaction forces on m_2

${}_rI_{i,j}$, j = 1-3 = Diagonal elements of $[{}_rI_{i,jk}]$

$\underline{T}_i$, i = 1,2 = Inertia torque vector on m_i

$\underline{T}_i'$, i = 1,2 = Resistive torque vector on m_i

$[\lambda_i]$, i = 10-12, $[{}_mA_i]$, $[\underline{y}^*]$ = Point mass parameters, defined by Eq. (1.70)

$k_{i,1}$, i = 13-16 = Constants for the springs connecting m_i to plate No. 1

$k_{i,2}$, i = 13-16 = Constants for the dampers connecting m_i to plate No. 2

$[\lambda_i]$, i = 13-15, $[{}_dA_i]$, $\{{}_d\underline{q}^*\}$ = Spring-mass-damper system parameters, defined by Eq. (1.76)

$[\lambda_i]$, i = 16-18, $[{}_rA_i]$, $\{{}_rq^*\}$ = Rigid body parameters, defined by Eq. (1.93)

ℓ_θ, ℓ_r = Lengths of the rigid bodies in the $\underline{b}_2$ and $\underline{b}_1$ directions, respectively

ψ_1, ψ_2, ψ_3 = Rotations of the body B relative to the inertially fixed coordinates

θ_1, θ_2, θ_3 = Rotations of the body A relative to the body B

Θ_{AB} = Matrix for transforming vectors in the A-based coordinates to the B-based coordinates

$\underline{F}_{BC}$, $\underline{T}_{BC}$ = Contact force and torque vectors exerted by the body C on the body B in B-based coordinates

$\underline{F}_{AC}$, $\underline{T}_{AC}$ = Contact force and torque vectors exerted by the body C on the body A in A-based coordinates

${}_b\underline{F}_{AC}$, ${}_b\underline{T}_{AC}$ = $\underline{F}_{AC}$, $\underline{T}_{AC}$ *expressed in B-based coordinates*

γ = $\dfrac{\|M\|_A}{\|M\|_B}$

η = Ratio of the viscous and elastic modulii of the body C (Eq. (1.111))

E_c, I_c, ℓ_c = The modulus of elasticity, moment of inertia of the cross-section and the length of the body C

E_c^* = The modulus of viscosity of the body C

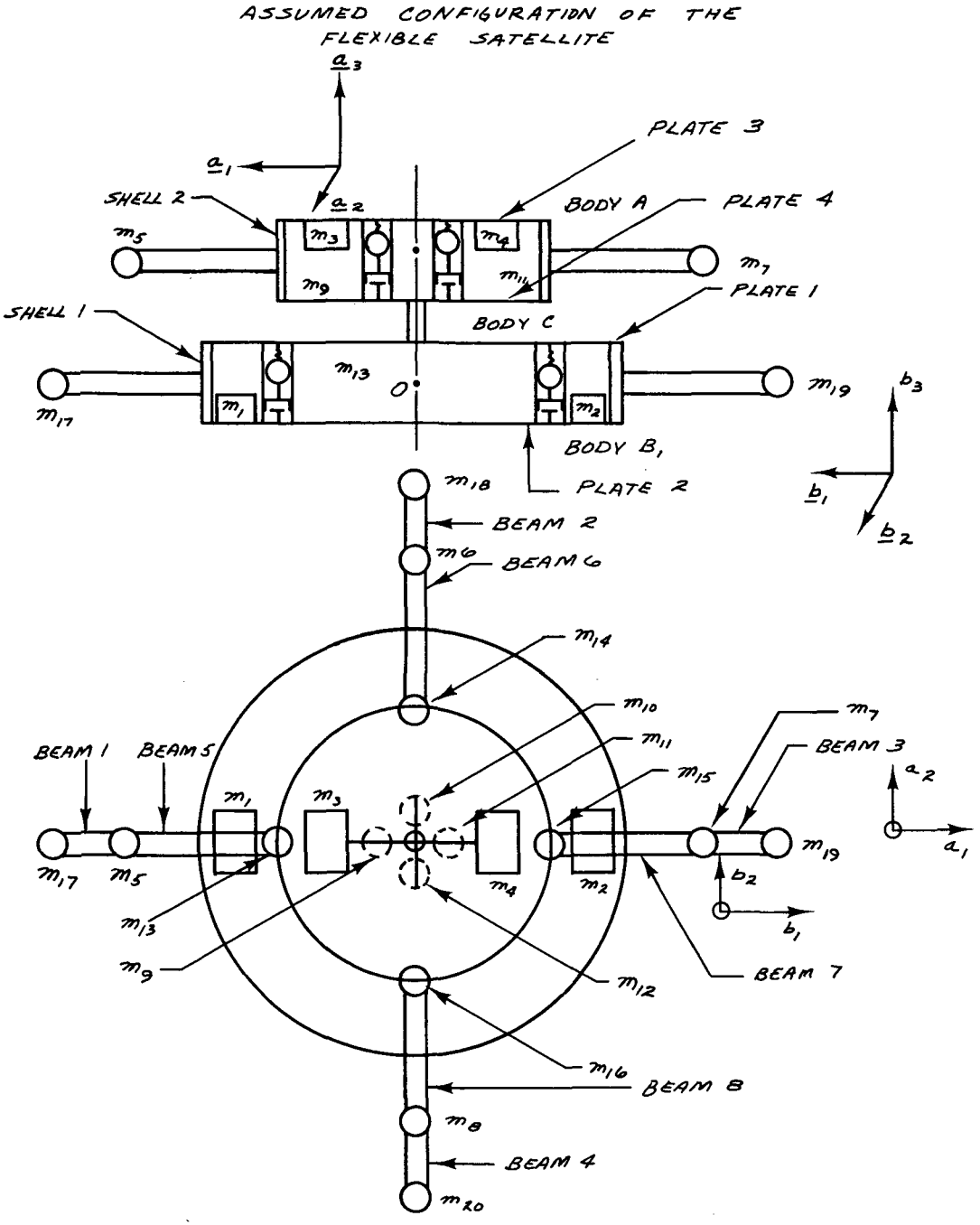
ASSUMED CONFIGURATION OF THE FLEXIBLE SATELLITE
PLATE 3
PLATE 4
BODY A
SHELL 2
SHELL 1
PLATE 1
BODY C
BODY B1
PLATE 2
BEAM 2
BEAM 6
BEAM 1
BEAM 5
BEAM 3
BEAM 7
BEAM 8
BEAM 4

Figure 1

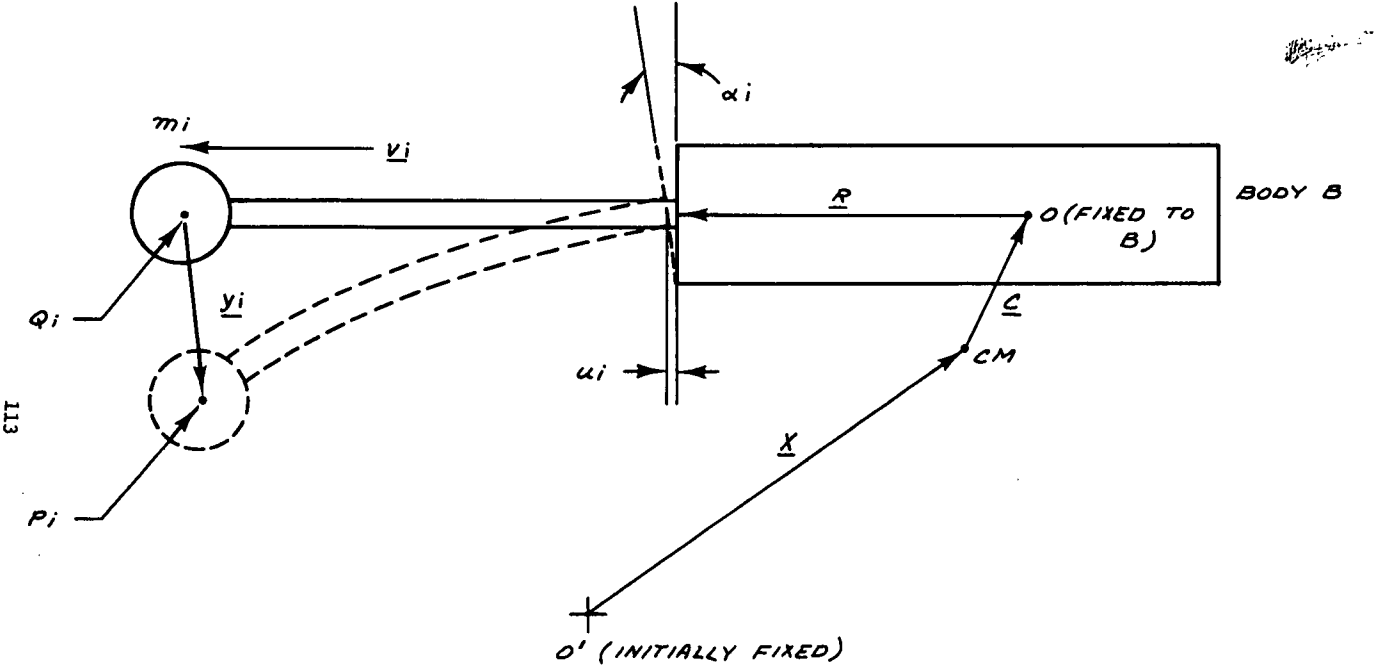

Figure 2

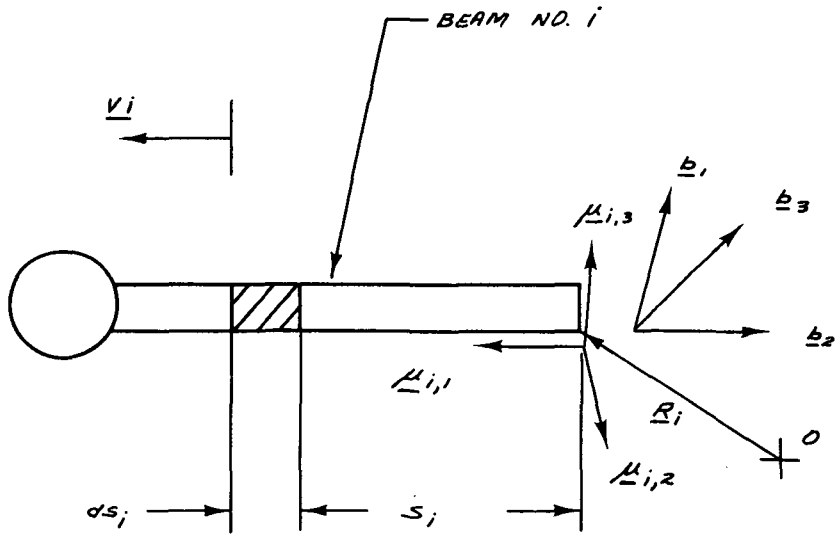

Figure 3

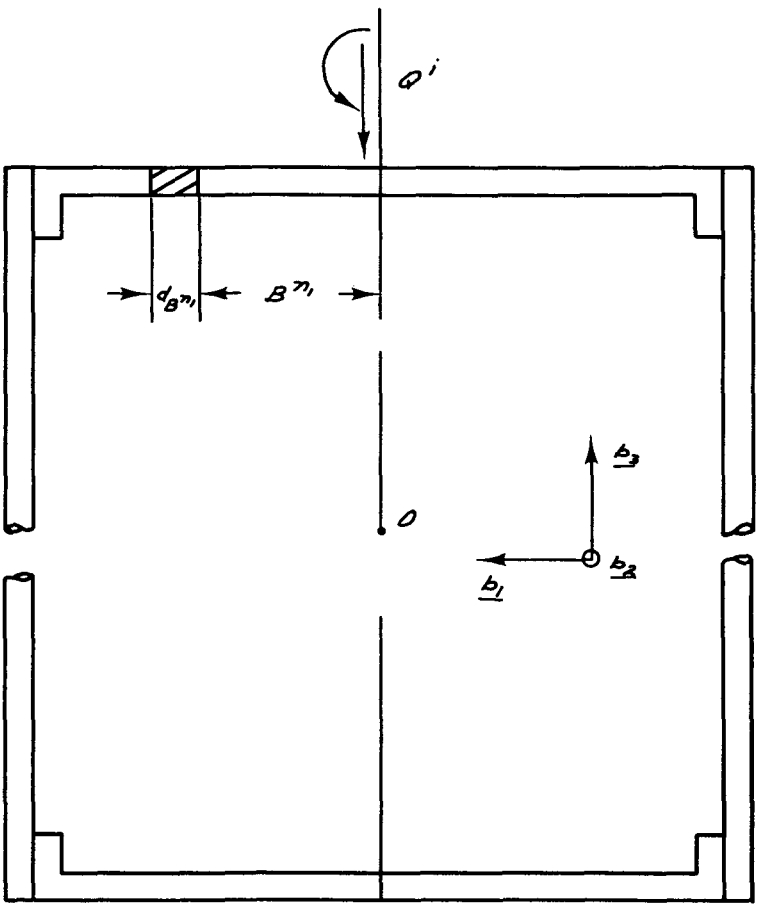

Figure 4

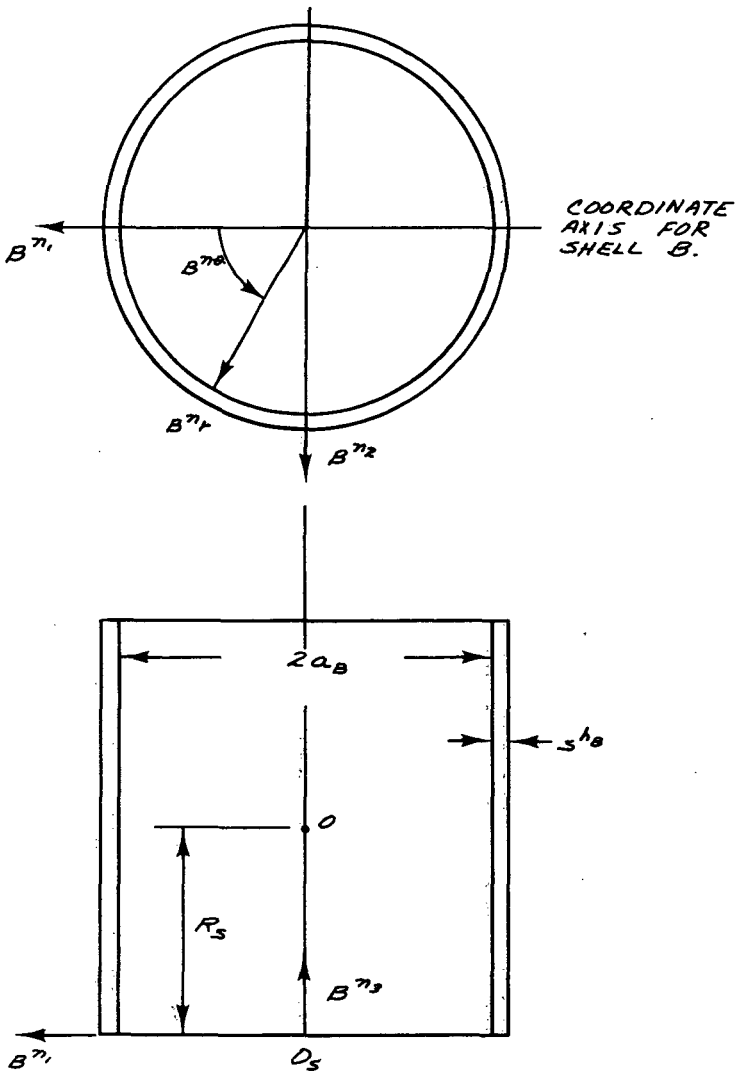
COORDINATE AXIS FOR SHELL B.
B^{n_1}
B^{n_θ}
B^{n_r}
B^{n_2}
$2a_B$
s^{h_B}
0
R_s
B^{n_3}
B^{n_1}
O_s

Figure 5

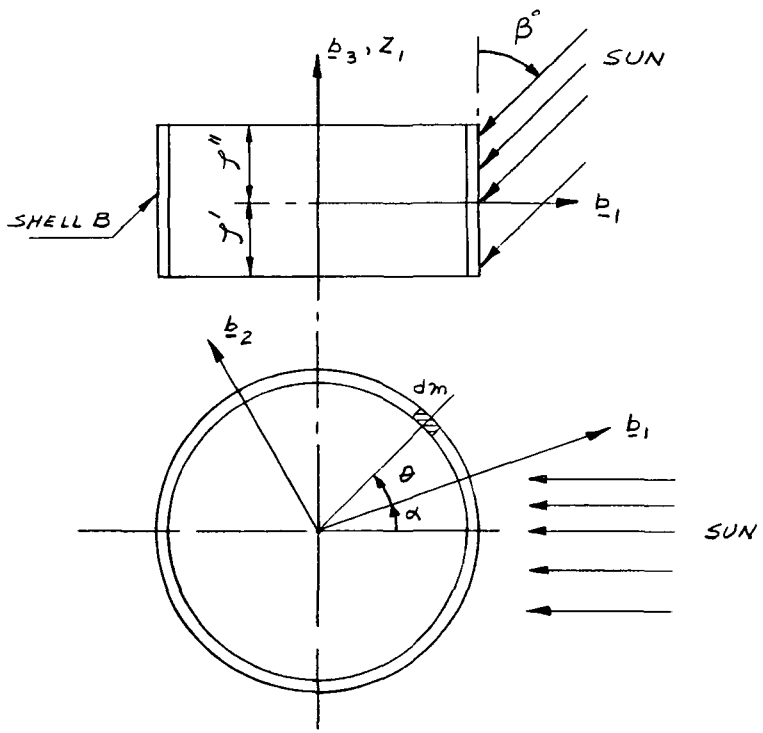
$\underline{b}_3, Z_1$
β°
SUN
ρ''
ρ'
SHELL B
$\underline{b}_1$
$\underline{b}_2$
dm
$\underline{b}_1$
θ
α
SUN

Figure 6

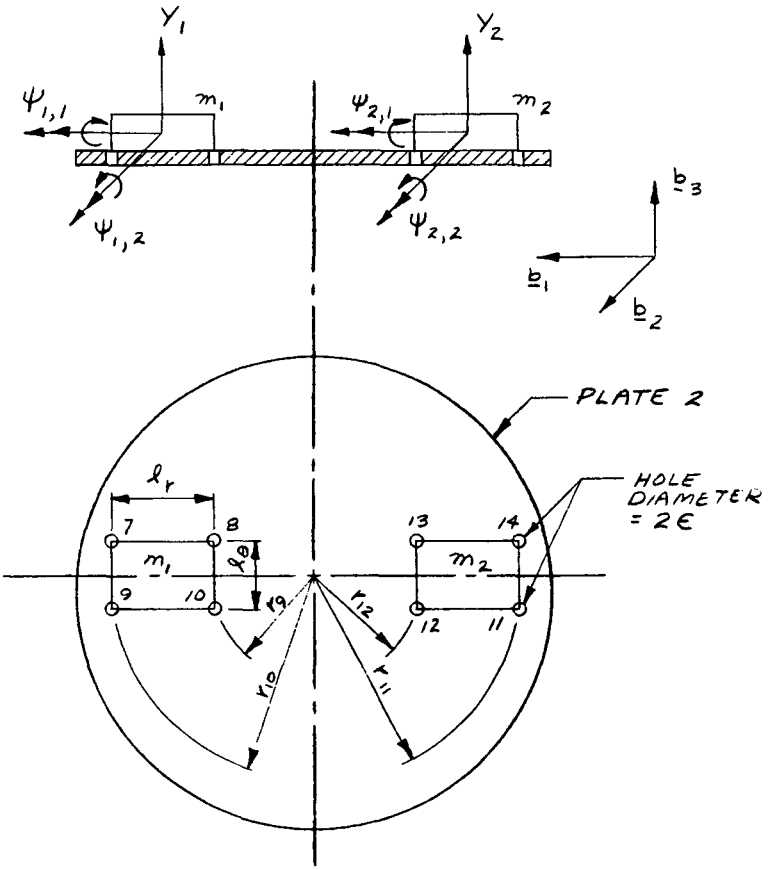
Y1
Y2
ψ1,1
m1
ψ2,1
m2
ψ1,2
ψ2,2
b3
b1
b2
PLATE 2
HOLE
DIAMETER
= 2ε
lr
lθ
7
8
9
10
13
14
12
11
r10
r11
r12

Figure 7

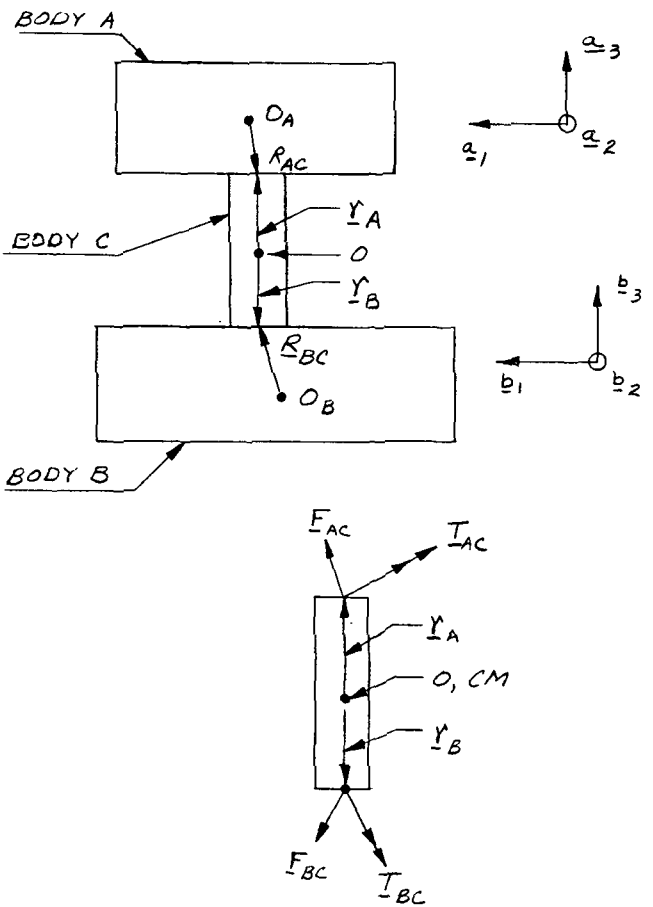
BODY A
O_A
R_{AC}
r_A
BODY C
O
r_B
R_{BC}
O_B
BODY B
a_3
a_1
a_2
b_3
b_1
b_2
F_{AC}
T_{AC}
r_A
O, CM
r_B
F_{BC}
T_{BC}

Figure 8

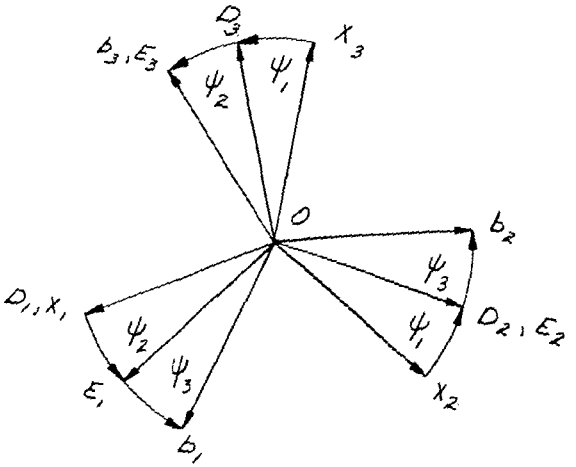

Figure 9

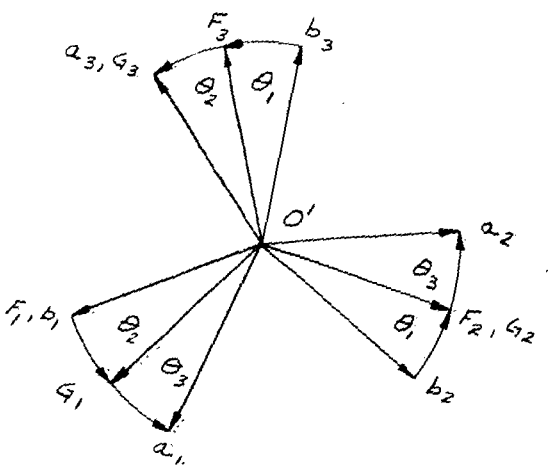

Figure 10.

1. Expressions for the Displacement of the Center of Mass

The expressions for the displacement of the center of mass are required for obtaining the equations for each individual structural element. But these expressions can only be obtained after the deformations of the individual elements are known. However, it becomes easier to grasp the analysis that follows when these expressions in general form are available.

The basic assumed configuration of the satellite is shown in Figure 1. It consists of two composite bodies A and B, each containing point masses, rigid bodies, beams, plates and shells. These two bodies are connected by a flexible connector C. The shift of the CM is shown by the vector $\underline{C}$ in Figure 2. Let us consider the body B and find $\underline{C}_B$, the shift of its center of mass in terms of the displacements of its elements. The case for the body A can be obtained in an analogous manner. The mass of C is negligible.

Using the B-based coordinates, it is easily seen that

$$\underline{C}_B = -\frac{1}{\|M\|_B}\left[\sum_i m_i \underline{y}_i + \sum_j \int_0^{\ell} {}_b\rho_j \cdot \underline{\eta}_j ds + \sum_k \iint {}_p\rho_k \, \underline{\chi}_k dA + \iint {}_s\rho_B \, \underline{\xi}_B dA\right] \tag{1.1}$$

where $i = 1,2$, and $13\text{-}20$; $j = 1\text{-}4$; $k = 1,2$. The integrals are taken over the lengths or areas of the elements as applicable. The length of the beam is ℓ. To evaluate the beam integrals from the beam displacements in local coordinates, we set

$$\underline{\eta}_i = [\mu_i^B]^T \cdot {}_b\underline{q}_i \tag{1.2}$$

in Eq. (1.1). The local coordinate system for the beams is a right-handed system of Cartesian coordinates, with its origin at the clamped end and $\underline{\mu}_{i,1}$ axis along the length of the beam. For each beam the three components of ${}_b\underline{q}_i$ are set up as follows:

$$
\left.
\begin{aligned}
{}_b q_{i,1} &= {}_1 q_{i,1}(t) \\
{}_b q_{i,2} &= {}_1 q_{i,2}(t) \cdot [\exp(p_1 s) - 1] + {}_2 q_{i,2}(t) \cdot s + {}_3 q_{i,2}(t) \\
{}_b q_{i,3} &= {}_1 q_{i,3}(t) \cdot [\exp(p_1 s) - 1] + {}_2 q_{i,3}(t) \cdot s + {}_3 q_{i,3}(t)
\end{aligned}
\right\} \qquad (1.3)
$$

$$
\therefore \int_0^{\ell} {}_b \rho_j \cdot \underline{\eta}_j \, ds = {}_b \rho_j \cdot [\mu_j^B]^T \cdot \int_0^{\ell} {}_b \underline{q}_j \, ds
$$

$$
= {}_b \rho_j \cdot [\mu_j^B]^T \cdot \begin{bmatrix} B_3 \cdot {}_1 q_{j,1} \\ B_1 \cdot {}_1 q_{j,2} + B_2 \cdot {}_2 q_{j,2} + B_3 \cdot {}_3 q_{j,2} \\ B_1 \cdot {}_1 q_{j,3} + B_2 \cdot {}_2 q_{j,3} + B_3 \cdot {}_3 q_{j,3} \end{bmatrix} \cdot \qquad (1.4)
$$

Here obviously
$$
\left.
\begin{aligned}
B_1 &= \left[\frac{1}{p_1} (e^{p_1 \ell} - 1) - \ell \right] \\
B_2 &= \frac{\ell^2}{2} \quad \text{and} \quad B_3 = \ell
\end{aligned}
\right\} \qquad . \qquad (1.5)
$$

The sum of the beam integrals is obtained by evaluating $[\mu_j^B]$ for each beam and then using Eqs. (1.4).

The rigid bodies and the point masses in the spring-mass-damper systems are assumed to move only in the direction of $\underline{b}_3$ (see Fig. 1). The masses at the ends of the beams can move in all directions. The shell is assumed to deform only radially. The plates are assumed to deform only laterally. So we can rewrite Eq. (1.1) as:

$$\underline{C}_B = -\frac{1}{\|M\|_B} \cdot$$

$$\begin{bmatrix} (m_{17}\cdot y_{17,1} + m_{18}\cdot y_{18,1} + m_{19}\cdot y_{19,1} + m_{20}\cdot y_{20,1} + {}_s\rho_B \cdot \iint \xi_{B,r} \cos\theta \cdot a_B^2 \, d\theta dz_1) \\ (m_{17}\cdot y_{17,2} + m_{18}\cdot y_{18,2} + m_{19}\cdot y_{19,2} + m_{20}\cdot y_{20,2} + {}_s\rho_B \iint \xi_{B,r} \sin\theta \cdot a_B^2 d\theta dz_1) \\ (m_{17}\, y_{17,3} + m_{18}\, y_{18,3} + m_{19}\, y_{19,3} + m_{20}\, y_{20,3} + m_1 y_1 + m_2 y_2 + m_{13} y_{13} + m_{14}\cdot y_{14} \\ \quad + m_{15} y_{15} + m_{16} y_{16} + {}_p\rho_1 \iint \chi_1 dA + {}_p\rho_2 \iint \chi_2 dA) \end{bmatrix}$$

$$-\frac{1}{\|M\|_B} \cdot \sum_j \int_0^{\ell} b\rho_j \underline{\eta}_j ds \quad . \tag{1.6}$$

We have taken the shell displacements later on as

$$\xi_{B,r} = \sum_{i=1} b_i(t)\cdot\phi_i(\theta,z_1) \ , \tag{1.7}$$

where $\phi_i(\theta,z_1)$ are purely spatial functions. Similarly, the plate displacements have been taken as

$$\chi_1 = \sum_{i=1}^{15} a_{1,i}(t)\cdot\psi_{1,j}(r,\theta) + \sum_j \chi_{1,j}(t)\cdot\psi^*_{1,j}(r,\theta); \quad j = 1 \text{ and } 7\text{-}11. \tag{1.8}$$

$$\chi_2 = \sum_{i=1}^{15} a_{2,i}(t)\cdot\psi_{2,i}(r,\theta) + \sum_j \chi_{2,j}(t)\cdot\psi^*_{2,j}(r,\theta); \quad j = 1 \text{ and } 7\text{-}18 \ . \tag{1.9}$$

Equations (1.3) to (1.7) will become clear when we come to the individual analyses of the beams, plates and shells later. It is evident from Eq. (1.6) that when the integrations there are carried out, $\underline{C}_B$ becomes a linear

combination of only the time-dependent functions in (1.3), (1.7), (1.8), (1.9) and the $\underline{\gamma}_i(t)$, $i = 1,2$ and 13-20.

Now, let $\underline{q}_B^*(t)$ be the (110 × 1) column vector of all the time-dependent functions $\underline{\gamma}_i$, ${}_b\underline{q}_i$, $a_{1,i}$, $a_{2,i}$, $\chi_{1,i}$, $\chi_{2,i}$ and b_i mentioned so far. These generalized position coordinates $\underline{q}_B^*$ define the deformations and displacements of the spacecraft. Then we can write $\underline{C}_B$ explicitly as

$$\underline{C}_B = [G_B]\cdot\underline{q}_B^* \tag{1.10}$$

where $[G_B]$ is a (3 × 110) matrix of known constants. The detailed forms of $[G_B]$ and $\underline{q}_B^*$ will be given in Appendix 1.

2. Beams

(a) Inertia Forces

Referring to Figures 2 and 3, the equations for the inertia forces on a beam element are first obtained. We follow Likins [10] in doing this.

Let dm_i be the mass of a beam element in body B.

$$\therefore \quad dm_i = {}_b\rho_i \cdot d({}_Bs_i) . \tag{1.11}$$

Let the position of the element with respect to the CM of body B be given by $(\underline{C}_B + {}_B\underline{R}_i + {}_B\underline{s}_i + \underline{\eta}_i)$. Then the inertia force is given by

$$\therefore \quad {}_b\underline{F}_{B_i} = -dm_i[\ddot{\Theta}\underline{X}_B + \ddot{\underline{C}}_B + \ddot{\underline{\eta}}_i + 2\underline{\omega}_B \times (\dot{\underline{C}}_B + \dot{\underline{\eta}}_i)$$

$$+ (\dot{\underline{\omega}}_B + \underline{\omega}_B \times \underline{\omega}_B) \times (\underline{C}_B + {}_B\underline{R}_i + {}_B\underline{s}_i + \underline{\eta}_i)]$$

where $\underline{X}_B$ locates the CM of the body B in inertially fixed coordinates.

Let $\underline{V}$ and $\underline{\omega}$ be two vectors given in matrix form by $\underline{V} = [V_1, V_2, V_3]^T$ and $\underline{\omega} = [\omega_1, \omega_2, \omega_3]^T$. If we define

$$\tilde{V} = \begin{bmatrix} 0 & -V_3 & V_2 \\ V_3 & 0 & -V_1 \\ -V_2 & V_1 & 0 \end{bmatrix} ,$$

then $\underline{V} \times \underline{\omega} = \tilde{V}\omega = -\tilde{\omega}V = -\underline{\omega} \times \underline{V}$. Therefore

$$_{b}\underline{F}_{B_i} = -dm_i[\ddot{\Theta X}_B + \ddot{C}_B + \ddot{\eta}_i + 2\tilde{\omega}_B(\dot{C}_B + \dot{\eta}_i)$$

$$+ (\dot{\tilde{\omega}}_B + \tilde{\omega}_B\tilde{\omega}_B)(C_B + {}_BR_i + {}_Bs_i + \eta_i)] \quad . \tag{1.12}$$

As mentioned before, the axes of the local coordinate frame μ_i, corresponding to the i^{th} beam, are $\mu_{i,1}$, $\mu_{i,2}$ and $\mu_{i,3}$. This is a right-handed system with $\mu_{i,1}$ being always along the axis of the beam pointing away from the CM. $\mu_{i,3}$ is always parallel to the $\underline{b}_3$ axis. The origin is always at the clamped end of the beam.

So $[\mu_i^B]$, the transformation matrix for converting B-based vectors into $\underline{\mu}$-based vectors, is given by

$$[\mu_i^B] = \begin{bmatrix} \mu_{i,1}\cdot b_1 & \mu_{i,1}\cdot b_2 & \mu_{i,1}\cdot b_3 \\ \mu_{i,2}\cdot b_1 & \mu_{i,2}\cdot b_2 & \mu_{i,2}\cdot b_3 \\ \mu_{i,3}\cdot b_1 & \mu_{i,3}\cdot b_2 & \mu_{i,3}\cdot b_3 \end{bmatrix} \quad . \tag{1.13}$$

If $_{b}\underline{q}_i$ are the beam displacements in local coordinates, then

$$_{b}\underline{q}_i = [\mu_i^B]\cdot\underline{\eta}_i \tag{1.2a}$$

$$s_i = [\mu_i^B]\cdot(_{B}\underline{s}_i) \quad . \tag{1.14}$$

Then in local coordinates, the Eq. (1.12) becomes

$$_{b}\underline{F}_{\mu_i} = -[\mu_i^B](_{b}\underline{F}_{B_i}) = dm_i[\mu_i^B\ddot{\Theta X}_B + \mu_i^B\ddot{C}_B + {}_{b}\ddot{q}_i + 2\mu_i^B\tilde{\omega}_B\dot{C}_B$$

$$+ 2(\mu_i^B\cdot\tilde{\omega}_B(\mu_i^B)^T)_{b}\dot{q}_i + (\mu_i^B\dot{\tilde{\omega}}_B + \mu_i^B\tilde{\omega}_B\tilde{\omega}_B)C_B + \mu_i^B(\dot{\tilde{\omega}}_B + \tilde{\omega}_B\tilde{\omega}_B)(\mu_i^B)^T\ (R_i + s_i + {}_{b}q_i)] \quad . \tag{1.15}$$

Let us define

$$(\mu_i^B)\cdot\tilde{\omega}_B\cdot(\mu_i^B)^T = \omega_B^* \tag{1.16}$$

and

$$(\mu_i^B)\tilde{\omega}_B\tilde{\omega}_B(\mu_i^B)^T = \omega_B^{**} \quad . \tag{1.17}$$

Then Eq. (1.15) becomes

$$\begin{aligned} {}_b\underline{F}_{\mu_i} = -{}_b\rho_i\cdot ds_i\cdot[\mu_i^B\Theta\ddot{X}_B + \mu_i^B G_B\ddot{q}_B^* + {}_b\ddot{\underline{q}}_i + (2\mu_i^B\tilde{\omega}_B G_B)\dot{q}_B^* \\ + 2\omega_B^*\cdot{}_b\dot{q}_i + [\mu_i^B(\tilde{\dot{\omega}}_B + \tilde{\omega}_B\tilde{\omega}_B)G_B]q_B^* + (\dot{\omega}_B^* + \omega_B^{**})(R_i + s_i + {}_bq_i)] \quad . \end{aligned} \tag{1.18}$$

(b) Thermoelastic Forces

The thermal oscillations of the outstretched beams can cause considerable changes in the attitudes of the spacecraft. This problem was first successfully modelled by Etkin [27] and later on by Yu [28]. Here we follow the method of Yu, and assume that the thermal curvature of the beam is linearly proportional to the local heat input from the sun.

Let $\kappa_{T_{i,2}}$ and $\kappa_{T_{i,3}}$ be the thermal curvatures about the $\mu_{i,2}$ and $\mu_{i,3}$ axes. Then we have the relation from Yu [28] as

$$\frac{\partial\kappa_{T_{i,2}}}{\partial t} = -\frac{\kappa_{T_{i,2}}}{{}_b\tau_i} + {}_bk_i\cos(\alpha_{i,2} + \frac{\partial\,{}_bq_{i,2}}{\partial s_i}) \tag{1.19}$$

for the $\mu_{i,2}$ direction and a similar relation for the $\mu_{i,3}$ direction. Eq. (1.19) has the series solution (see Appendix 2)

$$\kappa_{T_{i,2}} = {}_bk_i\cdot{}_b\tau_i[\cos\alpha_{i,2} - (\theta_2 - {}_b\tau_i\dot{\theta}_2 + {}_b\tau_i^2\ddot{\theta} - \ldots)\sin\alpha_{i,2}]$$

where $\theta_2 = \frac{\partial}{\partial s_i}\,{}_bq_{i,2}$.

If we set ${}_b k_i \cdot {}_b \tau_i = \kappa^*_{T_{i,2}}$, then for small values of ${}_b \tau_i$, we get

$$\kappa_{T_{i,2}} = \kappa^*_{T_{i,2}} [\cos \alpha_{i,2} - (\frac{\partial}{\partial s_i} {}_b q_{i,2} - {}_b \tau_i \cdot \frac{\partial^2}{\partial s_i \partial t} {}_b q_{i,2}) \sin \alpha_{i,2}] \tag{1.20}$$

and a similar equation about the $\mu_{i,3}$ axis. Then the thermal moment on the beam, ${}_b M_{T_{i,2}}$ is given by

$${}_b M_{T_{i,2}} = ({}_b E_i) \cdot ({}_b I_{i,3}) \cdot \kappa_{T_{i,2}} .$$

The thermoelastic shear force gradient on the beam is

$$\frac{\partial^2}{\partial s_i^2} ({}_b M_{T_{i,2}}) = ({}_b E_i) \cdot ({}_b I_{i,3}) \cdot \frac{\partial^2}{\partial s_i^2} (\kappa_{T_{i,2}}) . \tag{1.21}$$

(c) Elastic Forces and the Equation of Motion

If ${}_b f_E$ is the elastic force gradient along the beam, then the equation of motion is given by

$${}_b \underline{f}_E - \frac{\partial^2}{\partial s_i^2} ({}_b M_{T_i}) = \frac{\partial}{\partial s_i} ({}_b \underline{F}_{\mu_i}) \cdot$$
$$\Delta s_i$$

The beams are assumed to be axially rigid, so

$${}_b f_{E,1} = 0,$$

$${}_b f_{E,2} = ({}_b E_i) \cdot ({}_b I_{i,3}) \cdot \frac{\partial^4}{\partial s_i^4} ({}_b q_{i,2}),$$

and

$${}_b f_{E,3} = ({}_b E_i) \cdot ({}_b I_{i,2}) \cdot \frac{\partial^4}{\partial s_i^4} ({}_b q_{i,3}) ,$$

so the final governing equations become

$$
\begin{bmatrix}
0 \\
({}_bE_i)\cdot({}_bI_{i,3})\left[\frac{\partial^4}{\partial s_i^4}({}_bq_{i,2}) + \kappa^*_{T_{i,2}}\left\{\frac{\partial^3}{\partial s_i^3}(1 - {}_b\tau_i\frac{\partial}{\partial t})({}_bq_{i,2})\right\}\sin\alpha_{i,2}\right] \\
({}_bE_i)\cdot({}_bI_{i,2})\left[\frac{\partial^4}{\partial s_i^4}({}_bq_{i,3}) + \kappa^*_{T_{i,3}}\left\{\frac{\partial^3}{\partial s_i^3}(1 - {}_b\tau_i\frac{\partial}{\partial t})({}_bq_{i,3})\right\}\sin\alpha_{i,3}\right]
\end{bmatrix}
$$

$$
+ {}_b\rho_i \cdot \left\{\left[\frac{d^2}{dt^2} + (\dot{\omega}^*_B + \omega^{**}_B)\right]({}_bq_i) + \mu^B_i[\ddot{\Theta X}_B + G_B\ddot{q}^*_B + 2\tilde{\omega}_B G_B\dot{q}^*_B + \right.
$$

$$
\left. + (\dot{\tilde{\omega}}_B + \tilde{\omega}_B\tilde{\omega}_B)G_Bq^*_B] + \dot{\omega}^*_B + \omega^{**}_B)\begin{Bmatrix} s_i + R_{i,1} \\ R_{i,2} \\ R_{i,3} \end{Bmatrix}\right\} = 0. \qquad (1.22)
$$

(d) Galerkin's Method

The solution is approached through Galerkin's method. The solution vector is assumed to be a finite sum of known space-dependent functions multiplied by unknown time-dependent functions. To keep the dimension of the reduced problem small, the solution is taken to be an exponential flexure term superposed on rigid body rotation and translation terms. Thus

$$
{}_b\underline{q}_i = \begin{Bmatrix} {}_bq_{i,1} \\ {}_bq_{i,2} \\ {}_bq_{i,3} \end{Bmatrix} = \begin{Bmatrix} {}_1q_{i,1}(t) \\ {}_1q_{i,2}(t)\cdot(e^{p_1 s}-1) + {}_2q_{i,2}(t)\cdot s + {}_3q_{i,2}(t) \\ {}_1q_{i,3}(t)\cdot(e^{p_1 s}-1) + {}_2q_{i,3}(t)\cdot s + {}_3q_{i,3}(t) \end{Bmatrix}, \qquad (1.3)
$$

When Eq. (1.3) is substituted into Eqs. (1.22), the left-hand side becomes

$$\begin{bmatrix} 0 \\ ({}_bE_i)\cdot({}_bI_{i,3})\cdot p_i^3\cdot e^{p_i s}[{}_1q_{i,2}\cdot p_i + \{\kappa^*_{T_{i,2}}\{({}_1q_{i,2}) - ({}_b\tau_i)({}_1\dot{q}_{i,2})\}\sin\alpha_{i,2}] \\ ({}_bE_i)({}_bI_{i,2})\cdot p_i^3\cdot e^{p_i s}[{}_1q_{i,3}\cdot p_i + \kappa^*_{T_{i,3}}\{({}_1q_{i,3}) - ({}_b\tau_i)({}_1\dot{q}_{i,3})\}\sin\alpha_{i,3}] \end{bmatrix} .$$

The resulting equations become free of the partial differential operators. Each equation is then multiplied by 1, $e^{p_i s}$ and s, successively, and integrated between $(0,\ell)$. This gives us nine equations in seven unknowns. We reject the two equations generated from the first row equation by $e^{p_i s}$ and 1. This leaves seven equations in seven unknowns for each beam. These equations also involve the other 103 unknowns in the vector $\underline{q}^*_B$. Another 103 equations will be generated from the other structural elements. The vector $\theta\ddot{\underline{X}}_B$ is expressed later as a function of $\underline{q}^*_B$.

If we form a (7×1) vector for each beam, given by

$$\{{}_b\underline{q}^*_i\} = [{}_1q_{i,1}, {}_1q_{i,2}, {}_2q_{i,2}, {}_3q_{i,2}, {}_1q_{i,3}, {}_2q_{i,3}, {}_3q_{i,3}]^T$$

then the generated equations for each beam will be of the form

$$[{}_bA_{i1}]\{{}_b\ddot{q}^*_i\} + [{}_bA_{i2}]\{{}_b\dot{q}^*_i\} + [{}_bA_{i3}]\{{}_bq^*_i\}$$

$$+ \lambda_1 G_B\ddot{q}^*_B + \lambda_2 G_B\dot{q}^*_B + \lambda_3 G_B q^*_B = \{{}_bA_{i4}\} , \qquad (1.23)$$

where $[{}_bA_{i1}]$ is a constant square matrix. Also, λ_1 is a constant. All other quantities are functions of $\underline{\omega}_B$ and $\dot{\underline{\omega}}_B$. The reduction of Eqs. (1.22) to Eqs. (1.23) in the cases of the four beams (Figure 1) is shown in Appendix 3.

The gravity gradient and other environmental torques are not considered to be acting on the beams. They are included in the equations for the

composite bodies as concentrated torques. The continuity conditions at the free ends will be used in the equations of motion of the tip-masses. The conditions for the shell-beam junctions will be obtained later.

3. Plates

(a) Load System

The load system on the plates is shown in Figures 1 and 4. As in the case of the beams, the general equations of motion for the plates under inertial and thermal loads will be derived first. These will be reduced to time-dependent, second-order, ordinary differential equations by using Galerkin's method. The continuity conditions at the junctions to the spring-mass-damper systems and to the rigid bodies will be used in the equations of motion of those systems. The conditions at the shell-plate connections will be defined later.

(b) Inertia Forces

To keep the governing equations linear in the space coordinates, the in-plane deformations are considered to be negligible. The lateral deformation of the i^{th} plate, χ_i, is parallel to the axis $\underline{b}_3$. This makes the introduction of a local coordinate frame unnecessary.

Let $\mathcal{L}_3$ be the matrix $\begin{bmatrix} 0 & 0 & 0 \\ 0 & 0 & 0 \\ 0 & 0 & 1 \end{bmatrix}$. Then the inertia force on a plate element is given by

$$
\begin{aligned}
{}_pF_i = - {}_p\rho_i [\mathcal{L}_3][\Theta \ddot{X}_B + G_B \ddot{q}_B^* + \ddot{\chi}_i + 2\tilde{\omega}_B (G_B \dot{q}_B^* + \dot{\chi}_i) \\
+ (\dot{\tilde{\omega}}_B + \tilde{\omega}_B \tilde{\omega}_B)(G_B q_B^* + \chi_i) + (\dot{\tilde{\omega}}_B + \tilde{\omega}_B \tilde{\omega}_B)(\underline{R}_{p-i})] dA \, ,
\end{aligned}
\tag{1.23}
$$

where ${}_pR_i$ is the position coordinate of the element of area dA in B-based coordinates. Equation (1.23) is only a scalar equation.

(c) Thermoelastic Forces

The distribution of the thermal bending moments over the surface of the plate is assumed to be first-order, time-dependent. This model is obtained in a way similar to that used in the beam. The plates are assumed to be thin and homogeneous, so that a linear temperature distribution across the thickness of the plate can be assumed. This assumption also makes the thermal bending moments and curvatures at any point on the plate in two orthogonal directions equal.

Let ${}_p\kappa_{i,1}$ and ${}_p\kappa_{i,2}$ be the thermal curvature of the plate parallel to the plane formed by axes $\underline{b}_1$ and $\underline{b}_2$. Also, let ${}_p\kappa_i = {}_p\kappa_{i,1} + {}_p\kappa_{i,2}$ be defined as the average curvature of the i^{th} plate. Then ${}_p\kappa_i$ is an invariant of the plate with respect to a rotation of coordinates in the plane of the plate. Now let ${}_p\kappa_{i,1}$ be given by

$$\frac{\partial\, {}_p\kappa_{i,1}}{\partial t} + \frac{{}_p\kappa_{i,1}}{{}_p\tau_i} = {}_pk_i \cos({}_p\beta_i + {}_p\beta^*_{i,1})$$

where

${}_p\beta_i$ = the angle between the plate nominal normal and the sun vector

${}_p\beta^*_{i,1}$ = the rotation of the plate surface normal, due to flexure, along $\underline{b}_1$.

The solution of this equation (see Appendix 2) is given by

$${}_p\kappa_{i,1} = ({}_pk_i \cdot {}_p\tau_i)[\cos {}_p\beta_i - ({}_p\dot{\beta}^*_{i,1} - {}_p\tau_i \cdot {}_p\ddot{\beta}^*_{i,1} + {}_p\tau_i^2 \cdot {}_p\dddot{\beta}^*_{i,1}$$

$$- {}_p\tau_i^3 \cdot {}_p\ddddot{\beta}^*_{i,1} + \ldots)\sin {}_p\beta_i].$$

Keeping only the first power of ${}_p\tau_i$, the solution takes the form

$$ {}_{p}\kappa_{i,1} = {}_{p}\kappa_{i,0}[\cos {}_{p}\beta_i - ({}_{p}\beta^{*}_{i,1} - {}_{p}\tau_i \cdot {}_{p}\dot{\beta}^{*}_{i,1})\sin {}_{p}\beta_i] \cdot \tag{1.24} $$

Similarly we have the solution along $\underline{b}_2$ as

$$ {}_{p}\kappa_{i,2} = {}_{p}\kappa_{i,0}[\cos {}_{p}\beta_i - ({}_{p}\beta^{*}_{i,2} - {}_{p}\tau_i \cdot {}_{p}\dot{\beta}^{*}_{i,2})\sin {}_{p}\beta_i] \tag{1.25} $$

where

${}_{p}\kappa_{i,0} = {}_{p}k_i \cdot {}_{p}\tau_i$ = the maximum value of ${}_{p}\kappa_{i,1}$

${}_{p}\kappa_{i,2}$ = a constant.

Let x_1 and x_2 be the distances in the directions $\underline{b}_1$ and $\underline{b}_2$. Then

$$ {}_{p}\beta^{*}_{i,1} = \frac{\partial \chi_i}{\partial x_1}, \quad {}_{p}\beta^{*}_{i,2} = \frac{\partial \chi_i}{\partial x_2} $$

and

$$ {}_{p}\kappa_i = ({}_{p}\kappa_{i,1} + {}_{p}\kappa_{i,2}) = [2\,{}_{p}\kappa_{i,0}\cos {}_{p}\beta_i - {}_{p}\kappa_{i,0}[(\frac{\partial \chi_i}{\partial x_1} + \frac{\partial \chi_i}{\partial x_2}) $$

$$ - {}_{p}\tau_i \frac{\partial}{\partial t}(\frac{\partial \chi_i}{\partial x_1} + \frac{\partial \chi_i}{\partial x_2})]\sin {}_{p}\beta_i] \cdot \tag{1.26} $$

If ${}_{p}M_{T_{i,1}}$ and ${}_{p}M_{T_{i,2}}$ are the bending moments along the $\underline{b}_1$ and $\underline{b}_2$ axes, respectively, then

$$ {}_{p}M_{T_{i,1}} = {}_{p}D_i[{}_{p}\kappa_{i,1} + {}_{p}\mu_i \cdot {}_{p}\kappa_{i,2}] $$

and

$$ {}_{p}M_{T_{i,2}} = {}_{p}D_i[{}_{p}\kappa_{i,2} + {}_{p}\mu_i \cdot {}_{p}\kappa_{i,1}] \cdot $$

It is assumed that the thermal twisting moments in the plate are absent. Thus the equation of motion is obtained as

$$ \frac{\partial^2}{\partial x_1^2}({}_{p}M_{i,1} + {}_{p}M_{T_{i,1}}) + \frac{\partial^2}{\partial x_2^2}({}_{p}M_{i,2} + {}_{p}M_{T_{i,2}}) - 2\frac{\partial^2}{\partial x_1 \partial x_2}({}_{p}M_{i,2}) = -q $$

where q is the plate loading, ${}_{p}M_{i,1}$, ${}_{p}M_{i,2}$ and ${}_{p}M_{i,12}$ are the usual elastic bending and twisting moments of the plate. The above equation can be written as

$$- {}_pD_i \cdot \nabla_i^4 \chi_i + {}_pD_i(1 + {}_p\mu_i)\nabla_i^2({}_p\kappa_{i,1} + {}_p\kappa_{i,2}) = -q , \tag{1.27}$$

where

$$\nabla_i^2 = \left(\frac{\partial^2}{\partial x_1^2} + \frac{\partial^2}{\partial x_2^2}\right),$$

and ${}_pD_i$ and ${}_p\mu_i$ are the stiffness and Poisson's ratio of the plate, respectively. So from (1.23), (1.26) and (1.27), we obtain

$$\begin{aligned} &{}_pD_i[\nabla_i^4 \chi_i + (1 + {}_p\mu_i)\cdot {}_p\kappa_{i,0}\{(\frac{\partial}{\partial x_1} + \frac{\partial}{\partial x_2})\nabla_i^2 \chi_i \\ &- {}_p\tau_i \cdot \frac{\partial}{\partial t}(\frac{\partial}{\partial x_1} + \frac{\partial}{\partial x_2})\nabla_i^2 \chi_i\}\sin {}_p\beta_i] \\ &+ {}_p\rho_i[\vartheta_3][\ddot{\Theta X}_B + G_B\ddot{q}_B^* + \ddot{\chi}_i + 2\tilde{\omega}_B(G_B\dot{q}_B^* + \dot{\chi}_i) \\ &+ (\dot{\tilde{\omega}}_B + \tilde{\omega}_B\tilde{\omega}_B)(G_B q_B^* + \chi_i + {}_pR_i) = 0. \end{aligned} \tag{1.28}$$

In Eq. (1.28), $\ddot{\Theta X}_B$ is the inertial acceleration of the body B in B-based coordinates. As was done in the case of beams, $\ddot{\Theta X}_B$ is replaced by $F_{BC}/\|M\|_B$ as

$$\ddot{\Theta X}_B = \frac{1}{\|M\|_B} F_{BC} \tag{1.29}$$

where F_{BC} is the contact force between the bodies B and C. F_{BC} is expressed in turn as

$$\underline{F}_{BC} = (\frac{1}{\gamma}\tau_1 - \tau_2)G_B q_B^* - \tau_3\underline{\theta} + (\frac{1}{\gamma}\tau_7 - \tau_8)G_B\dot{q}_B^* - \tau_9\underline{\dot{\theta}} . \tag{1.29}$$

Equation (1.29) will be explained in detail later.

(d) Galerkin's Functions for Plate Nos. 1 and 4

Before applying Galerkin's method to Eq. (1.28), it is first transformed into plane polar coordinates. Let

$$x_1 = r_1 \cos\theta \quad \text{and} \quad x_2 = r_1 \sin\theta$$

where $0 \leq r_1 \leq a_B$.

Now, with

$$\nabla_1^2 \equiv \frac{\partial^2}{\partial r_1^2} + \frac{1}{r_1}\frac{\partial}{\partial r_1} + \frac{1}{r_1^2}\frac{\partial^2}{\partial \theta^2}$$

$$\frac{\partial}{\partial x_1} = \cos\theta \cdot \frac{\partial}{\partial r_1} - \frac{1}{r_1}\sin\theta \cdot \frac{\partial}{\partial \theta}$$

$$\frac{\partial}{\partial x_2} = \cos\theta \frac{\partial}{\partial r_1} - \frac{1}{r_1}\sin\theta \cdot \frac{\partial}{\partial \theta}$$

we have

$$\frac{\partial}{\partial x_1} + \frac{\partial}{\partial x_2} = (\sin\theta + \cos\theta)\left(\frac{\partial}{\partial r_1} + \frac{1}{r_1}\frac{\partial}{\partial \theta}\right) .$$

So the left-hand side of Eq. (1.28) is transformed into

$$ {}_pD_i[\nabla_i^4 \chi_i + \{(1 + {}_p\mu_i)\cdot {}_pK_{i,0} \sin {}_p\beta_i\}(\sin\theta + \cos\theta)\left(\frac{\partial}{\partial r_1} + \frac{1}{r_1}\frac{\partial}{\partial \theta}\right)\nabla_1^2 \chi_1$$

$$- \{(1 + {}_p\mu_i)\cdot {}_pK_{i,0} \cdot {}_p\tau_i \sin {}_p\beta_i\}(\sin\theta + \cos\theta)\left(\frac{\partial}{\partial r_1} + \frac{1}{r_1}\frac{\partial}{\partial \theta}\right)\nabla_i^2 \dot{\chi}_1] \cdot \qquad (1.30)$$

Now let $a_B r = r_1$, so that $0 \leq r \leq 1$, and $0 \leq \theta \leq 2\pi$. Then $\nabla_i^2 = \frac{1}{a_B^2}\nabla^2$

where $$\nabla^2 = \frac{\partial^2}{\partial r^2} + \frac{1}{r}\frac{\partial}{\partial r} + \frac{1}{r^2}\frac{\partial^2}{\partial \theta^2} .$$

Expression (1.30) becomes

$$ {}_pD_i[\frac{1}{a_B^4}\nabla^4 \chi_i + \{\frac{1}{a_B^3}(1 + {}_p\mu_i)_pK_{i,0} \sin {}_p\beta_i\}(\sin\theta + \cos\theta)\left(\frac{\partial}{\partial r} + \frac{1}{r}\frac{\partial}{\partial \theta}\right)\nabla^2 \dot{\chi}_1$$

$$- \{\frac{1}{a_B^3}(1 + {}_p\mu_i)\cdot {}_pK_{i,0} \cdot {}_p\tau_i \sin {}_p\beta_i\}(\sin\theta + \cos\theta)\left(\frac{\partial}{\partial r} + \frac{1}{r}\frac{\partial}{\partial \theta}\right)\nabla^2 \dot{\chi}_1] \cdot$$

Since $\underline{\chi}_i$ is a vector $[0, 0, \chi_i]^T$, $\mathscr{I}_3\tilde{\omega}_B\dot{\underline{\chi}}_i = 0 = \mathscr{I}_3\dot{\tilde{\omega}}_B\chi_i$. Also $\mathscr{I}_3\tilde{\omega}_B\tilde{\omega}_B\chi_i = -(\omega_{B,1}^2 + \omega_{B,2}^2)\chi_i$. Let $\underline{R}_{pi}$ be the vector $[a_B r\cos\theta, a_B r\sin\theta, R_i]^T$. Then

$$\mathscr{I}_3(\dot{\tilde{\omega}}_B + \tilde{\omega}_B\tilde{\omega}_B)\underline{R}_{pi} = (\omega_{B,1}\omega_{B,3} - \dot{\omega}_{B,2})a_B r\cos\theta + (\omega_{B,2}\omega_{B,3} + \dot{\omega}_{B,1})a_B r\sin\theta - (\omega_{B,1}^2 + \omega_{B,2}^2)R_i .$$

So the right-hand side of Eq. (1.28) becomes

$$-{}_p\rho_i[\ddot{\chi}_i - (\omega_{B,1}^2 + \omega_{B,2}^2)\chi_i + (\omega_{B,1}\omega_{B,3} - \dot{\omega}_{B,2})a_B r\cos\theta + (\omega_{B,2}\omega_{B,3} + \dot{\omega}_{B,1})a_B r\sin\theta - (\omega_{B,1}^2 + \omega_{B,2}^2)R_i]$$
$$+ {}_p\rho_i[\mathscr{I}_3][G_B\ddot{q}_B^* + \{2\tilde{\omega}_B + \frac{1}{\|M\|_B}(\frac{1}{\gamma}\tau_1 - \tau_2)\}G_B\dot{q}_B^*$$
$$+ \{\dot{\tilde{\omega}}_B + \tilde{\omega}_B\tilde{\omega}_B + \frac{1}{\|M\|_B}(\frac{1}{\gamma}\tau_7 - \tau_8)\}G_B q_B^* - \frac{1}{\|M\|_B}(\tau_9\dot{\theta} + \tau_3\theta)] \qquad (1.32)$$

Equating the expressions (1.31) and (1.32), the equation for the plates is obtained as

$${}_pD_i\left[\frac{1}{a_B^4}\nabla^4\chi_i + \left\{\frac{1}{a_B^3}(1 + {}_p\mu_i){}_p\kappa_{i,0}\sin{}_p\beta_i\right\}(\sin\theta + \cos\theta)(\frac{\partial}{\partial r} + \frac{1}{r}\frac{\partial}{\partial\theta})\nabla^2\chi_i\right.$$
$$\left. - {}_p\tau_i\left\{\frac{1}{a_B^3}(1 + {}_p\mu_i){}_p\kappa_{i,0}\sin{}_p\beta_i\right\}(\sin\theta + \cos\theta)(\frac{\partial}{\partial r} + \frac{1}{r}\frac{\partial}{\partial\theta})\nabla^2\dot{\chi}_i\right]$$
$$+ {}_p\rho_i[\ddot{\chi}_i - (\omega_{B,1}^2 + \omega_{B,2}^2)\chi_i + (\omega_{B,1}\omega_{B,3} - \dot{\omega}_{B,2})a_B r\cos\theta + (\omega_{B,2}\omega_{B,3} + \dot{\omega}_{B,1})a_B r\sin\theta - (\omega_{B,1}^2 + \omega_{B,2}^2)R_i]$$
$$+ {}_p\rho_i[\mathscr{I}_3][G_B\ddot{q}_B^* + \{2\tilde{\omega}_B + \frac{1}{\|M\|_B}(\frac{1}{\gamma}\tau_1 - \tau_2)\}G_B\dot{q}_B^* + \qquad (1.33)$$

$$+ \{\tilde{\omega}_B + \tilde{\omega}_B\tilde{\omega}_B + \frac{1}{\|M\|_B}(\frac{1}{r}\tau_1 - \tau_2)\}G_B q_B^* - \frac{1}{\|M\|_B}(\tau_9\dot{\theta} + \tau_3\theta)] = 0.$$

Now the choice of the Galerkin's functions must be made so that the solution matches the load system and satisfies the boundary conditions. As there are four spring-mass-damper systems and a central junction on the plates (numbers 1 and 4), the solution should contain five terms which are singular at the connecting points. This has to be done because the loads are taken to be concentrated forces. We also apply the boundary condition that the space-dependent solutions be zero on the boundary $r = 1$ of the plates. It is also assumed that the nature of the solution is close to the free vibration mode for thin plates. Therefore the solution is taken to be

$$\begin{aligned}\chi_i = {} & \chi_{i,1}(t) + \chi_{i,2}(r,t) + \chi_{i,3}(r,t)\cos\theta + \chi_{i,4}(r,t)\sin\theta \\ & + \chi_{i,5}(r,t)\cos 2\theta + \chi_{i,6}(r,t)\sin 2\theta + \chi_{i,7}(t)\, r^2\log r \\ & + \chi_{i,8}(t)\psi_{i,8}(r,\theta) + \chi_{i,9}(t)\psi_{i,9}(r,\theta) + \chi_{i,10}(t)\psi_{i,10}(r,\theta) \\ & + \chi_{i,11}(t)\psi_{i,11}(r,\theta)\,. \end{aligned} \tag{1.34}$$

The functions $\psi_{i,j}(r,\theta)$ are basically the static point load solutions for plates.

$\chi_{i,2}$, $\chi_{i,3}$, $\chi_{i,4}$, $\chi_{i,5}$ and $\chi_{i,6}$ are chosen in the following way:

$$\left.\begin{aligned}\chi_{i,5}(r,t) &= a_{i,1}J_2(\lambda_2 r) + a_{i,2}(r-1)r^2 + a_{i,3}(r-1)r^3 \\ \chi_{i,6}(r,t) &= a_{i,4}J_2(\lambda_2 r) + a_{i,5}(r-1)r^2 + a_{i,6}(r-1)r^3 \\ \chi_{i,3}(r,t) &= a_{i,7}J_1(\lambda_1 r) + a_{i,8}(r-1)r + a_{i,9}(r-1)r^2 \\ \chi_{i,4}(r,t) &= a_{i,10}J_1(\lambda_1 r) + a_{i,11}(r-1)r + a_{i,12}(r-1)r^2\end{aligned}\right\} \tag{1.35}$$

$$\chi_{i,2}(r,t) = a_{i,13}J_0(\lambda_0 r) + a_{i,14}(r-1)r^2 + a_{i,15}(r-1)r^3 \Big] .$$

Here $J_0(x)$, $J_1(x)$ and $J_2(x)$ are the ordinary Bessel functions. λ_0, λ_1 and λ_2 are the first zero of $J_0(x)$, and the second zeros of $J_1(x)$ and $J_2(x)$, respectively. Apart from a quadratic term in r, the coefficient of $\chi_{i,7}(t)$ is the solution to the problem of a plate with a steady concentrated force at the center.

(e) Coefficient of $\chi_{i,8}(t)$

The functional form of $\psi_{i,j}(r,\theta)$, which have coefficients $\chi_{i,j}$, $j = 8\text{-}11$, are similar. The expression for $\psi_{i,8}$ is derived here. The forms of $\psi_{i,9}$, $\psi_{i,10}$ and $\psi_{i,11}$ can be obtained in a similar manner.

Let $\psi_{i,8}$ be the mode corresponding to the spring-mass-damper system containing m_{13}. Let $z = r\exp(i\theta)$ represent the points in a complex plane. Let $\alpha_8 = (\alpha_{8,1} + i\alpha_{8,2})$ be the coordinate of the load point on the plate number 1, corresponding to m_{13}. The plate geometry is the unit circle $r = 1$. Let the function $w = w(z)$ map this unit circle onto another unit circle $w = 1$ and the point $z = \alpha$ to $w = 0$. This mapping is given by

$$w = \frac{z - \alpha_8}{1 - \bar{\alpha}_8 z} \tag{1.36}$$

when $\bar{\alpha}_8 = (\alpha_{8,1} - i\alpha_{8,2})$ = the complex conjugate of α. Then the solution to the problem of a circular plate with a concentrated load at $z = \alpha$ in the z-plane corresponds to the problem of a circular plate with a concentrated load at its center in the w-plane. The problem then reduces to choosing a biharmonic function $\psi_{i,8}(w)$ which i) will be zero at $w = 1$, ii) will have a logarithmic singularity at $w = 0$, iii) will not be harmonic, iv) will tend to $r^2 \log r$ as $\alpha_8 \to 0$, and v) will be real valued. It can be noted here that

$$\nabla^2 \equiv 4 \cdot \frac{\partial^2}{\partial z \partial \bar{z}} \quad \text{and} \quad \nabla^4 \equiv 16 \frac{\partial^4}{\partial z^2 \partial \bar{z}^2} \cdot$$

This leads us to choose the required function from the list of functions ψ_i^* given below.

$$\psi_1^* = (z-\alpha_8)(\bar{z}-\bar{\alpha}_8)\log(w\bar{w})$$

$$\psi_2^* = (z-\alpha_8)\bar{w} \log \bar{w} + (\bar{z}-\bar{\alpha}_8)w \log w$$

$$\psi_3^* = \mathrm{Re}[(z-\alpha_8)(\bar{z}-\bar{\alpha}_8)\log w]$$

$$\psi_4^* = \mathrm{Re}[(z-\alpha_8)(\bar{z}-\bar{\alpha}_8)\log \bar{w}]$$

$$\psi_5^* = \mathrm{Re}[(z-\alpha_8)\bar{w} \log \bar{w}]$$

$$\psi_6^* = \mathrm{Re}[(\bar{z}-\bar{\alpha}_8)w \log w]$$

where

$$\bar{w} = \frac{\bar{z} - \bar{\alpha}_8}{1 - \alpha_8 \bar{z}} \cdot$$

It can be shown (Appendix 4) that ψ_1^* is the most suitable choice. Thus

$$\psi_{i,8}(r,\theta) = (z-\alpha_8)(\bar{z}-\bar{\alpha}_8)\log(w\bar{w}) \cdot \tag{1.37}$$

Let $\mathrm{Im}[\alpha_8] = 0$. Then $\alpha_8 = \bar{\alpha}_8 =$ a real number. Therefore

$$\psi_{i,8} = (z-\alpha_8)(\bar{z}-\alpha_8)\log\left[\frac{z-\alpha_8}{1-\alpha_8 z} \cdot \frac{\bar{z}-\alpha_8}{1-\alpha_8 \bar{z}}\right] \quad \text{or}$$

$$\psi_{i,8} = (r^2 - 2\alpha_8 r \cos\theta + \alpha_8^2)\log\left(\frac{r^2-2\alpha_8 r \cos\theta + \alpha_8^2}{1-2\alpha_8 r \cos\theta + \alpha_8^2 r^2}\right) \tag{1.38}$$

(f) Final Equations for Plates 1 and 4

Equations (1.34), (1.35) and (1.38) are substituted into Eq. (1.33). The resulting equation is then successively multiplied by the 21 spatial functions introduced in Eqs. (1.34), (1.35) and (1.38), and then integrated

between the limits of $0 \leq \theta \leq 2\pi$, $0 \leq r \leq 1$. This leads to a set of 21 second-order ordinary differential equations of the form

$$[{}_pA_{i1}]\{{}_p\ddot{q}_i^*\} + [{}_pA_{i2}]\{{}_p\dot{q}_i^*\} + [{}_pA_{i3}]\{{}_pq_i^*\}$$

$$+ \lambda_4 G_B \ddot{q}_B^* + \lambda_5 G_B \dot{q}_B^* + \lambda_6 G_B q_B^* = \{{}_pA_{i4}\} \quad . \tag{1.39}$$

In this equation, $\{{}_pq_i^*\}$ is a (21×1) vector consisting of the unknown time-dependent plate functions. The detailed form of Eq. (1.39) is shown in Appendix 5.

The plates 1 and 4 have similar equations with the same number of unknown time-dependent functions $\{{}_pq_i^*\}$.

(g) Equations for Plates 2 and 3

The basic equation for the plates 2 and 3 are also given by Eq. (1.33), but the load conditions are different because there are two rigid bodies attached to each of these plates along with the spring-mass-damper systems. While the central load is absent in these plates, each rigid body is assumed to be fixed at four points of the plates, so four concentrated load functions for each rigid body are added to the assumed plate displacements. The form of these functions is similar to that of $\psi_{i,8}$. Therefore the solution to the plates 2 and 3 is taken to be

$$\chi_i = \chi_{i,1}(t) + \chi_{i,2}(r,t) + \chi_{i,3}(r,t)\cos\theta + \chi_{i,4}(r,t)\sin\theta$$

$$+ \chi_{i,5}(r,t)\cos 2\theta + \chi_{i,6}(r,t)\sin 2\theta + \sum_{j=1}^{12} \chi_{i,6+j}(t)\psi_{i,6+j}(r,\theta) \quad . \tag{1.40}$$

The functions $\chi_{i,j}$, $j = 2 - 6$, are given by Eq. (1.35), and the functions $\psi_{i,j}$, $j = 7 - 18$, are given by Eq. (1.38) where α_8 is replaced by the

corresponding coordinates of the load points.

The final equations for the plates 2 and 3 are also similar to Eq. (1.39), but in these cases the generalized coordinates $\{{}_{p}q_{i}^{*}\}$ is a (28 × 1) vector. The detailed form of these equations is given in Appendix 6.

4. Shells

The analysis for the shells A and B are similar. Only the procedure for the shell B is given here.

The shell B is assumed to be a uniform, thin, isotropic, circular cylindrical shell. For the elastic analysis, the linear equations of Vlasov [36] are used. The analysis of the thermal effects follows that made by Kraus [37]. The orientation of the coordinate axes is shown in Figure 5.

(a) Inertia Forces

Let $\underset{s}{\underline{F}}_{B} = [{}_{s}F_{B,1}, {}_{s}F_{B,2}, {}_{s}F_{B,3}]^{T}$ be the inertia force vector on a shell element in the B-based rectangular coordinates.

Let $\underset{s}{\underline{F}}^{r}_{B} = [{}_{s}F_{B,r}, {}_{s}F_{B,\theta}, {}_{s}F_{B,z}]$ be the inertia force vector on the shell element of area dA, in the B-based cylindrical coordinates.

Proceeding as in the case of beams and plates, we have

$$\underset{s}{\underline{F}}_{B} = -dm[\ddot{\Theta}\underline{X}_{B} + \ddot{\underline{C}}_{B} + \ddot{\underline{\xi}}_{B} + 2\tilde{\omega}_{B}(\dot{\underline{C}}_{B} + \dot{\underline{\xi}}_{B}) + (\dot{\tilde{\omega}}_{B} + \tilde{\omega}_{B}\tilde{\omega}_{B})(\underline{C}_{B} + \underline{R}_{B} + \underline{\xi}_{B})] \tag{1.41}$$

where

$\underline{R}_{B}$ = position vector of the undeformed shell element in B-based coordinates,

$\underline{\xi}_{B} = [\xi_{B,1}, \xi_{B,2}, \xi_{B,3}]^{T}$ = displacement vector of the shell element in rectangular B-based coordinates, and

$d_{m} = {}_{s}\rho_{B} \cdot dA$.

Let $\underline{\xi}_B^r = [\xi_{B,r}, \xi_{B,\theta}, \xi_{B,z}]^T$ be the displacement vector of the shell element in B-based cylindrical coordinates, and

$$[\mu_B^r] = \begin{bmatrix} \cos\theta & \sin\theta & 0 \\ -\sin\theta & \cos\theta & 0 \\ 0 & 0 & 1 \end{bmatrix} .$$

Then

$$\{\xi_B^r\} = [\mu_B^r]\{\xi_B\}$$

and

$$\{{}_sF_B^r\} = [\mu_B^r]\{{}_sF_B\}.$$

Let

$$[\mu_B^r]\tilde{\omega}_B[\mu_B^r]^T = \omega_{B,r}^*$$

and

$$[\mu_B^r]\tilde{\omega}_B\tilde{\omega}_B[\mu_B^r]^T = \omega_{B,r}^{**} .$$

Then

$$\{{}_sF_B^r\} = -dm[\mu_B^r\ddot{\Theta X}_B + \mu_B^r\ddot{C}_B + \ddot{\xi}_B^r + 2\mu_B^r\tilde{\omega}_B\dot{C}_B + 2\mu_B^r\tilde{\omega}_B(\mu_B^r)^T\dot{\xi}_B^r$$

$$+ \mu_B^r(\tilde{\dot{\omega}}_B + \tilde{\omega}_B\tilde{\omega}_B)(C_B+R_B) + \mu_B^r(\tilde{\dot{\omega}}_B+\tilde{\omega}_B\tilde{\omega}_B)(\mu_B^r)^T\xi_B^r]$$

$$= -dm\{\ddot{\xi}_B^r + 2\omega_{B,r}^*\dot{\xi}_B^r + (\dot{\omega}_{B,r}^* + \omega_{B,r}^{**})\xi_B^r$$

$$+ [\mu_B^r\ddot{\Theta X}_B + \ddot{C}_B + 2\omega_B\dot{C}_B + (\tilde{\dot{\omega}}_B + \tilde{\omega}_B\tilde{\omega}_B)(C_B + R_B)] . \qquad (1.42)$$

In this analysis, it is assumed that

$$\xi_{B,\theta} = \xi_{B,z} = 0 .$$

So

$$\omega_{B,r}^*\xi_B^r = \begin{Bmatrix} 0 \\ \omega_{B,3} \\ (\omega_{B,1}\sin\theta - \omega_{B,2}\cos\theta \end{Bmatrix} \xi_{B,r}$$

and

$$\overset{**}{\omega}_{B,r}{}^{\xi}{}_{B}^{r} = \begin{Bmatrix} -\omega_{B,3}^2 - (\omega_{B,1}\sin\theta - \omega_{B,2}\cos\theta)^2 \\ -(\omega_{B,2}\sin\theta + \omega_{B,1}\cos\theta)(\omega_{B,1}\sin\theta - \omega_{B,2}\cos\theta) \\ \omega_{B,3}(\omega_{B,2}\sin\theta + \omega_{B,1}\cos\theta) \end{Bmatrix} \xi_{B,r} \quad .$$

With

$$\{R_B\} = [a_B\cos\theta,\ a_B\sin\theta,\ z]^T$$

we have

$$[\mathscr{A}_1][\mu_B^r](\dot{\tilde{\omega}}_B + \tilde{\omega}_B\tilde{\omega}_B)\{R_B\} = \{z(\dot{\omega}_{B,2}\cos\theta - \dot{\omega}_{B,1}\sin\theta) - a_B(\omega_{B,1}\sin\theta - \omega_{B,2}\cos\theta)^2 - a_B\omega_{B,3}^2\},$$

where

$$[\mathscr{A}_1] = \begin{bmatrix} 1 & 0 & 0 \\ 0 & 0 & 0 \\ 0 & 0 & 0 \end{bmatrix} \quad .$$

Let $\{\ddot{\theta X}_B + \ddot{C}_B + 2\dot{\tilde{\omega}}_B\dot{}_B + (\dot{\tilde{\omega}}_B + \tilde{\omega}_B\tilde{\omega}_B)C_B\} = [f_1,\ f_2,\ f_3]^T$. Then, using the results obtained above, ${}_sF_{B,r}$ is given by

$$\begin{aligned} {}_sF_{B,r} = [\mathscr{A}_1]\{{}_sF_B^r\} = -dm\{&\ddot{\xi}_{B,r} - [\omega_{B,3}^2 + (\omega_{B,1}\sin\theta - \omega_{B,2}\cos\theta)^2]\xi_{B,r} \\ &+ z(\dot{\omega}_{B,2}\cos\theta - \dot{\omega}_{B,1}\sin\theta) - a_B(\omega_{B,1}\sin\theta - \omega_{B,2}\cos\theta)^2 - a_B\omega_{B,3}^2 \\ &+ \cos\theta\cdot f_1 + \sin\theta\cdot f_2\} \quad . \end{aligned} \tag{1.43}$$

(b) Thermoelastic Forces

The distribution of the thermal bending moments over the surface of the shell is obtained in the way used for plates. The shell is assumed to be thin, homogeneous and isotropic, so a linear temperature distribution across the thickness of the shell can be assumed. This assumption also

makes the thermal bending moments and curvatures at any point on the shell in two orthogonal directions equal.

Let ${}_s\kappa_{B,\theta}$ and ${}_s\kappa_{B,z}$ be the thermal curvatures of the shell in the tangential and axial directions. Then

$$\frac{\partial\, {}_s\kappa_{B,\theta}}{\partial t} + \frac{{}_s\kappa_{B,\theta}}{{}_s\tau_B} = {}_s k_B({}_s\beta_B + {}_s\beta^*_{B,\theta}) \tag{1.44}$$

where

${}_s\beta_B$ = the angle between the shell nominal normal and the sun vector at any point,

${}_s\beta^*_{B,\theta}$ = the rotation of the shell surface normal due to flexure in the tangential direction.

As shown before, keeping only the first power of ${}_s\tau_B$, the solution to Eq. (1.44) takes the form

$${}_s\kappa_{B,\theta} = {}_s\kappa_{B,0}[\cos {}_s\beta_B - ({}_s\beta^*_{B,\theta} - {}_s\tau_B \cdot {}_s\dot{\beta}^*_{B,\theta})\sin {}_s\beta_B] \,. \tag{1.45}$$

Similarly

$${}_s\kappa_{B,z} = {}_s\kappa_{B,0}[\cos {}_s\beta_B - ({}_s\beta^*_{B,z} - {}_s\tau_B \cdot {}_s\dot{\beta}^*_{B,z})\sin {}_s\beta_B] \tag{1.46}$$

where

${}_s\beta^*_{B,z}$ = the rotation of the shell surface normal due to flexure in the axial direction.

Now from Eq. (2.27) of Kraus [37],

2. $${}_sM_{T_B} = {}_sD_B\,(1 - {}_s\mu_B^2)({}_s\kappa_{B,\theta} + {}_s\kappa_{B,z})$$

or

$${}_sM_{T_B} = \frac{1}{24} \cdot {}_sE_B \cdot ({}_sh_B)^3({}_s\kappa_{B,\theta} + {}_s\kappa_{B,z}) \,. \tag{1.47}$$

Let $\zeta = \pm \frac{1}{2}({}_sh_B)$ be defined as the cylindrical surfaces of the shell. It is assumed that the temperature distribution across the thickness of the

shell be given by $T_B(\theta,z,\zeta)$. Then, combining Eqs. (2.28) and (5.6) of Kraus [37], we have

$$ {}_sM_{T_B} = {}_sE_B \cdot {}_s\alpha_B \int_\zeta T_B(\theta,z,\zeta)\zeta d\zeta \cdot $$

Let ${}_sT_{B1}$ be defined such that

$$ {}_sM_{T_B} = \frac{1}{12} \cdot {}_sE_B \cdot {}_s\alpha_B \cdot {}_sh_B^3 \cdot {}_sT_{B1} \cdot \tag{1.48} $$

From Eqs. (1.47) and (1.48), we obtain

$$ {}_sT_{B1} = \frac{1}{2({}_s\alpha_B)} ({}_s\kappa_{B,\theta} + {}_s\kappa_{B,z}) \cdot \tag{1.49} $$

This result will be used to derive the equation of motion of the shell.

(c) Equation of Motion

Let

$$ a_B z_1 = z $$

where z is the distance along the $\underline{b}$-axis. We also define

$$ \nabla^2 = \frac{\partial^2}{\partial z_1^2} + \frac{\partial^2}{\partial \theta^2} \cdot $$

The equation for the radial displacement of the shell, obtained by combining Eq. (13.2), Part 2, of Vlasov [36] and Eqs. (6.11d) and (6.13c) of Kraus [37], is given by

$$ \frac{{}_sh_B^2}{12a_B^2}(\nabla^4 + 2\nabla^2 + 1)\nabla^4\xi_{B,r} - \frac{{}_sh_B^2}{6a_B^2}(1-{}_s\mu_B)\left(\frac{\partial^4}{\partial z_1^4} - \frac{\partial^4}{\partial z_1^2\partial\theta^2}\right)\nabla^2\xi_{B,r} $$

$$ + (1 - {}_s\mu_B^2)\frac{\partial^4}{\partial z_1^4}\xi_{B,r} = -\frac{a_B^2(1-{}_s\mu_B^2)}{{}_sE_B \cdot {}_sh_B}\nabla^4 q - \frac{(1+{}_s\mu_B)\,{}_s\alpha_B}{12} \cdot {}_sh_B^2 \cdot \nabla^6 \cdot {}_sT_{B1} \tag{1.50} $$

where q is the shell radial loading. In this analysis, q consists of only inertia loading given by

$$- qdA = {}_sF_{B,r} \cdot \tag{1.51}$$

Therefore from Eqs. (1.51) and (1.43), we have

$$\nabla^4 q = {}_s\rho_B\Big\{\nabla^4\ddot{\xi}_{B,r} - [\omega_{B,3}^2 + \tfrac{1}{2}(\omega_{B,1}^2 + \omega_{B,2}^2)]\nabla^4\xi_{B,r}$$

$$+ \tfrac{1}{2}[(\omega_{B,1}^2 - \omega_{B,2}^2)\cos 2\theta + 2\omega_{B,1}\omega_{B,2}\sin 2\theta][\nabla^4\xi_{B,r} - 8\nabla^2\xi_{B,r}$$

$$- 16(\frac{\partial^2\xi_{B,r}}{\partial\theta^2} + \xi_{B,r})] - 4[(\omega_{B,1}^2 - \omega_{B,2}^2)\sin 2\theta - 2\omega_{B,1}\omega_{B,2}\cos 2\theta] \cdot$$

$$\cdot[\frac{\partial}{\partial\theta}\nabla^2\xi_{B,r} - 4\frac{\partial}{\partial\theta}\xi_{B,r}] + f_1\cos\theta + f_2\sin\theta\Big\} . \tag{1.52}$$

Now, from Figure 6, it is seen that

$$\cos {}_s\beta_B = \sin\beta\cos(\omega_{B,3}t + \theta + \alpha) \tag{1.53}$$

where α is the angle between the plane containing $\underline{b}_1$ and $\underline{b}_3$ and the plane containing $\underline{b}_3$ and the sun vector, at $t = 0$. For simplicity, α is taken to be zero.

Then, from Eq. (1.46) and Eq. (1.53), we have

$$\nabla^6({}_s\kappa_{B,z}) = - {}_s\kappa_{B,0}\sin\beta\cos(\omega_{B,3}t + \theta)$$

$$- {}_s\kappa_{B,0}\nabla^6({}_s\beta^*_{B,z} - {}_s\tau_B \cdot {}_s\dot{\beta}^*_{B,z})\sin {}_s\beta_B\}$$

$$- {}_s\kappa_{B,0}[\sin\beta\cos(\omega_{B,3}t + \theta) + \sin {}_s\beta_B\nabla^6({}_s\beta^*_{B,z} - {}_s\tau_B \dagger {}_s\dot{\beta}^*_{B,z})].$$

Similarly

$$\nabla^6({}_s\kappa_{B,\theta}) \quad - {}_s\kappa_{B,0}[\sin\beta\cos(\omega_{B,3}t + \theta) + \sin {}_s\beta_B\nabla^6({}_s\beta^*_{B,\theta} - {}_s\tau_B \cdot {}_s\dot{\beta}^*_{B,\theta})].$$

Hence, from Eq. (1.49), we obtain

$$\nabla^6({}_sT_{B,1}) = -\frac{{}_sK_{B,0}}{{}_s\alpha_B}\left[\sin\beta\cos(\omega_{B,3}t+\theta)+\frac{1}{2}\sin{}_s\beta_B\left(1-{}_s\tau_B\frac{\partial}{\partial t}\right)\right.$$

$$\left.\cdot\frac{1}{a_B}\left(\frac{\partial}{\partial z_1}+\frac{\partial}{\partial\theta}\right)\nabla^6\xi_{B,r}\right]$$

$$\cong \frac{{}_sK_{B,0}}{{}_s\alpha_B}\sin\beta\left[\cos(\omega_{B,3}t+\theta)+\frac{1}{2a_B}\sin(\omega_{B,3}t+\theta)\left(1-{}_s\tau_B\cdot\frac{\partial}{\partial t}\right)\right.$$

$$\left.\cdot\left(\frac{\partial}{\partial z_1}+\frac{\partial}{\partial\theta}\right)\nabla^6\xi_{B,r}\right] \quad . \tag{1.54}$$

Now substituting Eqs. (1.52) and (1.54) in Eq. (1.50), we obtain the equation of motion of the shell as

$$\frac{{}_sh_B^2}{12a_B^2}(\nabla^4+2\nabla^2+1)\nabla^4\xi_{B,r}-\frac{{}_sh_B^2}{6a_B^2}(1-{}_s\mu_B)\left(\frac{\partial^4}{\partial z_1^4}-\frac{\partial^4}{\partial z_1^2\partial\theta^2}\right)\nabla^2\xi_{B,r}$$

$$+(1-{}_s\mu_B^2)\frac{\partial^4}{\partial z_1^4}\xi_{B,r}+\frac{a_B^2(1-{}_s\mu_B^2){}_s\rho_B}{{}_sE_B\cdot{}_sh_B}\left\{\nabla^4\ddot{\xi}_{B,r}\right.$$

$$-\left[\omega_{B,3}^2+\frac{1}{2}(\omega_{B,1}^2+\omega_{B,2}^2)\right]\nabla^4\xi_{B,r}+\frac{1}{2}\left[(\omega_{B,1}^2-\omega_{B,2})\cos 2\theta\right.$$

$$+2\omega_{B,1}\omega_{B,2}\sin 2\theta\left][\nabla^4\xi_{B,r}-8\nabla^2\xi_{B,r}-16\left(\frac{\partial^2\xi_{B,r}}{\partial\theta^2}+\xi_{B,r}\right)\right]$$

$$-4\left[(\omega_{B,1}^2-\omega_{B,2}^2)\sin 2\theta-2\omega_{B,1}\omega_{B,2}\cos 2\theta\right]\left[\frac{\partial}{\partial\theta}\nabla^2\xi_{B,r}-4\frac{\partial}{\partial\theta}\xi_{B,r}\right]$$

$$\left.+f_1\cos\theta+f_2\sin\theta\right\}+\frac{1}{12}(1+{}_s\mu_B){}_sh_B^2\sin\beta\left[\cos(\omega_{B,3}t+\theta)\right.$$

$$\left.+\frac{1}{2a_B}\sin(\omega_{B,3}t+\theta)\left(1-{}_s\tau_B\frac{\partial}{\partial t}\right)\left(\frac{\partial}{\partial z_1}+\frac{\partial}{\partial\theta}\right)\nabla^6\xi_{B,r}\right] = 0 \; . \tag{1.55}$$

(d) Galerkin's Functions

The Galerkin's functions for the shell are chosen so that the solution remains compatible with the load conditions. The shell loading consists of

i) the moments applied at the plate-shell junctions,

ii) concentrated forces and moments applied at the beam-shell junctions, and

iii) the inertia and the thermal forces.

To accommodate the loading i), the solution must include some exponential functions of z_1. To accommodate the loading ii), the solution must contain the delta functions $\delta(z_1-\rho_i,\ \theta-\theta_i)$, where $z_1=\rho_i$ and $\theta=\theta_i$ are the coordinates of the junction of the i^{th} beam and the shell. The forces in iii) are taken into consideration by the equation of motion itself. The flexural displacements must be equal to zero at the boundaries $z_1=-\rho'$ and $z_1=+\rho''$ of the shell.

Now, two expressions for $\delta(x-\xi)$, given by Eqs. (4.7), (4.43) of Stakgold [38] are

$$\begin{aligned}\delta(x-\xi) &= \frac{1}{\ell}+\sum_{n=1}^{\infty}\frac{2}{\ell}\cos\frac{n\pi x}{\ell}\cos\frac{n\pi\xi}{\ell}\\ &= \sum_{n=1}^{\infty}\frac{2}{\ell}\sin\frac{n\pi x}{\ell}\sin\frac{n\pi\xi}{\ell}\end{aligned} \tag{1.56}$$

where ℓ is the domain of the one-dimensional delta function.

Since

$$\delta[z_1,\ \theta;\ \rho_i,\ \theta_i]=\delta(z_1-\rho_i)\delta(\theta-\theta_i) \tag{1.57}$$

the form of the solution of the shell problem should be given by

$$\xi_{B,r} = b_1(t) + (z_1+\rho')(z_1-\rho'')[b_2(t)e^{p_2 z_1} + b_3(t)e^{p_3 z_1} + \ldots]$$

$$+ \sum_{m=1}^{\infty}\sum_{n=1}^{\infty} [b^1_{3+m,n}(t)\sin\frac{m\pi(\rho'+\rho_1)}{\ell_1} \sin\frac{m\pi(\rho'+z_1)}{\ell_1} \cos n\theta_1 \cos n\theta]$$

$$+ \sum_{m=1}^{\infty}\sum_{p=1}^{\infty} [b^2_{3+m,p}(t) \sin\frac{m\pi(\rho'+\rho_2)}{\ell_1} \sin\frac{m\pi(\rho'+z_1)}{\ell_1} \sin p\theta_2 \sin p\theta]$$

$$+ \sum_{m=1}^{\infty}\sum_{q=1}^{\infty} [b^3_{3+m,q}(t) \sin\frac{m\pi(\rho'+z_3)}{\ell_1} \sin\frac{m\pi(\rho'+z_1)}{\ell_1} \cos q\theta_3 \cos q\theta]$$

$$+ \sum_{m=1}^{\infty}\sum_{r=1}^{\infty} [b^4_{3+m,r}(t) \sin\frac{m\pi(\rho'+\rho_4)}{\ell_1} \sin\frac{m\pi(\rho'+z_1)}{\ell_1} \sin r\theta_4 \sin r\theta] \qquad (1.58)$$

where ℓ_1 is the length of the shell. The last four infinite sums correspond to the four shell-beam junctions. Here $\theta_1 = 0$, $\theta_2 = \pi/2$, $\theta_3 = \pi$ and $\theta_4 = 3\frac{\pi}{2}$. Thus the cosine series is used for $\delta(\theta-\theta_1)$ and $\delta(\theta-\theta_2)$. The right-hand side of Eq. (1.58) is then truncated to keep only the first and the second harmonic terms, and so the assumed solution is finally given by

$$\xi_{B,r} = b_1(t) + (z_1+\rho')(z_1-\rho'')[b_2(t)e^{p_2 z_1} + b_3(t)e^{p_3 z_1}]$$

$$+ b_4(t)\sin\frac{\pi(\rho'+z_1)}{\ell_1}\cos\theta + b_5(t) \sin\frac{2\pi(\rho'+z_1)}{\ell_1}\cos\theta$$

$$+ b_6(t) \sin\frac{\pi(\rho'+z_1)}{\ell_1}\sin\theta + b_7(t) \sin\frac{2\pi(\rho'+z_1)}{\ell_1}\sin\theta$$

$$+ b_8(t) \sin\frac{\pi(\rho'+z_1)}{\ell_1}\cos 2\theta + b_9(t) \sin\frac{2\pi(\rho'+z_1)}{\ell_1}\cos 2\theta$$

$$+ b_{10}(t) \sin\frac{\pi(\rho'+z_1)}{\ell_1}\sin 2\theta + b_{11}(t) \sin\frac{2\pi(\rho'+z_1)}{\ell_1}\sin 2\theta . \qquad (1.59)$$

The coefficients p_2 and p_3 correspond to the free vibration modes of the shell.

Equation (1.59) is now substituted in Eq. (1.55) and the Galerkin's method is applied. This gives eleven time-dependent equations of the form:

$$[{}_sA_1]\{{}_s\ddot{q}_B^*\} + [{}_sA_2]\{{}_s\dot{q}_B^*\} + [{}_sA_3]\{{}_sq_B^*\}$$

$$+ [\lambda_7]\{\ddot{q}_B^*\} + [\lambda_8]\{\dot{q}_B^*\} + [\lambda_9]\{q_B^*\} = \{{}_sA_4\} \cdot \qquad (1.60)$$

The vector $\{{}_sq_B^*\}$ is the (11 × 1) vector with b_i, $i = 1 - 11$, as its elements. The details of Eq. (1.60) are in Appendix 6.

5. Beam-end Masses

(a) Inertia forces

The expressions for the beam-end masses of the body B are derived here. Similar expressions can be obtained when the body A is considered. These masses are assumed to be point objects.

Let $\underline{F}_i = [F_{i,1}, F_{i,2}, F_{i,3}]^T$ be the inertia forces on the i^{th} mass along the beam local coordinate axes.

Let $\underline{y}_i$ be the displacement vector of the i^{th} mass in B-based coordinates. Then, as before,

$$\underline{F}_i = -m_i[\mu_i^B][\Theta\ddot{X}_B + \ddot{C}_B + \ddot{y}_i + 2\tilde{\omega}_B(\dot{C}_B+\dot{y}_i)$$

$$+ (\dot{\tilde{\omega}}_B + \tilde{\omega}_B\tilde{\omega}_B)(C_B + y_i + R_i + r_i)] \cdot \qquad (1.61)$$

Here (R_i+r_i) is the position vector of m_i in the B-based coordinates in the undeformed state. Also, as noted before, $\Theta\ddot{X}_B$ and C_B are expressed in terms of the generalized position vector $\{q_B^*\}$.

(b) Elastic Forces

Let $\underline{F}_i' = [F_{i,1}', F_{i,2}', F_{i,3}']^T$ be the elastic forces on the i^{th} mass along the beam local coordinate axes. Then

$F'_{i,1}$ = (Radial force exerted by the shell on the beam at the corresponding junction point) + (the total inertia force of the beam) (1.62)

$F'_{i,2}$ = Transverse shear force along μ_2, exerted by the i^{th} beam on the tip-mass

$F'_{i,3}$ = Transverse shear force along μ_3, exerted by the i^{th} beam on the tip-mass.

An expression for the shell outward load q is obtained from Eq. (6.11c), Kraus [37]. The expression is

$$\frac{{}_sh_B^2}{12a_B^2}\nabla^4\xi_{B,r} + \xi_{B,r} = -\frac{(1-{}_s\mu_B^2)a_B^2}{{}_sE_B \cdot {}_sh_B}q_i - \frac{{}_sh_B^2}{12}(1+{}_s\mu_B)\cdot{}_s\alpha_B\nabla^2{}_sT_{B,1}$$

where q_i is the outward load on the shell at the junction with the i^{th} beam. The above equation is rewritten as

$$q_i = -\left[\frac{{}_sE_B \cdot {}_sh_B^3}{12(1-{}_s\mu_B)^2a_B^4}\nabla^4\xi_{B,r} + \frac{{}_sE_B \cdot {}_sh_B}{(1-{}_s\mu_B^2)a_B^2}\xi_{B,r} + \frac{{}_sE_B \cdot {}_sh_B^3}{12(1-{}_s\mu_B)}\cdot\frac{{}_s\alpha_B}{a_B^2}\nabla^2({}_sT_{B1})\right]_{\substack{z_1=\rho_i \\ \theta=\theta_i}} \tag{1.63}$$

Now the expressions for $\xi_{B,r}$ and ${}_sT_{B1}$ are substituted in Eq. (1.63) and evaluated at (ρ_i,θ_i) to give q_i in the form

$$q_i = \sum_{j=1}^{11} c_{i,j}b_j + \sum_{j=12}^{12} c_{i,j}\dot{b}_j + f_i^*(t) \cdot \tag{1.64}$$

All $c_{i,j}$ are constants. The details are in Appendix 7.

The total inertia force of the i^{th} beam, ${}_b\underline{F}_i^*$, is given by

$${}_b\underline{F}_i^* = -[\mathscr{A}_1]\int_0^{\ell}({}_b\rho_i)\{{}_b\ddot{q}_i + 2\omega_B^*({}_b\dot{q}_i) + (\dot{\omega}_B^* + \omega_B^{**})({}_bq_i + R_i + s_i)$$

$$+ [\mu_i^B][\ddot{\Theta X}_B + \ddot{C}_B + 2\tilde{\omega}_B\dot{C}_B + (\dot{\tilde{\omega}}_B + \tilde{\omega}_B\tilde{\omega}_B)C_B]\}ds_i \tag{1.65}$$

where

$$[\mathscr{D}_1] = \begin{bmatrix} 1 & 0 & 0 \\ 0 & 0 & 0 \\ 0 & 0 & 0 \end{bmatrix} .$$

The transverse shear forces along $\underline{\mu}_2$ and $\underline{\mu}_3$ are given by

$$F'_{i,2} = ({}_bE_i)({}_bI_{i,3}\, p_i^3\, e^{p_i \ell}\, {}_1q_{i,2}) \tag{1.66}$$

$$F'_{i,3} = ({}_bE_i)({}_bI_{i,2}\, p_i^3\, e^{p_i \ell}\, {}_1q_{i,3}) . \tag{1.67}$$

Then $\underline{F}'_i$ is obtained from Eqs. (1.62), (1.64), (1.65), (1.66) and (1.67).

(c) Equations of Motion

The equations of motion of the beam-end masses are obtained by setting

$$\underline{F}_i + \underline{F}'_i = 0 . \tag{1.68}$$

Rewriting Eq. (1.68), we have

$$\begin{aligned} & m_i[\mu_i^B][\ddot{\Theta X}_B + G_B\ddot{q}_B^* + \ddot{y}_i + 2\tilde{\omega}_B(G_B\dot{q}_B^* + \dot{y}_i) \\ & \quad + (\dot{\tilde{\omega}}_B + \tilde{\omega}_B\tilde{\omega}_B)(G_Bq_B^* + y_i + R_i + r_i)] \\ = & \begin{bmatrix} \{[\sum_{j=1}^{11} c_{i,j}b_j + \sum_{j=12}^{22} c_{i,j}\dot{b}_j + f_i^*(t)] - [\mathscr{D}_1]\int_0^{\ell} ({}_b\rho_i)[{}_b\ddot{q}_i + 2\omega_B^*({}_b\dot{q}_i) \\ \quad + (\dot{\omega}_B^* + \omega_B^{**})({}_bq_i + R_i + s_i) + [\mu_i^B]\{\ddot{\Theta X}_B + G_B\ddot{q}_B^* \\ \quad + 2\tilde{\omega}_BG_B\dot{q}_B^* + (\dot{\tilde{\omega}}_B + \tilde{\omega}_B\tilde{\omega}_B)G_Bq_B^*\}]ds\} \\ \\ - ({}_bE_i)({}_bI_{i,3}\, p_i^3\, e^{p_i \ell}\, {}_1q_{i,2}) \\ - ({}_bE_i)({}_bI_{i,3}\, p_i^3\, e^{p_i \ell}\, {}_1q_{i,3}) \end{bmatrix} \end{aligned} \tag{1.69}$$

There are three equations in Eq. (1.69) for the three variables $y_{i,1}$, $y_{i,2}$ and $y_{i,3}$. The four beam-end masses will be described by 12 equations which will be of the form

$$[{}_mA_1]\{\ddot{y}^*\} + [{}_mA_2]\{\dot{y}^*\} + [{}_mA_3]\{y^*\}$$

$$+ [\lambda_{10}]\{\ddot{q}_B^*\} + [\lambda_{11}]\{\dot{q}_B^*\} + [\lambda_{12}]\{q_B\} = \{{}_mA_4\}. \tag{1.70}$$

Here $\{y^*\}$ is the (12×1) vector of the displacements of the four beam-end masses. The details are given in Appendix 8.

6. Spring-mass-damper Systems

The masses in the spring-mass-damper systems are assumed to move only along the $\underline{b}$ -axis, so the displacement vector in B-based coordinates is given by

$$\underline{y}_i = [0,\ 0,\ y_i]^T \ . \tag{1.71}$$

Let

$$[\mathcal{I}_3] = \begin{bmatrix} 0 & 0 & 0 \\ 0 & 0 & 0 \\ 0 & 0 & 1 \end{bmatrix} \ . \tag{1.72}$$

Then the inertia force on the masses is given by

$$F_i = -m_i[\mathcal{I}_3]\left[\left\{\frac{d^2}{dt^2} + 2\tilde{\omega}_B \frac{d}{dt} + (\tilde{\dot{\omega}}_B + \tilde{\omega}_B\tilde{\omega}_B)\right\}(\underline{y}_i + G_B q_B^*)\right\}$$

$$+ (\tilde{\dot{\omega}}_B + \tilde{\omega}_B\tilde{\omega}_B)R_i + \ddot{\Theta X}_B\Big] \ . \tag{1.73}$$

Let $k_{i,1}$ be the stiffness of the spring connecting the mass m_i to the plate No. 1, and $k_{i,2}$ be the coefficient of the damper connecting m_i to the plate no. 2. Then the equation of motion of m_i is given by

$$F_i = k_{i,1}[y_i - \chi_1(\alpha_i)] + k_{i,2}(\dot{y}_i - \dot{\chi}_2(\alpha_i)] \tag{1.74}$$

where α_i is the position coordinates, in the plane of the plates, of the mass m_i. Substituting Eqs. (1.71), (1.72), and (1.73) in (1.74), we obtain the equation of motion of m_i as

$$m_i[\ddot{y}_i - (\omega_{B,1}^2 + \omega_{B,2}^2)y_i + (\dot{\omega}_{B,1} + \omega_{B,2}\omega_{B,3})R_{i,2} + (\omega_{B,1}\omega_{B,3} - \dot{\omega}_{B,2})R_{i,1}$$

$$- (\omega_{B,1}^2 + \omega_{B,2}^2)R_{i,3} + [\mathcal{J}_3](\frac{d^2}{dt^2} + 2\omega_B \frac{d}{dt} + \tilde{\dot{\omega}}_B + \tilde{\omega}_B\tilde{\omega}_B)G_B q_B^*)$$

$$+ [\mathcal{J}_3]\ddot{\Theta}\ddot{X}_B] + k_{i,1}[y_i - \chi_1(\alpha_i)] + k_{i,2}[\dot{y}_i - \dot{\chi}_2(\alpha_i)] = 0 . \qquad (1.75)$$

Equation (1.75) is a scalar equation. For each of the bodies A and B, a system of four such equations are obtained, corresponding to the four spring-mass-damper systems in each body. Let

$$\{{}_d q^*\} = [y_{13}, y_{14}, y_{15}, y_{16}]^T$$

be the (4 × 1) vector representing the motion of the spring-mass-damper systems. Then the four equations of each body is obtained in the form

$$[{}_d A_1]\{{}_d \ddot{q}^*\} + [{}_d A_2]\{{}_d \dot{q}^*\} + [{}_d A_3]\{{}_d q^*\}$$

$$+ [\lambda_{13}]\ddot{q}_B^* + [\lambda_{14}]\dot{q}_B^* + [\lambda_{15}]q_B^* = \{{}_d A_4\} . \qquad (1.76)$$

Details of Eq. (1.76) are given in Appendix 9.

7. Rigid Bodies

The force and moment equations for the rigid bodies are now derived. As before, the required equations are derived for the rigid bodies in the body B only. The corresponding derivations for the body A are similar. The positions of rigid bodies are shown in Fig. 7.

(a) Force Equations

The rigid bodies are assumed to be so constrained as to have a translation only along the $\underline{b}_3$-axis and to have two rotations about the $\underline{b}_1$- and $\underline{b}_2$-axes. So the motion of the rigid bodies with masses m_1 and m_2 are described by

$$\{{}_r q_i^*\} = [y_i, \theta_{i,1}, \theta_{i,2}]^T, \quad i = 1,2. \tag{1.77}$$

The mass m_1 is fixed to the plate no. 2 at the four points with position coordinates α_i, $i = 7 - 10$, in the plane of the plate. Similarly, α_i, $i = 11 - 14$ are the junction points of m_2 with the plate no. 2. Let the reaction forces of the plate on m_1 at the points α_i, $i = 7 - 10$, be given by $P_{2,1}^{(7)}$, $P_{2,1}^{(8)}$, $P_{2,1}^{(9)}$ and $P_{2,1}^{(10)}$, respectively. The reaction forces on the mass m_2 are given as $P_{2,2}^{(11)}$, $P_{2,2}^{(12)}$, $P_{2,2}^{(13)}$ and $P_{2,2}^{(14)}$.

Summing the inertia forces and the reaction forces to zero the force equation of motion for m_1 is obtained as

$$\begin{aligned} m_1\{&\ddot{y}_1 - (\omega_{B,1}^2+\omega_{B,2}^2)y_1 - (\dot{\omega}_{B,2} - \omega_{B,1}\omega_{B,3})R_{1,1} + (\dot{\omega}_B + \omega_{B,2}\omega_{B,3})R_{1,2} \\ &- (\omega_{B,1}^2 + \omega_{B,2}^2)R_{1,3} + [\mathcal{J}_3][\frac{d^2}{dt^2} + 2\omega_B \frac{d}{dt} + (\tilde{\dot{\omega}}_B + \tilde{\omega}_B\tilde{\omega}_B)]G_B q_B^* \\ &+ [\mathcal{J}_3]\ddot{\Theta X}_B\} - (P_{2,1}^{(7)} + P_{2,1}^{(8)} + P_{2,1}^{(9)} + P_{2,1}^{(10)}) = 0 . \end{aligned} \tag{1.78}$$

The plate reactions are obtained from the singular components of the assumed plate solution. The total shear force on a small circle of radius ε at a distance r_j from the center of the plate due to the function

$$f_j = \chi_{2,j}(z - \alpha_j)(\bar{z} - \bar{\alpha}_j)\log(w\bar{w}) \tag{1.37}$$

on the mass m_1, is given by

$$p_{2,1}^{(j)} = 24\ {}_pD_2\pi\epsilon^2 r_j^2(1 - r_j^2)\chi_{2,j} \tag{1.79}$$

where

$$r_j^2 = \alpha_j\bar{\alpha}_j\ . \tag{1.80}$$

Equation (1.79) is derived in detail in Appendix 4.

Substitution of Eq. (1.79) in Eq. (1.78) gives

$$\begin{aligned} m_1\{&\ddot{y}_1 - (\omega_{B,1}^2+\omega_{B,2})y_1 - (\dot{\omega}_{B,2}-\omega_{B,1}\omega_{B,3})R_{1,1} + (\dot{\omega}_{B,1}+\omega_{B,2}\omega_{B,3})R_{1,2} \\ &- (\omega_{B,1}^2+\omega_{B,2}^2)R_{1,3} + [\mathcal{I}_3][\frac{d^2}{dt^2} + 2\tilde{\omega}_B\frac{d}{dt} + (\tilde{\dot{\omega}}_B+\tilde{\omega}_B\tilde{\omega}_B)]G_Bq_B^* \\ &+ [\mathcal{I}_3]\Theta\ddot{X}_B\} - 24\ {}_pD_2\pi\epsilon^2\ [\sum_{j=7}^{10} r_j^2(1-r_j^2)\chi_{2,j}] = 0\ . \end{aligned} \tag{1.81}$$

The equation for y_2 is similarly obtained as

$$\begin{aligned} m_2\{&\ddot{y}_2 - (\omega_{B,1}^2+\omega_{B,2}^2)y_2 - (\dot{\omega}_{B,2}-\omega_{B,1}\omega_{B,3})R_{2,1} + (\dot{\omega}_{B,1}+\omega_{B,2}\omega_{B,3})R_{2,2} \\ &- (\omega_{B,1}^2+\omega_{B,2})R_{2,3} + [\mathcal{I}_3][\frac{d^2}{dt^2} + 2\tilde{\omega}_B\frac{d}{dt} + (\tilde{\dot{\omega}}_B + \tilde{\omega}_B\tilde{\omega}_B)]G_Bq_B^* \\ &+ [\mathcal{I}_3]\Theta\ddot{X}_B\} - 24\ {}_pD_2\pi\epsilon^2[\sum_{j=11}^{14} r_j^2\ (1-r_j^2)\chi_{2,j}] = 0\ . \end{aligned} \tag{1.82}$$

In these equations, $[\mathcal{I}_3]$ is given by

$$[\mathcal{I}_3] = \begin{bmatrix} 0 & 0 & 0 \\ 0 & 0 & 0 \\ 0 & 0 & 1 \end{bmatrix}\ .$$

(b) The Moment Equations

Let $[{}_rI_i]$ be the inertia dyadic of the rigid body m_i about its centroidal axes, and $\underline{T}_i$ be the inertia torque. Then

$$\underline{T}_i = -\ {}^N\frac{d}{dt}[{}_rI_i(\underline{\omega}_B + \underline{\dot{\theta}}_i)] \tag{1.83}$$

where

$$\{\underline{\dot{\theta}}_i\} = [\dot{\theta}_{i,1},\ \dot{\theta}_{i,2},\ 0]. \tag{1.84}$$

Equation (1.83) is rewritten as

$$\underline{T}_i = -\frac{d}{dt}\left[{}_rI_i(\underline{\omega}_B + \dot{\underline{\theta}}_i)\right] - (\underline{\omega}_B + \dot{\underline{\theta}}_i) \times \left[{}_rI_i(\underline{\omega}_B + \dot{\underline{\theta}}_i)\right]$$

$$- {}_rI_i(\dot{\underline{\omega}}_B + \ddot{\underline{\theta}}_i) - \omega_B \times {}_rI_i \cdot \underline{\omega}_B - \underline{\omega}_B \times {}_rI_i \cdot \dot{\theta}_i - \dot{\theta}_i \times {}_rI_i \cdot \underline{\omega}_B$$

or

$$\underline{T}_i = -[{}_rI_i](\dot{\underline{\omega}}_B + \ddot{\underline{\theta}}_i) - \tilde{\underline{\omega}}_B[{}_rI_i]\underline{\omega}_B - \tilde{\underline{\omega}}_B[{}_rI_i]\underline{\theta}_i + [\widetilde{{}_rI_B \cdot \underline{\omega}_B}]\underline{\theta}_i \,. \qquad (1.85)$$

It is assumed that $[{}_rI_i]$ is of the form

$$[{}_rI_i] = \begin{bmatrix} {}_rI_{i,1} & 0 & 0 \\ 0 & {}_rI_{i,2} & 0 \\ 0 & 0 & {}_rI_{i,3} \end{bmatrix} . \qquad (1.86)$$

Then Eq. (1.85) reduces to

$$\{\underline{T}_i\} = [T_{i,1}, T_{i,2}, T_{i,3}]^T$$

$$= -\begin{Bmatrix} [{}_rI_{i,1}(\dot{\omega}_{B,1} + \ddot{\theta}_{i,1}) + \omega_{B,3}(\omega_{B,2} + \dot{\theta}_{i,2})({}_rI_{i,3} - {}_rI_{i,2})] \\ [{}_rI_{i,2}(\dot{\omega}_{B,2} + \ddot{\theta}_{i,2}) + \omega_{B,3}(\omega_{B,1} + \dot{\theta}_{i,1})({}_rI_{i,1} - {}_rI_{i,3})] \\ [{}_rI_{i,3}\dot{\omega}_{B,3} + ({}_rI_{i,2} - {}_rI_{i,1})(\omega_{B,1}\omega_{B,2} + \omega_{B,2}\dot{\theta}_{i,1} + \omega_{B,1}\dot{\theta}_{i,2})] \end{Bmatrix} \qquad (1.87)$$

Let $T'_{i,1}$ and $T'_{i,2}$ be the reaction torques exerted by the plate on the rigid body m_i about the centroidal axes parallel to $\underline{b}_1$ and $\underline{b}_2$, respectively. Then, from Figure 7, we have

$$T'_{1,1} = \tfrac{1}{2}(P^{(9)}_{2,1} + P^{(10)}_{2,1} - P^{(7)}_{2,1} - P^{(8)}_{2,1})\ell_\theta \qquad (1.88)$$

and

$$T'_{1,2} = \tfrac{1}{2}(P^{(8)}_{2,1} + P^{(9)}_{2,1} - P^{(7)}_{2,1} - P^{(10)}_{2,1})\ell_r \,. \qquad (1.89)$$

Similarly,

$$T'_{2,1} = \frac{1}{2}(P^{(11)}_{2,2} + P^{(12)}_{2,2} - P^{(13)}_{2,2} - P^{(14)}_{2,2})\ell_\theta \tag{1.90}$$

and

$$T'_{2,2} = \frac{1}{2}(P^{(11)}_{2,2} + P^{(14)}_{2,2} - P^{(12)}_{2,2} - P^{(13)}_{2,2})\ell_r \ . \tag{1.91}$$

Then the moment equations of the rigid bodies nos. 1 and 2 are given by

$$[T_{1,1},\ T_{1,2},\ T_{2,1},\ T_{2,2}]^T + [T'_{1,1},\ T'_{1,2},\ T'_{2,1},\ T'_{2,2}]^T = 0 \ . \tag{1.92}$$

Let $\{{}_rq^*\} = [y_1,\ \theta_{1,1},\ \theta_{1,2},\ y_2,\ \theta_{2,1},\ \theta_{2,2}]^T$ be the vector which defines the motion of the two rigid bodies. Then, combining Eqs. (1.81), (1.82) and (1.92), an equation of the form

$$[{}_rA_1]\{{}_r\ddot{q}^*\} + [{}_rA_2]\{{}_r\dot{q}^*\} + [{}_rA_3]\{{}_rq^*\}$$

$$+ [\lambda_{16}]\{\ddot{q}^*_B\} + [\lambda_{17}]\{\dot{q}^*_B\} + [\lambda_{18}]\{q^*_B\} = \{{}_rA_4\} \tag{1.93}$$

is obtained. Details of this equation are shown in Appendix 10.

8. Transformation Matrices

The angular positions of the body B defined by three successive rotations of coordinate axes are shown in Figure 9.

$\underline{X}_1$, $\underline{X}_2$ and $\underline{X}_3$ are the inertially fixed coordinate axes. The B-based coordinate axes $\underline{b}_1$, $\underline{b}_2$ and $\underline{b}_3$ coincide originally with $\underline{X}_1$, $\underline{X}_2$ and $\underline{X}_3$, respectively. First, a rotation by an angle ψ_1 about X_1 brings the axes $\underline{b}_1$ in the positions shown by $\underline{D}_1$. Second, a rotation by an angle ψ_2 about $\underline{D}_2$ takes the axes $\underline{b}_1$ into the positions shown by $\underline{E}_1$. Finally, a rotation by an angle ψ_3 about $\underline{E}_3$ takes the B-based coordinates to the general position shown by $\underline{b}_1$ in Figure 9.

Now, the matrix Θ transforms vectors based in the inertially fixed coordinates to the B-based coordinates. So Θ is given by:

$$\Theta = \begin{bmatrix} \cos\psi_3 & \cos\psi_3 & 0 \\ -\sin\psi_3 & \cos\psi_3 & 0 \\ 0 & 0 & 1 \end{bmatrix} \begin{bmatrix} \cos\psi_2 & 0 & -\sin\psi_2 \\ 0 & 1 & 0 \\ \sin\psi_2 & 0 & \cos\psi_2 \end{bmatrix} \begin{bmatrix} 1 & 0 & 0 \\ 0 & \cos\psi_1 & \sin\psi_1 \\ 0 & -\sin\psi_1 & \cos\psi_1 \end{bmatrix}$$

$$= \begin{bmatrix} \cos\psi_2\cos\psi_3 & (\cos\psi_1\sin\psi_3 + \sin\psi_1\sin\psi_2\cos\psi_3) & (\sin\psi_1\sin\psi_3 - \cos\psi_1\sin\psi_2\cos\psi_3) \\ -\cos\psi_2\sin\psi_3 & (\cos\psi_1\cos\psi_3 - \sin\psi_1\sin\psi_2\sin\psi_3) & (\sin\psi_1\cos\psi_3 + \cos\psi_1\sin\psi_2\sin\psi_3) \\ \sin\psi_2 & -\sin\psi_1\cos\psi_2 & \cos\psi_1\cos\psi_2 \end{bmatrix} \tag{1.94}$$

The rotation coordinates of the body A are defined relative to the body B, in Figure 10. First, a rotation by an angle θ_1 about $\underline{b}_1$ brings $\underline{a}_1$ in the position shown by $\underline{F}_1$. Then, a rotation by an angle θ_2 about $\underline{F}_2$ brings the axes $\underline{a}_1$ in the position shown by $\underline{G}_1$. Finally, a rotation by an angle θ_3 about $\underline{G}_3$ brings the A-based coordinates in the general position shown by $\underline{a}_1$ in Figure 10.

Let Θ_{AB} be the matrix that transforms vectors in the A-based coordinates to B-based coordinates. Then Θ_{AB}^{-1} is also given by Eq. (1.94), but in which the angles ψ_1, ψ_2 and ψ_3 are replaced by θ_1, θ_2 and θ_3. Now, taking θ_1 and θ_2 small but keeping θ_3 arbitrary, Θ_{AB}^{-1} is given by

$$\Theta_{AB}^{-1} = \begin{bmatrix} \cos\theta_3 & \sin\theta_3 & -\theta_2\cos\theta_3 \\ -\sin\theta_3 & \cos\theta_3 & \theta_1\cos\theta_3 \\ \theta_2 & -\theta_1 & 1 \end{bmatrix} . \tag{1.95}$$

9. Contact Forces and Torques

The expressions for the contact forces and torques between the bodies B and C will be derived. The body C is assumed to have negligible mass, so the forces and torques between the bodies A and C will be equal and opposite to those between the bodies B and C. We now refer to Figure 8 for the following analysis.

Let $\underline{F}_{AC}$ and $\underline{T}_{AC}$ be the contact force and torque vectors, respectively, applied by the body C on the body A, and are expressed in the A-based coordinates. Let $\underline{F}_{BC}$ and $\underline{T}_{BC}$ be the force and torque vectors applied by the body C on the body B and are expressed in the B-based coordinates. Let $\underline{C}_B$ and $\underline{C}_A$ be the shift of the center of mass of the body B in B-based coordinates and that of the body A in A-based coordinates. The vectors $\underline{r}_A$ and $\underline{r}_B$, defined in Figure 8, are expressed in A-based and B-based coordinates, respectively. In this section, the terms $_{b}\underline{F}_{AC}$, $_{b}\underline{T}_{AC}$, $_{b}\underline{C}_{A}$ etc. will mean the vectors $\underline{F}_{AC}$, $\underline{T}_{AC}$, $\underline{C}_A$ expressed in the B-based coordinates.

Let θ_1, θ_2 and θ_3 be the relative angular positions of the body A with respect to the body B. It is assumed that θ_1 and θ_2 are small, and θ_3 is large. It is also assumed that the slopes of the body C at the end of A with respect to the end B along the axes $\underline{b}_1$ and $\underline{b}_2$ are given by θ_2 and $-\theta_1$, respectively.

Now, let $_{b}\underline{F}_{AC}$ and $_{b}\underline{T}_{AC}$ be expressed as

$$\begin{Bmatrix} {}_{b}\underline{F}_{AC} \\ {}_{b}\underline{T}_{AC} \end{Bmatrix} = \begin{bmatrix} \tau_1 & \tau_2 & \tau_3 \\ \tau_4 & \tau_5 & \tau_6 \end{bmatrix} \begin{Bmatrix} {}_{b}\underline{C}_{A} \\ \underline{C}_B \\ \underline{\theta} \end{Bmatrix} + \begin{bmatrix} \tau_7 & \tau_8 & \tau_9 \\ \tau_{10} & \tau_{11} & \tau_{12} \end{bmatrix} \begin{Bmatrix} {}_{b}\dot{\underline{C}}_{A} \\ \dot{\underline{C}}_B \\ \dot{\underline{\theta}} \end{Bmatrix} \qquad (1.96)$$

where

$$\underline{\theta} = [\theta_1, \theta_2, \theta_3]^T \, . \qquad (1.97)$$

Then

$$\underline{F}_{BC} = - {}_b\underline{F}_{AC} \tag{1.98}$$

and

$$\underline{T}_{BC} = - \underline{T}_{AC} - \tilde{\underline{r}}_{BA}({}_b\underline{F}_{AC}) \tag{1.99}$$

where

$$\underline{r}_{BA} = {}_b\underline{r}_A - \underline{r}_B \ .$$

From Eqs. (1.96) and (1.98), we have

$$\underline{F}_{BC} = - [\tau_1({}_bC_A) + \tau_2(C_B) + \tau_3\theta] - [\tau_7({}_b\dot{C}_A) + \tau_8(\dot{C}_B) + \tau_9\dot{\theta}] \ . \tag{1.100}$$

Now let $\|M\|_A$ and $\|M\|_B$ be the total masses of the bodies A and B. Then because of the force-free environment of the satellite, we have

$$\|M\|_A({}_bC_A) + \|M\|_BC_B = 0 \ .$$

Therefore

$${}_b\underline{C}_A = - \frac{1}{\gamma} \underline{C}_B \tag{1.101}$$

where

$$\gamma = \frac{\|M\|_A}{\|M\|_B} \ . \tag{1.102}$$

Therefore, from Eqs. (1.100) and (1.101),

$$\underline{F}_{BC} = (\frac{1}{\gamma}\tau_1 - \tau_2)\underline{C}_B + (\frac{1}{\gamma}\tau_7 - \tau_8)\underline{C}_B - (\tau_3\underline{\theta} + \tau_9\underline{\dot{\theta}}) \ . \tag{1.103}$$

Similarly

$$\begin{aligned}\underline{F}_{AC} = {} & [\Theta_{AB}^{-1}(\tau_1 - \gamma\tau_2)\Theta_{AB}]\underline{C}_A + [\Theta_{AB}^{-1}(\tau_7 - \gamma\tau_8)\Theta_{AB}]\underline{C}_A \\ & + [\Theta_{AB}^{-1}(\tau_7 - \gamma\tau_8)\dot{\Theta}_{AB}]\underline{C}_A + (\Theta_{AB}^{-1}\tau_3\underline{\theta} + \Theta_{AB}^{-1}\tau_9\underline{\dot{\theta}}) \\ & [\Theta_{AB}^{-1}(\tau_1 - \gamma\tau_2)\Theta_{AB}]\underline{\dot{C}}_A + [\Theta_{AB}^{-1}(\tau_7 - \gamma\tau_8)\Theta_{AB}]\underline{\dot{C}}_A + (\Theta_{AB}^{-1}\tau_3\underline{\theta} + \Theta_{AB}^{-1}\tau_9\underline{\dot{\theta}})\end{aligned} \tag{1.104}$$

In the above equation, Θ_{AB} transforms vectors in the A-based coordinates to vectors in the B-based coordinates. The neglected term is due to small angular accelerations. From Eqs. (1.96), (1.99) and (1.101),

$$\underline{T}_{BC} = [\frac{1}{\gamma}(\tau_4 + \tilde{r}_{AB}\tau_1) - (\tau_5 + \tilde{r}_{AB}\tau_2)]\underline{C}_B + [\frac{1}{\gamma}(\tau_{10} + \tilde{r}_{AB}\tau_7) - (\tau_{11} + \tilde{r}_{AB}\tau_8)]\underline{C}_B - [\tau_6 + \tilde{r}_{AB}\tau_3]\underline{\theta} - [\tau_{12} + \tilde{r}_{AB}\tau_9]\dot{\underline{\theta}} \tag{1.105}$$

and

$$\underline{T}_{AC} = [\Theta_{AB}^{-1}(\tau_4 - \gamma\tau_5)\Theta_{AB}]\underline{C}_A + [\Theta_{AB}^{-1}(\tau_{10} - \gamma\tau_{11})\Theta_{AB}]\dot{\underline{C}}_A + [\Theta_{AB}^{-1}(\tau_{10} - \gamma\tau_{11})\dot{\Theta}_{AB}]\underline{C}_A + \Theta_{AB}^{-1}(\tau_6\underline{\theta} + \tau_{12}\dot{\theta})$$

$$\cong [\Theta_{AB}^{-1}(\tau_4 - \gamma\tau_5)\Theta_{AB}]\underline{C}_A + [\Theta_{AB}^{-1}(\tau_{10} - \gamma\tau_{11})\Theta_{AB}]\dot{\underline{C}}_A + \Theta_{AB}^{-1}(\tau_6\theta + \tau_{12}\dot{\theta}). \tag{1.106}$$

Now let the body C be taken to be a uniform shaft having E_C and I_C as its modulus of elasticity and the area moment of inertia of the cross-section, respectively. Let ℓ_C be the length of the shaft. It is now assumed that the displacements of the shaft at the ends A and B are equal to ${}_bC_A$ and C_B, respectively. It is also assumed that the rotations of the shaft at the ends A and B, about the axes $\underline{b}_1$ and $\underline{b}_2$, are the same as those of the bodies A and B, respectively. Then

$$[\tau_1] = \begin{bmatrix} \frac{12E_CI_C}{\ell_C^3} & 0 & 0 \\ 0 & \frac{12E_CI_C}{\ell_C^3} & 0 \\ 0 & 0 & \frac{A_CE_C}{\ell_C} \end{bmatrix} \tag{1.107}$$

$$[\tau_2] = -[\tau_1] \tag{1.108}$$

$$[\tau_3] = \begin{bmatrix} 0 & \frac{6E_CI_C}{\ell_C^2} & 0 \\ -\frac{6E_CI_C}{\ell_C^2} & 0 & 0 \\ 0 & 0 & 0 \end{bmatrix} \tag{1.109}$$

$$\tau_7 = \eta\tau_1, \quad \tau_8 = \eta\tau_2 \quad \text{and} \quad \tau_9 = \eta\tau_3 \tag{1.110}$$

where A_C is the cross-sectional area of the shaft, and

$$\eta = \frac{E_C^*}{E_C} . \tag{1.111}$$

The symbol E_C^* stands for the modulus of viscosity of the shaft material.

$$[\tau_4] = \begin{bmatrix} \frac{6E_CI_C}{\ell^2} & 0 & 0 \\ 0 & \frac{6E_CI_C}{\ell^2} & 0 \\ 0 & 0 & 0 \end{bmatrix} \tag{1.112}$$

$$[\tau_5] = -[\tau_4] \tag{1.113}$$

$$[\tau_6] = \begin{bmatrix} \frac{4E_C I_C}{\ell_C} & 0 & 0 \\ 0 & \frac{4E_C I_C}{\ell_C} & 0 \\ 0 & 0 & 0 \end{bmatrix} \tag{1.114}$$

$$[\tau_{10}] = \eta[\tau_4], \quad [\tau_{11}] = \eta[\tau_5], \quad [\tau_{12}] = \eta[\tau_6] + c[\mathcal{O}_3] \ . \tag{1.115}$$

Substituting the expression for θ_{AB} and the Eqs. (1.107) through (1.115) in Eqs. (1.103) through (1.106), the values of the contact forces and torques are obtained.

10. The Assembled Equations

In this Part I, the equations of motion of the different structural elements have been obtained. The derivations are shown for the body B. A similar set of equations can be obtained for the body A.

The configuration shown in Figure 1 has been described by 110 generalized time-dependent position coordinates. Accordingly, a total of 110 equations are generated for the body B. This set of equations in matrix notation has the form

$$[\bar{A}_1]\{\ddot{q}_B^*\} + [\bar{A}_2(\omega,\dot{\omega},t)]\{\dot{q}_B^*\} + [\bar{A}_3(\omega,\dot{\omega},t)]\{q_B^*\} = \{\bar{A}_4(\omega,\dot{\omega},t)\} \ . \tag{1.116}$$

Similarly, the equations for the body A take the form

$$[\bar{A}_1']\{\ddot{q}_A^*\} + [\bar{A}_2'(\omega,\dot{\omega},t)]\{\dot{q}_A^*\} + [\bar{A}_3'(\omega,\dot{\omega},t)]\{q_A^*\} = \{\bar{A}_4'(\omega,\dot{\omega},t)\} \ . \tag{1.117}$$

In these equations, $[\bar{A}_1]$ and $[\bar{A}_1']$ are (110 × 110) square matrices of constants. These final forms of the equations will be used in the next part of this work.

11. Error Bounds of the Solutions

The complete analysis of this report is based primarily on the assumed solutions of the partial differential equations for the beams, plates and shells. These solutions obviously are not exact. The Galerkin's method only minimizes the error corresponding to the assumed form of the solution. A scheme is now devised to estimate this error based on the assumed solution.

In each of the cases of beams, plates and shells, the solution u is sought for an equation of the form

$$Au = \mu u + f \tag{1.118}$$

where A is a linear differential operator, μ and f are functions independent of u. Let v be the error in the assumed solution, which is given by $(u + v)$. Now, let $(u + v)$ actually satisfy an equation

$$A(u + v) = \mu(u + v) + f - A_1(u + v) \tag{1.119}$$

where A_1 also is a linear operator. Then from Eqs. (1.118) and (1.119), we obtain

$$Av = \mu v - A_1(u + v),$$

or

$$(\mu - A)v = A_1(u + v),$$

or

$$v = (I - \mu^{-1}A)^{-1}\mu^{-1}A_1(u + v).$$

Now, it is assumed that $\mu^{-1}A$ is a contraction operator. Then

$$v \cong (I + A\mu^{-1})\mu^{-1}A_1(u + v)$$

or

$$\|v\| = \|(I + \mu^{-1}A)\mu^{-1}A_1(u + v)\| . \tag{1.120}$$

In the Eq. (1.120), $A_1(u + v)$ is the quantity obtained by substituting

the assumed solution in the governing differential equation. Also A and μ^{-1} are known operators. Then the maximum values of the error v is obtained by taking suitable norms in the Eq. (1.120), over the complete time and spatial domain of the operators A and μ. A very easily calculated norm is in the space L_∞, and this norm will be used. Hence, the following operations are required:

a) Carry out the complete analysis, and obtain the coefficients of the Galerkin functions,

b) evaluate the norms in Eq. (1.120),

c) if $\|v\|$ is too high, increase the number of Galerkin's functions and repeat the procedure,

d) if $\|v\|$ is small, then the assumed solution is satisfactory.

References

1. Pilkington, N. C., 1958: "Vehicle Motions as Inferred from Radio Signal Strength Records," JPL, Pasadena, California, External Publication 551.

2. Bracewell, R. N. and Garriott, O. K., 1958: "Rotation of Artificial Earth Satellites," *Nature*, 182, pp. 760-762.

3. Perkel, H., 1958: "Space Vehicle Attitude Problems," *Advanc. Astro. Sci.*, Vol. 4, pp. 173-192.

4. Thomson, W. T. and Reiter, G. S., 1960: "Attitude Drift of Space Vehicles," *J. Astronaut. Sci.*, Vol. 7, pp. 29-34.

5. Likins, P. W., 1966: "Model Method for Analysis of Free Rotations of Spacecraft," *AIAA J.*, Vol. 5, pp. 1304-1308.

6. Likins, P. W., 1966: "Effects of Energy Dissipation on the Free Body Motions of Spacecraft," JPL, Tech. Rept. 32-860.

7. Iorillo, A. J., 1965: "Nutational Damping Dynamics of Axisymmetric Rotor Stabilized Satellites," ASME Winter Meeting, Chicago, Nov. 1965.

8. Karymov, A. A. and Kharitonova, T. V., 1967: "The Effect of External Perturbing Moments on the Dynamics of a Uni-axial Single Flywheel Attitude Control System of a Spacecraft," *J. of Appl. Math. & Mech.*, pp. 1098-1106.

9. Rossi, L. C. et al., 1969: "Attitude Dynamics and Stability Conditions of a Non-rigid Spinning Satellite,: *Aeronaut. Q.*, August, pp. 223-236.

10. Likins, P. W., 1966: "Attitude Stability of Dual-spin Systems," Space Systems Research Report, Hughes Aircraft Co., SSD 60377R, September.

11. Likins, P. W. and Mingori, D. L., 1967: "Liapunov Stability Analysis of Freely Spinning Systems," Proc. 18th Int. Astronaut. Congress, Belgrade, September, pp. 89-102.

12. Mingori, D. L., 1969: "Effects of Energy Dissipation on the Attitude Stability of Dual-spin Satellites," *AIAA J.*, Vol. 7, January, pp. 20-27.

13. Pringle, R., Jr., 1966: "On the Stability of a Body with Connected Moving Parts," *AIAA J.*, Vol. 4, pp. 1395-1404.

14. Flatley, T. W., 1971: "Equilibrium States for a Class of Dual-spin Spacecraft," NASA Technical Report TR R-362.

15. Flatley, T. W., 1969: "Attitude Stability of a Class of Partially Flexible Spinning Satellites," NASA Tech. Note D-5268.

16. Velman, J. R., 1966: "Attitude Dynamics of Dual-spin Satellites," Space Systems Division Research Report, Hughes Aircraft Co., SSD 60419R, September.

17. Likins, P. W., and Wirsching, P. H., 1968: "Use of Synthetic Modes in Hybrid Coordinate Dynamic Analysis," AIAA J., Vol. 6, October, pp. 1867-1872.

18. Likins, P. W. and Gale, A. H., 1968: "The Analysis of Interactions Between Attitude Control Systems and Flexible Appendages," Paper IAF AD29, October 1968, 19th Int. Aeronaut. Congress, New York.

19. Likins, P. W., and Gale, A. H., 1969: "A Study of the Dynamics of Spacecraft with Flexible Appendages with Special Attention to a Gyrostat with a Flexible Despun Section," Aerospace Technology Research Report, Hughes Aircraft Co., Space Systems Division, Report No. 35, SSD 90003R.

20. Likins, P. W. and Fleischer, G. E., 1970: "Results of Flexible Spacecraft Attitude Control Studies Utilizing Hybrid Coordinates," AIAA paper 70-20, New York.

21. Kane, T. R. and Robe, T. R., 1967: "Dynamics of an Elastic Satellite," *Int. J. of Solids and Structures*, May,July,Nov., 1967, pp. 333-352, 691-703, 1031-1051.

22. Bainum, P. M. et al., 1970: "Motion and Stability of Dual-spin Satellite with Nutation Damping," *J. of Spacecraft & Rockets*, Vol. 7, June, pp. 690-696.

23. Cretcher, C. K. and Mingori, D. L., 1971: "Nutation Damping and Vibration Isolation in a Flexibly Coupled Dual-spin Spacecraft," *J. of Spacecraft & Rockets*, Vol. 8, No. 8, August, pp. 817-823.

24. Wenglarz, R. A., 1971: "Dynamically Unbalanced Dual-spin Space Stations with Rigid or Low-coupling Interconnections," *J. of Spacecraft & Rockets*, Vol. 8, No. 10, October, pp. 1032-1037.

25. "Active Damping and Precision Pointing," Vols. 1 to 6, Avco Systems Division, 201 Lowell Street, Wilmington, Mass., AVSD-0152-71-CR, NASA Contract No. NAS 5-11800, March, 1971.

26. *Proceedings of the Symposium on Attitude Stabilization and Control of Dual-spin Spacecraft*, Air Force Report SAMSO-TR-68-191 (1968).

27. Etkin, B., and Hughes, P. C., 1967: "Exploration of the Anomalous Spin Behavior of Satellites with Long Flexible Antennae," *J. of Spacecraft and Rockets*, Vol. 4, No. 9, September, pp. 1139-1145.

28. Yu, Y. Y., 1969: "Thermally Induced Vibration and Flutter of a Flexible Boom," *J. of Spacecraft and Rockets*, August, pp. 902-910.

29. Zach, F. C., 1970: "Time-optimal Control of Gravity-gradient Satellites with Disturbances," *J. of Spacecraft and Rockets*, Vol. 7, No. 12, December, pp. 1434-1440.

30. Dobrotin, B., et al., 1970: "Mariner Limit Cycle and Self-disturbance Torques," *J. of Spacecraft and Rockets*, June, pp. 684-689.

31. Tidwell, N. W., 1970: "Modelling of Environmental Torques of a Spin-stabilized Spacecraft in a Near-Earth Orbit," *J. of Spacecraft and Rockets*, December, pp. 1425-1433.

32. Huang, T. C. and Lee, C. C. L., 1969: "Free Vibrations of Space Framed Structures," *Proc. 11th Midwestern Mech. Conf.*, pp. 861-885.

33. Huang, T. C., and Lee, C. C. L., "Orthogonality Conditions and Normalization of Normal Modes of Space Framed Structures and Applications to Initial Value and Forced Vibration Problems," in preparation.

34. Huang, T. C., and Saczalsky, K. J., 1971: "Elastodynamics of Complex Structural Systems," *Proc. 12th Midwestern Mechanics Conference*, August, pp. 675-688.

35. Huang, T. C., and Saczalsky, K. J., 1972: "Coupled Response of Spatial Vibratory Structures Mounted on Isotropic Plate Elements," *J. of Engineering for Industry*, February, pp. 15-22.

36. Vlasov, N. Z., "General Theory of Shells and Its Application in Engineering," National Technical Information Service translation no. N64-19883.

37. Kraus, H., 1967: *Thin Elastic Shells*, John Wiley and Sons, Inc.

38. Stakgold, I., 1967: *Boundary Value Problems of Mathematical Physics*, Vols. I and II, The Macmillan Co., New York.

PART II

EQUATIONS OF MOTION FOR THE COMPOSITE BODIES

Contents

		Page
	Nomenclature	74
1.	Introduction	77
2.	Continuity Conditions	77
	a) End mass - beam junctions	77
	b) Rigid body - plate junctions	78
	c) Beam-shell junctions	80
	d) Plate-shell junctions	83
	e) Remarks on reduction of dimensions	90
3.	External Torques	91
	a) Residual magnetic torque	91
	b) Eddy current torque	92
	c) Solar radiation torque	94
	d) Gravity gradient torque	96
	e) Total environmental torque	97
4.	Moment Equations for the Composite Bodies	98
	a) Angular momentum	98
	b) Equations of motion of the body B	100
	c) Equations of motion of the body A	101
5.	Equations for the Angular Velocities	102
	a) A review	102
	b) Condensation of the appendage equations	102
	c) Elimination of the coordinates	103
6.	References	107

Nomenclature

(Note: Unless otherwise mentioned, all vectors are in B-based coordinates. For symbols not defined in this list, see "Nomenclature" in Part I.)

$[{}_bL_{iB}]$ = Continuity matrices, defined in Eq. (2.3)

$[{}_rL_B]$ = Continuity matrix, defined in Eq. (2.12)

$[{}_sL_{iB}]$ = Continuity matrices, defined in Eq. (2.20)

$[{}_sL_B]$ = Continuity matrix, defined in Eq. (2.48)

$[L_B], [L_A]$ = Continuity matrices, defined in Eqs. (2.73) and (2.73a)

$\underline{M}_B$ = Residual magnetic moment vector

M = Element of $\underline{M}_B$, defined in Eq. (2.74)

$\underline{B}$ = The Earth's magnetic field vector

ϵ, B_3 = Elements of $\underline{B}$ defined in Eq. (2.75)

$\underline{T}_{EBM}$ = Magnetic torque vector on the body B

$\underline{T}_{EBC}$ = Eddy current torque vector on the body B

μ_0 = Permeability of the materials in the body B

c^* = Velocity of light in vacuum

$\underline{r}_c$ = Position vector of an element of the body B from the center of mass

$\underline{J}$ = Volume eddy-current density vector of the body B

σ = Static electrical conductivity of the body B

$[I_B]$ = Moment of inertia matrix of the body B

I_{B1}, I_{B2}, I_{B3} = Diagonal elements of $[I_B]$

$T_{EBC,i}$ $(i=1,2,3)$ = Elements of $\underline{T}_{EBC}$, defined in Eqs. (2.81-2.83)

ρ = Average density of the elements of the body B

$\underline{T}_{EBS}$ = Solar radiation torque on the body B, in B-based coordinates

P_e = 1×10^{-7} lbs/ft^2 for a surface normal to the Sun

ε_0 = Reflection coefficient of the body B

$\underline{n}$ = Unit outward normal vector to a surface element of the body B

$\underline{\tau}$ = Unit vector directed from the Sun

a_0, b_0, c_0 = Elements of $\underline{\tau}$ at $t = 0$

I_{EBG} = Gravity gradient torque vector on the body B

$\underline{d}$ = Unit vector towards the center of the Earth

d_1, d_2, d_3 = Elements of $\underline{d}$, defined in Eq. (2.92)

μ = The Earth's gravitational constant, 1.4082×10^6 ft^3/sec^2

R = The distance between the center of the Earth and the body B

$\underline{H}_B$ = Angular momentum vector of the body B

$\underline{r}$ = Position vector of a mass element of the body B

$\underline{h}_B$ = Angular momentum vector of rigid rotors or reaction wheels inside the body B

$\underline{T}_B^*$ = Control torque vector on the body B

T_{Bi}^*, $i = 1,2,3$ = Elements of $\underline{T}_B^*$, defined in Eq. (2.102)

$\underline{T}_B$ = Total torque vector on the body B

$[P_{Bi}]$, $i = 1$-4 = Matrices and vector, defined by Eqs. (2.104) and (2.105) for the body B

$\underline{H}_A$ = Angular momentum vector of the body A in A-based coordinates

$\underline{h}_A$ = Angular momentum vector of rigid rotors and reaction wheels inside the body A, in A-based coordinates

$\underline{T}_A^*$ = Control torque vector on the body A in A-based coordinates

T_{Ai}^*, i=1,2,3 = Elements of $\underline{T}_A^*$

$\underline{T}_{EA}$ = Environmental torque vector on the body A in A-based coordinates

$\underline{T}_A$ = Total torque vector on the body A in A-based coordinates

$[P_{Ai}]$, i = 1-4 = Matrices and vector for the body A corresponding to $[P_{Bi}]$, defined by Eq. (2.110)

$[A_{Bi}]$, i = 1-4 = Matrices and vector for the body B, defined by Eq. (2.112)

$[A_{Ai}]$, i = 1-4 = Matrices and vector for the body A defined by Eq. (2.113)

$[M_{Bi}]$, i = 1-5 = Matrices and vectors for the body B defined by Eqs. (2.115a) and (2.116b)

$[M_{Ai}]$, i = 1-5 = Matrices and vectors for the body A corresponding to $[M_{Bi}]$, and defined by Eqs. (2.123) and (2.124).

1. Introduction

We have obtained only the equations of motion of the individual structural elements in Part I. Now we shall use the continuity of displacements, rotations and moments at the junctions to reduce the dimensions of the problem. By eliminating the generalized position coordinates, equations are obtained involving only the angular velocities.

Equations (1.1) through (1.120), referred to in this Part II, were given in Part I.

2. Continuity Conditions

In the analysis thus far, only a few of the continuity conditions between the various elements of the structure have been considered. The remaining conditions will be considered now.

(a) End Mass - Beam Junctions

The condition that the sum of the beam-end mass inertia forces and the beam-end shear forces must be zero has already been introduced in the derivation of the equation of motion of these masses. The remaining conditions to be imposed are that the deflections of the tip-masses must be equal to the beam-tip deflections, i.e.,

$$Y_i = \eta_j]_{s=\ell} = [\mu_j^B]^T \cdot \{{}_b q_j\}_{s=\ell} \tag{2.1}$$

for the (i,j) pairs given by (17,1), (18,2), (19,3) and (20,4). For example, let the case $i = 17$, $j = 1$ be considered now.

Here $[\mu_1^B]^T$ is the identity matrix. So for $i = 17$, $j = 1$, Eq. (2.1) becomes

$$\begin{aligned} y_{17,1} &= q_{1,1} \\ y_{17,2} &= {}_1q_{1,2}(e^{p_1\ell}-1) + {}_2q_{1,2}\ell + {}_3q_{1,2} \\ y_{17,3} &= {}_1q_{1,3}(e^{p_1\ell}-1) + {}_2q_{1,3}\ell + {}_3q_{1,3} \cdot \end{aligned} \tag{2.2}$$

Thus, for each beam there is a relation

$$\{y_i\}_k = [{}_bL_{iB}]_{kj}\{{}_bq_j^*\} , \tag{213}$$

where $[{}_bL_{iB}]$ are constant matrices. More details of this equation for this and other end masses are given in Appendix 11.

(b) Rigid Body - Plate Junctions

The force and moment continuity conditions between the rigid bodies and the plates have already been considered in Eqs. (1.81) and (1.87). The displacement and rotation continuity equations are now obtained.

The displacements $(y_i, i = 1,2,3,4)$ of the centers of mass of the rigid bodies are taken to be the average of the plate displacements at the four points at which the rigid bodies are fixed to the plates. For the plate function which is singular at a junction point, the function is evaluated at a small distance ϵ away from that point. As an example, let the conditions for the rigid body of mass m_1 be considered here.

The four junction points of rigid body No. 1 and the plate No. 2 have their position coordinates in the plane of the plate given by α_7, α_8, α_9, and α_{10}. Then, referring to Fig. 7 and Eqs. (1.35) and (1.40), we have

$$y_1 = \frac{1}{4}[\chi_2(\alpha_7) + \chi_2(\alpha_8) + \chi_2(\alpha_9) + \chi_2(\alpha_{10})] \tag{2.4}$$

with

$$\alpha_j = r_j \exp(i\theta_j) . \tag{2.5}$$

Therefore

$$y_1 = \chi_{2,1}(t) + \frac{1}{2}\{a_{2,13}[J_0(\lambda_0 r_9) + J_0(\lambda_0 r_{10})] + a_{2,14}[(r_9-1)r_9^2$$

$$+ (r_{10}-1)r_{10}^2] + a_{2,15}[(r_9-1)r_9^3 + (r_{10}-1)r_{10}^3]$$

$$+ a_{2,7}[J_1(\lambda_1 r_9)\cos\theta_9 + J_1(\lambda_1 r_{10})\cos\theta_{10}] + a_{2,8}[(r_9-1)r_9\cos\theta_9$$

$$+ (r_{10}-1)r_{10}\cos\theta_{10}] + a_{2,9}[(r_9-1)r_9^2\cos\theta_9 + (r_{10}-1)r_{10}^2\cos\theta_{10}]$$

$$+ a_{2,1}[J_2(\lambda_2 r_9)\cos 2\theta_9 + J_2(\lambda_2 r_{10})\cos 2\theta_{10}] + a_{2,2}[(r_9-1)r_9^2\cos 2\theta_9$$

$$+ (r_{10}-1)r_{10}^2\cos 2\theta_{10}] + a_{2,3}[(r_9-1)r_9^3\cos 2\theta_9 + (r_{10}-1)r_{10}^2\cos 2\theta_{10}]\}$$

$$+ \frac{1}{4}\sum_{k=7}^{10}\sum_{j=7}^{18}\chi_{2,j}\,\psi_{2,j}(\alpha_k)\ . \qquad (2.6)$$

Similarly,

$$y_2 = \chi_{2,1}(t) + \frac{1}{2}\{a_{2,13}[J_0(\lambda_0 r_{11}) + J_0(\lambda_0 r_{12})$$

$$+ a_{2,14}[(r_{11}-1)r_{11}^2 + (r_{12}-1)r_{12}^2] + a_{2,15}[(r_{11}-1)r_{11}^3 + (r_{12}-1)r_{12}^3]$$

$$+ a_{2,7}[J_1(\lambda_1 r_{11})\cos\theta_{11} + J_1(\lambda_1 r_{12})\cos\theta_{12}]$$

$$+ a_{2,8}[(r_{11}-1)r_{11}\cos\theta_{11} + (r_{12}-1)r_{12}\cos\theta_{12}]$$

$$+ a_{2,9}[(r_{11}-1)r_{11}^2\cos\theta_{11} + (r_{12}-1)r_{12}^2\cos\theta_{12}]$$

$$+ a_{2,1}[J_2(\lambda_2 r_{11})2\cos\theta_{11} + J_2(\lambda_2 r_{12})2\cos\theta_{12}]$$

$$+ a_{2,2}[(r_{11}-1)r_{11}^2\cos 2\theta_{11} + (r_{12}-1)r_{12}^2\cos 2\theta_{12}]$$

$$+ a_{2,3}[(r_{11}-1)r_{11}^3\cos 2\theta_{11} + (r_{12}-1)r_{12}^3\cos 2\theta_{12}]\}$$

$$+ \frac{1}{4}\sum_{k=11}^{14}\sum_{j=7}^{18}\chi_{2,j}\,\psi_{2,j}(\alpha_k)\ . \qquad (2.7)$$

The rotational continuity conditions are now obtained for the rigid body No. 1. Again, referring to Figure 7 and Eqs. (1.35), (1.40) and (1.77), we have

$$\theta_{1,1} = \frac{1}{2\ell_\theta}[\chi_2(\alpha_9) + \chi_2(\alpha_{10}) - \chi_2(\alpha_7) - \chi_2(\alpha_8)] \tag{2.8}$$

$$\theta_{1,2} = \frac{1}{2\ell_r}[\chi_2(\alpha_8) + \chi_2(\alpha_9) - \chi_2(\alpha_7) - \chi_2(\alpha_{10})] \, . \tag{2.9}$$

Similarly, for the second rigid body, we have

$$\theta_{2,1} = \frac{1}{2\ell_\theta}[\chi_2(\alpha_{11}) + \chi_2(\alpha_{12}) - \chi_2(\alpha_{13}) - \chi_2(\alpha_{14})] \tag{2.10}$$

and

$$\theta_{2,2} = \frac{1}{2\ell_r}[\chi_2(\alpha_{11}) + \chi_2(\alpha_{14}) - \chi_2(\alpha_{12}) - \chi_2(\alpha_{13})] \, . \tag{2.11}$$

Combining Eqs. (2.6) through (2.11), the displacement and rotation continuity conditions for the two rigid bodies are obtained as

$$\begin{Bmatrix} {}^{*}q_1 \\ {}^{*}q_2 \end{Bmatrix} = [{}_rL_B] \, {}_pq_2^{*} \tag{2.12}$$

where $[{}_rL_B]$ is a matrix of constants.

(c) Beam-shell Junctions

The in-plane rotation of the shell and therefore the inplane moment have been assumed to be zero. The force continuity in the radial direction has already been considered while deriving the equations for the beam-end masses. The continuity conditions for the shear forces in the transverse direction of the beams are neglected, as the shell displacements in those directions are taken to be zero. The remaining continuity conditions for each beam-shell junction are three displacements, two rotations and two moments.

(i) Displacement relations—Referring to Eqs. (1.3) and (1.59), the displacement relations at the junction point $z_1 = \rho_i$ and $\theta = \theta_i$ are given by

$$ {}_3q_{i,2} = 0 \tag{2.13} $$

$$ {}_3q_{i,3} = 0 \tag{2.14} $$

$$ \begin{aligned} q_{i,1} = {} & b_1(t) + (z_1+\rho')(z_1-\rho'')[b_2(t)e^{p_2\rho_i} + b_3(t)e^{p_3\rho_i}] \\ & + b_4(t)\ \sin\frac{\pi(\rho'+\rho_i)}{\ell_1}\cos\theta_i + b_5(t)\ \sin\frac{2\pi(\rho'+\rho_i)}{\ell_1}\cos\theta_i \\ & + b_6(t)\ \sin\frac{\pi(\rho'+\rho_i)}{\ell_1}\sin\theta_i + b_7(t)\ \sin\frac{2\pi(\rho'+\rho_i)}{\ell_1}\sin\theta_i \\ & + b_8(t)\ \sin\frac{\pi(\rho'+\rho_i)}{\ell_1}\cos 2\theta_i + b_9(t)\ \sin\frac{2\pi(\rho'+\rho_i)}{\ell_1}\cos 2\theta_i \\ & + b_{10}(t)\ \sin\frac{\pi(\rho'+\rho_i)}{\ell_1}\sin 2\theta_i + b_{11}(t)\ \sin\frac{2\pi(\rho'+\rho_i)}{\ell_1}\sin 2\theta_i\ . \end{aligned} \tag{2.15} $$

(ii) Rotation relations—The conditions that the slopes of the beams at the joints are equal to the slopes of the shell there, are

$$ {}_2q_{i,2} + p_1[{}_1q_{i,2}] = \frac{1}{a_B}\frac{\partial \xi_{B,r}}{\partial\theta}\Big]_{\substack{z_1=\rho_i \\ \theta=\theta_i}} $$

$$ {}_2q_{i,3} + p_1[{}_1q_{i,3}] = \frac{1}{a_B}\frac{\partial \xi_{B,r}}{\partial\theta}\Big]_{\substack{z_1=\rho_i \\ \theta=\theta_i}} $$

from which

$$
\begin{aligned}
{}_2q_{i,2} &= -p_1[{}_1q_{i,2}] + \frac{1}{a_B}\frac{\partial \xi_{B,r}}{\partial \theta}\Bigg]_{\substack{z_1=\rho_i \\ \theta=\theta_i}} \\
{}_2q_{i,3} &= -p_1[{}_1q_{i,3}] + \frac{1}{a_B}\frac{\partial \xi_{B,r}}{\partial \theta}\Bigg]_{\substack{z_1=\rho_i \\ \theta=\theta_i}} \qquad (2.16)
\end{aligned}
$$

(iii) Moment relations—The bending moments on the i^{th} beam at the junction are given by

$$
\begin{aligned}
M_2 &= -({}_bE_i)({}_bI_{i,3})p_1^2({}_1q_{i,2}) \\
\text{and} \qquad & \qquad (2.17) \\
M_3 &= -({}_bE_i)({}_bI_{i,3})p_1^2({}_1q_{i,3}) \ .
\end{aligned}
$$

The bending moments on the shell at the junction in the tangential and axial directions are given by

$$
M_\theta = -\frac{{}_sE_B \cdot {}_sh_B^3}{12(1-{}_s\mu_B^2)a_B^2}\left[\frac{\partial^2 \xi_{B,r}}{\partial \theta^2} + {}_s\mu_B \frac{\partial^2 \xi_{B,r}}{\partial z_1^2}\right]_{\substack{z_1=\rho_i \\ \theta=\theta_i}}
$$

and

$$
M_z = -\frac{{}_sE_B \cdot {}_sh_B^3}{12(1-{}_s\mu_B^2)a_B^2}\left[\frac{\partial^2 \xi_{B,r}}{\partial z_1^2} + {}_s\mu_B \frac{\partial^2 \xi_{B,r}}{\partial \theta^2}\right]_{\substack{z_1=\rho_i \\ \theta=\theta_i}} \ . \qquad (2.18)
$$

Now, setting

$$
\begin{Bmatrix} M_2 \\ M_3 \end{Bmatrix} = \begin{Bmatrix} M_\theta \\ M_z \end{Bmatrix} \qquad (2.19)
$$

the moment relations are obtained.

Combining the Eqs. (2.13) through (2.19), the complete shell-beam junction continuity conditions for the i^{th} beam are given by the relation

$$\{{}_b q_i^*\} = [{}_s L_{iB}]\{{}_s q_B^*\} \tag{2.20}$$

where $[{}_s L_{iB}]$ are constant matrices.

(d) Plate-shell Junctions

In this problem the force continuity conditions at the plate-shell junction are neglected because the plate and shell displacements are assumed to be zero there. Only the displacement, slope and moment conditions will be set up. The corresponding equations will be obtained for each harmonic.

(i) Displacement relations—Let the Eqs. (1.34) and (1.59) be used to obtain the relations for the junction between the plate No. 1 and the shell B.

As the in-plane plate displacement is zero, so

$$b_1(t) = 0 \ . \tag{2.21}$$

Again as the shell axial displacement is zero, so

$$\chi_{1,1}(t) = 0 \ . \tag{2.22}$$

As all the other terms of the Eqs. (1.34) and (1.59) are zero on the boundary, so the shell and plate displacements are matched at the junction. Similarly for the boundary condition at the other end of the shell, one must have

$$\chi_{2,1}(t) = 0 \ . \tag{2.23}$$

(ii) Rotational relations—At the boundary, it is assumed that the joint is rigid, and the plate and the shell rotate by equal amounts. Therefore the relations are

$$-\frac{1}{a_B}\frac{\partial \chi_1}{\partial r}\Big]_{r=1} = \frac{1}{a_B}\frac{\partial \xi_{B,r}}{\partial z_1}\Big]_{z_1=\rho''} \tag{2.24}$$

and

$$-\frac{1}{a_B}\left[\frac{\partial \chi_2}{\partial r}\right]_{r=1} = \frac{1}{a_B}\left[\frac{\partial \xi_{B,r}}{\partial z_1}\right]_{z_1=-\rho'} . \tag{2.25}$$

To evaluate the Eqs. (2.24) and (2.25), the following result is to be noted:

$$\left[\frac{\partial \psi_{i,j}}{\partial r}\right]_{r=1} = 2(1 - \alpha_j \bar{\alpha}_j) \tag{2.26}$$

where $\psi_{i,j} = \psi_{i,j}(r,\theta,\alpha_j)$ is the plate displacement function exemplified by Eq. (1.38).

Equating the terms independent of θ in Eqs. (2.24) and (2.25), we obtain the relations

$$-\lambda_0 a_{1,13} J_1(\lambda_0) + a_{1,14} + a_{1,15} + \chi_{1,7} + 2\sum_{j=8}^{11}(1 - r_j^2)\chi_{1,j}$$

$$= -\ell_1[b_2(t)e^{p_2\rho''} + b_3(t)e^{p_3\rho''}] \tag{2.27}$$

and

$$-\lambda_0 a_{2,13} J_1(\lambda_0) + a_{2,14} + a_{2,15} + 2\sum_{j=7}^{18}(1 - r_j^2)\chi_{2,j}$$

$$= \ell_1[b_2(t)e^{-p_2\rho'} + b_3(t)e^{-p_3\rho'}] . \tag{2.28}$$

Similarly, equating the coefficients of $\cos\theta$ in Eqs. (2.24) and (2.25), we obtain

$$a_{1,7}\lambda_1 J_0(\lambda_1) + a_{1,8} + a_{1,9} = \frac{\pi}{\ell_1}[b_4 - 2b_5] \tag{2.29}$$

$$a_{2,7}\lambda_1 J_0(\lambda_1) + a_{2,8} + a_{2,9} = -\frac{\pi}{\ell_1}[b_4 + 2b_5] . \tag{2.30}$$

Equating the coefficients of $\sin\theta$, we get

$$a_{1,10}\lambda_1 J_0(\lambda_1) + a_{1,11} + a_{1,12} = \frac{\pi}{\ell_1}[b_6 - 2b_7] \tag{2.31}$$

$$a_{2,10}\lambda_1 J_0(\lambda_1) + a_{2,11} + a_{2,12} = -\frac{\pi}{\ell_1}[b_6 + 2b_7] . \tag{2.32}$$

The coefficients of $\cos 2\theta$ are equated to give

$$a_{1,1}\lambda_2 J_1(\lambda_2) + a_{1,2} + a_{1,3} = \frac{\pi}{\ell_1}[b_8 - 2b_9] \tag{2.33}$$

$$a_{2,1}\lambda_2 J_1(\lambda_2) + a_{2,2} + a_{2,3} = -\frac{\pi}{\ell_1}[b_8 + 2b_9] \ . \tag{2.34}$$

Similarly, the coefficients of $\sin 2\theta$ generate the relations

$$a_{1,4}\lambda_2 J_1(\lambda_2) + a_{1,5} + a_{1,6} = \frac{\pi}{\ell_1}[b_{10} - 2b_{11}] \tag{2.35}$$

$$a_{2,4}\lambda_2 J_1(\lambda_2) + a_{2,5} + a_{2,6} = -\frac{\pi}{\ell_1}[b_{10} + 2b_{11}] \ . \tag{2.36}$$

Now from the Eqs. (2.21) and (2.27) through (2.36), the shell displacements are given by

$$b_1(t) = 0 \tag{2.37}$$

$$b_2(t) = \frac{1}{\ell_1}[e^{(p_3\rho''-p_2\rho')} - e^{(p_2\rho''-p_3\rho')}]^{-1}\left\{e^{-p_3\rho'}[-\lambda_0 J_1(\lambda_0)a_{1,13} + a_{1,14} + a_{1,15} + \chi_{1,7} + 2\sum_{j=8}^{11}(1-r_j^2)\chi_{1,j}] + e^{p_3\rho''}[-\lambda_0 J_1(\lambda_0)a_{2,13} + a_{2,14} + a_{2,15} + 2\sum_{j=7}^{18}(1-r_j^2)\chi_{2,j}]\right\} \tag{2.38}$$

$$b_3(t) = \frac{1}{\ell_1}[e^{(p_2\rho''-p_3\rho')} - e^{(p_3\rho''-p_2\rho')}]^{-1}\left\{e^{-p_2\rho'}[-\lambda_0 J_1(\lambda_0)a_{1,13} + a_{1,14} + a_{1,15} + \chi_{1,7} + 2\sum_{j=8}^{11}(1-r_j^2)\chi_{1,j}] + e^{p_2\rho''}[-\lambda_0 J_1(\lambda_0)a_{2,13} + a_{2,14} + a_{2,15} + 2\sum_{j=7}^{18}(1-r_j^2)\chi_{2,j}]\right\} \tag{2.39}$$

$$b_4(t) = \frac{\ell_1}{2\pi}[\lambda_1 J_0(\lambda_1)(a_{1,7} - a_{2,7}) + a_{1,8} + a_{1,9} - a_{2,8} - a_{2,9}] \tag{2.40}$$

$$b_5(t) = -\frac{\ell_1}{4\pi}[\lambda_1 J_0(\lambda_1)(a_{1,7} + a_{2,7}) + a_{1,8} + a_{1,9} + a_{2,8} + a_{2,9}] \quad (2.41)$$

$$b_6(t) = \frac{\ell_1}{2\pi}[\lambda_1 J_0(\lambda_1)(a_{1,10} - a_{2,10}) + a_{1,11} + a_{1,12} - a_{2,11} - a_{2,12}] \quad (2.42)$$

$$b_7(t) = -\frac{\ell_1}{4\pi}[\lambda_1 J_0(\lambda_1)(a_{1,10} + a_{2,10}) + a_{1,11} + a_{1,12} + a_{2,11} + a_{2,12}] \quad (2.43)$$

$$b_8(t) = \frac{\ell_1}{2\pi}[\lambda_2 J_1(\lambda_2)(a_{1,1} - a_{2,1}) + a_{1,2} + a_{1,3} - a_{2,2} - a_{2,3}] \quad (2.44)$$

$$b_9(t) = -\frac{\ell_1}{4\pi}[\lambda_2 J_1(\lambda_2)(a_{1,1} + a_{2,1}) + a_{1,2} + a_{1,3} + a_{2,2} - a_{2,6}] \quad (2.45)$$

$$b_{10}(t) = \frac{\ell_1}{2\pi}[\lambda_2 J_1(\lambda_2)(a_{1,4} - a_{2,4}) + a_{1,5} + a_{1,6} - a_{2,5} - a_{2,6}] \quad (2.46)$$

$$b_{11}(t) = -\frac{\ell_1}{4\pi}[\lambda_2 J_1(\lambda_2)(a_{1,4} + a_{2,4}) + a_{1,5} + a_{1,6} + a_{2,5} + a_{2,6}] \quad (2.47)$$

Equations (2.37) through (2.47) is rewritten as

$$\{{}_sq_B^*\} = [{}_sL_B]\{{}_pq^*\} \quad (2.48)$$

where

$$\{{}_pq^*\} = [{}_pq_1^*, {}_pq_2^*]^T \quad (2.49)$$

and $[{}_sL_B]$ is a constant matrix.

(iii) Moment relations—The moment relations are obtained by summing to zero the radial bending moment on the plates and the axial bending moment on the shell at the shell-plate junctions. Thus the relations become

$$\frac{1}{a_\beta^2} \cdot {}_pD_1 \left[\frac{\partial^2\chi_1}{\partial r^2} + {}_p\mu_1\left(\frac{1}{r}\frac{\partial\chi_1}{\partial r} + \frac{1}{r^2}\frac{\partial^2\chi_1}{\partial\theta^2}\right)\right]_{r=1} = -\frac{{}_sE_B \cdot {}_sh_B^3}{12(1-{}_s\mu_B^2)a_B^2}\left[\frac{\partial^2\xi_{B,r}}{\partial z_1^2} + {}_s\mu_B\frac{\partial^2\xi_{B,r}}{\partial\theta^2}\right]_{z_1=\rho''} \quad (2.50)$$

and

$$\frac{1}{a_B^2}\,{}_pD_2\left[\frac{\partial^2\chi_2}{\partial r^2}+{}_p\mu_2\left(\frac{1}{r}\frac{\partial\chi_2}{\partial r}+\frac{1}{r^2}\frac{\partial^2\chi_2}{\partial\theta^2}\right)\right]_{r=1}$$

$$=-\frac{{}_sE_B\cdot{}_sh_B}{12(1-{}_s\mu_B^2)a_B^2}\left[\frac{\partial^2\xi_{B,r}}{\partial z_1^2}+{}_s\mu_B\frac{\partial^2\xi_{B,r}}{\partial\theta^2}\right]_{z_1=-\rho'}.$$

To evaluate Eqs. (2.50) and (2.51), the following results are to be used. If $\psi_{i,j}(r,\theta,\alpha)$ are the plate displacement functions, one of which is shown in Eq. (1.38), then

$$\left[\frac{\partial^2\psi_{i,j}}{\partial r^2}\right]_{r=1}=2(1-r_j^2)+4\frac{(1-r_j^2)^2}{1-2r_j\cos(\theta-\theta_j)+r_j^2} \tag{2.52}$$

$$\frac{1}{2\pi}\int_{-\pi}^{\pi}\frac{1-r_j^2}{1-2r_j\cos(\theta-\theta_j)+r_j^2}\,d\theta=1\quad\text{for}\quad 0<r_j<1 \tag{2.53}$$

$$\frac{1}{2\pi}\int_{-\pi}^{\pi}\frac{(1-r_j^2)\cos\theta}{1-2r_j\cos(\theta-\theta_j)+r_j^2}\,d\theta=r_j\cos\theta_j \tag{2.54}$$

$$\frac{1}{2\pi}\int_{-\pi}^{\pi}\frac{(1-r_j^2)\sin\theta}{1-2r_j\cos(\theta-\theta_j)+r_j^2}\,d\theta=r_j\sin\theta_j \tag{2.55}$$

$$\frac{1}{2\pi}\int_{-\pi}^{\pi}\frac{(1-r_j^2)\cos 2\theta}{1-2r_j\cos(\theta-\theta_j)+r_j^2}\,d\theta=r_j^2\cos 2\theta_j \tag{2.56}$$

$$\frac{1}{2\pi}\int_{-\pi}^{\pi}\frac{(1-r_j^2)\sin 2\theta}{1-2r_j\cos(\theta-\theta_j)+r_j^2}\,d\theta=r_j^2\sin 2\theta_j \tag{2.57}$$

$$\frac{1}{r^2}\left[\frac{\partial^2\psi_{i,j}}{\partial\theta^2}\right]_{r=1}=2(1-r_j^2) \tag{2.58}$$

and

$$\frac{1}{r}\left[\frac{\partial\psi_{i,j}}{\partial r}\right]_{r=1}=2(1-r_j^2). \tag{2.26}$$

The values of χ_1, χ_2 and $\xi_{B,r}$ given by Eqs. (1.34), (1.40) and (1.59) are now substituted in Eqs. (2.50) and (2.51). Then the terms independent of θ and the coefficients of different harmonics are equated separately.

Equating the terms independent of θ in Eq. (2.50), we obtain

$$
\begin{aligned}
&{}_pD_1\{a_{1,13}(1-{}_p\mu_1)\lambda_0 J_1(\lambda_0) + a_{1,14}(4+{}_p\mu_1) + a_{1,15}(6+{}_p\mu_1) + \chi_{1,7}(3+{}_p\mu_1) \\
&\quad + \sum_{j=8}^{11} [2(1-r_j^2)(3+2\ {}_p\mu_1)\chi_{1,j}]\} \\
&\quad = -\frac{{}_sE_B \cdot {}_sh_B^3}{12(1-{}_s\mu_B^2)}[2(1+p_2\ell_1)e^{p_3\rho''}b_2 + 2(1+p_3\ell_1)e^{p_3\rho''}b_3] \cdot \qquad (2.59)
\end{aligned}
$$

Similarly, from Eq. (2.51), we obtain

$$
\begin{aligned}
&{}_pD_2\{a_{2,13}(1-{}_p\mu_2)\lambda_0 J_1(\lambda_0) + a_{2,14}(4+{}_p\mu_2) + a_{2,15}(6+{}_p\mu_2) \\
&\quad + \sum_{j=7}^{18} [2(1-r_j^2)(3 + 2\ {}_p\mu_2)\chi_{2,j}]\} \\
&\quad = -\frac{{}_sE_B \cdot {}_sh_B^3}{12(1-{}_s\mu_B^2)} [2(1 - p_2\ell_1)e^{-p_2\rho'}b_2 + 2(1 - p_3\ell_1)e^{-p_3\rho'}b_3] \ . \qquad (2.60)
\end{aligned}
$$

To obtain the equations for the harmonic components in Eq. (2.50) and (2.51), these two equations are multiplied successively by $\cos\theta$, $\sin\theta$, $\cos 2\theta$ and $\sin 2\theta$ and integrated with respect to θ between the limits $(-\pi,\pi)$. This operation on Eq. (2.50) generates the following four equations:

$$
\begin{aligned}
&{}_pD_1\{\lambda_1 J_0(\lambda_1)({}_p\mu_1 - 1)a_{1,7} + (2 + {}_p\mu_1)a_{1,8} + (4 + {}_p\mu_1)a_{1,9} \\
&\quad + 8\sum_{j=8}^{11} [(1 - r_j^2)r_j\cos\theta_j\ \chi_{1,j}]\} = 0 \qquad (2.61)
\end{aligned}
$$

$$ {}_pD_1\{\lambda_1 J_0(\lambda_1)({}_p\mu_1-1)a_{1,10} + (2+{}_p\mu_1)a_{1,1} + (4+{}_p\mu_1)a_{1,12} $$

$$ + 8\sum_{j=8}^{11}[(1-r_j^2)r_j \sin\theta_j \chi_{1,j}]\} = 0 \qquad (2.62) $$

$$ {}_pD_1\{\lambda_2 J_1(\lambda_2)({}_p\mu_1-1)a_{1,1} + (4+{}_p\mu_1)a_{1,2} + (6+{}_p\mu_1)a_{1,3} $$

$$ + 8\sum_{j=8}^{11}[(1-r_j^2)r_j \cos 2\theta_j \chi_{1,j}]\} = 0 \qquad (2.63) $$

$$ {}_pD_1\{\lambda_2 J_1(\lambda_2)({}_p\mu_1-1)a_{1,4} + (4+{}_p\mu_1)a_{1,5} + (6+{}_p\mu_1)a_{1,6} $$

$$ + 8\sum_{j=8}^{11}[(1-r_j^2)r_j \sin 2\theta_j \chi_{1,j}]\} = 0\,. \qquad (2.64) $$

In a similar way, the following four equations are generated from Eq. (2.51):

$$ \lambda_1 J_0(\lambda_1)({}_p\mu_2 - 1)a_{2,7} + (2 + {}_p\mu_2)a_{1,8} + (4 + {}_p\mu_2)a_{1,9} $$

$$ +8\sum_{j=7}^{18}[(1-r_j^2)r_j^2 \cos\theta_j \chi_{2,j}] = 0 \qquad (2.65) $$

$$ \lambda_1 J_0(\lambda_1)({}_p\mu_2 - 1)a_{2,10} + (2 + {}_p\mu_2)a_{2,11} + (4 + {}_p\mu_2)a_{2,12} $$

$$ + 8\sum_{j=7}^{18}[(1-r_j^2)r_j^2 \sin\theta_j \chi_{2,j}] = 0 \qquad (2.66) $$

$$ \lambda_2 J_1(\lambda_2)({}_p\mu_2 - 1)a_{2,1} + (4 + {}_p\mu_2)a_{2,2} + (6 + {}_p\mu_2)a_{2,3} $$

$$ + 8\sum_{j=7}^{18}[(1-r_j^2)r_j^2 \cos 2\theta_j \chi_{2,j}] = 0 \qquad (2.67) $$

$$\lambda_2 J_1(\lambda_2)({}_p\mu_2 - 1)a_{2,4} + (4 + {}_p\mu_2)a_{2,5} + (6 + {}_p\mu_2)a_{2,6}$$

$$+ 8 \sum_{j=7}^{18} [(1 - r_j^2)r_j^2 \sin 2\theta_j \chi_{2,j}] = 0 \quad . \tag{2.68}$$

This completes the derivation of the continuity conditions for the individual elements.

(e) Remarks on Reduction of Dimensions

We shall determine the effect of the continuity conditions on the total number of the degrees of freedom in our complex structure.

From Eq. (2.48), it is seen that the shell coordinates can be expressed as a linear combination of the coordinates of the two plates, i.e.,

$$\{{}_s q_B^*\} = [{}_s L_B^*]\{{}_p q^*\} \quad . \tag{2.48}$$

From Eqs. (2.20) and (2.48), we have

$$\{{}_b q_i^*\} = [{}_s L_{iB}]\{{}_s q_B^*\} = [{}_s L_{iB}][{}_s L_B^*]\{{}_p q^*\} \quad . \tag{2.69}$$

This shows that the beam coordinates can be expressed in terms of the plate coordinates. The quation (2.12) states that the rigid body coordinates can also be expressed in terms of the plate coordinates, which are

$$[{}_r q_1^*, {}_r q_2^*]^T = [0; {}_r L_B]\{{}_p q^*\} \quad . \tag{2.70}$$

From Eqs. (2.3) and (2.69) the coordinates of the beam-end masses can be expressed in terms of the plate coordinates by the relation

$$\{y_i\} = [{}_b L_{iB}][{}_s L_{iB}][{}_s L_B^*]\{{}_p q^*\} \quad . \tag{2.71}$$

All these relations show that only the spring-mass-damper coordinates cannot be expressed in terms of the plate coordinates.

When Eqs. (2.38) and (2.39) are substituted into Eqs. (2.59) and (2.60), we obtain two relations between the plate coordinates themselves. So

Eqs. (2.59) through (2.68) and Eqs. (2.22) and (2.23) supply 12 dependence relations between the 28 + 21 = 49 coordinates for the two plates. This means that only 49 - 12 = 37 plate coordinates are independent, and the rest are dependent. These dependence relations are defined by an equation of the form

$$\{{}_p q^*\} = [{}_p L_B]\{{}_p q\} \tag{2.72}$$

where $\{{}_p q\}$ is a (37 × 1) column and $[{}_p L_B]$ is a (49 × 37) constant matrix. Since there are four spring-mass-damper coordinates, the motion of the body B is defined by the (41 × 1) vector $\{q_B\}$. So the originally mentioned (110 × 1) vector $\{q_B^*\}$ is given by

$$\{q_B^*\} = [L_B]\{q_B\} \tag{2.73}$$

where $[L_B]$ is a (110 × 41) constant matrix and is composed of matrices $[{}_p L_B]$, $[{}_s L_B^*]$, $[{}_s L_{ib}]$, $[{}_b L_{iB}]$ and $[{}_r L_B]$.

The equation for the body A is similarly given by

$$\{q_A^*\} = [L_A]\{q_A\} \ . \tag{2.73a}$$

3. External Torques

It has been assumed that the external forces on the satellite are negligible. The center of mass of the satellite remains static. But the existence of external torques cannot be neglected. The basic method of modelling the external torques follows that shown by Dobrotin, et al.[1] and Tidwell [2]. These torque models are derived for the body B. The torques for the body A are derived similarly.

(a) Residual Magnetic Torque

The flow of electric current in the electric circuits inside the space-

craft reacts with the Earth's magnetic field to create this torque on the spacecraft.

Let $\underline{M}_B$ be the residual magnetic moment vector of the body B in the B-based coordinates. Let $\underline{B}$ be the Earth's megnetic field vector in the B-based coordinates. The elements of $\underline{M}_B$ and $\underline{B}$ are assumed to be of the form

$$\{M_B\} = [M, M, M]^T \tag{2.74}$$

$$\{B\} = [\varepsilon \cos \omega_{B,3}t, -\varepsilon \sin \omega_{B,3}t, B_3]^T \ . \tag{2.75}$$

Then the external magnetic torque on the body B is given by

$$\underline{T}_{EBM} = \underline{M}_B \times \underline{B} = M \begin{Bmatrix} (B_3 + \varepsilon \sin \omega_{B,3}t) \\ (\varepsilon \cos \omega_{B,3}t - B_3 \\ -\varepsilon(\sin \omega_{B,3}t + \cos \omega_{B,3}t) \end{Bmatrix} \ . \tag{2.76}$$

(b) Eddy Current Torque

Eddy currents are induced in a satellite spinning in the Earth's magnetic field. These eddy currents in turn react with the surrounding magnetic field to create a torque on the satellite. The eddy current torques on the body B are given by a volume integral over the body B, as follows:

$$\underline{T}_{EBC} = \frac{1}{\mu_0 c^*} \int \underline{r}_c \times (\underline{J} \times \underline{B}) dv \tag{2.77}$$

where

μ_0 = the permeability of structural material of the satellite,

c^* = the speed of light in vacuum,

$\underline{r}_c$ = the position vector of a volume element from the center of mass

$\underline{J}$ = the volume eddy current density.

All vectors in Eq. (2.77) are in the B-based coordinates. The vector $\underline{J}$ is, in turn, given by

$$\underline{J} = \frac{1}{2\mu_0\sigma}(\underline{\omega}_B \times \underline{B}) \times \underline{r}_c + \underline{\nabla}\phi \tag{2.78}$$

where σ = the static electrical conductivity of the satellite material,

$\underline{\nabla}$ = the operator for spatial gradient,

and ϕ = a scalar potential for the body such that $\nabla^2\phi = 0$ and $\frac{\partial\phi}{\partial n} = 0$ on the bounding surfaces of the satellite.

In this problem the field of ϕ is the thin plates ahd shells. Therefore, ϕ is nearly a constant. This reduces Eq. (2.77) to the following form:

$$\underline{T}_{EBC} = \frac{1}{2\mu_0^2\sigma c^*}\int \underline{r}_c \times \{[(\underline{\omega}_B \times \underline{B}) \times \underline{r}_c] \times \underline{B}\}dv$$

$$= \frac{1}{2\mu_0^2\sigma c^*}\int \underline{r}_c \times \{[(\underline{\omega}_B \cdot \underline{r}_c)\underline{B} - (\underline{B} \cdot \underline{r}_c)\underline{\omega}_B] \times B\}dv$$

$$= \frac{1}{2\mu_0^2\sigma c^*}\int \{(\underline{\omega}_B \cdot \underline{r}_c)[\underline{r}_c \times (\underline{B} \times \underline{B})] - (\underline{B} \cdot \underline{r}_c)[\underline{r}_c \times (\underline{\omega}_B \times \underline{B})]\}dv$$

or

$$\underline{T}_{EBC} = -\frac{1}{2\mu_0^2\sigma c^*}\int (\underline{B} \cdot \underline{r}_c)[(\underline{r}_c \cdot \underline{B})\underline{\omega}_B - (\underline{r}_c \cdot \underline{\omega}_B)\underline{B}]dv \ . \tag{2.79}$$

It is now assumed that the moment of inertia matrix of the body B has the form

$$[I_B] = \begin{bmatrix} I_{B1} & 0 & 0 \\ 0 & I_{B2} & 0 \\ 0 & 0 & I_{B3} \end{bmatrix} \ . \tag{2.80}$$

Hence Eq. (2.79) reduces to

$$T_{EBC,1} = -\frac{1}{2\mu_0^2\sigma c^*\rho}[\varepsilon^2(\omega_{B,1}\sin^2\omega_{B,3}t + \frac{1}{2}\omega_{B,2}\sin 2\omega_{B,3}t)I_{B2}$$

$$+ (B_3^2\omega_{B,1} - B_3\omega_{B,3}\varepsilon\cos\omega_{B,3}t)I_{B3}] \tag{2.81}$$

$$T_{EBC,2} = -\frac{1}{2\mu_0^2\sigma c^* \rho}\left[\varepsilon^2(\omega_{B,2}\cos^2\omega_{B,3}t + \frac{1}{2}\omega_{B,1}\sin 2\omega_{B,3}t)I_{B1}\right.$$

$$\left. + (B_3^2\,\omega_{B,2} + B_3\omega_{B,3}\varepsilon\,\sin\omega_{B,3}t)I_{B,3}\right] \tag{2.82}$$

$$\underline{T}_{EBC,3} = -\frac{1}{2\mu_0^2\sigma c^* \rho}\left[(\varepsilon^2\omega_{B,3}\cos^2\omega_{B,3}t - B_3\varepsilon\omega_{B,1}\cos\omega_{B,3}t)I_{B1}\right.$$

$$\left. + (\varepsilon^2\omega_{B,3}\sin^2\omega_{B,3}t + B_3\varepsilon\omega_{B,2}\sin\omega_{B,3}t)I_{B2}\right] \tag{2.83}$$

where

$$\underline{T}_{EBC} = [T_{EBC,1},\ T_{EBC,2},\ T_{EBC,3}]^T \tag{2.84}$$

and ρ is the average density of the structural materials. Using the conditions that $\omega_{B,1}$ and $\omega_{B,2}$ are small compared to $\omega_{B,3}$ and ε is small compared to B_3, the Eqs. (2.81), (2.82) and (2.83) are simplified to

$$\underline{T}_{EBC} = \frac{1}{2\mu_0^2\sigma c^* \rho}\begin{Bmatrix}(B_3\varepsilon\omega_{B,3}\cos\omega_{B,3}t - B_3^2\,\omega_{B,1})I_{B,3}\\ -(B_3\varepsilon\omega_{B,3}\sin\omega_{B,3}t + B_3^2\,\omega_{B,2})I_{B,3}\\ 0\end{Bmatrix} \tag{2.85}$$

(c) Solar Radiation Torque

The solar radiation torque arises from the asymmetric pressure distribution developed on the surfaces of the satellite due to the electromagnetic radiation from the Sun. The formulae used here are taken from Beletskii [3].

The radiation torque vector, $\underline{T}_{EBS}$, on the body B, is given by the following integrals over the surface of the body B exposed to the Sun.

$$\underline{T}_{EBS} = P_e\{(1 - \varepsilon_0)[\underline{\tau} \times \int \underline{r}_c(\underline{n}\cdot\underline{\tau})ds] + \varepsilon_0[2\int \underline{n} \times \underline{r}_c(\underline{n}\cdot\underline{\tau})^2 ds]\} \tag{2.86}$$

In Eq. (2.86), all vectors are in the B-based coordinates, and

P_e = a constant = 1×10^{-7} lbs/ft^2 for a surface normal to the Sun,

ε_0 = the reflection coefficient of the body,

$\underline{n}$ = the unit outward normal to the surface element,

$\underline{\tau}$ = the unit vector directed from the Sun,

$\underline{r}_c$ = the position vector of the surface element from the center of the body B.

In this analysis, it is assumed that the angle of incidence of the solar radiation is large on the plates, which are also highly reflective. This assumption allows us to consider that the plate surfaces produce negligible torque, so the integrals in Eq. (2.86) are taken over the surface of the shell only.

Let

$$\underline{\tau}_0 = [a_0, b_0, c_0]^T$$

be the direction cosines of the sun-vector at the time $t = 0$. Then

$$\underline{\tau} = \begin{bmatrix} \cos \omega_{B,3}t & \sin \omega_{B,3}t & 0 \\ -\sin \omega_{B,3}t & \cos \omega_{B,3}t & 0 \\ 0 & 0 & 1 \end{bmatrix} \begin{bmatrix} a_0 \\ b_0 \\ c_0 \end{bmatrix}$$

or

$$\underline{\tau} = \begin{bmatrix} (a_0 \cos \omega_{B,3}t + b_0 \sin \omega_{B,3}t) \\ (-a_0 \sin \omega_{B,3}t + b_0 \cos \omega_{B,3}t) \\ c_0 \end{bmatrix} . \tag{2.87}$$

Let the unit outward normal on the shell element be given by

$$\underline{n} = [\cos\theta, \sin\theta, 0]^T .$$

Then

$$\underline{n} \cdot \underline{\tau} = \cos\theta(a_0 \cos \omega_{B,3}t + b_0 \sin \omega_{B,3}t) + \sin\theta(-a_0 \sin \omega_{B,3}t + b_0 \cos \omega_{B,3}t).$$

Now, using Eq. (2.88) and taking

$$\underline{r}_c = [a_B\cos\theta,\ a_B\sin\theta,\ a_B z_1]^T$$

Eq. (2.86) is reduced to the following form:

$$\underline{T}_{EBS} = P_e \cdot a_B^3(1-\varepsilon_0)\begin{bmatrix} \{a_0[(\rho'')^2-(\rho')^2]-\ell_1 c_0\omega_{B,3}t\}\{-a_0\sin\omega_{B,3}t + b_0\cos\omega_{B,3}t\} \\ \{\ell_1 c_0\omega_{B,3}t - a_0[(\rho'')-(\rho')^2]\}\{a_0\cos\omega_{B,3}t + b_0\sin\omega_{B,3}t\} \\ 0 \end{bmatrix}$$

$$- \frac{2}{3} P_e \cdot \varepsilon_0 \cdot a_B^3[(\rho'')^2-(\rho')^2](2a_0^2 + b_0^2)\begin{bmatrix} \sin\omega_{B,3}t \\ \cos\omega_{B,3}t \\ 0 \end{bmatrix} \qquad (2.89)$$

(d) Gravity-gradient Torques

The gravity-gradient torque vector $\underline{T}_{EBG}$, on the body B, in the B-based coordinates, is given by

$$\underline{T}_{EBG} = \frac{3\mu}{R^3}[\vec{d}\ I_B d] \qquad (2.90)$$

where

$\underline{d}$ = $[d_1, d_2, d_3]^T$

= the unit vector towards the center of the Earth,

μ = the Earth's gravitational constant

= 1.4082×10^6 ft^3/sec^2,

and

R = the distance of the center of the Earth from the body B.

Then, from Eqs. (2.80) and (2.90), we have

$$\underline{T}_{EBG} = \frac{3\mu}{R^3}\begin{bmatrix} (I_{B3} - I_{B2})d_2 d_3 \\ (I_{B1} - I_{B3})d_1 d_3 \\ (I_{B2} - I_{B1})d_1 d_2 \end{bmatrix} \qquad (2.91)$$

Now, let the inertially fixed reference coordinate axes be set up such that $\underline{X}_3$ points in the direction perpendicular to the orbital plane and along the angular momentum vector, $\underline{X}_2$ is along the line joining the centers of the masses, and $\underline{X}_1$ is along the orbital velocity vector. Then in the X-frame, located on the body B, $\underline{d}$ is given by

$$\underline{d}_X = [0, 1, 0]^T .$$

Therefore in the B-based coordinates, $\underline{d}$ is given by

$$\underline{d} = \Theta \cdot \underline{d}_X$$

where Θ is the transformation matrix given by Eq. (1.94).

Carrying out this transformation, we obtain

$$\begin{aligned} d_1 &= \cos\psi_1 \sin\psi_3 + \sin\psi_1 \sin\psi_2 \cos\psi_3 \\ d_2 &= \cos\psi_1 \cos\psi_3 - \sin\psi_1 \sin\psi_2 \sin\psi_3 \\ d_3 &= -\sin\psi_1 \cos\psi_2 \ . \end{aligned} \tag{2.92}$$

Substituting the Eqs. (2.92) in Eq. (2.91), and using small angle approximations for ψ_1 and ψ_2, we obtain

$$\underline{T}_{EBG} = \frac{3\mu}{R^3} \begin{Bmatrix} (I_{B3}-I_{B2})[-\psi_1^2\psi_2 \sin\psi_3 - (\psi_1 + \frac{1}{2}\psi_1\psi_2^2 - \frac{4}{3}\psi_1^3)\cos\psi_3] \\ (I_{B1}-I_{B3})[\psi_1^2\psi_2 \cos\psi_3 - (\psi_1 + \frac{1}{2}\psi_1\psi_2^2 - \frac{4}{3}\psi_1^3)\sin\psi_3] \\ (I_{B2}-I_{B1})[\frac{1}{2}(1+\psi_1^2)\sin 2\psi_3 + \psi_1\psi_2 \cos 2\psi_3] \end{Bmatrix} . \tag{2.93}$$

(e) Total Environmental Torque

In this analysis only the above-mentioned environmental torques are considered. Then the total external torque, $\underline{T}_{EB}$, on the body B is obtained as

$$\underline{T}_{EB} = \underline{T}_{EBM} + \underline{T}_{EBC} + \underline{T}_{EBS} + \underline{T}_{EBG} . \tag{2.94}$$

These torques do not involve the $\{q_B\}$ as the effects of the flexibility on them are ignored.

4. Moment Equations for the Composite Bodies

The moment equations for the body B are derived now. The corresponding equations for the body A can be obtained in an identical manner.

(a) Angular Momentum

Let $\underline{H}_B$ be the angular momentum about the center of mass of the body B in B-based coordinates. Then

$$\underline{H}_B = \int \underline{r}_e \times ({}^N\frac{d}{dt} \underline{r}_c)dm \tag{2.95}$$

where $\underline{r}_c$ is the position vector of a differential element of mass dm, expressed in the B-based coordinates, from the actual center of mass of the body B. Since

$$\underline{r}_c = \underline{c}_B + \underline{r} \tag{2.96}$$

we obtain

$$\underline{H}_B = \int(\underline{c}_B + \underline{r}) \times [(\dot{\underline{c}}_B + \dot{\underline{r}}) + \underline{\omega}_B \times (\underline{c}_B + \underline{r})]dm$$

where $\underline{r}$ is the B-based position vector of the element from the nominal center of mass, or

$$\underline{H}_B = \int[\underline{c}_B \times \dot{\underline{c}}_B + \underline{c}_B \times \dot{\underline{r}} + \underline{r} \times \dot{\underline{c}}_B + \underline{r} \times \dot{\underline{r}} + \underline{c}_B \times (\underline{\omega}_B \times \underline{c}_B)$$

$$+ \underline{c}_B \times (\underline{\omega}_B \times \underline{r}) + \underline{r} \times (\underline{\omega}_B \times \underline{c}_B) + \underline{r} \times (\underline{\omega}_B \times \underline{r})]dm \ . \tag{2.97}$$

Because $\underline{c}_B$ and $\dot{\underline{c}}_B$ are assumed to be small, and since

$$\int \underline{r}\, dm = -\|M\|_B \underline{c}_B$$

Eq. (2.97) is linearized by keeping only the fourth and the last terms. The

last term can be written as $\{[I_B]\underline{\omega}_B + \underline{h}_B\}$. In this expression $\underline{h}_B$ is the angular momenta of rigid rotors or reaction wheels inside the body B. Thus Eq. (2.97) reduces to

$$\underline{H}_B = [I_B]\underline{\omega}_B + \underline{h}_B + \int \underline{r} \times \dot{\underline{r}}\, dm \ . \tag{2.98}$$

Therefore

$$^N\frac{d}{dt}\underline{H}_B = \frac{d}{dt}\underline{H}_B + \underline{\omega}_B \times \underline{H}_B$$

or

$$^N\dot{\underline{H}}_B = \dot{I}_B\omega_B + I_B\dot{\omega}_B + \dot{h}_B + \int \underline{r} \times \ddot{\underline{r}}\, dm$$

$$+ \tilde{\omega}_B I_B \omega_B + \tilde{\omega}_B h_B + \underline{\omega}_B \times \left(\int \underline{r} \times \dot{\underline{r}}\, dm \right) . \tag{2.99}$$

Neglecting $\dot{I}_B$, and using the symbols from earlier parts of this analysis, we get

$$^N\dot{\underline{H}}_B = I_B\dot{\underline{\omega}}_B + \tilde{\omega}_B I_B \omega_B + \dot{h}_B + \tilde{\omega}_B h_B + \sum_j [m_j \widetilde{(R_j + r_j)}\ddot{y}_j + m_j \tilde{\omega}_B \widetilde{(R_j + r_j)}\dot{y}_j]$$

$$+ \sum_{i=1}^{4} \{ {}_b\rho_i \int_0^{\ell} [\widetilde{(R_i + s_i)}\ddot{\eta}_i] ds_i + {}_b\rho_i \tilde{\omega}_B \int_0^{\ell} [\widetilde{(R_i + s_i)}\dot{\eta}_i] ds_i \}$$

$$+ \sum_k {}_p\rho_k [\iint_p \tilde{R}_k \ddot{\chi}_k \, dS + \tilde{\omega}_B \iint_p \tilde{R}_k \dot{\chi}_k dS]$$

$$+ {}_s\rho_B [\iint \tilde{R}_B \ddot{\xi}_B dS + \tilde{\omega}_B \iint \tilde{R}_B \dot{\xi}_B dS] \tag{2.100}$$

where

$$j = 1,2 \text{ and } 13\text{-}20, \quad k = 1,2.$$

Introducing the expressions for $\underline{\eta}_i$, $\underline{\chi}_k$ and $\underline{\xi}_B$ obtained before, Eq. (2.100) is transformed into

$$^N\dot{\underline{H}}_B = I_B\dot{\underline{\omega}}_B + \tilde{\omega}_B I_B \underline{\omega}_B + \dot{h}_B + \tilde{\omega}_B \underline{\eta}_B + [P_{B1}]\ddot{\underline{q}}_B + \tilde{\omega}_B [P_{B1}]\dot{\underline{q}}_B \ . \tag{2.101}$$

Details of Eq. (2.101) are shown in Appendix 11.

(b) Equations of Motion of the Body B

Let the controlling torque vector $\underline{T}_B^*$ on the body B be expressed as

$$\underline{T}_B^* = [T_{B1}^*, T_{B2}^*, T_{B3}^*] \tag{2.102}$$

in B-based coordinates. Then the total torque $\underline{T}_B$, applied on the body B in B-based coordinates is given by

$$\underline{T}_B = \underline{T}_B^* + \underline{T}_{EB} + \underline{T}_{BC} + (\underline{R}_{BC} \times \underline{F}_{BC}) \tag{2.102}$$

in which $\underline{T}_{BC}$, $\underline{F}_{BC}$, and $\underline{R}_{BC}$ are shown in Figure 8. In this equation, $\underline{F}_{BC}$ is obtained from Eq. (1.103), $\underline{T}_{BC}$ from Eq. (1.105) and $\underline{T}_{EB}$ from Eq. (2.94). Therefore

$$\begin{aligned}\underline{T}_B = {} & \underline{T}_B^* + \underline{T}_{EB} + [\tfrac{1}{\gamma}(\tau_4 + \tilde{r}_{AB}\tau_1) - (\tau_5 + \tilde{r}_{AB}\tau_2) \\ & + \tilde{R}_{BC}(\tfrac{1}{\gamma}\tau_1 - \tau_2)]G_B L_B \underline{q}_B + [\tfrac{1}{\gamma}(\tau_{10} + \tilde{r}_{AB}\tau_7) - (\tau_{11} + \tilde{r}_{AB}\tau_8) \\ & + \tilde{R}_{BC}(\tfrac{1}{\gamma}\tau_7 - \tau_8)]G_B L_B \underline{q}_B - [\tau_6 + (\tilde{R}_{BC} + \tilde{r}_{AB})\tau_3]\underline{\theta} \\ & - [\tau_{12} + (\tilde{R}_{BC} + \tilde{r}_{AB})\tau_9]\dot{\underline{\theta}} \ . \end{aligned} \tag{2.103}$$

The equation of rotational motion for the body B is then given by

$$\underline{T}_B = {}^N\frac{d}{dt}\underline{H}_B \ .$$

Hence from Eqs. (2.101) and (2.103), we get

$$\begin{aligned}& [P_{B1}]\ddot{\underline{q}}_B + \{\tilde{\omega}_B[P_{B1}] - [\tfrac{1}{\gamma}(\tau_{10} + \tilde{r}_{AB}\tau_7) - (\tau_{11} + \tilde{r}_{AB}\tau_8) + \tilde{R}_{BC}(\tfrac{1}{\gamma}\tau_7 - \tau_8)]G_B L_B\}\dot{\underline{q}}_B \\ & + \{[(\tau_5 + \tilde{r}_{AB}\tau_2) - \tfrac{1}{\gamma}(\tau_4 + \tilde{r}_{AB}\tau_1) - \tilde{R}_{BC}(\tfrac{1}{\gamma}\tau_1 - \tau_2)]G_B L_B\}\underline{q}_B \\ & = \underline{T}_B^* + \underline{T}_{EB} - [\tau_6 + (\tilde{R}_{BC} + \tilde{r}_{AB})\tau_3]\underline{\theta} - [\tau_{12} + (\tilde{R}_{BC} + \tilde{r}_{AB})\tau_9]\dot{\underline{\theta}} \\ & - I_B\dot{\underline{\omega}}_B - \dot{\underline{h}}_B - \tilde{\omega}_B\underline{h}_B - \tilde{\omega}_B I_B\omega_B \end{aligned} \tag{2.104}$$

Equation (2.104) is rewritten as

$$[P_{B1}]\ddot{q}_B + [P_{B2}]\dot{q}_B + [P_{B3}]q_B = \{P_{B4}\} \cdot \tag{2.105}$$

In this equation $\{P_{B4}\}$ is a (3 × 1) vector. The symbols $[P_{B1}]$, $[P_{B2}]$, $[P_{B3}]$ stand for (3 × 41) matrices. The elements of $[P_{B1}]$ and $[P_{B3}]$ are constants, but those of $[P_{B2}]$ involve ω_B .

(c) Equations of Motion of the Body A

Let $\overset{N}{\dot{H}}_A$ be the inertial time derivative of the angular momentum vector of the body A in the A-based coordinates. Then the equation corresponding to Eq. (2.101) is given by

$$\overset{N}{\dot{H}}_A = I_A\dot{\omega}_A + \tilde{\omega}_A I_A\omega_A + \dot{h}_A + \tilde{\omega}_A h_A + [P_{A1}]\ddot{q}_A + \tilde{\omega}_A[P_{A1}]\dot{q}_B \cdot \tag{2.106}$$

Let T_A^* be the controlling torque vector on the body A in the A-based coordinates, so that

$$T_A^* = [T_{A1}^*, T_{A2}^*, T_{A3}^*] \cdot \tag{2.107}$$

Also, let T_{EA} and T_A be the external and the total torque, respectively, on the body A in A-based coordinates. Then, referring to Figure 8, we have

$$T_A = T_A^* + T_{EA} + T_{AC} + (R_{AC} \times F_{AC}) \cdot$$

Substituting Eqs. (1.104) and (1.106) in the above equation, we get

$$\begin{aligned} T_A = {} & T_A^* + T_{EA} + [\Theta_{AB}^{-1}(\tau_4 - \gamma\tau_5)\Theta_{AB} \\ & + \tilde{R}_{AC}\Theta_{AB}^{-1}(\tau_1 - \gamma\tau_2)\Theta_{AB}]G_A L_A q_A + [\Theta_{AB}^{-1}(\tau_{10} - \gamma\tau_{11})\Theta_{AB} \\ & + \tilde{R}_{AC}\Theta_{AB}^{-1}(\tau_7 - \gamma\tau_8)\Theta_{AB}]G_A L_A \dot{q}_A + [\Theta_{AB}^{-1}(\tau_6\underline{\theta} + \tau_{12}\dot{\underline{\theta}}) \\ & + \tilde{R}_{AC}\Theta_{AB}^{-1}(\tau_3\underline{\theta} + \tau_9\dot{\underline{\theta}})] \end{aligned} \tag{2.108}$$

Then the moment equations for the body A are given by

$$\underline{T}_A = \overset{N}{\underline{H}}_A \cdot \tag{2.109}$$

Hence, from Eqs. (2.106) and (2.108), the Eq. (2.109) reduces to a form given by

$$[P_{A1}]\ddot{\underline{q}}_A + [P_{A2}]\dot{\underline{q}}_A + [P_{A3}]\underline{q}_A = \{P_{A4}\} \cdot \tag{2.110}$$

More details of Eqs. (2.105) and (2.110) are in Appendix 11.

5. Equations for the Angular Velocities

(a) A Review of Various Equations

The behavior of the complex dynamic system shown in Figure 1 has been formulated into six sets of equations. These equations are:

$$\bar{A}_1 \ddot{q}_B^* + \bar{A}_2 \dot{q}_B^* + \bar{A}_3 q_B^* = \bar{A}_4 \tag{1.116}$$

$$\bar{A}_1' \ddot{q}_A^* + \bar{A}_2' \dot{q}_A^* + \bar{A}_3' q_A^* = A_4' \tag{1.117}$$

$$\dot{q}_B^* = L_B \dot{q}_B \tag{2.73}$$

$$q_A^* = L_A q_A \tag{2.73a}$$

$$P_{B1}\ddot{q}_B + P_{B2}\dot{q}_B + P_{B3}q_B = P_{B4} \tag{2.105}$$

$$P_{A1}\ddot{q}_A + P_{A2}\dot{q}_A + P_{A3}q_A = P_{A4} \tag{2.110}$$

These equations are linear in the generalized position coordinates $\underline{q}_A$ and $\underline{q}_B$, but nonlinear in the angular velocities $\underline{\omega}_A$ and $\underline{\omega}_B$. The analysis so far has been along well-known techniques, but now a completely new approach will be taken.

(b) Condensation of the Appendage Equations

The general appendage equations (1.116) and (1.117) involve very large

matrices. To try to solve these equations would require a great computational effort. The usual practice [9], [10], [11] is to truncate the coordinate vector by a considerable amount. Instead of gross truncation, the Eqs. (2.73) and (2.73a) are used now to reduce the dimensions of Eqs. (1.116) and (1.117) in the following analysis.

Equation (2.73) is first substituted into Eq. (1.116) to obtain

$$\bar{A}_1 L_B \ddot{q}_B + \bar{A}_2 L_B \dot{q}_B + \bar{A}_3 L_B q_B = \bar{A}_4 \,. \tag{2.111}$$

Now if q_B^* is an $(m \times 1)$ vector and if q_B is a $(n \times 1)$ vector, with $m > n$, then the Eq. (2.111) is a system of m equations in only n independent variables. The number of equations is reduced by premultiplying Eq. (2.111) by $(L_B)^T$. Thus we obtain

$$[(L_B)^T \bar{A}_1 L_B]\ddot{q}_B + [(L_B)^T \bar{A}_2 (L_B)]\dot{q}_B + [(L_B)^T \bar{A}_3 (L_B)]q_B = (L_B)^T \bar{A}_4 \,. \tag{2.111a}$$

This equation is rewritten as

$$A_{B1}\ddot{q}_B + A_{B2}\dot{q}_B + A_{B3}q_B = A_{B4} \,. \tag{2.112}$$

Similarly, using Eq. (2.73a), Eq. (1.117) is reduced to

$$A_{A1}\ddot{q}_A + A_{A2}\dot{q}_A + A_{A3}q_A = A_{A4} \,. \tag{2.113}$$

(c) Derivation of Angular Velocity Equations

We now eliminate q_B from Eqs. (2.105) and (2.112). It is to be noted that, as P_{Bi} are rectangular matrices, their inverses do not exist. Hence P_{Bi} of Eq. (2.105) are augmented by adding (n-3) rows of zeroes and then added to the square matrices A_{Bi} in Eq. (2.112) to form the equation

$$(A_{B1} + P_{B1})\ddot{q}_B + (A_{B2} + P_{B2})\dot{q}_B + (A_{B3} + P_{B3})q_B = (A_{B4} + P_{B4}) \,. \tag{2.114}$$

The matrix $(A_{B1} + P_{B1})$ is square with definite inverse.

Equation (2.114) is now pre-multiplied by $A_{B1}(A_{B1} + P_{B1})^{-1}$ and subtracted from Eq. (2.112) to get

$$[A_{B2} - A_{B1}(A_{B1} + P_{B1})^{-1}(A_{B2} + P_{B2})]\dot{q}_B + [A_{B3} - A_{B1}(A_{B1} + P_{B1})^{-1}(A_{B3} + P_{B3})]q_B$$

$$= [A_{B4} - A_{B1}(A_{B1} + P_{B1})^{-1}(A_{B4} + P_{B4})] \, . \tag{2.115}$$

The above equation is rewritten as

$$M_{B1}\dot{q}_B + M_{B2}q_B = M_{B3} \, . \tag{2.115a}$$

Differentiating Eq. (2.115a), we obtain

$$M_{B1}\ddot{q}_B + (\dot{M}_{B1} + M_{B2})\dot{q}_B + \dot{M}_{B2}q_B = \dot{M}_{B3} \, .$$

In this equation the value of $\ddot{q}_B$ is substituted from Eq. (2.112) to get

$$M_{B1}[A_{B1}^{-1}A_{B4} - A_{B1}^{-1}A_{B2}\dot{q}_B - A_{B1}^{-1}A_{B3}q_B] + (\dot{M}_{B1} + M_{B2})\dot{q}_B + \dot{M}_{B2}q_B = \dot{M}_{B3}$$

or

$$(\dot{M}_{B1} + M_{B2} - M_{B1}A_{B1}^{-1}A_{B2})\dot{q}_B + (\dot{M}_{B2} - M_{B1}A_{B1}^{-1}A_{B3})q_B = (\dot{M}_{B3} - M_{B1}A_{B1}^{-1}A_{B4}) \, .$$

Here $\dot{q}_B$ is replaced by its value from Eq. (2.115a), and we obtain

$$[\dot{M}_{B2} - M_{B1}A_{B1}^{-1}A_{B3} - (\dot{M}_{B1} + M_{B2} - M_{B1}A_{B1}^{-1}A_{B2})M_{B1}^{-1}M_{B2}]q_B$$

$$= [\dot{M}_{B3} - M_{B1}A_{B1}^{-1}A_{B4} - (\dot{M}_{B1} + M_{B2} - M_{B1}A_{B1}^{-1}A_{B2})M_{B1}^{-1}M_{B3}] \, . \tag{2.116}$$

Equation (2.116) is rewritten as

$$M_{B4}q_B = M_{B5} \tag{2.116a}$$

or

$$q_B = M_{B4}^{-1}M_{B5} \, . \tag{2.116b}$$

Equation (2.116b) is very useful as it gives q_B explicitly in terms of the $\underline{\omega}_B$ and $\underline{\omega}_A$.

Equation (2.112) is differentiated once and Eq. (2.115a) is differentiated twice to obtain

$$\ddot{q}_B + A_{B1}^{-1}A_{B2}\ddot{q}_B + A_{B1}^{-1}(\dot{A}_{B2} + A_{B3})\dot{q}_B + A_{B1}^{-1}\dot{A}_{B3}q_B = A_{B1}^{-1}\dot{A}_{B4} \tag{2.117}$$

and

$$M_{B1}\ddot{q}_B + (2\dot{M}_{B1} + M_{B2})\ddot{q}_B + (\ddot{M}_{B1} + 2\dot{M}_{B2})\dot{q}_B + \ddot{M}_{B2}q_B = \ddot{M}_{B3} \tag{2.118}$$

Substituting Eq. (2.117) into Eq. (2.118), we obtain

$$(2\dot{M}_{B1} + M_{B2} - M_{B1}A_{B1}^{-1}A_{B2})\ddot{q}_B + (\ddot{M}_{B1} + 2\dot{M}_{B2} - M_{B1}A_{B1}^{-1}\dot{A}_{B2} - M_{B1}A_{B1}^{-1}A_{B3})\dot{q}_B$$
$$+ (\ddot{M}_{B2} - M_{B1}A_{B1}^{-1}\dot{A}_{B3})q_B = (\ddot{M}_{B3} - M_{B1}A_{B1}^{-1}\dot{A}_{B4}) \ . \tag{2.119}$$

Substituting the value of $\ddot{q}_B$ from Eq. (2.112) in Eq. (2.119), we get

$$[\ddot{M}_{B1} + 2\dot{M}_{B2} - M_{B1}A_{B1}^{-1}\dot{A}_{B2} - M_{B1}A_{B1}^{-1}A_{B3} - (2\dot{M}_{B1} + M_{B2} - M_{B1}A_{B1}^{-1}A_{B2})A_{B1}^{-1}A_{B2}]\dot{q}_B$$
$$+ [\ddot{M}_{B2} - M_{B1}A_{B1}^{-1}\dot{A}_{B3} - (2\dot{M}_{B1} + M_{B2} - M_{B1}A_{B1}^{-1}A_{B2})A_{B1}^{-1}A_{B3}]q_B$$
$$= [\ddot{M}_{B3} - M_{B1}A_{B1}^{-1}\dot{A}_{B4} - (2\dot{M}_{B1} + M_{B2} - M_{B1}A_{B1}^{-1}A_{B2})A_{B1}^{-1}A_{B4}] \ . \tag{2.120}$$

Now, substituting Eqs. (2.115a) and (2.116b) into Eq. (2.120) and simplifying, we obtain

$$[A_{B1}M_{B2}^{-1}]\ddot{M}_{B3} + [(A_{B2} - A_{B3}M_{B2}^{-1}M_{B1} + A_{B1}M_{B2}^{-1}M_{B1}A_{B1}^{-1}A_{B3})M_{B2}^{-1}]\dot{M}_{B3}$$
$$+ [A_{B3}M_{B2}^{-1}]M_{B3} = A_{B4} \ . \tag{2.121}$$

In deriving Eq. (2.121), it has been assumed that $[A_{B2}]$ is small compared to $[A_{B1}]$ and $[A_{B3}]$, and so only the terms linear in $A_{B1}^{-1}A_{B2}$ and $A_{B3}^{-1}A_{B2}$ were retained. On further simplification, Eq. (2.121) reduces to

$$[(P_{B1}A_{B1}^{-1} - P_{B3}A_{B3}^{-1})A_{B1}M_{B2}^{-1}]\ddot{M}_{B3} + [(P_{B2}A_{B2}^{-1} - P_{B3}A_{B3}^{-1})A_{B2}M_{B2}^{-1}]\dot{M}_{B3} + M_{B3}$$

$$= (P_{B1}A_{B1}^{-1} - P_{B3}A_{B3}^{-1})A_{B4} \quad . \tag{2.122}$$

The equation (2.122) is the basic differential equation in the angular velocities only. It is a general equation where the effects of any number of flexible elements can be taken into account. Beginning with the equations (2.113) and (2.110), a similar set of equations for the body A can also be obtained in the forms

$$q_A = M_{A4}^{-1}M_{A5} \tag{2.123}$$

and

$$[(P_{A1}A_{A1}^{-1} - P_{A3}A_{A3}^{-1})A_{A1}M_{A2}^{-1}]\ddot{M}_{A3} + [(P_{A2}A_{A2}^{-1} - P_{A3}A_{A3}^{-1})A_{A2}M_{A2}^{-1}]\dot{M}_{A3} + M_{A3}$$

$$= (P_{A1}A_{A1}^{-1} - P_{A3}A_{A3}^{-1})A_{A4} \quad . \tag{2.124}$$

In the next part of this work we will begin with these highly nonlinear equations and look for special cases and their solutions in transient, intermediate and long-time ranges.

References

1. Dobrotin, B., et al., "Mariner Limit Cycle and Self-disturbance Torques," *Journal of Spacecraft and Rockets*, June 1970, pp. 684-689.

2. Tidwell, N. W., "Modelling of Environmental Torques of a Spin-stabilized Spacecraft in a Near-Earth Orbit," *Journal of Spacecraft and Rockets*, December 1970, pp. 1425-1433.

3. Beletskii, V. V., "Motions of an Artificial Satellite About its Center of Mass," NASA TTF-429, 1966.

CONTENTS

		Page
	Nomenclature	110
1.	Introduction	112
2.	Asymptotic Solutions of $\underline{M}_3$	112
	a) The equation	112
	b) The perturbation series	113
	c) The perturbed equations	115
3.	Convergence Criteria of the Asymptotic Solutions of $\underline{M}_3$	117
	a) Selection of the time domain	117
	b) Truncation of the solution series	120
	c) Validity of the asymptotic solutions - jump conditions	122
4.	The Inner Boundary Layer Solutions of $\underline{M}_3$	124
5.	The Outer Boundary Layer Solutions of $\underline{M}_3$	125
6.	Special Cases	126
	a) Case 1: $M_2 = 0$	127
	i) Case 1-1: $M_2 = M_1 = 0$	127
	ii) Case 1-2: $M_2 = 0;\ P_2A_2^{-1} < P_1A_1^{-1}$	128
	iii) Case 1-3: $M_2 = 0;\ P_2A_2^{-1} > P_1A_1^{-1}$	128
	b) Case 2: $M_2 \neq 0;\ P_3A_3^{-1} < P_1A_1^{-1}$	129
	i) Case 2-1: $M_2 \neq 0;\ P_3A_3^{-1} < P_1A_1^{-1};\ M_1 = 0$	129
	ii) Case 2-2: $M_2 \neq 0;\ P_3A_3^{-1} < P_1A_1^{-1};\ P_2A_2^{-1} < P_1A_1^{-1}$	130
	iii) Case 2-3: $M_2 \neq 0;\ P_3A_3^{-1} < P_1A_1^{-1};\ P_2A_2^{-1} > P_1A_1^{-1}$	130
	c) Case 3: $M_2 \neq 0;\ P_3A_3^{-1} > P_1A_1^{-1}$	130
	i) Case 3-1: $M_2 \neq 0;\ P_3A_3^{-1} > P_1A_1^{-1};\ M_1 = 0$	131
	ii) Case 3-2: $M_2 \neq 0;\ P_3A_3^{-1} > P_1A_1^{-1};\ P_2A_2^{-1} < P_1A_1^{-1}$	131
	iii) Case 3-3: $M_2 \neq 0;\ P_3A_3^{-1} > P_1A_1^{-1};\ P_2A_2^{-1} > P_1A_1^{-1}$	131
	d) Solutions for the special cases	131
7.	Stability Criteria of $\underline{M}_3$	132
8.	Conclusions	133
9.	References	133

Nomenclature

M_i, $i = 1,2,3$	=	Same as M_{Ai} or M_{Bi} of the previous report
A_i, $i = 1\text{-}4$	=	Same as A_{Ai} or A_{Bi} of the previous report
P_i, $i = 1\text{-}4$	=	Same as P_{Ai} or P_{Bi} of the previous report
$\underline{q}$	=	Independent set of the generalized position coordinates (see Part II)
N_3	=	$\int_0^t M_3 dt$
I	=	Identity matrix
$\underline{y}$	=	$\underline{M}_3(\underline{\omega},t)$
$\underline{\omega}$	=	$[\underline{\omega}_A, \dot{\underline{\omega}}_A]^T$ or $[\underline{\omega}_B, \dot{\underline{\omega}}_B]^T$
ϵ	=	The largest element in $(A_1 A_3^{-1})$
A_{ij}, B_{ij}	=	Matrices, defined by Eqs. (3.6) and (3.7), respectively
$\underline{d}$	=	Vector defined in Eq. (3.34)
$\underline{\omega}_n$, $n = 0,1,2,\ldots$	=	Components of $\underline{\omega}$, defined in Eq. (3.11)
$\underline{h}$	=	Component of $\underline{\omega}$, defined in Eq. (3.12)
$\underline{x}$	=	$\dot{\underline{y}}$
$\underline{u}$	=	$[\underline{x},\underline{y}]^T$
$\underline{v}$	=	$[\underline{d},0]^T$
$\underline{f}$	=	$P\underline{u} + Q\underline{d}$
P,Q	=	Matrices, defined in Eqs. (3.30) and (3.31), respectively
F	=	Operator, defined by Eqs. (3.32) and (3.33)
$\underline{u}_1$, $\underline{u}_2$	=	Solutions of $\underline{u}$
$\mathbb{R}$	=	Cartesian vector space $\underline{x} \times \underline{y}$

δ	=	Inf $\lvert \underline{u}(t) - \underline{u}(0) \rvert$ for $0 \leq t \leq T > 0$.
k	=	A constant, defined in Eqs. (3.36) and (3.39)
M	=	A constant, defined in Eq. (3.37)
T	=	Outer limit for t
$\underline{\omega}_n^*$	=	Component of $\underline{\omega}$, defined by Eq. (3.43)
$\underline{y}_n^*$	=	Component of $\underline{y}$, defined by Eq. (3.44)
$\underline{\nabla}_y$	=	Gradient operator with respect to $\underline{y}$
$\underline{\nabla}$	=	Gradient operator with respect to $\underline{\omega}$
$\underline{f}^*(\underline{x},\underline{y})$, $\underline{g}(\underline{x},\underline{y})$	=	Vectors defined by Eqs. (3.52) and (3.53), respectively
τ	=	Enlarged time scale, defined in Eqs. (3.56) and (3.67)

1. Introduction

In this part of our work we begin to explore the consequences of Eqs. (2.122) and (2.124) derived earlier. These are very general and highly nonlinear equations. For convenience, Eq. (2.122) together with Eqs. (2.112) and (2.115a) are repeated here without the subscript B as follows:

$$[(P_1A_1^{-1} - P_3A_3^{-1})A_1M_2^{-1}]\ddot{\underline{M}}_3 + [(P_2A_2^{-1} - P_3A_3^{-1})A_2M_2^{-1}]\dot{\underline{M}}_3 + \underline{M}_3 = (P_1A_1^{-1} - P_3A_3^{-1})\underline{A}_4 \qquad (2.122),\ (3.1)$$

$$A_1\ddot{\underline{q}} + A_2\dot{\underline{q}} + A_3\underline{q} = \underline{A}_4 \qquad (2.112),\ (3.2)$$

$$M_1\dot{\underline{q}} + M_2\underline{q} = \underline{M}_3 \qquad (2.115a),(3.3)$$

First, we shall obtain perturbation series solutions for the generalized forces $\underline{M}_{A3}$ and $\underline{M}_{B3}$, valid for different time zones. Then we shall consider some special cases when the structural parameters combine in a way to simplify these equations to a great extent.

In what follows, the subscripts A and B are dropped from the symbols M_{A1}, M_{B1}, A_{A1}, A_{B1}, P_{A1}, P_{B1}, $\underline{q}_A$ and $\underline{q}_B$, as the analysis is similar for either of the two bodies A and B.

2. Asymptotic Solutions of $\underline{M}_3$

a) The Equation

We now look for the asymptotic solutions of the general equations (2.122) or (2.124) represented by Eq. (3.1). For the present, we assume that the generalized stiffness matrix A_3 is large. Noting that M_2^{-1} involves A_3^{-1}, Eq. (3.1) can be represented as

$$\varepsilon A_{ij}(\underline{\omega},t)\ddot{y}_j + \varepsilon B_{ij}(\underline{\omega},t)\dot{y}_j + y_i = \varepsilon d_i(\underline{\omega},t) \qquad (3.4)$$

where

$$\underline{y} = \underline{M}_3(\underline{\omega}, t)$$

ε = the largest element in $(A_1 A_3^{-1})$,

$$A_{ij} = \varepsilon^{-1}[(P_1 A_1^{-1} - P_3 A_3^{-1}) A_1 M_2^{-1}] \tag{3.6}$$

$$B_{ij} = \varepsilon^{-1}[(P_2 A_2^{-1} - P_3 A_3^{-1}) A_2 M_2^{-1}] \tag{3.7}$$

$$d_i = \varepsilon^{-1}(P_1 A_1^{-1} - P_3 A_3^{-1}) \underline{A}_4 \tag{3.8}$$

$$\underline{\omega} = [\underline{\omega}_A, \dot{\underline{\omega}}_A]^T \quad \text{or} \quad [\underline{\omega}_B, \dot{\underline{\omega}}_B]^T . \tag{3.9}$$

This shows that A_{ij}, B_{ij} remain quantities of comparable magnitude even though ε is small. The form of the Eq. (3.4) makes it clear that as the structure becomes increasingly rigid, ε tends to zero and the Eq. (3.4) approaches the equation

$$y_i = 0 . \tag{3.10}$$

On further simplification, Eq. (3.10) becomes the rigid body equation for the two bodies A and B.

b) The perturbation series

We begin the process of solving Eq. (3.4) by assuming $\underline{\omega}$ in the following form:

$$\omega_i = \omega_{0i} + \varepsilon\omega_{1i} + \varepsilon^2\omega_{2i} + \varepsilon^3\omega_{3i} + \ldots \tag{3.11}$$

Defining

$$h_i = \varepsilon\omega_{1i} + \varepsilon^2\omega_{2i} + \varepsilon^3\omega_{3i} + \ldots \tag{3.12}$$

we get

$$\omega_i = \omega_{0i} + h_i . \tag{3.13}$$

Since

$$\underline{y} = \underline{y}(\underline{\omega}, t) = \underline{y}(\underline{\omega}_0 + h, t)$$

We now expand $\underline{y}$ in a Taylor's series around $(\underline{\omega}_0, t)$.

Defining

$$y_{i,j} = \frac{\partial y_i}{\partial \omega_j}$$

and

$$y_{i,jk} = \frac{\partial^2 y_i}{\partial \omega_j \partial \omega_k}$$

we obtain

$$y_i(\underline{\omega},t) = y_i(\underline{\omega}_0,t) + y_{i,j}(\underline{\omega}_0,t)h_j + \frac{1}{2} y_{i,jk}(\underline{\omega}_0,t)h_j h_k + \cdots$$

or

$$y_i(\underline{\omega},t) = y_i(\underline{\omega}_0,t) + \varepsilon y_{i,j}(\underline{\omega}_0,t)\omega_{1j} + \varepsilon^2[y_{i,j}(\underline{\omega}_0,t)\omega_{2j} + \frac{1}{2} y_{i,jk}\omega_{1j}\omega_{1k}] + \cdots \tag{3.14}$$

Therefore

$$\dot{y}_i(\underline{\omega},t) = \dot{y}_i(\underline{\omega}_0,t) + \varepsilon[\dot{y}_{i,j}(\underline{\omega}_0,t)\omega_{1j} + y_{i,j}(\omega_0,t)\dot{\omega}_{1j}]$$
$$+ \varepsilon^2[\dot{y}_{i,j}(\underline{\omega}_0,t)\omega_{2j} + y_{i,j}(\underline{\omega}_0,t)\dot{\omega}_{2j} + \frac{1}{2}\dot{y}_{i,jk}(\underline{\omega}_0,t)\omega_{1j}\omega_{1k}$$
$$+ y_{i,jk}(\underline{\omega}_0,t)\dot{\omega}_{1j}\omega_{1k}] + \cdots \tag{3.15}$$

Hence

$$\ddot{y}_i(\underline{\omega},t) = \ddot{y}_i(\underline{\omega}_0,t) + \varepsilon[\ddot{y}_{i,j}(\underline{\omega}_0,t)\omega_{1j} + 2\dot{y}_{i,j}(\underline{\omega}_0,t)\dot{\omega}_{1j}$$
$$+ y_{i,j}(\underline{\omega}_0,t)\ddot{\omega}_{1j}] + \varepsilon^2[\ddot{y}_{i,j}(\underline{\omega}_0,t)\omega_{2j} + 2\dot{y}_{i,j}(\underline{\omega}_0,t)\dot{\omega}_{2j}$$
$$+ y_{i,j}(\underline{\omega}_0,t)\ddot{\omega}_{2j} + \frac{1}{2}\ddot{y}_{i,jk}(\underline{\omega}_0,t)\omega_{1j}\omega_{1k} + 2\dot{y}_{i,jk}\dot{\omega}_{1j}\omega_{1k} + y_{i,jk}(\underline{\omega}_0,t)\ddot{\omega}_{1j}\omega_{1k}] + \cdots \tag{3.16}$$

Expanding $A_{ij}(\underline{\omega},t)$ in a Taylor's series about $\underline{\omega}_0$, we obtain

$$A_{ij}(\underline{\omega},t) = A_{ij}(\underline{\omega}_0,t) + A_{ij,k}(\underline{\omega}_0,t)h_k + \frac{1}{2} A_{ij,k\ell}(\underline{\omega}_0,t)h_k h_\ell + \cdots$$

or

$$A_{ij}(\underline{\omega},t) = A_{ij}(\underline{\omega}_0,t) + \varepsilon A_{ij,k}(\underline{\omega}_0,t)\omega_{1k}$$

$$+ \varepsilon^2[A_{ij,k}(\underline{\omega}_0,t)\omega_{2k} + \tfrac{1}{2}A_{ij,k\ell}(\underline{\omega}_0,t)\omega_{1k}\omega_{1\ell}] + \ldots \qquad (3.17)$$

Similarly,

$$B_{ij}(\underline{\omega},t) = B_{ij}(\underline{\omega}_0,t) + \varepsilon B_{ij,k}(\underline{\omega}_0,t)\omega_{1k}$$

$$+ \varepsilon^2[B_{ij,k}(\underline{\omega}_0,t)\omega_{2k} + \tfrac{1}{2}B_{ij,k\ell}(\underline{\omega}_0,t)\omega_{1k}\omega_{1\ell}] + \ldots \qquad (3.18)$$

We also have

$$d_i(\underline{\omega},t) = d_i(\underline{\omega}_0,t) + \varepsilon d_{i,j}(\underline{\omega}_0,t)\omega_{1j}$$

$$+ \varepsilon^2[d_{i,j}(\underline{\omega}_0,t)\omega_{2j} + \tfrac{1}{2}d_{i,jk}(\underline{\omega}_0,t)\omega_{1j}\omega_{1k}] + \ldots \qquad (3.19)$$

The series given by Eqs. (3.14) through (3.19) will now be used to generate the perturbed equations from which $\underline{\omega}$ will be solved. With our choice of ε, it is seen that each expansion series approaches the corresponding nominal value as the satellite becomes increasingly rigid. This characteristic is in agreement with the physical nature of our problem.

c) The perturbed equations

Substituting Eqs. (3.14) through (3.19) in Eq. (3.4), and separating the coefficients of $\varepsilon^0, \varepsilon^1, \varepsilon^2$ we obtain the following equations: The coefficient of ε^0 gives

$$y_i(\underline{\omega}_0,t) = 0 \,. \qquad (3.20)$$

The coefficients of ε give

$$A_{ij}(\underline{\omega}_0,t)\ddot{y}_j(\underline{\omega}_0,t) + B_{ij}(\underline{\omega}_0,t)\dot{y}_j(\underline{\omega}_0,t) + y_{i,j}(\underline{\omega}_0,t)\omega_{1j} = d_i(\underline{\omega}_0,t)$$

or

$$y_{ij}(\underline{\omega}_0,t)\omega_{1j} = d_i(\underline{\omega}_0,t) \,. \qquad (3.21)$$

From the coefficients of ε^2, we get

$$A_{ij}(\underline{\omega}_0,t)[\ddot{y}_{j,k}(\underline{\omega}_0,t)\omega_{1k} + 2\dot{y}_{j,k}(\underline{\omega}_{0,t})\dot{\omega}_{1k} + y_{j,k}(\underline{\omega}_0,t)\ddot{\omega}_{1k}]$$

$$+ A_{ij,k}(\underline{\omega}_0,t)\omega_{1k}\ddot{y}_j(\underline{\omega}_0,t) + B_{ij}(\underline{\omega}_0,t)[\dot{y}_{j,k}(\underline{\omega}_0,t)\omega_{1k} + y_{j,k}(\underline{\omega}_0,t)\dot{\omega}_{1k}]$$

$$+ [y_{i,j}(\underline{\omega}_0,t)\omega_{2j} + \tfrac{1}{2}\, y_{i,jk}(\underline{\omega}_0,t)\omega_{1j}\omega_{1k}]$$

$$= d_{i,j}(\underline{\omega}_0,t)\omega_{2j} + \tfrac{1}{2}\, d_{i,jk}(\omega_0,t)\omega_{1j}\omega_{1k}$$

or

$$A_{ij}(\underline{\omega}_0,t)\ddot{d}_j(\underline{\omega}_0,t) + B_{ij}(\underline{\omega}_0,t)\dot{d}_j(\underline{\omega}_0,t) + y_{i,j}(\underline{\omega}_0,t)\omega_{2j}$$

$$+ \tfrac{1}{2}\, y_{i,jk}(\underline{\omega}_0,t)\omega_{1j}\omega_{1k} = d_{i,j}(\underline{\omega}_0,t)\omega_{2j} + \tfrac{1}{2}\, d_{i,jk}(\underline{\omega}_0,t)\omega_{1j}\omega_{1k}$$

or

$$(d_{i,j} - y_{i,j})(\underline{\omega}_0,t)\omega_{2j} + \tfrac{1}{2}(d_{i,jk} - y_{i,jk})(\underline{\omega}_0,t)\omega_{1j}\omega_{1k}$$

$$= A_{ij}(\underline{\omega}_0,t)\ddot{d}_j(\underline{\omega}_0,t) + B_{ij}(\underline{\omega}_0,t)\dot{d}_j(\underline{\omega}_0,t) \ . \tag{3.22}$$

Now, differentiating Eq. (3.21) with respect to $\underline{\omega}$, we have

$$d_{i,j} = y_{i,kj}\omega_{1k} + y_{i,j} \ . \tag{3.23}$$

Differentiating Eq. (3.23) with respect to $\underline{\omega}$, we obtain

$$d_{i,jk} - y_{i,jk} = y_{i,jk\ell}\omega_{1\ell} + y_{i,jk} \ . \tag{3.24}$$

Substituting Eqs. (3.23) and (3.24) in Eq. (3.21), and neglecting $\ddot{d}_j(\underline{\omega}_0,t)$ and $\dot{d}_j(\underline{\omega}_0,t)$, we get

$$y_{i,kj}(\underline{\omega}_0,t)\omega_{1k}\omega_{2j} + \tfrac{1}{2}\, y_{i,jk\ell}(\underline{\omega}_0,t)\omega_{1j}\omega_{1k}\omega_{1\ell} + \tfrac{1}{2}\, y_{i,jk}(\underline{\omega}_0,t)\omega_{1j}\omega_{1k} = 0 \ .$$

Then neglecting the cubic term in the above equation,

$$\omega_{2j} = -\tfrac{1}{2}\omega_{1j} \ . \tag{3.25}$$

Then from Eqs. (3.11), (3.21) and (3.25),

$$\omega_i = \omega_{0i} + \varepsilon(1 + \frac{\varepsilon}{2})[y_{i,j}(\underline{\omega}_0,t)]^{-1}d_j(\underline{\omega}_0,t) \tag{3.26}$$

where $\underline{\omega}_0$ is to be obtained from Eq. (3.20).

3. Convergence Criteria of the Asymptotic Solutions of M_3

a) Selection of the time domain

In view of the simplifications made in solving Eq. (3.4), it may be argued that the obtained solution of that equation is quite different from the actual solution. To check if such is the case, we proceed in the following way:

Let

$$\dot{y}_i = x_i \ . \tag{3.27}$$

Then Eq. (3.4) is given by

$$\varepsilon A(\underline{\omega},t)\dot{\underline{x}} = \varepsilon\underline{d} - \varepsilon B(\underline{\omega},t)\underline{x} - \underline{y} \ . \tag{3.28}$$

Let the vectors $\underline{u}$ and $\underline{v}$ be defined by

$$\underline{u} = [\underline{x},\underline{y}]^T$$

and

$$\underline{v} = [\underline{d},0]^T \ .$$

Then Eqs. (3.27) and (3.28) are represented by

$$\dot{\underline{u}} = P\underline{u} + Q\underline{d} = f(\underline{u}(t),t) \tag{3.29}$$

where P and Q are given by

$$P = \begin{bmatrix} -A^{-1}B & -\frac{1}{\varepsilon}A^{-1} \\ I & 0 \end{bmatrix} \tag{3.30}$$

and

$$Q = \begin{bmatrix} A^{-1} & 0 \\ 0 & 0 \end{bmatrix} \ . \tag{3.31}$$

From Eq. (3.29), the formal solution for $\underline{u}$ is

$$\underline{u}(t) = \underline{u}(0) + \int_0^t f(\underline{u}(t),t)dt \tag{3.32}$$

or

$$\underline{u}(t) = F[\underline{u}(t)] \tag{3.33}$$

where the operator F is defined by the Eqs. (3.32) and (3.33).

Now our problem can be stated as follows:

Suppose $u_1(t)$ is the exact solution of Eq. (3.32) and $u_2(t)$ is an approximate solution, such that both solutions have the same initial value, i.e.

$$\underline{u}(0) = u_1(0) = u_2(0).$$

Then if $[F(\underline{u}_1) - F(\underline{u}_2)]$ is small, will $[u_1(t) - u_2(t)]$ be also small? If the answer is in the affirmative, then we also want to know the conditions under which it is so. It can be proved by applying the Contraction Mapping theorem [1], that $[u_1(t) - u_2(t)]$ is small if F is a contraction operator. We now obtain the conditions for F to be a contraction operator in our problem.

Let $\mathbb{R}$ be the 2n-dimensional Cartesian space containing the n-dimensional vectors $\underline{x}$ and $\underline{y}$. Let $\underline{u}$ belong to a set U such that

$$\underline{u} \in U = \{\underline{u} : \underline{u} \in \mathbb{R}, \ |\underline{u}(t) - \underline{u}(0)| \leq \delta\} \tag{3.34}$$

$$\text{for } 0 \leq t \leq T > 0$$

and

$$\|\underline{u}\| = \max_{t\in[0,T]} |\underline{u}(t)| \tag{3.35}$$

where δ is a positive constant.

Now it is assumed that there exists a constant k such that

$$|f(\underline{u}_1,t) - f(\underline{u}_2,t)| \leq k|\underline{u}_1 - \underline{u}_2| \tag{3.36}$$

where

$$\underline{u}_1, \underline{u}_2 \in U \quad \text{and} \quad t \in [0,T].$$

It is also assumed that there exists a positive constant M such that

$$|f(\underline{u},t)| \leq M, \quad u \in U, \quad t \in [0,T]. \tag{3.37}$$

Now, from Eqs. (3.30), (3.31) and (3.32), we have

$$\begin{aligned} |f(\underline{u}_1,t) - f(\underline{u}_2,t)| &= |P\underline{u}_1 - P\underline{u}_2 + Qd(\underline{u}_1,t) - Qd(\underline{u}_2,t) \\ &\quad |P(\underline{u}_1 - \underline{u}_2) + [Q\nabla d](\underline{u}_1 - \underline{u}_2)| \\ &\leq |P + Q\cdot\nabla d| \cdot |\underline{u}_1 - \underline{u}_2| \\ &= \left| \begin{bmatrix} A^{-1}(\nabla d - B) & -\frac{1}{\varepsilon} A^{-1} \\ I & 0 \end{bmatrix} \right| \cdot |\underline{u}_1 - \underline{u}_2| \cdot \end{aligned} \tag{3.38}$$

Then comparing Eqs. (3.36) and (3.38), we get the constant k as

$$k = \text{the greatest eigenvalue of } \begin{bmatrix} A^{-1}(\nabla d - B) & -\frac{1}{\varepsilon} A^{-1} \\ I & 0 \end{bmatrix}. \tag{3.39}$$

From Eqs. (3.32), (3.34) and (3.37) we have

$$|u(t) - u(0)| \leq \int_0^t |f(\underline{u},t)|dt \leq MT. \tag{3.40}$$

From Eqs. (3.32), (3.33) and (3.36), we have

$$\begin{aligned} \|F(\underline{u}_1) - F(\underline{u}_2)\| &= \max_{t\in[0,T]} \left| \int_0^t [f(\underline{u}_1,t) - f(\underline{u}_2,t)]dt \right| \\ &\leq \max_{t\in[0,T]} \int_0^t k|\underline{u}_1(t) - \underline{u}_2(t)|dt \\ &\leq kT \|\underline{u}_1 - \underline{u}_2\|. \end{aligned} \tag{3.41}$$

Then from Eqs. (3.40) and (3.41), we see that the operation F will be

a contraction if we choose T such that $MT < \delta$, $kT < 1$. Therefore

$$T < \min\{\frac{\delta}{M}, \frac{1}{k}\} \quad . \tag{3.42}$$

Thus, Eq. (3.42) gives the time interval in which our approximate solutions will remain close to the exact solution. This also shows that the system is unstable if k is very large.

b) Truncation of the solution series

An important piece of information we require in this analysis is the number of terms of the series given in Eq. (3.11) that are necessary for the solution to be arbitrarily close to the exact one when $t \in [0,T]$. We now show how to estimate any term of that series from the value of the preceding sequence.

Let the partial sums of the series in Eq. (3.11) be denoted by ω_n^* such that

$$\omega_n^* = \sum_{n=0}^{n} \varepsilon^n \underline{\omega}_n(t) \quad . \tag{3.43}$$

Let $\underline{y}_n^*$ be defined by

$$\underline{y}_n^* = \underline{y}(\underline{\omega}_n^*, t) \quad . \tag{3.44}$$

Then Eq. (3.4) can be expressed as

$$\underline{y}_{n+1}^* = \varepsilon[\underline{d}(\underline{\omega}_{n+1}^*, t) - A(\underline{\omega}_n^*, t)\ddot{\underline{y}}_n^* - B(\underline{\omega}_n^*, t)\dot{\underline{y}}_n^*]$$

or

$$\underline{y}_{n+1}^* = \varepsilon[\underline{d}(\underline{\omega}_n^*, t) + \underline{\nabla}_y \underline{d}(\underline{y}_{n+1}^* - \underline{y}_n^*) - A(\underline{\omega}_n^*, t)\ddot{\underline{y}}_n^* - B(\underline{\omega}_n^*, t)\dot{\underline{y}}_n^*]$$

where $\underline{\nabla}_y$ is the gradient operator with respect to $\underline{y}$, or

$$\underline{y}_{n+1}^* = \varepsilon[\underline{d}(\underline{\omega}_n^*, t) + \underline{\nabla} \underline{d}(\underline{\omega}_n^*, t)(\underline{y}_{n+1}^* - \underline{y}_n^*) - A(\underline{\omega}_n^*, t)\ddot{\underline{y}}_n^* - B(\underline{\omega}_n^*, t)\dot{\underline{y}}_n^*]$$

where $\underline{\nabla}$ is the gradient operator with respect to $\underline{\omega}_A$ or $\underline{\omega}_B$.

Therefore

$$[I - \varepsilon \underline{\nabla d}(\underline{\omega}_n^*,t)]\underline{y}_{n+1}^* = \varepsilon \underline{d}(\underline{\omega}_n^*,t)$$

$$- \varepsilon[\underline{\nabla d}(\underline{\omega}_n^*,t) + A(\underline{\omega}_n^*,t)\frac{d^2}{dt^2} + B(\underline{\omega}_n^*,t)\frac{d}{dt}]\underline{y}_n^* . \tag{3.45}$$

With $n = 0$, Eq. (3.45) becomes

$$[I - \varepsilon \underline{\nabla d}(\underline{\omega}_0,t)]\underline{y}_1^* = \varepsilon \underline{d}(\underline{\omega}_0,t)$$

or

$$\underline{y}_1^* = \varepsilon[I + \varepsilon \underline{\nabla d}(\underline{\omega}_0,t)]\underline{d}(\underline{\omega}_0,t) \tag{3.46}$$

provided $\varepsilon \underline{\nabla d}(\underline{\omega}_0,t) \leq \frac{1}{3}$. Similarly

$$[I - \varepsilon \underline{\nabla d}(\underline{\omega}_1^*,t)]\underline{y}_2^* = \varepsilon \underline{d}(\underline{\omega}_1^*,t) - \varepsilon[\underline{\nabla d}(\underline{\omega}_1^*,t)$$

$$+ A(\underline{\omega}_1^*,t)\frac{d^2}{dt^2} + B(\underline{\omega}_1^*,t)\frac{d}{dt}]\underline{y}_1^* . \tag{3.47}$$

Substituting Eq. (3.46) in Eq. (3.47) and dropping the term involving ε^3 we get

$$[I - \varepsilon \underline{\nabla d}(\underline{\omega}_1^*,t)]\underline{y}_2^* = \varepsilon \underline{d}(\underline{\omega}_1^*,t) - \varepsilon^2[\underline{\nabla d}(\underline{\omega}_1^*,t)$$

$$+ A(\underline{\omega}_1^*,t)\frac{d^2}{dt^2} + B(\underline{\omega}_1^*,t)\frac{d}{dt}]\underline{d}(\underline{\omega}_0^*,t)$$

or

$$\underline{y}_2^* \cong \varepsilon[I + \varepsilon \underline{\nabla d}(\underline{\omega}_1^*,t)]\underline{d}(\underline{\omega}_1^*,t)$$

since

$$\underline{y}_0^*(\underline{\omega}_0^*,t) = 0$$

so

$$\underline{d}(\underline{\omega}_1^*,t) = \underline{\nabla}\,\underline{d}(\underline{\omega}_0^*,t)\underline{y}_1^* .$$

Therefore

$$\underline{y}_2^* \cong \varepsilon[I + \varepsilon \underline{\nabla d}(\underline{\omega}_1^*,t)][\underline{\nabla d}(\underline{\omega}_0^*,t)]\underline{y}_1^* . \tag{3.48}$$

Carrying on this procedure we get

$$\underline{y}^*_{n+1} = \varepsilon[I + \varepsilon\underline{\nabla}\underline{d}(\underline{\omega}^*_n,t)][\underline{\nabla}\underline{d}(\underline{\omega}^*_{n-1},t)](\underline{y}^*_n - \underline{y}^*_{n-1}) \quad \text{for} \quad n \geq 1 \ . \tag{3.49}$$

This shows that after choosing T, we have to choose n such that the difference of $(\underline{y}^*_{n+1} - \underline{y}^*_n)$ obtained from Eq. (3.49) becomes small for $t \in [0,T]$.

c) Validity of asymptotic solutions - Jump conditions

We now consider Eqs. (3.27) and (3.28) to obtain another important characteristic of that system. These two equations are represented by

$$\begin{aligned} \varepsilon\dot{\underline{x}} &= \underline{f}^*(\underline{x},\underline{y}) \\ \dot{\underline{y}} &= \underline{g}(\underline{x},\underline{y}) \end{aligned} \tag{3.50}$$

where ε is a small parameter. The property that ε appears with the highest derivative of the state vector makes it a singularly perturbed system. In the previous section we have assumed that the system should tend to a definite limiting mode as ε approaches zero. We will now examine whether or not an asymptotic solution of the system exists.

To understand the problem, we consider the phase velocity vector $\underline{v}$ given by

$$\underline{v} = [\dot{\underline{x}},\dot{\underline{y}}]^T = [\frac{1}{\varepsilon}\underline{f}^*(\underline{x},\underline{y}),\ \underline{g}(\underline{x},\underline{y})]^T$$

or

$$\underline{v} = [\frac{1}{\varepsilon}\underline{f}^*(\underline{x},\underline{y}),0]^T + [0,\ \underline{g}(\underline{x},\underline{y})]^T \ . \tag{3.51}$$

The second vector on the right-hand side of Eq. (3.51) does not depend on ε. The first vector becomes infinite as ε approaches zero if $\underline{f}^*(\underline{x},\underline{y}) \neq 0$. This means that when the phase point $P(\underline{x},\underline{y})$ is not on the surface $\underline{f}^*(\underline{x},\underline{y}) = 0$, the component $\dot{\underline{x}}$ of the phase velocity away from the surface is great. At the same time, the component $\dot{\underline{y}}$ is limited. Such motion is

maintained until $P(\underline{x},\underline{y})$ comes very close to the surface $f^*(\underline{x},\underline{y}) = 0$. After that the variables change with finite velocities. However, for some $\underline{y}$, the point $P(\underline{x},\underline{y})$ may again move away from this surface and the system may lose equilibrium. This phenomenon makes the singularly perturbed systems difficult for analysis.

The equilibrium state of the system is given by the degenerate system

$$\underline{f}^*(\underline{x},\underline{y}) = 0 \tag{3.52}$$

$$\underline{g}(\underline{x},\underline{y}) = \dot{\underline{y}} \ . \tag{3.53}$$

If the system is at equilibrium, then $\underline{x}$ can be solved as

$$\underline{x} = \underline{x}(\underline{y}) \tag{3.54}$$

from Eq. (3.52), and then Eq. (3.54) can be substituted into Eq. (3.53) to yield an explicit solution for $\underline{y}$.

But if the system is not at equilibrium, then it will not be possible to obtain Eq. (3.54) from Eq. (3.52). This means that the jump condition is given by the relation

$$\det\left[\frac{\partial \underline{f}^*}{\partial \underline{x}}\right] = 0 \ . \tag{3.55}$$

Using this relation in our problem, we see from Eq. (3.27)

$$\underline{f}^*(\underline{x},\underline{y}) = \varepsilon A^{-1}[\underline{d} - B\underline{x}] - A^{-1}\underline{y} \ .$$

Hence

$$\dim_{\varepsilon \to 0}\left[\frac{\partial \underline{f}^*}{\partial \underline{x}}\right] = 0 \quad \text{for all} \quad t \ .$$

But though Eq. (3.55) is satisfied, our system is in equilibrium, as

$$\lim_{\varepsilon \to 0} \dot{\underline{x}} = \lim_{\varepsilon \to 0} \frac{1}{\varepsilon} \underline{f}^*(\underline{x},\underline{y}) = \lim_{\varepsilon \to 0} [A^{-1}(\underline{d} - B\underline{x}) - \frac{1}{\varepsilon} A^{-1}\underline{y}]$$

$$= A^{-1}(d - B\underline{x}) < \infty$$

since

$$\lim_{\varepsilon \to 0} \underline{y} = 0 .$$

So it is seen that the jump condition does not exist in this problem, and the asymptotic solution is applicable for all time.

4. The Inner Boundary Layer Solution of M_3

We now consider the governing Eq. (3.4) of our system and its basic solution given by Eqs. (3.20), (3.21) and (3.25). It is evident that the asymptotic series has reduced the differential equations to algebraic relations. It has happened because the time scale chosen for these solutions is unity. This means that these solutions are valid for large values of time. So, the time scale is now enlarged near $t = 0$. The boundary layer solutions thus obtained exhibit marked changes in their nature.

Let τ be given by

$$t = \varepsilon\tau \quad \text{for} \quad 0 \leq t \leq \varepsilon \ . \tag{3.56}$$

Then, expanding $A_{ij}(\underline{\omega},t)$ around $t = 0$, and $\underline{\omega} = \underline{\omega}_0$, we get

$$A_{ij}(\underline{\omega},t) = A_{ij}(\underline{\omega},0) + \varepsilon\dot{A}_{ij}(\underline{\omega},0)\tau + \frac{\varepsilon^2}{2}\ddot{A}_{ij}(\underline{\omega},0)\tau^2 + \ldots \tag{3.57}$$

$$A_{ij}(\underline{\omega},0) = A_{ij}(\underline{\omega}_0,0) + \varepsilon A_{ij,k}(\underline{\omega}_0,0)\omega_{1k} + \varepsilon^2[A_{ij,k}(\underline{\omega}_0,0)\omega_{2k} + \frac{1}{2}A_{ij,k\ell}(\underline{\omega}_0,0)\omega_{1k}\omega_{1\ell}] + \ldots \tag{3.58}$$

$$\dot{A}_{ij}(\underline{\omega},0) = \dot{A}_{ij}(\underline{\omega}_0,0) + \varepsilon\dot{A}_{ij,k}(\underline{\omega}_0,0)\omega_{1k} + \ldots \tag{3.59}$$

Similarly, $B_{ij}(\underline{\omega},t)$ and $d_i(\underline{\omega},t)$ are expanded in Taylor's series around $t = 0$ and $\underline{\omega} = \underline{\omega}_0$.

Then, substituting these expansions in Eq. (3.4), and using the relations

$$\frac{d\underline{y}}{dt} = \frac{1}{\varepsilon}\frac{d\underline{y}}{d\tau} \tag{3.60}$$

and

$$\frac{d^2\underline{y}}{dt^2} = \frac{1}{\varepsilon^2}\frac{d^2\underline{y}}{d\tau^2} \tag{3.61}$$

the coefficients of ε^{-1} and ε^0 generate the following equations:

$$\frac{d^2}{d\tau^2}\underline{y}(\underline{\omega}_0,\tau) = 0 \tag{3.62}$$

$$[A(\underline{\nabla}\, y)](\underline{\omega}_0,0)\frac{d^2\underline{\omega}_1}{d\tau^2} + B(\underline{\omega}_0,0)\frac{d}{d\tau}\underline{y}(\underline{\omega}_0,0) + \underline{y}(\underline{\omega}_0,0) = 0. \tag{3.63}$$

Hence, for $\tau \leq 1$, we have

$$\underline{y}(\underline{\omega}_0,\tau) = a\tau + b \tag{3.64}$$

and

$$\underline{\omega}_1(\tau) = -[(\underline{\nabla}\, \underline{y})^{-1} A^{-1}](\underline{\omega}_0,0)[B(\underline{\omega}_0,0)a + b]\tau \tag{3.65}$$

where a,b are constants and

$$\underline{\omega}_1(0) = 0 .$$

Thus at the inner boundary layer, $\underline{\omega}$ is given by

$$\underline{\omega} = \underline{\omega}_0 + \varepsilon\underline{\omega}_1 \tag{3.66}$$

where $\underline{\omega}_0$ is the solution of Eq. (3.64). The constants a and b will be obtained by matching this solution with the asymptotic solution at $\tau = 1$.

5. The Outer Boundary Layer Solution

A necessary condition to be satisfied by all boundary layer solutions is that these solutions must coincide with the large time solutions as τ becomes infinite. It is seen that the basic large time solution for $\underline{y}(\underline{\omega},t)$ is given by

$$\underline{y}(\underline{\omega}_0,t) = 0 . \tag{3.20}$$

The corresponding inner boundary layer solution is given by

$$\underline{y}(\underline{\omega}_0,\tau) = a\tau + b \ . \tag{3.64}$$

As these two solutions are incompatible as $\tau \to \infty$, we look for an outer boundary layer solution with a different time scale.

Let τ be given by

$$t = \sqrt{\varepsilon}\tau \quad \text{for} \quad 0 \le t \le \sqrt{\varepsilon} \ . \tag{3.67}$$

With this scale, we have

$$\frac{d\underline{y}}{dt} = \frac{1}{\sqrt{\varepsilon}} \frac{d\underline{y}}{d\tau} \tag{3.68}$$

$$\frac{d^2\underline{y}}{dt^2} = \frac{1}{\varepsilon} \frac{d^2\underline{y}}{d\tau^2} \ . \tag{3.69}$$

The functions $A(\underline{\omega},t)$, $B(\underline{\omega},t)$, $\underline{d}(\underline{\omega},t)$ and $\underline{y}(\underline{\omega},t)$ we expanded as before around $\underline{\omega} = \underline{\omega}_0$ and $t = 0$. These expansions and the relations (3.68) and (3.69) are then substituted into Eq. (3.4). Then, collecting the terms containing ε^0 and $\sqrt{\varepsilon}$, and equating that to zero, we get

$$A_{ij}(\underline{\omega}_0,0)\ddot{y}_j(\underline{\omega}_0,\tau) + \sqrt{\varepsilon}\, B_{ij}(\underline{\omega}_0,0)\dot{y}_j(\underline{\omega}_0,\tau) + y_i(\underline{\omega}_0,\tau) = 0. \tag{3.70}$$

Equating the coefficients of ε to zero, we get

$$[A(\underline{\nabla}\, \underline{y})](\underline{\omega}_0,0)\ddot{\underline{\omega}}_1 + 2[A(\underline{\nabla}\, \dot{\underline{y}})]\dot{\underline{\omega}}_1 + \underline{\nabla}[A\ddot{\underline{y}} + \underline{y}](\underline{\omega}_0,0)\underline{\omega}_1 = \underline{d}(\underline{\omega}_0,0) \tag{3.71}$$

Thus it is seen that with this time scale, the quantities $\underline{y}(\underline{\omega}_0,\tau)$ and $\underline{\omega}_1(\underline{\omega}_0,\tau)$ satisfy the equations for damped oscillations. Setting $\tau = \infty$ in these solutions leads to the long term solutions. Equations (3.70) and (3.71) are solved by using $\underline{\omega}(0)$ instead of $\underline{\omega}_0$ in the coefficients of $\dot{y}_j$, $\ddot{y}_j$, $\underline{\omega}_1$, $\dot{\underline{\omega}}_1$ and $\ddot{\underline{\omega}}_1$.

6. Special Cases

We now consider some special cases of Eq. (3.1).

a) Case 1: $M_2 = 0$

If for a given set of parameters, the nominal value of M_2 is either zero or very small compared to M_1, then from Eq. (3.3), we have

$$M_1\dot{\underline{q}} = \underline{M}_3 \tag{3.72}$$

or

$$\dot{\underline{q}} = M_1^{-1}\underline{M}_3 \ . \tag{3.73}$$

Differentiating Eq. (3.72) and neglecting $\dot{M}_1$, we get

$$\ddot{q} = M_1^{-1}\dot{M}_3 \ . \tag{3.74}$$

Integrating Eq. (3.73) by parts, and neglecting $\frac{d}{dt}(M_1^{-1})$, we have

$$q = M_1^{-1}\int_0^t M_3 dt \ . \tag{3.75}$$

Substituting $\ddot{q}$, $\dot{q}$, and q from Eqs. (3.74), (3.73) and (3.75) into Eq. (3.2), we get

$$A_1M_1^{-1}\dot{M}_3 + A_2M_1^{-1}M_3 + A_3M_1^{-1}\int_0^t M_3 dt = A_4 \ . \tag{3.76}$$

We now consider the three possible variations of M_1 when M_2 is zero.

i) <u>Case 1-1</u>: $M_2 = M_1 = 0$. In this case the only solution for (3.1) from Eq. (3.3) is

$$M_3 = 0 \ . \tag{3.77}$$

Again,

$$M_1 = M_2 = M_3 = 0$$

implies

$$P_1 = P_2 = P_3 = P_4 = 0 \ .$$

This means that the angular velocities are given by the rigid body motion of the satellite, and are not influenced by the flexibilities of the elements.

ii) Case 1-2: $M_2 = 0$ and $P_2A_2^{-1} < P_1A_1^{-1}$. In this case $(I + P_1A_1^{-1})^{-1}(I + P_2A_2^{-1}) < I$, where I is the identity matrix. Therefore

$$M_1^{-1} = A_2^{-1}[I - (I + P_1A_1^{-1})^{-1}(I + P_2A_2^{-1})]^{-1}$$

$$= A_2^{-1}[I + (I + P_1A_1^{-1})^{-1}(I + P_2A_2^{-1}) + (I + P_1A_1^{-1})^{-2}(I + P_2A_2^{-1})^2 + \ldots]$$

or

$$M_1^{-1} \cong 3A_2^{-1}[I - P_1A_1^{-1} + P_2A_2^{-1}] \quad . \tag{3.78}$$

Then Eq. (3.76) reduces to

$$A_1A_2^{-1}[I - P_1A_1^{-1} + P_2A_2^{-1}]\dot{M}_3 + [I - P_1A_1^{-1} + P_2A_2^{-1}]M_3 + A_3A_2^{-1}[I - P_1A_1^{-1} + P_2A_2^{-1}] \int_0^t M_3 dt = \frac{1}{3} A_4 \quad . \tag{3.79}$$

Now, usually $[A_2]$ is small. Therefore, Eq. (3.76) becomes

$$(M_1A_3^{-1}A_1M_1^{-1})\ddot{N}_3 = (M_1A_3^{-1}A_4) \tag{3.80}$$

where

$$N_3 = \int_0^t M_3 dt \quad . \tag{3.81}$$

Then using Eq. (3.78), Eq. (3.80) becomes

$$\ddot{N}_3 + 3[(P_1A_1^{-1} - P_2A_2^{-1})A_2A_1^{-1}A_3A_2^{-1}]N_3 = 3(P_1A_1^{-1} - P_2A_2^{-1})A_2A_1^{-1}A_4. \tag{3.82}$$

iii) Case 1-3: $M_2 = 0$ and $P_2A_2^{-1} > P_1A_1^{-1}$. In this case,

$$(I + P_1A_1^{-1})^{-1}(I + P_2A_2^{-1}) > I \quad .$$

Then

$$M_1^{-1} = -A_2^{-1}(I + P_2A_2^{-1})^{-1}(I + P_1A_1^{-1})[I - (I + P_2A_2^{-1})^{-1}(I + P_1A_1^{-1})]^{-1}$$

or

$$M_1^{-1} \cong -A_2^{-1}[2I - 3P_2A_2^{-1} + 3P_1A_1^{-1}] \ . \tag{3.83}$$

Then Eq. (3.76) reduces to

$$A_1A_2^{-1}(2I - 3P_2A_2^{-1} + 3P_1A_1^{-1})\dot{M}_3 + (2I - 3P_2A_2^{-1} + 3P_1A_1^{-1})M_3$$

$$+ A_3A_2^{-1}(2I - 3P_2A_2^{-1} + 3P_1A_1^{-1}) \int_0^t M_3 dt = -A_4 \ . \tag{3.84}$$

If $[A_2]$ is small, then Eq. (3.80) becomes

$$\ddot{N}_3 + 2[(P_2A_2^{-1} - P_1A_1^{-1})A_2A_1^{-1}A_3A_2^{-1}]N_3 = (P_1A_1^{-1} - P_2A_2^{-1})A_2A_1^{-1}A_4 \ . \tag{3.85}$$

b) Case 2: $M_2 \neq 0$ and $P_3A_3^{-1} < P_1A_1^{-1}$

If $M_2 \neq 0$, then the general equation (3.1) is to be considered. A simplified form of M_2 is derived now. We have

$$(I + P_3A_3^{-1}) < (I + P_1A_1^{-1}).$$

Therefore

$$M_2^{-1} = A_3^{-1}[I - (I + P_1A_1^{-1})^{-1}(I + P_3A_3^{-1})]^{-1}$$

$$= A_3^{-1}[I + (I + P_1A_1^{-1})^{-1}(I + P_3A_3^{-1}) + (I + P_1A_1^{-1})^{-2}(I + P_3A_3^{-1})^2 + \ldots]$$

or

$$M_2^{-1} \cong 3A_3^{-1}[I - P_1A_1^{-1} + P_3A_3^{-1}] \tag{3.86}$$

i) <u>Case 2-1</u>: $M_2 \neq 0$, $P_3A_3^{-1} < P_1A_1^{-1}$, $M_1 = 0$. From Eq. (3.3), we have

$$M_2q = M_3 \tag{3.87}$$

or

$$q = M_2^{-1}M_3 \ . \tag{3.87a}$$

Differentiating Eq. (3.15) and neglecting $\dot{M}_2$, we get

$$M_2\dot{q} = \dot{M}_3 \tag{3.88}$$

and

$$M_2\ddot{q} = \ddot{M}_3 \cdot \tag{3.89}$$

Substituting q, $\dot{q}$, $\ddot{q}$ from Eqs. (3.87), (3.88) and (3.89) in Eq. (3.2), we get

$$A_1M_2^{-1}\ddot{M}_3 + A_2M_2^{-1}\dot{M}_3 + A_3M_2^{-1}M_3 = A_4 \cdot \tag{3.90}$$

Then from Eqs. (3.86) and (3.90), for small A_2, we get

$$\ddot{M}_3 + 3M_2A_1^{-1}(I - P_1A_1^{-1} + P_3A_3^{-1})M_3 = M_2A_1^{-1}A_4$$

or

$$\ddot{M}_3 + [3(P_1A_1^{-1} - P_3A_3^{-1})A_3A_1^{-1}]M_3 = (P_1A_1^{-1} - P_3A_3^{-1})A_3A_1^{-1}A_4 \tag{3.91}$$

ii) Case 2-2: $M_2 \neq 0$; $P_3A_3^{-1} < P_1A_1^{-1}$; $P_2A_2^{-1} < P_1A_1^{-1}$.

The Eq. (3.86) is substituted in Eq. (3.1) to obtain

$$3[(P_1A_1^{-1} - P_3A_3^{-1})A_1A_3^{-1}]\ddot{M}_3 + 3[(P_2A_2^{-1} - P_3A_3^{-1})A_2A_3^{-1}]\dot{M}_3 + M_3 = (P_1A_1^{-1} - P_3A_3^{-1})A_4 \cdot \tag{3.92}$$

This is the required equation for M_3 in this case.

iii) Case 2-3: $M_2 \neq 0$; $P_3A_3^{-1} < P_1A_1^{-1}$; $P_2A_2^{-1} > P_1A_1^{-1}$. Here the form of the reduced equation does not change and Eq. (3.92) remains valid.

c) Case 3: $M_2 \neq 0$; $P_3A_3^{-1} > P_1A_1^{-1}$.

In this case,

$$(I + P_3A_3^{-1}) > (I + P_1A_1^{-1}) \cdot$$

Therefore

$$M_2^{-1} = A_3^{-1}[I - (I + P_1A_1^{-1})^{-1}(I + P_3A_3^{-1})]^{-1}$$

$$= -A_3^{-1}(I + P_3A_3^{-1})^{-1}(I + P_1A_1^{-1})[I + (I + P_3A_3^{-1})^{-1}(I + P_1A_1^{-1})$$

$$+ (I + P_3A_3)^{-2}(I + P_1A_1^{-1})^2 + \ldots]$$

or

$$M_2^{-1} = -A_3^{-1}[2I + 3P_1A_1^{-1} - 3P_3A_3^{-1}] \ . \qquad (3.93)$$

i) Case 3-1: $M_2 \neq 0$; $P_3A_3^{-1} > P_1A_1^{-1}$; $M_1 = 0$. For small A_2, Substituting Eq. (3.93) in Eq. (3.90), the equation for M_3 is obtained as

$$\ddot{M}_3 - M_2A_1^{-1}(2I + 3P_1A_1^{-1} - 3P_3A_3^{-1})M_3 = M_2A_1^{-1}A_4$$

or

$$\ddot{M}_3 + [2(P_3A_3^{-1} - P_1A_1^{-1})A_3A_1^{-1}]M_3 = (P_1A_1^{-1} - P_3A_3^{-1})A_3A_1^{-1}A_4. \qquad (3.94)$$

ii) Case 3-2: $M_2 \neq 0$; $P_3A_3^{-1} > P_1A_1^{-1}$; $P_2A_2^{-1} < P_1A_1^{-1}$. The Eq. (3.93) is substituted in Eq. (3.1) to obtain

$$[2(P_3A_3^{-1} - P_1A_1^{-1})A_1A_3^{-1}]\ddot{M}_3 + [2(P_3A_3^{-1} - P_2A_2^{-1})A_2A_3^{-1}]\dot{M}_3 + M_3$$

$$= (P_1A_1^{-1} - P_3A_3^{-1})A_4 \ . \qquad (3.95)$$

This is the required equation for M_3 in this case.

iii) Case 3-3: $M_2 \neq 0$; $P_3A_3^{-1} > P_1A_1^{-1}$; $P_2A_2^{-1} > P_1A_1^{-1}$. In this case, too, the equation for M_3 remains the same as Eq. (3.95).

d) Solutions for the special cases

The long-time solution and the boundary layer solutions have been obtained for Eq. (3.4) which is the general equation for the system. By redefining the variables y, A_{ij}, B_{ij} and d, the equations for all the special cases derived earlier can be brought in the form of Eq. (3.29). After that the analysis for the special cases is identical to that of the general case. It is interesting to observe that the basic solutions for $\omega_0(t)$ are not affected by those simplifications except in the cases 1-2 and 1-3.

7. Stability Criteria of $\underline{M}_3$

In our present notations, the Eqs. (2.122) and (2.124) are given by

$$[(P_1A_1^{-1} - P_3A_3^{-1})A_1M_2^{-1}]\ddot{M}_3 + [(P_2A_2^{-1} - P_3A_3^{-1})A_2M_2^{-1}]\dot{M}_3 + M_3$$

$$= (P_1A_1^{-1} - P_3A_3^{-1})A_4 \ . \tag{3.1}$$

It is to be noted here that the motion is stable when the angular velocities $\underline{\omega}_A$ and $\underline{\omega}_B$ are stable. Now M_3 is a complex differential form involving $\underline{\omega}_A$ and $\underline{\omega}_B$. So for the motion to be stable, a necessary but not sufficient condition is that M_3 should be bounded.

Examining Eq. (3.1), it is evident that as P_1, P_3, A_1, A_3 and A_4 are bounded, M_3 will be bounded if and only if the coefficients of $\ddot{M}_3$ and $\dot{M}_3$ are positive semidefinite. It is also seen that A_1 is positive definite as it is the generalized mass matrix. So this makes the coefficient of $\ddot{M}_3$ positive-semidefinite. Then the remaining required condition is that $[(P_2A_2^{-1} - P_3A_3^{-1})A_2M_2^{-1}]$ must be positive-semidefinite.

Now, M_2 is positive if $P_1A_1^{-1} > P_3A_3^{-1}$ and M_2 is negative if $P_1A_1^{-1} < P_3A_3^{-1}$. Considering our previous analysis, we see that if P_2 and A_2 are basically negative while A_1, A_3, P_1 and P_3 are positive, the coefficient of M_3 will be positive-definite if the following inequalities hold:

$$P_1A_1^{-1} < P_3A_3^{-1} < P_2A_2^{-1} \tag{3.96}$$

$$P_1A_1^{-1} > P_3A_3^{-1} > P_2A_2^{-1} \ . \tag{3.97}$$

If

$$M_1 = 0,$$

then from Eq. (3.18) we see that stability is ensured if A_2 is positive-semidefinite.

Again, if

$$M_2 = 0,$$

then from Eq. (3.4), the stability is also ensured if A_2 is positive-semidefinite.

If all the quantities P_1, P_2, P_3, A_1, A_2 and A_3 are positive, then the stability criterion for $\underline{M}_3$ is given by the following inequalities:

$$P_1A_1^{-1} > P_3A_3^{-1} > P_2A_2^{-1} \tag{3.98}$$

and

$$P_1A_1^{-1} < P_3A_3^{-1} > P_2A_2^{-1} \ . \tag{3.99}$$

8. Conclusions

In this report, we have analyzed several characteristics of the system and obtained solutions for the vector $\underline{y}$ defined by Eq. (3.30). The function $\underline{y}$ is an implicit function of the angular velocities $\underline{\omega}_A$ or $\underline{\omega}_B$. In the next part of our work we will discuss a few other features of the system before discussing the solutions for $\underline{\omega}_A$ or $\underline{\omega}_B$.

References

1. Holtzman, J. M., *Nonlinear System Theory; A Functional Analysis Approach*, Englewood Cliffs, N.J., Prentice-Hall, 1970, page 129.